The Theory of Porous Media in the Framework of the Mesh-in-Element Method

Von der Fakultät für Ingenieurwissenschaften,
Abteilung Bauwissenschaften
der Universität Duisburg-Essen
zur Erlangung des akademischen Grades

Doktor-Ingenieur

genehmigte Dissertation

von

Simon Maike, M.Sc.

1. Gutachter: Prof. Dr.-Ing. habil. Jörg Schröder
2. Gutachter: Univ.-Prof. Dr.-Ing. Tim Ricken

Tag der Einreichung: 25. Mai 2023
Tag der mündlichen Prüfung: 15. Dezember 2023

Fakultät für Ingenieurwissenschaften,
Abteilung Bauwissenschaften
der Universität Duisburg-Essen
Institut für Mechanik
Prof. Dr.-Ing. habil. J. Schröder

Berichte des Instituts für Mechanik, Universität Duisburg-Essen

Nr. 30

Herausgeber:

Prof. Dr.-Ing. habil. J. Schröder

Organisation und Verwaltung:

Prof. Dr.-Ing. habil. J. Schröder
Institut für Mechanik
Fakultät für Ingenieurwissenschaften
Abteilung Bauwissenschaften
Universität Duisburg-Essen
Universitätsstraße 2
45141 Essen
Tel.: 0201 / 183 - 2682
Fax.: 0201 / 183 - 2680

ISBN-13 978-3-9821811-6-5

Vorwort

Die vorliegende Arbeit entstand während meiner Tätigkeit als wissenschaftlicher Mitarbeiter am Institut für Mechanik (Abteilung Bauwissenschaften, Fakultät für Ingenieurwissenschaften) an der Universität Duisburg-Essen. An dieser Stelle möchte ich meinen persönlichen Dank an einige Menschen aussprechen, die zum Gelingen dieser Arbeit beigetragen haben.

An erster Stelle möchte ich meinem geschätzten Doktorvater Professor Jörg Schröder danken, der mir die Möglichkeit gab, unter seiner Leitung zu promovieren. Für seine Förderung und das entgegengebrachte Vertrauen bedanke ich mich sehr, auch im Bereich der zahlreichen gemeinsam betreuten Lehrveranstaltungen. Ein großer Dank gilt zudem Professor Tim Ricken für die Übernahme des Zweitgutachten und die fachlichen Diskussionen während der Promotionszeit. Gleiches gilt im Besonderen für Prof. Joachim Bluhm, der zwar im Rahmen dieser Promotion nicht als Gutachter fungiert hat, jedoch über all die Jahre stets außerordentlich hilfsbereit in allen Fragen rund um die Mechanik und im Speziellen im Kontext der Theorie der Porösen Medien war.

Seit meiner Themenanpassung während der Promotionszeit in Richtung der Mesh-in-Element Methode nahm Dr. Alexander Schwarz eine hervorzuhebende Rolle ein. Durch sein leidenschaftliches Interesse für Diskretisierungsmethoden hatte ich stets einen ausdauernden und voranbringenden Diskussionspartner. Darüber hinaus gilt mein Dank Dr. Dominik Brands, der viele Male, auch außerhalb der üblichen Bürozeiten, für technischen Support erreichbar war.

Neben der fachlichen Komponente, möchte ich mich auch beim gesamten Insitut für die angenehme gemeinsame Zeit bedanken. Auch wenn ich als einer der wenigen von einer externen Hochschule zum Team hinzugestoßen bin, habe ich mich von Beginn an heimisch gefühlt. Besonders hervorzuheben sind dabei meine langjährigen Bürokollegen Nils Viebahn und Maximilian Scheunemann, die in zahlreichen treffsicheren Auseinandersetzungen zum Abschluss meiner Promotion beigetragen haben. Speziell für die Endphase meiner Promotionszeit möchte ich mich bei Julia Sunten, Sonja Hellebrand und Yasemin von Hoegen bedanken, die seit der Pandemie bis zur Promotionsfeier bei vielen organisatorischen Angelegenheiten stets zuvorkommend geholfen und mir somit viele Fahrten aus der Ferne nach Essen erspart haben. Herzlichst möchte ich mich bei den verbleibenden Mitarbeitern in meiner Zeit am Institut für Mechanik bedanken: Solveigh Averweg, Daniel Balzani, Marcos Margalho de Barros, Simon Fausten, Ashutosh Gandhi, Philipp Hartwig, Markus von Hoegen, Veronika Jorisch, Simon Kugai, Veronika Lemke, Matthias Labusch, Petra Lindner-Roullé, Sascha Maassen, Rainer Niekamp, Paulo Nigro, Mangesh Pise, Markus Prangs, Sabine Ressel, Maximilian Reichel, Mohammad Sarhil, Lisa Scheunemann, Thomas Schmidt, Carina Schwarz, Serdar Serdaş, Steffen Specht, Karl Steeger, Masato Tanaka, Huy Ngoc Thai und Xiaodong Xia.

Der abschließende Dank gilt meiner gesamten Familie für die Unterstützung und das Verständnis auf dem zugegebenermaßen langen Weg. Im Speziellen bin ich meiner Frau Annika und indirekt unseren Kindern Jannis und Layla auf ewig dafür dankbar, dass sie mir in der anstrengenden Phase der Familiengründung stets die Freiräume gewährt haben, das Ziel der Promotion trotz Rückschlägen weiterzuverfolgen und abzuschließen.

Kempen, im Dezember 2023 Simon Maike

Abstract

The simulation of porous media with full resolution of the heterogeneous microstructure is challenging because of its complexity. This leads to exceeding computational costs in case the investigated domain is way larger than the length scale of the microscopic heterogeneities. Homogenization approaches as the Theory of Porous Media (TPM) can be applied to address this problem. Nevertheless, the system of equation can still be to large to solve within the classical Finite Element Method (FEM) in case of remaining macroscopic scale heterogeneities.
In this context, this thesis presents the TPM within the framework of the Mesh-in-Element (MIEL) multiscale approach. The goal is to benefit from the classical homogenization within the TPM but still being able to cover lower level effects in a strong scale coupling multiscale approach at reasonable computational costs. The theoretical concepts are elaborated for the TPM, the FEM as well as the MIEL method. The latter is first applied to pure elasticity in solid mechanics within academical numerical examples to reveal the basic characteristics of the MIEL method without the higher complexity of the TPM. Subsequently, the fusion of TPM and MIEL method is investigated for academical as well as more realistic problems to determine its performance and range of application. The focus therein lies on the comparison to single scale computations in terms of information loss and numerical efficiency.

Zusammenfassung

Die Simulation poröser Medien bei voller Auflösung der heterogenen Mikrostruktur ist aufgrund ihrer Komplexität eine Herausforderung. Dies führt zu einem sehr hohen Rechenaufwand, falls der untersuchte Bereich viel größer als die Längenskala der mikroskopischen Heterogenitäten ist. Homogenisierungsansätze wie die Theorie Poröser Medien (TPM) können zur Lösung dieses Problems eingesetzt werden. Dennoch kann das Gleichungssystem zu groß bleiben, um es mit der klassischen Finite Elemente Methode (FEM) zu lösen, falls Heterogenitäten auf der makroskopischen Ebene verbleiben.
In diesem Zusammenhang präsentiert die vorliegende Arbeit die TPM im Rahmen des Mesh-in-Element (MIEL) Multiskalenansatzes. Das Ziel ist, von der klassischen Homogenisierung in der TPM zu profitieren, aber dennoch in der Lage zu sein, Effekte auf niedrigerer Ebene in einem Multiskalenansatz mit starker Skalenkopplung unter vertretbarem Rechenaufwand abzubilden. Die theoretischen Konzepte werden für die TPM, die FEM sowie die MIEL Methode erarbeitet. Letztere wird zunächst auf die reine Elastizität in der Festkörpermechanik in akademischen numerischen Beispielen angewandt, um die grundlegenden Eigenschaften der MIEL Methode ohne die höhere Komplexität der TPM aufzuzeigen. Anschließend wird die Kombination von TPM mit MIEL Methode sowohl für akademische, als auch für realitätsnähere Probleme untersucht, um ihre Leistungsfähigkeit und ihren Anwendungsbereich zu bestimmen. Der Schwerpunkt liegt dabei auf dem Vergleich mit Einskalenberechnungen in Bezug auf Informationsverluste und numerische Effizienz.

Contents

1 Introduction and Motivation

Porous media are heterogeneous materials which consist of a solid skeleton filled by at least one liquid. Several geomaterials as clay but as well human tissue and also industrially manufactured materials like foams belong to this class. Problems arise if these complex structures are to be simulated at larger scale than a small detail. Even today, such a simulation with full resolution of the microstructure is almost impossible due to exceeding computational costs.

One possibility to circumvent this problem is the application of a macroscopic homogenization approach as the Theory of Porous Media (TPM). Its fundamentals are given by the classical continuum mechanics to describe a single component material, which is discussed in detail in e.g. Holzapfel [2000], Stein and Barthold [1996], Truesdell and Noll [2004] or Schröder et al. [2024]. The Theory of Mixtures (TM) extends this principle to a compound of miscible, interacting constituents homogenized as a smeared model, see exemplary Truesdell and Toupin [1960], Bowen [1976] and Truesdell [1984]. Based on this, Bowen [1980; 1982] combined the Theory of Mixtures with the Concept of Volume Fractions, see e.g. Biot [1941; 1956], to investigate immiscible constituents which allows tracking the evolution of the different phases at every point within the domain. For an overview on the TPM, see Ehlers [1989], Bluhm [2002], Ehlers [2002] and de Boer [2005] while an extensive work on the historical development of the approach can be found in de Boer [2000].

But even after applying the TPM to the simulation of heterogeneous materials, the discrete macroscopic system of equations can get too large for a single scale computation due to remaining heterogeneities within the boundary value problem. Such a problem can be interpreted as a three scale problem of micro-, meso- and macroscale. At this point, adding a multiscale scheme seems promising. In literature exists a large amount of multiscale approaches which could be considered, see e.g. Fish [2014], Efendiev and Hou [2009] and Geers et al. [2010] for an overview. These strategies can roughly be divided into two groups, depending on whether the coupling of the scales is weak or strong. A weak coupling of the scales, often called scale separation, assumes that the size of the heterogeneities is way smaller than the investigated structure. Following this argumentation, the effective properties necessary for computations on macroscopic level are determined by solving microscale problems on a unit cell or a representative volume element (RVE), see Nemat-Nasser and Hori [1999].

One class of multiscale methods including scale separation is based on asymptotic expansion, see Bensoussan et al. [1978] and Sanchez-Palencia [1980]. This mathematically motivated method relies on the assumption of periodic structures and fields on the microscale. Another option at hand which originally considers scale separation is the so-called FE^2 method, see exemplary Smit et al. [1998], Miehe et al. [1999b], Miehe et al. [1999a], Terada et al. [2000], Feyel and Chaboche [2000], Kouznetsova et al. [2001] and Schröder [2014]. The crucial assumption of this method is the equivalence of the macroscopic internal power with its microscopic counterpart, commonly known as macro-homogeneity or Hill-Mandel condition, going back on Hill [1965] and Mandel [1972]. This condition defines the scale transition and leads to consistent boundary conditions on the RVE. A noteworthy possible third option within the framework of scale separation is the Heterogeneous Multiscale Method (HMM), cf. E and Engquist [2003] and Abdulle [2005]. Even if the motivation for

the methods varies, they often lead to similar problems to solve. This has been shown exemplary in Eidel and Fischer [2018] for the HMM with respect to the FE^2 scheme.

All of these methods have been applied to various problems, but the treatment of the Theory of Porous Media or similar approaches to consider fluid-solid interactions within such a scheme is comparatively rare. Within a first order FE^2 scheme, where constant gradients are passed from the macroscale to drive the microscale response, Jänicke et al. [2015] applied the TPM at the mesoscale, but a single phase medium on the macroscale. TPM on both FE^2 scales, denoted as TPM^2, was applied by Ricken et al. [2022]. Therein, the application of the preferable periodic boundary conditions remains an open challenge. This issue has been a part of the early stages of research leading to this thesis.

To get further insights into the topic of lower level boundary conditions, the consideration of volume or inertia loads in single phase elasticity within the FE^2 method can be taken into account. This is motivated by the fact that the fluid pressure gradient acts on the solid phase within the TPM similar to a volume load in single phase elasticity, briefly outlined in Chapter 4. In literature, the volume load is often at the most considered on the macroscale but neglected on the microscale. This approach is commonly justified by the assumption of scale separation. In contrast to this, volume and inertia loads have been taken into account within the frameworks of Irving-Kirkwood statistical mechanics by Mandadapu et al. [2012] and extended Hill-Mandel conditions by Ricker et al. [2009], de Souza Neto et al. [2015] and Tamsen and Balzani [2021]. While the work of Ricker et al. [2009] leads to self-equilibrated volume loads, de Souza Neto et al. [2015] set up a theory which allows arbitrary distributions with help of the introduction of a kinematic constraint on the microscopic fluctuations which has been adopted by Tamsen and Balzani [2021]. Nevertheless, the classical FE^2 scheme remains limited in resolving the response of vector valued loading types as a body force due to the scale separation. For example, a constant body force on microscopic level does not trigger any fluctuations for the simplest case of a homogeneous material following the approach by de Souza Neto et al. [2015]. This leads to constant strain over the RVE even though the analytical solution would be linear. That effect, discussed in detail in Chapter 4, can be justified by the assumption of scale separation but redirects interest for such problems, in this work for poroelastic mediums described by the TPM, towards methods with a strong coupling between the scales. For the sake of completeness, please note that there exist numerous strategies to improve the performance of homogenization techniques with scale separation for applications where the classical approaches are limited. For example the consideration of higher order gradients, respectively generalized continua, e.g. Kouznetsova et al. [2002], Forest [2002] and Jänicke and Diebels [2010] is of great interest in current research. Furthermore, Larsson and Runesson [2011] developed an approach named Scalebridging Variational Multiscale Strategy (SVMS) where the intensity of scale coupling is a model parameter.

A huge variety of multiscale methods with strong scale coupling have been developed during the last decades, for an overview see Efendiev and Hou [2009] and Fish [2014] and the references therein. In contrast to the scale separation for weak coupling strategies, the physical size of the microscale problem is directly connected to the corresponding domain on the macroscale. An approach which has been adopted and extended by great extend was introduced by Hou and Wu [1997] as the Multiscale Finite Element Method (MsFEM). Therein, the macroscopic basis functions are enhanced with help of

pre-computed microscopic problems. In the initial work, they chose a larger microscopic problem domain than the corresponding macroscopic element to reduce the influence of the applied boundary conditions on the microscopic scale. Another significant contribution was made by Hughes [1995] who introduced the Variational Multiscale Method (VMM), where the problem on the macroscale is solved within the Finite Element Method (FEM), but each element contains a microscopic problem which is solved analytically towards a Green's function. The method is based on the additive split into coarse and fine scale displacements. The scale transition requires that the fine scale displacements vanish at the boundary of the microscopic problem. This rather strict constraint on the scale transition has been softened subsequently to exemplary take into account cracks within the microscopic problem boundary, cf. Hund and Ramm [2007]. Please note that such phenomena are not in the scope of this work since the TPM is already a homogenized continuum theory. An approach similar to the VMM but with the FEM on both scales was made by Ibrahimbegović and Markovič [2003]. They relaxed the constraint of fixing the degrees of freedom at the microscopic problem boundary according to the macroscopic counterparts by defining the transition within a variational concept with help of Lagrange multipliers in Markovič and Ibrahimbegović [2004]. This enhancement comes with the cost of an additional iteration loop at microscopic level. They adopted this strategy from Park and Felippa [2000] who introduced it within domain decomposition to model the interface between disjunct parts of the domain. One major advantage of such a multiscale approach with FE models on both scales compared to a single scale FE computation with a fine mesh density is the parallelizability of the microscopic problems, cf. Markovič et al. [2005] and Niekamp et al. [2009].

The approach by Markovič and Ibrahimbegović [2004] has been adopted recently by Zupan and Korelc [2018] as Mesh-in-Element (MIEL) method investigating finite elasticity where they restrict themselves again to the direct scale coupling solely depending on the macroscopic degrees of freedom. The comparatively straight forward scheme allows a nearly general-purpose theory which can be applied to wide range of problems. They deviate from the initial work in terms of the method for extracting the macroscopic element tangent and residual from the respective microscopic problem by using a sensitivity analysis instead of a combination of static condensation and subsequent transformation.

The MIEL method is chosen to be applied to the TPM within this thesis. This strong scale coupling approach avoids the discussed remaining issues on the scale separation for weak coupling schemes of such problems. Numerical efficiency seems promising due to a robust scheme including easy parallelizability of the microscopic problems. Additionally, the rather strict interface condition can be improved by increasing the interpolation order of the macroscopic element, see Chapter 7. The finite element implementations and computations within this thesis have been done using the *AceGen* and *AceFEM* package (version 7.403), see Korelc [2009] and Korelc and Wriggers [2016] of *Mathematica* (version 12.3), see Wolfram Research, Inc. [2021]. Some parts of this thesis have been published in Maike et al. [2023].

This thesis is organized as follows. Chapter 2 starts with the introduction of the general framework of the TPM. Subsequently, a few simplifying assumptions lead to a binary model. The chapter closes with some remarks on linear theory for a single solid phase material which is taken as first example to analyze the MIEL method. The Finite Element Method is outlined in Chapter 3, starting with finite elasticity before turning to the

TPM. Afterwards, both formulations are covered by a generalized notation which enables a neat notation for the following MIEL method. Additionally, the algorithmic treatment is outlined and the used finite element formulations within this thesis are presented. A slight detour is taken in Chapter 4 where the mentioned model deficit of the classical FE^2 scheme with respect to body forces in elasticity on the microscale is discussed. These findings are transferred to the TPM as well. The MIEL method is derived in Chapter 5 which consists of the definition of the microscopic problem, the subsequent derivation of the macroscopic problem, the construction of the scale transition matrix and the algorithmic treatment. The performance of this framework is first investigated with numerical examples for elasticity in Chapter 6 to allow for an simpler analysis of the arising effects compared to the more complex TPM model. The obtained findings are validated and extended with the aid of additional numerical examples of the TPM within the MIEL method in Chapter 7. The thesis in concluded in Chapter 8 with a summary and an outlook.

2 Theory of Porous Media

The following fundamentals of the Theory of Porous Media (TPM) in this chapter are based on Ehlers [2002] and Bluhm [2002]. Most of the derivations are given with respect to the current configuration. The pull back on the reference configuration, which is often favorable for the implementation in the framework of the FEM, is outlined at the end of the chapter after deriving the set of equations to solve. Overall, the theory in this chapter is limited to the scope of the thesis. In general, the TPM can be applied to numerous alternative equations requiring additional field quantities.

This chapter starts with an introduction into the Theory of Mixtures (TM) and the Concept of Volume Fractions before the continuum mechanical basics as kinematics, concept of stresses and balance principles with respect to the TPM are presented. Based on this, a binary model is derived and prepared towards an efficient numerical implementation. The chapter is closed by some remarks on the application to single solid phase materials and linear theory which is relevant for the first numerical examples within the MIEL method.

2.1 Theory of Mixtures

A real multi-phase structure consists of a set of k constituents φ^α with $\alpha = \{1, ..., k\}$. Investigating this usually complex structure in full resolution is computational too expensive for many applications. The Theory of Mixtures circumvents this problem as a homogenization approach which superimposes continua by assuming that every material point $\boldsymbol{x}$ within the body $\mathcal{B}$ is occupied by each constituent φ^α at time t, see Figure 2.1 for a binary model consisting of a solid and a liquid phase.

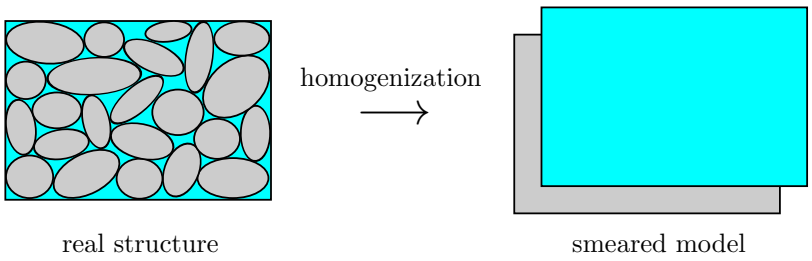

Figure 2.1: From real structure to smeared model.

In this context, $\mathcal{B}$ is the observed control space on which all the constituents are statistically distributed as a smeared model. Throughout this thesis, the control space is chosen to be the domain of the solid $\mathcal{B}_\mathrm{S}$. As a consequence, the solid phase is not able to leave or enter the control space while the remaining liquid or gaseous phases can.

Please note that the classical Theory of Mixtures assumes miscible constituents. Towards the Theory of Porous Media, the concept of volume fractions is added resulting in the investigation of immiscible phases.

2.2 Concept of Volume Fractions

The volume fraction n^α is given as a function of the position $\boldsymbol{x}$ and the time t as

$$n^\alpha = n^\alpha(\boldsymbol{x}, t) = \frac{\mathrm{d}v^\alpha}{\mathrm{d}v} \tag{2.1}$$

with the volume element $\mathrm{d}v^\alpha$ of the constituent φ^α and the volume element $\mathrm{d}v$ of the mixture. With this definition of the volume fraction, the partial volume of the constituent φ^α within the control space $\mathcal{B}_\mathrm{S}$ is defined as

$$v_\mathrm{S}^\alpha = \int_{\mathcal{B}_\mathrm{S}} \mathrm{d}v^\alpha = \int_{\mathcal{B}_\mathrm{S}} n^\alpha \, \mathrm{d}v \,. \tag{2.2}$$

The total volume of the control space $\mathcal{B}_\mathrm{S}$ can be written as the sum of all partial volumes as

$$v_\mathrm{S} = \int_{\mathcal{B}_\mathrm{S}} \mathrm{d}v = \sum_{\alpha=1}^{k} v_\mathrm{S}^\alpha \,. \tag{2.3}$$

As a direct consequence of Eq. (2.2) and (2.3), the saturation condition

$$\sum_{\alpha=1}^{k} n^\alpha = 1 \tag{2.4}$$

holds for saturated mixtures with no vacant space. Additionally, following the concept of volume fractions leads to two different density functions for each constituent with the real material density $\rho^{\alpha\mathrm{R}}$ and the partial density ρ^α as

$$\rho^{\alpha\mathrm{R}} = \frac{\mathrm{d}m^\alpha}{\mathrm{d}v^\alpha} \quad \text{and} \quad \rho^\alpha = \frac{\mathrm{d}m^\alpha}{\mathrm{d}v} \,. \tag{2.5}$$

While the real material density is the ratio of the local mass $\mathrm{d}m^\alpha$ of the constituent with respect to its partial volume $\mathrm{d}v^\alpha$, the partial density is defined as the ratio of the local mass $\mathrm{d}m^\alpha$ with respect to the total volume $\mathrm{d}v$. The partial density can be expressed in terms of the volume fraction and the real density as

$$\rho^\alpha = n^\alpha \, \rho^{\alpha\mathrm{R}} \,. \tag{2.6}$$

Please note that an incompressible material ($\rho^{\alpha\mathrm{R}} = \text{constant}$) does not imply a constant partial density since the volume fraction can still change. The overall density of the mixture is given by

$$\rho = \sum_{\alpha=1}^{k} \rho^\alpha = \sum_{\alpha=1}^{k} n^\alpha \, \rho^{\alpha\mathrm{R}} \,. \tag{2.7}$$

2.3 Kinematics

The kinematics within the TPM which originate from the TM are taken to describe a saturated porous solid as an immiscible mixture of k constituents φ^α with $\alpha = \{1, ..., k\}$. For this purpose, each constituent is assigned an own motion function, given in the Lagrangian form as

$$\boldsymbol{x} = \boldsymbol{\chi}_\alpha(\boldsymbol{X}_\alpha, t) \,, \tag{2.8}$$

where $\boldsymbol{x}$ is the position vector in the current configuration at time t while the position vector of a particle of constituent φ^α in the reference configuration at time t_0 is denoted by $\boldsymbol{X}_\alpha$. This implies that a particle of each phase occupies the same position $\boldsymbol{x}$ within the control space $\mathcal{B}_\mathrm{S}$ in the current configuration but has in general different positions in

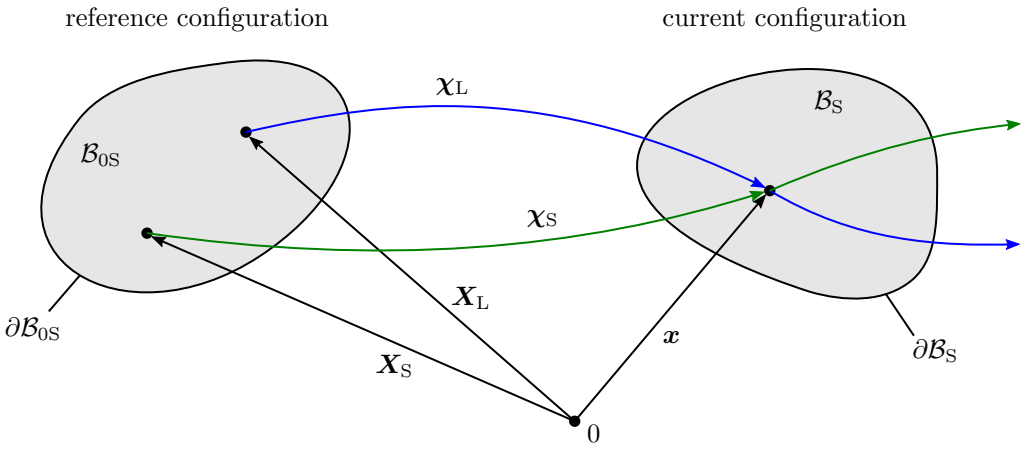

Figure 2.2: Motions of a solid and liquid particle in a binary model.

the reference or any future configurations. This framework is schematically depicted in Figure 2.2 for a binary model consisting of a solid and a liquid phase as $\alpha = \{\mathrm{S}, \mathrm{L}\}$.

Please note that the reference position $\boldsymbol{X}_\alpha$ of any other but the solid phase does not require to be an element of the control space in reference configuration $\mathcal{B}_{0\mathrm{S}}$. This analogously holds for any later than the current configuration as well.

If the motion function $\boldsymbol{\chi}_\alpha$ in Eq. (2.8) is unique and uniquely invertible at any time, there exists a motion function in Eulerian form as

$$\boldsymbol{X}_\alpha = \boldsymbol{\chi}_\alpha^{-1}(\boldsymbol{x}, t)\,. \tag{2.9}$$

The displacement $\boldsymbol{u}_\alpha$ of the constituent φ^α is defined as

$$\boldsymbol{u}_\alpha = \boldsymbol{x} - \boldsymbol{X}_\alpha \tag{2.10}$$

while the velocity $\boldsymbol{x}'_\alpha$ and the acceleration $\boldsymbol{x}''_\alpha$ can be written as

$$\boldsymbol{x}'_\alpha = \frac{\partial \boldsymbol{\chi}_\alpha(\boldsymbol{X}_\alpha, t)}{\partial t} \quad \text{and} \quad \boldsymbol{x}''_\alpha = \frac{\partial^2 \boldsymbol{\chi}_\alpha(\boldsymbol{X}_\alpha, t)}{\partial t^2} = \frac{\partial \boldsymbol{x}'_\alpha}{\partial t}\,. \tag{2.11}$$

For the following derivations it is reasonable to define the difference velocity of a liquid phase φ^β to the solid phase φ^{S}, denoted as seepage velocity, as

$$\boldsymbol{w}_{\beta\mathrm{S}} = \boldsymbol{x}'_\beta - \boldsymbol{x}'_{\mathrm{S}}\,. \tag{2.12}$$

The deformation gradient of the constituent φ^α is defined as

$$\boldsymbol{F}_\alpha = \frac{\partial \boldsymbol{\chi}_\alpha(\boldsymbol{X}_\alpha, t)}{\partial \boldsymbol{X}_\alpha} = \frac{\partial \boldsymbol{x}}{\partial \boldsymbol{X}_\alpha} = \mathrm{Grad}_\alpha(\boldsymbol{x}) \tag{2.13}$$

leading to its inverse as

$$\boldsymbol{F}_\alpha^{-1} = \frac{\partial \boldsymbol{\chi}_\alpha^{-1}(\boldsymbol{x}, t)}{\partial \boldsymbol{x}} = \frac{\partial \boldsymbol{X}_\alpha}{\partial \boldsymbol{x}} = \mathrm{grad}(\boldsymbol{X}_\alpha)\,. \tag{2.14}$$

The differential operator $\mathrm{Grad}_\alpha(\bullet)$ denotes a partial differentiation with respect to the position vector in reference configuration $\boldsymbol{X}_\alpha$, respectively $\mathrm{grad}(\bullet)$ with respect to the

position vector in current configuration $\boldsymbol{x}$. The mathematical requirement for the existence of the inverse of the deformation gradient in Eq. (2.14) as well as the inverse of the motion function in Eq. (2.9) is a nonzero Jacobian determinant

$$J_\alpha = \det(\boldsymbol{F}_\alpha)\,. \tag{2.15}$$

With the initial undeformed shape resulting in $\boldsymbol{F}_\alpha(t_0) = \mathbf{1}$ follows $J_\alpha > 0$ as a further constraint on the magnitude of the Jacobian determinant.

The fundamental transport theorems of classical continuum mechanics for line, area and volume elements can be adopted as

$$\begin{aligned} \mathrm{d}\boldsymbol{x} &= \boldsymbol{F}_\alpha \cdot \mathrm{d}\boldsymbol{X}_\alpha\,, \\ \mathrm{d}\boldsymbol{a} &= J_\alpha\, \boldsymbol{F}_\alpha^{-T} \cdot \mathrm{d}\boldsymbol{A}_\alpha = \mathrm{Cof}_\alpha(\boldsymbol{F}_\alpha) \cdot \mathrm{d}\boldsymbol{A}_\alpha\,, \\ \mathrm{d}v &= J_\alpha\, \mathrm{d}V_\alpha\,. \end{aligned} \tag{2.16}$$

There exists a variety of strain measures in continuum mechanics. Two important examples, applied to the constituent φ^α, are the right Cauchy-Green tensor $\boldsymbol{C}_\alpha$ and the Green-Lagrange strain tensor $\boldsymbol{E}_\alpha$. Both have the property to be independent from rigid body motions. Additionally, they are symmetric which is favorable for the implementation and computation. The right Cauchy-Green tensor is given

$$\boldsymbol{C}_\alpha = \boldsymbol{F}_\alpha^T \cdot \boldsymbol{F}_\alpha \tag{2.17}$$

which can be identified by using the line element transport theorem in Eq. (2.16) on the square of the line element in current configuration as

$$\mathrm{d}\boldsymbol{x} \cdot \mathrm{d}\boldsymbol{x} = (\boldsymbol{F}_\alpha \cdot \mathrm{d}\boldsymbol{X}_\alpha) \cdot (\boldsymbol{F}_\alpha \cdot \mathrm{d}\boldsymbol{X}_\alpha) = \mathrm{d}\boldsymbol{X}_\alpha \cdot \boldsymbol{C}_\alpha \cdot \mathrm{d}\boldsymbol{X}_\alpha\,. \tag{2.18}$$

On the other hand, the Green-Lagrange strain tensor is defined by

$$\boldsymbol{E}_\alpha = \frac{1}{2}(\boldsymbol{C}_\alpha - \boldsymbol{I}) \tag{2.19}$$

which is obtained by taking the difference of the square of the line elements in the current and reference configuration and inserting once more Eq. (2.16) leading to

$$\mathrm{d}\boldsymbol{x} \cdot \mathrm{d}\boldsymbol{x} - \mathrm{d}\boldsymbol{X}_\alpha \cdot \mathrm{d}\boldsymbol{X}_\alpha = 2\,\mathrm{d}\boldsymbol{X}_\alpha \cdot \boldsymbol{E}_\alpha \cdot \mathrm{d}\boldsymbol{X}_\alpha\,. \tag{2.20}$$

Please note that the Green-Lagrange strain tensor is zero in the undeformed state. The material velocity gradient is defined as

$$(\boldsymbol{F}_\alpha)'_\alpha = \frac{\partial}{\partial t}\left(\frac{\partial \boldsymbol{\chi}_\alpha(\boldsymbol{X}_\alpha, t)}{\partial \boldsymbol{X}_\alpha}\right) = \frac{\partial}{\partial \boldsymbol{X}_\alpha}\left(\frac{\partial \boldsymbol{\chi}_\alpha(\boldsymbol{X}_\alpha, t)}{\partial t}\right) = \frac{\partial \boldsymbol{x}'_\alpha}{\partial \boldsymbol{X}_\alpha} = \mathrm{Grad}_\alpha(\boldsymbol{x}'_\alpha) \tag{2.21}$$

while the spatial velocity gradient is given by

$$\boldsymbol{L}_\alpha = (\boldsymbol{F}_\alpha)'_\alpha \cdot \boldsymbol{F}_\alpha^{-1} = \frac{\partial \boldsymbol{x}'_\alpha}{\partial \boldsymbol{X}_\alpha} \cdot \frac{\partial \boldsymbol{X}_\alpha}{\partial \boldsymbol{x}} = \frac{\partial \boldsymbol{x}'_\alpha}{\partial \boldsymbol{x}} = \mathrm{grad}(\boldsymbol{x}'_\alpha)\,. \tag{2.22}$$

The spatial velocity gradient can be split additively as

$$\boldsymbol{L}_\alpha = \boldsymbol{D}_\alpha + \boldsymbol{W}_\alpha \tag{2.23}$$

into a symmetric part $\boldsymbol{D}_\alpha$ called rate of deformation tensor and a skew-symmetric part $\boldsymbol{W}_\alpha$ also known as spin tensor yielding to

$$\boldsymbol{D}_\alpha = \frac{1}{2}(\boldsymbol{L}_\alpha + \boldsymbol{L}_\alpha^T) \quad \text{and} \quad \boldsymbol{W}_\alpha = \frac{1}{2}(\boldsymbol{L}_\alpha - \boldsymbol{L}_\alpha^T)\,. \tag{2.24}$$

The material time derivative of the right Cauchy-Green tensor is given by

$$\begin{aligned}(\boldsymbol{C}_\alpha)'_\alpha &= (\boldsymbol{F}_\alpha^T \cdot \boldsymbol{F}_\alpha)'_\alpha = (\boldsymbol{F}_\alpha^T)'_\alpha \cdot \boldsymbol{F}_\alpha + \boldsymbol{F}_\alpha^T \cdot (\boldsymbol{F}_\alpha)'_\alpha \\ &= \boldsymbol{F}_\alpha^T \cdot \boldsymbol{L}_\alpha^T \cdot \boldsymbol{F}_\alpha + \boldsymbol{F}_\alpha^T \cdot \boldsymbol{L}_\alpha \cdot \boldsymbol{F}_\alpha = 2\,\boldsymbol{F}_\alpha^T \cdot \boldsymbol{D}_\alpha \cdot \boldsymbol{F}_\alpha\end{aligned} \tag{2.25}$$

leading to the material time derivative of the Green-Lagrange strain tensor as

$$(\boldsymbol{E}_\alpha)'_\alpha = \frac{1}{2}(\boldsymbol{C}_\alpha)'_\alpha = \boldsymbol{F}_\alpha^T \cdot \boldsymbol{D}_\alpha \cdot \boldsymbol{F}_\alpha\,. \tag{2.26}$$

Important for the following derivations of the balance equations in Section 2.5 is the material time derivative of the Jacobian determinant which can be written with Eq. (2.21) and (2.22) as

$$(J_\alpha)'_\alpha = \frac{\partial J_\alpha}{\partial \boldsymbol{F}_\alpha} : \frac{\partial \boldsymbol{F}_\alpha}{\partial t} = J_\alpha\, \boldsymbol{F}_\alpha^{-T} : (\boldsymbol{F}_\alpha)'_\alpha = J_\alpha\, \boldsymbol{F}_\alpha^{-T} : (\boldsymbol{L}_\alpha \cdot \boldsymbol{F}_\alpha) = J_\alpha\, \mathrm{tr}(\boldsymbol{L}_\alpha) = J_\alpha\, \mathrm{div}(\boldsymbol{x}'_\alpha)\,, \tag{2.27}$$

where

$$\frac{\partial J_\alpha}{\partial \boldsymbol{F}_\alpha} = J_\alpha\, \boldsymbol{F}_\alpha^{-T}\,. \tag{2.28}$$

Additionally, the material time derivative of an arbitrary scalar quantity depending on the current position vector and the time such as $\gamma^\alpha(\boldsymbol{x}(t), t)$ is defined as

$$(\gamma^\alpha)'_\alpha = \frac{\partial \gamma^\alpha}{\partial t} + \mathrm{grad}(\gamma^\alpha) \cdot \boldsymbol{x}'_\alpha\,. \tag{2.29}$$

2.4 Tractions and Stresses

The application of an arbitrary mechanical load to a body results in internal forces. To investigate these forces and the consequential stresses, the body is imaginary cut into two parts. The internal forces have to be transmitted across the cutting plane to preserve equilibrium. This results in the partial Cauchy traction vector $\boldsymbol{t}^\alpha = \boldsymbol{t}^\alpha(\boldsymbol{x}, t, \boldsymbol{n})$ of constituent φ^α which acts at the position $\boldsymbol{x}$ on an infinitesimal surface element of the cutting plane $\mathrm{d}a$ under the unit outward normal $\boldsymbol{n}$ in the current configuration at time t. The corresponding partial first Piola-Kirchhoff traction vector $\boldsymbol{t}_0^\alpha = \boldsymbol{t}_0^\alpha(\boldsymbol{X}_\alpha, t_0, \boldsymbol{N}_\alpha)$ relates to the position $\boldsymbol{X}_\alpha$ on the surface element on the cutting plane $\mathrm{d}A_\alpha$ in the reference configuration with the unit outward normal $\boldsymbol{N}_\alpha$ at time t_0^α. With this the resulting partial forces $\mathrm{d}\hat{\boldsymbol{f}}^\alpha$ on the respective surface elements are given by

$$\mathrm{d}\hat{\boldsymbol{f}}^\alpha = \boldsymbol{t}^\alpha\, \mathrm{d}a = \boldsymbol{t}_0^\alpha\, \mathrm{d}A_\alpha\,. \tag{2.30}$$

Cauchy's theorem states the existence of second-order tensor fields for linear mappings as

$$\boldsymbol{t}^\alpha(\boldsymbol{x}, t, \boldsymbol{n}) = \boldsymbol{\sigma}^\alpha(\boldsymbol{x}, t) \cdot \boldsymbol{n} \tag{2.31}$$

and

$$\boldsymbol{t}_0^\alpha(\boldsymbol{X}_\alpha, t_0, \boldsymbol{N}_\alpha) = \boldsymbol{P}^\alpha(\boldsymbol{X}_\alpha, t_0) \cdot \boldsymbol{N}_\alpha \,. \tag{2.32}$$

Therein, the Cauchy stress $\boldsymbol{\sigma}^\alpha$ is solely based on the current configuration evaluating the current force on the current cutting plane leading to the term of the true stress. In contrast to this, the first Piola-Kirchhoff stress tensor $\boldsymbol{P}^\alpha$ is a two-point tensor with one basis in the current and one in the reference configuration. From a physical point of view, it relates the current force to the geometry in reference configuration. The relation between these two stress tensors can be deduced by inserting their definitions into Eq. (2.30) and utilize the transport theorem in Eq. $(2.16)_2$ leading to

$$\boldsymbol{P}^\alpha = J_\alpha \, \boldsymbol{\sigma}^\alpha \cdot \boldsymbol{F}_\alpha^{-T} \quad \text{and} \quad \boldsymbol{\sigma}^\alpha = \frac{1}{J_\alpha} \boldsymbol{P}^\alpha \cdot \boldsymbol{F}_\alpha^T \,. \tag{2.33}$$

An additional stress tensor is the second Piola-Kirchhoff stress tensor

$$\boldsymbol{S}^\alpha = \boldsymbol{F}_\alpha^{-1} \cdot \boldsymbol{P}^\alpha \tag{2.34}$$

which is purely related to the reference configuration and often used due to its inherent symmetry. In contrast to the other presented stress tensors, the second Piola-Kirchhoff stress tensor has no physical interpretation.

2.5 Balance Principles

A set of four balance laws and one inequality which are required within this thesis is presented in this section. They have their origin in classical continuum mechanics but are extended to take into account the different constituents and their interactions within the mixture in the framework of the TPM. These equations, which have to be fulfilled at each point in the body, have axiomatic character as they are based on observation rather than being deduced from other laws.

In classical one-component continuum mechanics, the considered balance equations have the structure

$$\dot{\mathcal{K}} = \mathcal{L} \tag{2.35}$$

with $\mathcal{K}$ and $\mathcal{L}$ as placeholders for the internal quantity to balance and their external counterpart. In contrast to this, the balance equations for the constituent φ^α within the mixture have the structure

$$(\mathcal{K}^\alpha)'_\alpha = \mathcal{L}^\alpha + \mathcal{M}^\alpha \tag{2.36}$$

where $\mathcal{K}^\alpha$ and $\mathcal{L}^\alpha$ are the corresponding placeholders to the single phase formulation. Additionally, $\mathcal{M}^\alpha$ denotes the total production term of the constituent φ^α which is introduced to take the interaction between the phases into account.

An important requirement which was formulated by Truesdell [1984] within the TM implies that for each balance principle the sum over all constituents have to result in the corresponding conservation law of one-component material from classical continuum mechanics. One possibility to achieve this is to enforce

$$\dot{\mathcal{K}} - \mathcal{L} = \sum_{\alpha=1}^{k} [(\mathcal{K}^\alpha)'_\alpha - \mathcal{L}^\alpha] \tag{2.37}$$

which yields that the sum over all constituents of the respective production term has to vanish as

$$\sum_{\alpha=1}^{k} \mathcal{M}^{\alpha} = 0\,. \tag{2.38}$$

2.5.1 Balance of Mass

The balance of mass in the framework of the TPM for the constituent φ reads as

$$(m^{\alpha})'_{\alpha} = \int_{\mathcal{B}_{\alpha}} \hat{\rho}^{\alpha}\,\mathrm{d}v \tag{2.39}$$

where m^{α} is the mass and $\hat{\rho}^{\alpha}$ is the total production term of mass of the constituent φ^{α}. The comparison with the general structure in Eq. (2.37) with $\mathcal{L} = \mathcal{L}^{\alpha} = 0$ yields

$$\sum_{\alpha=1}^{k} \int_{\mathcal{B}_{\alpha}} \hat{\rho}^{\alpha}\,\mathrm{d}v = 0 \tag{2.40}$$

which is in agreement with Eq. (2.38). The material time derivative of the mass can be reformulated by using Eq. $(2.16)_3$ and (2.27) as

$$\begin{aligned}(m^{\alpha})'_{\alpha} = \left(\int_{\mathcal{B}_{\alpha}} \rho^{\alpha}\,\mathrm{d}v\right)'_{\alpha} = \left(\int_{\mathcal{B}_{0\alpha}} \rho^{\alpha} J_{\alpha}\,\mathrm{d}V_{\alpha}\right)'_{\alpha} &= \int_{\mathcal{B}_{0\alpha}} \left[(\rho^{\alpha})'_{\alpha}\, J_{\alpha} + \rho^{\alpha}(J_{\alpha})'_{\alpha}\right]\mathrm{d}V_{\alpha} \\ &= \int_{\mathcal{B}_{\alpha}} \left[(\rho^{\alpha})'_{\alpha} + \rho^{\alpha}\,\mathrm{div}(\boldsymbol{x}'_{\alpha})\right]\mathrm{d}v\end{aligned} \tag{2.41}$$

leading to the global form of the balance of mass

$$\int_{\mathcal{B}_{\alpha}} \left[(\rho^{\alpha})'_{\alpha} + \rho^{\alpha}\,\mathrm{div}(\boldsymbol{x}'_{\alpha})\right]\mathrm{d}v = \int_{\mathcal{B}_{\alpha}} \hat{\rho}^{\alpha}\,\mathrm{d}v\,. \tag{2.42}$$

The corresponding local form reads as

$$(\rho^{\alpha})'_{\alpha} + \rho^{\alpha}\,\mathrm{div}(\boldsymbol{x}'_{\alpha}) = \hat{\rho}^{\alpha}\,, \tag{2.43}$$

where the condition

$$\sum_{\alpha=1}^{k} \hat{\rho}^{\alpha} = 0 \tag{2.44}$$

is postulated which is fulfilling Eq. (2.40).

2.5.2 Balance of Linear Momentum

The balance of linear momentum for the constituent φ^{α} within the mixture is given as

$$(\boldsymbol{l}^{\alpha})'_{\alpha} = \boldsymbol{k}^{\alpha} + \int_{\mathcal{B}_{\alpha}} \hat{\boldsymbol{s}}^{\alpha}\,\mathrm{d}v\,, \tag{2.45}$$

where

$$\boldsymbol{l}^{\alpha} = \int_{\mathcal{B}_{\alpha}} \rho^{\alpha}\,\boldsymbol{x}'_{\alpha}\,\mathrm{d}v \quad \text{and} \quad \boldsymbol{k}^{\alpha} = \int_{\mathcal{B}_{\alpha}} \rho^{\alpha}\,\boldsymbol{b}^{\alpha}\,\mathrm{d}v + \int_{\partial\mathcal{B}_{\alpha}} \boldsymbol{t}^{\alpha}\,\mathrm{d}a\,. \tag{2.46}$$

The material time derivative of the linear momentum $\boldsymbol{l}^\alpha$ has to equal the external forces $\boldsymbol{k}^\alpha$ and the volume integral over the total production term of linear momentum $\hat{\boldsymbol{s}}^\alpha$. The external forces can be split in a part containing the external volume load $\boldsymbol{f}^\alpha = \rho^\alpha \, \boldsymbol{b}^\alpha$ and a part including the external surface tractions $\boldsymbol{t}^\alpha$. Applying Eq. (2.37) to the balance of linear momentum results in the condition for the sum of all total production terms of the momentum corresponding to Eq. (2.38) as

$$\sum_{\alpha=1}^{k} \int_{\mathcal{B}_\alpha} \hat{\boldsymbol{s}}^\alpha \, \mathrm{d}v = \boldsymbol{0} \, . \tag{2.47}$$

The material time derivative of the linear momentum can be rewritten with Eq. $(2.16)_3$ and (2.27) in combination with the local form of the balance of mass in Eq. (2.43) as

$$\begin{aligned}
(\boldsymbol{l}^\alpha)'_\alpha &= \left(\int_{\mathcal{B}_\alpha} \rho^\alpha \, \boldsymbol{x}'_\alpha \, \mathrm{d}v \right)'_\alpha = \left(\int_{\mathcal{B}_{0\alpha}} \rho^\alpha \, \boldsymbol{x}'_\alpha \, J_\alpha \, \mathrm{d}V_\alpha \right)'_\alpha \\
&= \int_{\mathcal{B}_{0\alpha}} \left[(\rho^\alpha)'_\alpha \, \boldsymbol{x}'_\alpha \, J_\alpha + \rho^\alpha \, \boldsymbol{x}''_\alpha \, J_\alpha + \rho^\alpha \, \boldsymbol{x}'_\alpha \, (J_\alpha)'_\alpha \right] \mathrm{d}V_\alpha \\
&= \int_{\mathcal{B}_\alpha} \left\{ \left[(\rho^\alpha)'_\alpha + \rho^\alpha \, \mathrm{div}(\boldsymbol{x}'_\alpha) \right] \boldsymbol{x}'_\alpha + \rho^\alpha \, \boldsymbol{x}''_\alpha \right\} \mathrm{d}v \\
&= \int_{\mathcal{B}_\alpha} \left(\hat{\rho}^\alpha \, \boldsymbol{x}'_\alpha + \rho^\alpha \, \boldsymbol{x}''_\alpha \right) \mathrm{d}v \, .
\end{aligned} \tag{2.48}$$

Employing the Cauchy theorem in Eq. (2.31) and the divergence theorem on the traction term yields

$$\int_{\partial\mathcal{B}_\alpha} \boldsymbol{t}^\alpha \, \mathrm{d}a = \int_{\partial\mathcal{B}_\alpha} \boldsymbol{\sigma}^\alpha \cdot \boldsymbol{n} \, \mathrm{d}a = \int_{\mathcal{B}_\alpha} \mathrm{div}(\boldsymbol{\sigma}^\alpha) \, \mathrm{d}v \, . \tag{2.49}$$

With this, the global form of the balance of linear momentum is written as

$$\int_{\mathcal{B}_\alpha} \mathrm{div}(\boldsymbol{\sigma}^\alpha) \, \mathrm{d}v + \int_{\mathcal{B}_\alpha} \rho^\alpha \, (\boldsymbol{b}^\alpha - \boldsymbol{x}''_\alpha) \, \mathrm{d}v = - \int_{\mathcal{B}_\alpha} \hat{\boldsymbol{s}}^\alpha \, \mathrm{d}v + \int_{\mathcal{B}_\alpha} \hat{\rho}^\alpha \, \boldsymbol{x}'_\alpha \, \mathrm{d}v \tag{2.50}$$

leading to the local form

$$\mathrm{div}(\boldsymbol{\sigma}^\alpha) + \rho^\alpha \, (\boldsymbol{b}^\alpha - \boldsymbol{x}''_\alpha) = -\hat{\boldsymbol{p}}^\alpha \tag{2.51}$$

with

$$\hat{\boldsymbol{p}}^\alpha = \hat{\boldsymbol{s}}^\alpha - \hat{\rho}^\alpha \, \boldsymbol{x}'_\alpha \, , \tag{2.52}$$

where $\hat{\boldsymbol{p}}^\alpha$ is the direct production term of linear momentum. The sum of the production terms is constrained as

$$\sum_{\alpha=1}^{k} \hat{\boldsymbol{s}}^\alpha = \sum_{\alpha=1}^{k} (\hat{\boldsymbol{p}}^\alpha + \hat{\rho}^\alpha \, \boldsymbol{x}'_\alpha) = \boldsymbol{0} \tag{2.53}$$

in accordance with Eq. (2.47).

2.5.3 Balance of Angular Momentum

The balance of angular momentum for non-polar partial bodies demands equilibrium of angular momentum with respect to a fixed reference point (0) for the constituent φ^α as

$$(\boldsymbol{h}^\alpha_{(0)})'_\alpha = \boldsymbol{m}^\alpha_{(0)} + \hat{\boldsymbol{h}}^\alpha_{(0)} \tag{2.54}$$

with the angular momentum $\boldsymbol{h}^\alpha_{(0)}$ and the angular momentum of the external forces $\boldsymbol{m}^\alpha_{(0)}$ given by

$$\boldsymbol{h}^\alpha_{(0)} = \int_{\mathcal{B}_\alpha} \boldsymbol{x} \times \rho^\alpha \, \boldsymbol{x}'_\alpha \, \mathrm{d}v \quad \text{and} \quad \boldsymbol{m}^\alpha_{(0)} = \int_{\mathcal{B}_\alpha} \boldsymbol{x} \times \rho^\alpha \, \boldsymbol{b}^\alpha \, \mathrm{d}v + \int_{\partial\mathcal{B}_\alpha} \boldsymbol{x} \times \boldsymbol{t}^\alpha \, \mathrm{d}a \tag{2.55}$$

and the production term of angular momentum

$$\hat{\boldsymbol{h}}^\alpha_{(0)} = \int_{\mathcal{B}_\alpha} \boldsymbol{x} \times \hat{\boldsymbol{s}}^\alpha \, \mathrm{d}v \,. \tag{2.56}$$

The constraint condition on the sum of the production terms of angular momentum reads as

$$\sum_{\alpha=1}^{k} \hat{\boldsymbol{h}}^\alpha_{(0)} = \sum_{\alpha=1}^{k} \int_{\mathcal{B}_\alpha} \boldsymbol{x} \times \hat{\boldsymbol{s}}^\alpha \, \mathrm{d}v = \boldsymbol{0} \,. \tag{2.57}$$

in agreement with Eq. (2.38). Reformulating the material time derivative of the angular momentum by inserting Eq. $(2.16)_3$, (2.27) and (2.43) leads to

$$\begin{aligned}
(\boldsymbol{h}^\alpha_{(0)})'_\alpha &= \left(\int_{\mathcal{B}_\alpha} \boldsymbol{x} \times \rho^\alpha \, \boldsymbol{x}'_\alpha \, \mathrm{d}v \right)'_\alpha = \left(\int_{\mathcal{B}_{0\alpha}} \boldsymbol{x} \times \rho^\alpha \, \boldsymbol{x}'_\alpha \, J_\alpha \, \mathrm{d}V_\alpha \right)'_\alpha \\
&= \int_{\mathcal{B}_{0\alpha}} \left[\boldsymbol{x}'_\alpha \times \rho^\alpha \, \boldsymbol{x}'_\alpha \, J_\alpha + \boldsymbol{x} \times \left\{ (\rho^\alpha)'_\alpha \, \boldsymbol{x}'_\alpha \, J_\alpha + \rho^\alpha \, \boldsymbol{x}''_\alpha \, J_\alpha + \rho^\alpha \, \boldsymbol{x}'_\alpha \, (J_\alpha)'_\alpha \right\} \right] \mathrm{d}V_\alpha \\
&= \int_{\mathcal{B}_\alpha} \boldsymbol{x} \times \left\{ \left[(\rho^\alpha)'_\alpha + \rho^\alpha \operatorname{div}(\boldsymbol{x}'_\alpha) \right] \boldsymbol{x}'_\alpha + \rho^\alpha \, \boldsymbol{x}''_\alpha \right\} \mathrm{d}v \\
&= \int_{\mathcal{B}_\alpha} \boldsymbol{x} \times (\hat{\rho}^\alpha \, \boldsymbol{x}'_\alpha + \rho^\alpha \, \boldsymbol{x}''_\alpha) \, \mathrm{d}v \,,
\end{aligned} \tag{2.58}$$

where the characteristic has been exploited that the cross product of colinear vector equals zero. The term containing the surface traction in the angular momentum of the external forces in Eq. $(2.55)_2$ is rewritten by applying the Cauchy theorem in Eq. (2.31) and the divergence theorem as

$$\int_{\partial\mathcal{B}_\alpha} \boldsymbol{x} \times \boldsymbol{t}^\alpha \, \mathrm{d}a = \int_{\partial\mathcal{B}_\alpha} \boldsymbol{x} \times (\boldsymbol{\sigma}^\alpha \cdot \boldsymbol{n}) \, \mathrm{d}a = \int_{\mathcal{B}_\alpha} \left[\boldsymbol{x} \times \operatorname{div}(\boldsymbol{\sigma}^\alpha) + \boldsymbol{I} \times \boldsymbol{\sigma}^\alpha \right] \mathrm{d}v \,. \tag{2.59}$$

Inserting all reformulations into Eq. (2.54) yields

$$\int_{\mathcal{B}_\alpha} \boldsymbol{x} \times \left[\operatorname{div}(\boldsymbol{\sigma}^\alpha) + \rho^\alpha \, (\boldsymbol{b}^\alpha - \boldsymbol{x}''_\alpha) + \hat{\boldsymbol{s}}^\alpha - \hat{\rho}^\alpha \, \boldsymbol{x}'_\alpha \right] \mathrm{d}v + \int_{\mathcal{B}_\alpha} \boldsymbol{I} \times \boldsymbol{\sigma}^\alpha \, \mathrm{d}v = \boldsymbol{0} \,. \tag{2.60}$$

Including the local form of the balance of linear momentum from Eq. (2.51) and (2.52) reduces the expression to the global form of the balance of angular momentum

$$\int_{\mathcal{B}_\alpha} \boldsymbol{I} \times \boldsymbol{\sigma}^\alpha \, \mathrm{d}v = \boldsymbol{0} \tag{2.61}$$

leading to the local statement

$$\boldsymbol{I} \times \boldsymbol{\sigma}^\alpha = \boldsymbol{0} \tag{2.62}$$

which is fulfilled for

$$\boldsymbol{\sigma}^\alpha = (\boldsymbol{\sigma}^\alpha)^T \tag{2.63}$$

stating that the partial Cauchy stress tensor $\boldsymbol{\sigma}^\alpha$ is symmetric.

2.5.4 Balance of Energy

The balance of energy (first principle of thermodynamics) for the constituent φ^α is given by

$$(e^\alpha)'_\alpha + (k^\alpha)'_\alpha = w^\alpha + q^\alpha + \int_{\mathcal{B}_\alpha} \hat{e}^\alpha \, \mathrm{d}v \tag{2.64}$$

with the total production term of energy denoted as $\hat{e}^\alpha$. The internal energy e^α is defined as

$$e^\alpha = \int_{\mathcal{B}_\alpha} \rho^\alpha \, \varepsilon^\alpha \, \mathrm{d}v \tag{2.65}$$

including the internal energy density ε^α. The kinetic energy k^α is given by

$$k^\alpha = \int_{\mathcal{B}_\alpha} \frac{1}{2} \, \rho^\alpha \, \boldsymbol{x}'_\alpha \cdot \boldsymbol{x}'_\alpha \, \mathrm{d}v \, . \tag{2.66}$$

The mechanical and thermal power w^α and q^α are defined as

$$w^\alpha = \int_{\mathcal{B}_\alpha} \boldsymbol{x}'_\alpha \cdot \rho^\alpha \, \boldsymbol{b}^\alpha \, \mathrm{d}v + \int_{\partial\mathcal{B}_\alpha} \boldsymbol{x}'_\alpha \cdot \boldsymbol{t}^\alpha \, \mathrm{d}a \tag{2.67}$$

and

$$q^\alpha = \int_{\mathcal{B}_\alpha} \rho^\alpha \, r^\alpha \, \mathrm{d}v - \int_{\partial\mathcal{B}_\alpha} \boldsymbol{q}^\alpha_{\mathrm{H}} \cdot \boldsymbol{n} \, \mathrm{d}a \tag{2.68}$$

with the external heat supply r^α and the heat influx vector $\boldsymbol{q}^\alpha_{\mathrm{H}}$.

Following the structure in Eq. (2.37) with respect to the balance of energy leads to the condition for the sum of total energy production terms

$$\sum_{\alpha=1}^{k} \int_{\mathcal{B}_\alpha} \hat{e}^\alpha \, \mathrm{d}v = 0 \, . \tag{2.69}$$

which is in agreement with Eq. (2.38). Taking into account Eq. $(2.16)_3$ and (2.27) as well as the local form of the balance of mass in Eq. (2.43), the material time derivatives of the

internal energy and the kinetic energy can be written as

$$\begin{aligned}(e^\alpha)'_\alpha &= \left(\int_{\mathcal{B}_\alpha} \rho^\alpha\, \varepsilon^\alpha \,\mathrm{d}v\right)'_\alpha = \left(\int_{\mathcal{B}_{0\alpha}} \rho^\alpha\, \varepsilon^\alpha\, J_\alpha \,\mathrm{d}V_\alpha\right)'_\alpha \\ &= \int_{\mathcal{B}_{0\alpha}} \left[(\rho^\alpha)'_\alpha\; \varepsilon^\alpha\, J_\alpha + \rho^\alpha\; (\varepsilon^\alpha)'_\alpha\; J_\alpha + \rho^\alpha\, \varepsilon^\alpha\, (J_\alpha)'_\alpha\right] \mathrm{d}V_\alpha \\ &= \int_{\mathcal{B}_\alpha} \left\{\varepsilon^\alpha \left[(\rho^\alpha)'_\alpha + \rho^\alpha \operatorname{div}(\boldsymbol{x}'_\alpha)\right] + \rho^\alpha\; (\varepsilon^\alpha)'_\alpha\right\} \mathrm{d}v \\ &= \int_{\mathcal{B}_\alpha} \left[\hat{\rho}^\alpha\, \varepsilon^\alpha + \rho^\alpha\; (\varepsilon^\alpha)'_\alpha\right] \mathrm{d}v\end{aligned} \tag{2.70}$$

and

$$\begin{aligned}(k^\alpha)'_\alpha &= \left(\int_{\mathcal{B}_\alpha} \frac{1}{2}\,\rho^\alpha\, \boldsymbol{x}'_\alpha \cdot \boldsymbol{x}'_\alpha \,\mathrm{d}v\right)'_\alpha = \left(\int_{\mathcal{B}_{0\alpha}} \frac{1}{2}\,\rho^\alpha\, \boldsymbol{x}'_\alpha \cdot \boldsymbol{x}'_\alpha\, J_\alpha \,\mathrm{d}V_\alpha\right)'_\alpha \\ &= \int_{\mathcal{B}_{0\alpha}} \left[\frac{1}{2}\,(\rho^\alpha)'_\alpha\; \boldsymbol{x}'_\alpha \cdot \boldsymbol{x}'_\alpha\, J_\alpha + \rho^\alpha\, \boldsymbol{x}'_\alpha \cdot \boldsymbol{x}''_\alpha\, J_\alpha + \frac{1}{2}\,\rho^\alpha\, \boldsymbol{x}'_\alpha \cdot \boldsymbol{x}'_\alpha\, (J_\alpha)'_\alpha\right] \mathrm{d}V_\alpha \\ &= \int_{\mathcal{B}_\alpha} \left\{\frac{1}{2}\,\boldsymbol{x}'_\alpha \cdot \boldsymbol{x}'_\alpha \left[(\rho^\alpha)'_\alpha + \rho^\alpha \operatorname{div}(\boldsymbol{x}'_\alpha)\right] + \rho^\alpha\, \boldsymbol{x}'_\alpha \cdot \boldsymbol{x}''_\alpha\right\} \mathrm{d}v \\ &= \int_{\mathcal{B}_\alpha} \left(\frac{1}{2}\,\hat{\rho}^\alpha\, \boldsymbol{x}'_\alpha + \rho^\alpha\, \boldsymbol{x}''_\alpha\right) \cdot \boldsymbol{x}'_\alpha \,\mathrm{d}v\,.\end{aligned} \tag{2.71}$$

The surface terms in the mechanical power and thermal power in Eq. (2.67) and (2.68) can be transformed by the divergence theorem and the Cauchy theorem in Eq. (2.31) to

$$\begin{aligned}\int_{\partial\mathcal{B}_\alpha} \boldsymbol{x}'_\alpha \cdot \boldsymbol{t}^\alpha \,\mathrm{d}a = \int_{\partial\mathcal{B}_\alpha} \boldsymbol{x}'_\alpha \cdot (\boldsymbol{\sigma}^\alpha \cdot \boldsymbol{n}) \,\mathrm{d}a &= \int_{\mathcal{B}_\alpha} \operatorname{div}\left(\boldsymbol{\sigma}^{\alpha,T} \cdot \boldsymbol{x}'_\alpha\right) \mathrm{d}v \\ &= \int_{\mathcal{B}_\alpha} \left[\operatorname{div}(\boldsymbol{\sigma}^\alpha) \cdot \boldsymbol{x}'_\alpha + \boldsymbol{\sigma}^\alpha : \boldsymbol{L}_\alpha\right] \mathrm{d}v\end{aligned} \tag{2.72}$$

and

$$\int_{\partial\mathcal{B}_\alpha} \boldsymbol{q}^\alpha_{\mathrm{H}} \cdot \boldsymbol{n} \,\mathrm{d}a = \int_{\mathcal{B}_\alpha} \operatorname{div}(\boldsymbol{q}^\alpha_{\mathrm{H}}) \,\mathrm{d}v\,. \tag{2.73}$$

Inserting all reformulations into the balance of energy in Eq. (2.64) leads to

$$\begin{aligned}&\int_{\mathcal{B}_\alpha} \left[\hat{\rho}^\alpha\, \varepsilon^\alpha + \rho^\alpha\; (\varepsilon^\alpha)'_\alpha\right] \mathrm{d}v + \int_{\mathcal{B}_\alpha} \left(\frac{1}{2}\,\hat{\rho}^\alpha\, \boldsymbol{x}'_\alpha + \rho^\alpha\, \boldsymbol{x}''_\alpha\right) \cdot \boldsymbol{x}'_\alpha \,\mathrm{d}v \\ &\qquad = \int_{\mathcal{B}_\alpha} \left[\operatorname{div}(\boldsymbol{\sigma}^\alpha) + \rho^\alpha\, \boldsymbol{b}^\alpha\right] \cdot \boldsymbol{x}'_\alpha \,\mathrm{d}v + \int_{\mathcal{B}_\alpha} \boldsymbol{\sigma}^\alpha : \boldsymbol{L}_\alpha \,\mathrm{d}v \\ &\qquad\quad + \int_{\mathcal{B}_\alpha} \rho^\alpha\, r^\alpha \,\mathrm{d}v - \int_{\mathcal{B}_\alpha} \operatorname{div}(\boldsymbol{q}^\alpha_{\mathrm{H}}) \,\mathrm{d}v + \int_{\mathcal{B}_\alpha} \hat{e}^\alpha \,\mathrm{d}v\,.\end{aligned} \tag{2.74}$$

This equation is modified once more towards the global form of the balance of energy by inserting the local form of the balance of linear momentum from Eq. (2.51) and (2.52). In addition, the symmetry of the partial Cauchy stress is utilized such that $\boldsymbol{\sigma}^\alpha : \boldsymbol{L}_\alpha = \boldsymbol{\sigma}^\alpha : \boldsymbol{D}_\alpha$

holds leading to

$$\begin{aligned}\int_{\mathcal{B}_\alpha} \left[\hat{\rho}^\alpha\, \varepsilon^\alpha + \rho^\alpha\, (\varepsilon^\alpha)'_\alpha\right] \mathrm{d}v + \int_{\mathcal{B}_\alpha} \frac{1}{2}\, \hat{\rho}^\alpha\, \boldsymbol{x}'_\alpha \cdot \boldsymbol{x}'_\alpha \,\mathrm{d}v \\ = -\int_{\mathcal{B}_\alpha} \hat{\boldsymbol{p}}^\alpha \cdot \boldsymbol{x}'_\alpha \,\mathrm{d}v + \int_{\mathcal{B}_\alpha} \boldsymbol{\sigma}^\alpha : \boldsymbol{D}_\alpha \,\mathrm{d}v \\ + \int_{\mathcal{B}_\alpha} \rho^\alpha\, r^\alpha \,\mathrm{d}v - \int_{\mathcal{B}_\alpha} \mathrm{div}(\boldsymbol{q}^\alpha_{\mathrm{H}}) \,\mathrm{d}v + \int_{\mathcal{B}_\alpha} \hat{e}^\alpha \,\mathrm{d}v\,.\end{aligned} \tag{2.75}$$

The corresponding local statement can be written as

$$\rho^\alpha\, (\varepsilon^\alpha)'_\alpha - \boldsymbol{\sigma}^\alpha : \boldsymbol{D}_\alpha - \rho^\alpha\, r^\alpha + \mathrm{div}(\boldsymbol{q}^\alpha_{\mathrm{H}}) = \hat{\varepsilon}^\alpha \tag{2.76}$$

with

$$\hat{\varepsilon}^\alpha = \hat{e}^\alpha - \hat{\boldsymbol{p}}^\alpha \cdot \boldsymbol{x}'_\alpha - \hat{\rho}^\alpha \left(\varepsilon^\alpha + \frac{1}{2}\, \boldsymbol{x}'_\alpha \cdot \boldsymbol{x}'_\alpha\right), \tag{2.77}$$

where $\hat{\varepsilon}^\alpha$ denotes the direct production term of energy. It is postulated that the sum of the total production term over all constituents vanishes as

$$\sum_{\alpha=1}^{k} \hat{e}^\alpha = \sum_{\alpha=1}^{k} \left[\hat{\varepsilon}^\alpha + \hat{\boldsymbol{p}}^\alpha \cdot \boldsymbol{x}'_\alpha + \hat{\rho}^\alpha \left(\varepsilon^\alpha + \frac{1}{2}\, \boldsymbol{x}'_\alpha \cdot \boldsymbol{x}'_\alpha\right)\right] = 0 \tag{2.78}$$

which fulfills Eq. (2.69).

2.5.5 Entropy Inequality

The treatment of the entropy inequality (second principle of thermodynamics) within the TM has been discussed extensively within the 1960s. It was not clear whether the entropy inequality has to be fulfilled for each constituent separately, as it is the case for the balance laws, or just for the whole mixture, for details see e.g. de Boer and Ehlers [1986] and Ehlers [1989]. The result is that fulfilling the entropy inequality for each constituent is too restrictive such that the entropy inequality for the mixture is considered instead as

$$\sum_{\alpha=1}^{k} (h^\alpha)'_\alpha \geq \sum_{\alpha=1}^{k} \int_{\mathcal{B}_\alpha} \frac{1}{\Theta^\alpha}\, \rho^\alpha\, r^\alpha \,\mathrm{d}v - \sum_{\alpha=1}^{k} \int_{\partial\mathcal{B}_\alpha} \frac{1}{\Theta^\alpha}\, \boldsymbol{q}^\alpha_{\mathrm{H}} \cdot \boldsymbol{n} \,\mathrm{d}a \tag{2.79}$$

with the absolute temperature Θ^α of the constituent φ^α and the respective entropy as

$$h^\alpha = \int_{\mathcal{B}_\alpha} \rho^\alpha\, \eta^\alpha \,\mathrm{d}v\,, \tag{2.80}$$

where the specific entropy is denoted by η^α. The material time derivative of the entropy can be reformulated with Eq. $(2.16)_3$, (2.27) and (2.43) to

$$\begin{aligned}(h^\alpha)'_\alpha &= \left(\int_{\mathcal{B}_\alpha} \rho^\alpha \eta^\alpha \,\mathrm{d}v\right)'_\alpha = \left(\int_{\mathcal{B}_{0\alpha}} \rho^\alpha \eta^\alpha J_\alpha \,\mathrm{d}V_\alpha\right)'_\alpha \\ &= \int_{\mathcal{B}_{0\alpha}} \left[(\rho^\alpha)'_\alpha \,\eta^\alpha J_\alpha + \rho^\alpha (\eta^\alpha)'_\alpha \, J_\alpha + \rho^\alpha \eta^\alpha (J_\alpha)'_\alpha\right] \mathrm{d}V_\alpha \\ &= \int_{\mathcal{B}_\alpha} \left\{\eta^\alpha \left[(\rho^\alpha)'_\alpha + \rho^\alpha \operatorname{div}(\boldsymbol{x}'_\alpha)\right] + \rho^\alpha (\eta^\alpha)'_\alpha\right\} \mathrm{d}v \\ &= \int_{\mathcal{B}_\alpha} \left[\hat{\rho}^\alpha \eta^\alpha + \rho^\alpha (\eta^\alpha)'_\alpha\right] \mathrm{d}v\,.\end{aligned} \tag{2.81}$$

The entropy flux in Equations (2.79) can be transformed to a volume integral with the divergence theorem as

$$\int_{\partial\mathcal{B}_\alpha} \frac{1}{\Theta^\alpha} \boldsymbol{q}^\alpha_{\mathrm{H}} \cdot \boldsymbol{n} \,\mathrm{d}a = \int_{\mathcal{B}_\alpha} \operatorname{div}\left(\frac{1}{\Theta^\alpha} \boldsymbol{q}^\alpha_{\mathrm{H}}\right) \mathrm{d}v \tag{2.82}$$

Inserting both terms into Eq. (2.79) leads to the global form of the entropy inequality of the mixture as

$$\sum_{\alpha=1}^{k} \int_{\mathcal{B}_\alpha} [\hat{\rho}^\alpha \eta^\alpha + \rho^\alpha (\eta^\alpha)'_\alpha] \,\mathrm{d}v \geq \sum_{\alpha=1}^{k} \int_{\mathcal{B}_\alpha} \frac{1}{\Theta^\alpha} \rho^\alpha r^\alpha \,\mathrm{d}v - \sum_{\alpha=1}^{k} \int_{\mathcal{B}_\alpha} \operatorname{div}\left(\frac{1}{\Theta^\alpha} \boldsymbol{q}^\alpha_{\mathrm{H}}\right) \mathrm{d}v \tag{2.83}$$

resulting in the corresponding local statement

$$\sum_{\alpha=1}^{k} \left[\hat{\rho}^\alpha \eta^\alpha + \rho^\alpha (\eta^\alpha)'_\alpha - \frac{1}{\Theta^\alpha} \rho^\alpha r^\alpha + \operatorname{div}\left(\frac{1}{\Theta^\alpha} \boldsymbol{q}^\alpha_{\mathrm{H}}\right)\right] \geq 0\,. \tag{2.84}$$

The term containing the heat flux vector is transformed as

$$\operatorname{div}\left(\frac{1}{\Theta^\alpha} \boldsymbol{q}^\alpha_{\mathrm{H}}\right) = \operatorname{grad}\left(\frac{1}{\Theta^\alpha}\right) \cdot \boldsymbol{q}^\alpha_{\mathrm{H}} + \frac{1}{\Theta^\alpha} \operatorname{div}(\boldsymbol{q}^\alpha_{\mathrm{H}}) = -\frac{1}{(\Theta^\alpha)^2} \boldsymbol{q}^\alpha_{\mathrm{H}} \cdot \operatorname{grad}(\Theta^\alpha) + \frac{1}{\Theta^\alpha} \operatorname{div}(\boldsymbol{q}^\alpha_{\mathrm{H}}) \tag{2.85}$$

to rewrite the local form as

$$\sum_{\alpha=1}^{k} \left\{\hat{\rho}^\alpha \eta^\alpha + \rho^\alpha (\eta^\alpha)'_\alpha - \frac{1}{\Theta^\alpha} [\rho^\alpha r^\alpha - \operatorname{div}(\boldsymbol{q}^\alpha_{\mathrm{H}})] - \frac{1}{(\Theta^\alpha)^2} \boldsymbol{q}^\alpha_{\mathrm{H}} \cdot \operatorname{grad}(\Theta^\alpha)\right\} \geq 0\,. \tag{2.86}$$

The existence of a Helmholtz free energy function for the constituent φ^α as

$$\psi^\alpha = \varepsilon^\alpha - \Theta^\alpha \eta^\alpha \tag{2.87}$$

is assumed. This equation can be transformed such that

$$\varepsilon^\alpha = \psi^\alpha + \Theta^\alpha \eta^\alpha \tag{2.88}$$

leading to the material time derivative of the internal energy as

$$(\varepsilon^\alpha)'_\alpha = (\psi^\alpha + \Theta^\alpha \eta^\alpha)'_\alpha = (\psi^\alpha)'_\alpha + (\Theta^\alpha)'_\alpha \,\eta^\alpha + \Theta^\alpha (\eta^\alpha)'_\alpha\,. \tag{2.89}$$

These correlations are inserted into Eq. (2.86) along with a rearrangement of the local statement of the balance of energy in Eq. (2.76) as

$$\rho^\alpha r^\alpha - \operatorname{div}(\boldsymbol{q}_{\mathrm{H}}^\alpha) = \rho^\alpha (\varepsilon^\alpha)'_\alpha - \boldsymbol{\sigma}^\alpha : \boldsymbol{D}_\alpha - \hat{e}^\alpha + \hat{\boldsymbol{p}}^\alpha \cdot \boldsymbol{x}'_\alpha + \hat{\rho}^\alpha \left(\varepsilon^\alpha + \frac{1}{2} \boldsymbol{x}'_\alpha \cdot \boldsymbol{x}'_\alpha \right) \tag{2.90}$$

leading to the local form of the entropy inequality for the mixture as

$$\begin{aligned} \sum_{\alpha=1}^{k} \frac{1}{\Theta^\alpha} \Big\{ & - \rho^\alpha [(\psi^\alpha)'_\alpha + (\Theta^\alpha)'_\alpha \, \eta^\alpha] + \boldsymbol{\sigma}^\alpha : \boldsymbol{D}_\alpha - \frac{1}{\Theta^\alpha} \boldsymbol{q}_{\mathrm{H}}^\alpha \cdot \operatorname{grad}(\Theta^\alpha) \\ & + \hat{e}^\alpha - \hat{\boldsymbol{p}}^\alpha \cdot \boldsymbol{x}'_\alpha - \hat{\rho}^\alpha \left(\psi^\alpha + \frac{1}{2} \boldsymbol{x}'_\alpha \cdot \boldsymbol{x}'_\alpha \right) \Big\} \\ & + p \, (1 - \sum_{\alpha=1}^{k} n^\alpha)'_{\mathrm{S}} \geq 0 \,. \end{aligned} \tag{2.91}$$

Therein, the rate of the saturation condition following the trajectory of the solid multiplied by the Lagrange multiplier p is added. The saturation condition is a constraint within the framework of the TPM such that it has to be considered during the evaluation of the entropy inequality. If all k phases are incompressible, the saturation condition is an equation in excess leading to p as an unknown field. In case of at least one compressible constituent, p is a constitutive quantity. The Lagrange multiplier is an unknown reaction force whose physical interpretation is obtained by the evaluation of the entropy inequality. The choice of the sign of the extension is in general arbitrary but will become reasonable in accordance to the physical interpretation in Section 2.6.2.

2.6 Binary Model

Within this thesis, a simple binary model consisting of a solid and a liquid phase as $\alpha = \{\mathrm{S}, \mathrm{L}\}$ is investigated. To focus on the capabilities of the TPM in combination with the MIEL method, the following assumptions are included to reduce the complexity of the model. Dynamic effects are neglected with $\boldsymbol{x}''_\alpha = \boldsymbol{0}$, the same external acceleration is applied as $\boldsymbol{b}^\alpha = \boldsymbol{b}$ and incompressible phases are assumed such that $\rho^{\alpha R} = \text{constant}$. Furthermore, the model excludes mass exchange as $\hat{\rho}^\alpha = 0$ and is restricted to isothermal processes, i.e., $r^\alpha = 0$, $\boldsymbol{q}_{\mathrm{H}}^\alpha = \boldsymbol{0}$ and $\Theta^\alpha = \Theta = \text{constant}$.

2.6.1 Field Equations

The field equations are required to built the system of equations to solve. For the presented binary model they consist of the balance of mass for the mixture and the solid phase, the balance of linear momentum for the mixture and the liquid phase as well as the rate of the saturation condition. In contrast to this, there is no need to solve the balance of energy explicitly because of the restriction to isothermal processes. In addition, the conclusion of the balance of angular momentum, i.e. $\boldsymbol{\sigma}^\alpha = (\boldsymbol{\sigma}^\alpha)^T$, is included a priori.

Inserting the definition of the partial density in Eq. (2.6) into the local statement of the balance of mass in Eq. (2.43) and considering the assumptions of a constant real density and the neglection of mass exchange between the phases leads to

$$(n^\alpha)'_\alpha + n^\alpha \operatorname{div}(\boldsymbol{x}'_\alpha) = 0 \tag{2.92}$$

for the constituent φ^α. Applying this to the solid and the liquid phase yields for the balance of mass of the mixture and the solid phase

$$\begin{aligned}(n^{\mathrm{S}})'_{\mathrm{S}} + n^{\mathrm{S}} \operatorname{div}(\boldsymbol{x}'_{\mathrm{S}}) + (n^{\mathrm{L}})'_{\mathrm{L}} + n^{\mathrm{L}} \operatorname{div}(\boldsymbol{x}'_{\mathrm{L}}) &= 0\,,\\ (n^{\mathrm{S}})'_{\mathrm{S}} + n^{\mathrm{S}} \operatorname{div}(\boldsymbol{x}'_{\mathrm{S}}) &= 0\,.\end{aligned} \tag{2.93}$$

The local form of the balance of linear momentum in Eq. (2.51) is taken into account for the mixture and the liquid phase including the assumption of the same volume load on each phase as well as vanishing acceleration as

$$\begin{aligned}\operatorname{div}(\boldsymbol{\sigma}) + \rho\,\boldsymbol{b} &= \boldsymbol{0}\,,\\ \operatorname{div}(\boldsymbol{\sigma}^{\mathrm{L}}) + \rho^{\mathrm{L}}\,\boldsymbol{b} &= -\hat{\boldsymbol{p}}^{\mathrm{L}}\end{aligned} \tag{2.94}$$

with the the Cauchy stress of the mixture $\boldsymbol{\sigma} = \boldsymbol{\sigma}^{\mathrm{S}} + \boldsymbol{\sigma}^{\mathrm{L}}$ and the overall density $\rho = \rho^{\mathrm{S}} + \rho^{\mathrm{L}}$ correspondent to Eq. (2.7). The balances of mass and momentum are both chosen once with respect to the mixture instead of a specific phase because of the vanishing direct production terms and the fact that the application of boundary conditions in experiments or other real applications is most likely related to the mixture instead of single constituents.

Introducing the concept of volume fractions, compared to the TM, leads to the necessity of an additional equation. The saturation condition, here in its rate formulation with respect to the trajectory of the solid, constraints the rates of volumetric changes of the constituents, see [de Boer 2000], as

$$\left(n^{\mathrm{S}} + n^{\mathrm{L}} - 1\right)'_{\mathrm{S}} = 0\,. \tag{2.95}$$

Applying the material time derivative in Eq. (2.29) to the volume fraction of the liquid leads to

$$\frac{\partial n^{\mathrm{L}}}{\partial t} = (n^{\mathrm{L}})'_{\mathrm{L}} - \operatorname{grad}(n^{\mathrm{L}}) \cdot \boldsymbol{x}'_{\mathrm{L}} \tag{2.96}$$

which can be inserted into the corresponding material time derivative with respect to the trajectory of the solid as

$$(n^{\mathrm{L}})'_{\mathrm{S}} = \frac{\partial n^{\mathrm{L}}}{\partial t} + \operatorname{grad}(n^{\mathrm{L}}) \cdot \boldsymbol{x}'_{\mathrm{S}} = (n^{\mathrm{L}})'_{\mathrm{L}} - \operatorname{grad}(n^{\mathrm{L}}) \cdot \boldsymbol{w}_{\mathrm{LS}}\,, \tag{2.97}$$

where $\boldsymbol{w}_{\mathrm{LS}} = \boldsymbol{x}'_{\mathrm{L}} - \boldsymbol{x}'_{\mathrm{S}}$ is the difference velocity between the liquid and the solid. With this, the rate of the saturation condition in Eq. (2.95) can be reformulated to

$$(n^{\mathrm{S}})'_{\mathrm{S}} + (n^{\mathrm{L}})'_{\mathrm{L}} - \operatorname{grad}(n^{\mathrm{L}}) \cdot \boldsymbol{w}_{\mathrm{LS}} = 0\,. \tag{2.98}$$

2.6.2 Constitutive Theory

The previous section presented in total nine field equations for the binary model including 28 appearing quantities. This set is extended by the quantity p to in total 29 field quantities as

$$\mathcal{F} = \{\boldsymbol{\chi}_{\mathrm{S}}, \boldsymbol{\chi}_{\mathrm{L}}, \boldsymbol{\sigma}^{\mathrm{S}}, \boldsymbol{\sigma}^{\mathrm{L}}, \boldsymbol{b}, n^{\mathrm{S}}, n^{\mathrm{L}}, \rho^{\mathrm{SR}}, \rho^{\mathrm{LR}}, \hat{\boldsymbol{p}}^{\mathrm{L}}, p\}\,. \tag{2.99}$$

The additional quantity p is necessary as an extra unknown field to close the system of equation as a counterpart to the rate of the saturation condition which is an equation in excess. This issue becomes evident by analyzing the five known field quantities

$$\mathcal{K} = \{\boldsymbol{b}, \rho^{\mathrm{SR}}, \rho^{\mathrm{LR}}\} \tag{2.100}$$

and the required 15 constitutive and evolution relations

$$\mathcal{C} = \{\boldsymbol{\sigma}^{\mathrm{S}}, \boldsymbol{\sigma}^{\mathrm{L}}, \hat{\boldsymbol{p}}^{\mathrm{L}}\} \tag{2.101}$$

leading to the set of nine unknown quantities as

$$\mathcal{U} = \{\boldsymbol{\chi}_{\mathrm{S}}, \boldsymbol{\chi}_{\mathrm{L}}, n^{\mathrm{S}}, n^{\mathrm{L}}, p\} \tag{2.102}$$

to close the system. To determine the required constitutive and evolution relations, the entropy inequality is evaluated analogous to Coleman and Noll [1963]. For this purpose, the entropy inequality in Eq. (2.91) can be rewritten by taking into account the assumptions for the binary model as

$$\begin{aligned} -\rho^{\mathrm{S}} \left(\psi^{\mathrm{S}}\right)'_{\mathrm{S}} - \rho^{\mathrm{L}} \left(\psi^{\mathrm{L}}\right)'_{\mathrm{L}} + \boldsymbol{\sigma}^{\mathrm{S}} : \boldsymbol{D}_{\mathrm{S}} + \boldsymbol{\sigma}^{\mathrm{L}} : \boldsymbol{D}_{\mathrm{L}} - \hat{\boldsymbol{p}}^{\mathrm{L}} \cdot \boldsymbol{w}_{\mathrm{LS}} \\ - p \left[(n^{\mathrm{S}})'_{\mathrm{S}} + (n^{\mathrm{L}})'_{\mathrm{L}} - \operatorname{grad}(n^{\mathrm{L}}) \cdot \boldsymbol{w}_{\mathrm{LS}}\right] \geq 0 \,, \end{aligned} \tag{2.103}$$

where the constraint $\hat{\boldsymbol{p}}^{\mathrm{S}} = -\hat{\boldsymbol{p}}^{\mathrm{L}}$ resulting from Eq. (2.53) is utilized.

A crucial step for the evolution of the entropy inequality is the choice of process variables. The entropy inequality has to be fulfilled for fixed values of these process variable and for arbitrary values for the free available quantities, which are the derivatives in time and space of the aforementioned process variables. An important requirement for a reasonable evaluation is that all process variables have to be independent from each other. Possible dependencies have to be taken into account in the entropy inequality once again with the concept of Lagrange multipliers or have to be eliminated beforehand. The latter is carried out for the presented incompressible binary model as shown in the following.

Choosing the set of process variables

$$\mathcal{P} = \{\boldsymbol{C}_{\mathrm{S}}, \boldsymbol{C}_{\mathrm{L}}, \operatorname{grad}(n^{\mathrm{L}}), \boldsymbol{w}_{\mathrm{LS}}\} \tag{2.104}$$

yields $\boldsymbol{D}_{\mathrm{S}}$ and $\boldsymbol{D}_{\mathrm{L}}$ as free available quantities. A possibility to eliminate dependencies within the entropy inequality is to reformulate as many variables as possible in terms of the process variables and the free available quantities. In the present case, the balance of mass in Eq. (2.92) is rewritten for both constituents with

$$\operatorname{div}(\boldsymbol{x}'_\alpha) = \frac{\partial \boldsymbol{x}'_\alpha}{\partial \boldsymbol{x}} : \boldsymbol{I} = \boldsymbol{L}_\alpha : \boldsymbol{I} = \boldsymbol{D}_\alpha : \boldsymbol{I} \tag{2.105}$$

as

$$(n^\alpha)'_\alpha = -n^\alpha \, \boldsymbol{D}_\alpha : \boldsymbol{I} \,. \tag{2.106}$$

In addition, postulating dependencies for the Helmholtz free energy function as $\psi^{\mathrm{S}} = \psi^{\mathrm{S}}(\boldsymbol{C}_{\mathrm{S}})$ and $\psi^{\mathrm{L}} = \psi^{\mathrm{L}}(-)$ leads with the relation in Eq. (2.25) to

$$(\psi^{\mathrm{S}})'_{\mathrm{S}} = \frac{\partial \psi^{\mathrm{S}}}{\partial \boldsymbol{C}_{\mathrm{S}}} : (\boldsymbol{C}_{\mathrm{S}})'_{\mathrm{S}} = \frac{\partial \psi^{\mathrm{S}}}{\partial \boldsymbol{C}_{\mathrm{S}}} : \left(2 \, \boldsymbol{F}_{\mathrm{S}}^T \cdot \boldsymbol{D}_{\mathrm{S}} \cdot \boldsymbol{F}_{\mathrm{S}}\right) \quad \text{and} \quad (\psi^{\mathrm{L}})'_{\mathrm{L}} = 0 \,. \tag{2.107}$$

Inserting both reformulations into Eq. (2.103) leads to

$$\begin{aligned} -\rho^{\mathrm{S}}\frac{\partial\psi^{\mathrm{S}}}{\partial\boldsymbol{C}_{\mathrm{S}}} : (2\boldsymbol{F}_{\mathrm{S}}^{T}\cdot\boldsymbol{D}_{\mathrm{S}}\cdot\boldsymbol{F}_{\mathrm{S}}) + \boldsymbol{\sigma}^{\mathrm{S}} : \boldsymbol{D}_{\mathrm{S}} + \boldsymbol{\sigma}^{\mathrm{L}} : \boldsymbol{D}_{\mathrm{L}} - \hat{\boldsymbol{p}}^{\mathrm{L}}\cdot\boldsymbol{w}_{\mathrm{LS}} \\ - p\left[-n^{\mathrm{S}}\,\boldsymbol{D}_{\mathrm{S}} : \boldsymbol{I} - n^{\mathrm{L}}\,\boldsymbol{D}_{\mathrm{L}} : \boldsymbol{I} - \operatorname{grad}(n^{\mathrm{L}})\cdot\boldsymbol{w}_{\mathrm{LS}}\right] \geq 0\,. \end{aligned} \tag{2.108}$$

such that the entropy inequality can be rewritten to extract the constitutive relation and the dissipation mechanism as

$$\begin{aligned} &\boldsymbol{D}_{\mathrm{S}} : \left(\boldsymbol{\sigma}^{\mathrm{S}} - 2\rho^{\mathrm{S}}\boldsymbol{F}_{\mathrm{S}}\cdot\frac{\partial\psi^{\mathrm{S}}}{\partial\boldsymbol{C}_{\mathrm{S}}}\cdot\boldsymbol{F}_{\mathrm{S}}^{T} + n^{\mathrm{S}}\,p\,\boldsymbol{I}\right) \\ &+ \boldsymbol{D}_{\mathrm{L}} : \left(\boldsymbol{\sigma}^{\mathrm{L}} + n^{\mathrm{L}}\,p\,\boldsymbol{I}\right) \\ &- \boldsymbol{w}_{\mathrm{LS}}\cdot\left[\hat{\boldsymbol{p}}^{\mathrm{L}} - p\,\operatorname{grad}(n^{\mathrm{L}})\right] \geq 0\,. \end{aligned} \tag{2.109}$$

The entropy inequality is fulfilled if the constitutive relations for the solid and liquid stress

$$\begin{aligned} \boldsymbol{\sigma}^{\mathrm{S}} &= \boldsymbol{\sigma}_{\mathrm{E}}^{\mathrm{S}} - n^{\mathrm{S}}\,p\,\boldsymbol{I}\,, \\ \boldsymbol{\sigma}^{\mathrm{L}} &= -n^{\mathrm{L}}\,p\,\boldsymbol{I} \end{aligned} \tag{2.110}$$

with the solid effective stress

$$\boldsymbol{\sigma}_{\mathrm{E}}^{\mathrm{S}} = 2\rho^{\mathrm{S}}\boldsymbol{F}_{\mathrm{S}}\cdot\frac{\partial\psi^{\mathrm{S}}}{\partial\boldsymbol{C}_{\mathrm{S}}}\cdot\boldsymbol{F}_{\mathrm{S}}^{T} \tag{2.111}$$

hold and the dissipation is greater or equal to zero as

$$\mathcal{D} = -\boldsymbol{w}_{\mathrm{LS}}\cdot\left[\hat{\boldsymbol{p}}^{\mathrm{L}} - p\,\operatorname{grad}(n^{\mathrm{L}})\right] \geq 0\,. \tag{2.112}$$

As a result of the obtained constitutive relation, the Lagrange multiplier p can be interpreted as a pore pressure from the physical point of view. The stress of the mixture results in

$$\boldsymbol{\sigma} = \boldsymbol{\sigma}^{\mathrm{S}} + \boldsymbol{\sigma}^{\mathrm{L}} = \boldsymbol{\sigma}_{\mathrm{E}}^{\mathrm{S}} - p\,\boldsymbol{I} \tag{2.113}$$

under consideration of the saturation condition. Within this thesis, the free energy function for the solid phase is of Neo-Hookean type if not stated otherwise as

$$\psi^{\mathrm{S}} = \psi^{\mathrm{NH}} = \frac{1}{\rho_{0\mathrm{S}}^{\mathrm{S}}}\left\{\frac{\lambda^{\mathrm{S}}}{2}\left[\ln(J_{\mathrm{S}})\right]^{2} - \mu^{\mathrm{S}}\ln(J_{\mathrm{S}}) + \frac{\mu^{\mathrm{S}}}{2}\left[\operatorname{tr}(\boldsymbol{C}_{\mathrm{S}}) - 3\right]\right\} \tag{2.114}$$

with the first and second Lamé constants λ^{S} and μ^{S}. The ansatz to fulfill the requirement on the dissipation mechanism is given in dependence of the material parameter β^{L} as

$$\mathcal{D} = \boldsymbol{w}_{\mathrm{LS}}\cdot\beta^{\mathrm{L}}\,\boldsymbol{w}_{\mathrm{LS}} \quad \text{with} \quad \beta^{\mathrm{L}} \geq 0 \tag{2.115}$$

and

$$\beta^{\mathrm{L}}\,\boldsymbol{w}_{\mathrm{LS}} = -\hat{\boldsymbol{p}}^{\mathrm{L}} + p\,\operatorname{grad}(n^{\mathrm{L}})\,. \tag{2.116}$$

2.6.3 Towards an Efficient Numerical Model

The set of field equations of the binary model in Section 2.6.1 can be reduced to develop a simple and efficient formulation. At first, writing the time integrated form of of the balance of mass in Eq. (2.43) for the solid phase and inserting the assumption of no mass exchange and using Eq. (2.27) as

$$\int_{t_0}^{t} \frac{1}{\rho^{\mathrm{S}}} \left(\rho^{\mathrm{S}}\right)'_{\mathrm{S}} \,\mathrm{d}t + \int_{t_0}^{t} \frac{1}{J_{\mathrm{S}}} \left(J_{\mathrm{S}}\right)'_{\mathrm{S}} \,\mathrm{d}t = 0 \tag{2.117}$$

executing the integration as

$$\ln\left[\rho^{\mathrm{S}}(t)\right] - \ln\left[\rho^{\mathrm{S}}(t_0)\right] + \ln\left[J_{\mathrm{S}}(t)\right] - \ln\left[J_{\mathrm{S}}(t_0)\right] = 0 \tag{2.118}$$

with $\rho^{\mathrm{S}} = \rho^{\mathrm{S}}(t)$, $\rho^{\mathrm{S}}_{0\mathrm{S}} = \rho^{\mathrm{S}}(t_0)$, $J_{\mathrm{S}} = J_{\mathrm{S}}(t)$ and $J_{\mathrm{S}}(t_0) = 1$ leads to

$$J_{\mathrm{S}} = \frac{\rho^{\mathrm{S}}_{0\mathrm{S}}}{\rho^{\mathrm{S}}} \,. \tag{2.119}$$

This rather general applicable relation becomes more specific for the binary model by additionally including the incompressibility condition and the formula for the Jacobian determinant leading to

$$\sqrt{\det(\boldsymbol{C}_{\mathrm{S}})} = J_{\mathrm{S}} = \frac{n^{\mathrm{S}}_{0\mathrm{S}}}{n^{\mathrm{S}}} \,. \tag{2.120}$$

With this, the volume fractions of solid n^{S} can be calculated from the solid deformation and subsequently the one of the liquid n^{L} with help of the saturation condition. Consequently, it is not necessary to solve the balances of mass in Eq. (2.93) separately. Instead, the rate of the saturation condition in Eq. (2.98) is inserted into the balance of mass of the mixture such that

$$n^{\mathrm{S}} \operatorname{div}(\boldsymbol{x}'_{\mathrm{S}}) + n^{\mathrm{L}} \operatorname{div}(\boldsymbol{x}'_{\mathrm{L}}) + \operatorname{grad}(n^{\mathrm{L}}) \cdot \boldsymbol{w}_{\mathrm{LS}} = 0 \,. \tag{2.121}$$

holds. Exploiting the saturation condition and

$$\operatorname{div}(n^{\mathrm{L}} \boldsymbol{w}_{\mathrm{LS}}) = \operatorname{grad}(n^{\mathrm{L}}) \cdot \boldsymbol{w}_{\mathrm{LS}} + n^{\mathrm{L}} \operatorname{div}(\boldsymbol{w}_{\mathrm{LS}}) \tag{2.122}$$

leads to the modified balance of mass of the mixture

$$\operatorname{div}(\boldsymbol{x}'_{\mathrm{S}} + n^{\mathrm{L}} \boldsymbol{w}_{\mathrm{LS}}) = 0 \,. \tag{2.123}$$

Furthermore, the focus of the investigations is on the motion of the solid constituent $\boldsymbol{\chi}_{\mathrm{S}}$ since the domain of the solid $\mathcal{B}_{\mathrm{S}}$ is considered as control space. Consequently the motion of the liquid phase $\boldsymbol{\chi}_{\mathrm{L}}$ respectively the balance of momentum of the liquid in Eq. $(2.94)_2$ does not need to be solved. Nevertheless, the equation is needed in the following to find an expression for the seepage velocity $\boldsymbol{w}_{\mathrm{LS}}$ as part of the balance of mass of the mixture. Inserting the constitutive relation for the liquid stress in Eq. $(2.110)_2$ and the ansatz for the dissipation in Eq. (2.116) into the balance of momentum of the liquid in Eq. $(2.94)_2$ leads to

$$\operatorname{div}\left(-n^{\mathrm{L}} p \boldsymbol{I}\right) + \rho^{\mathrm{L}} \boldsymbol{b} = \beta^{\mathrm{L}} \boldsymbol{w}_{\mathrm{LS}} - p \operatorname{grad}(n^{\mathrm{L}}) \,. \tag{2.124}$$

This equation can be reformulated with

$$\operatorname{div}\left(-n^{\mathrm{L}} p \boldsymbol{I}\right) = -p \operatorname{grad}(n^{\mathrm{L}}) - n^{\mathrm{L}} \operatorname{grad}(p) \tag{2.125}$$

to

$$n^{\mathrm{L}}\,\boldsymbol{w}_{\mathrm{LS}} = -\frac{\left(n^{\mathrm{L}}\right)^2}{\beta^{\mathrm{L}}}\left[\operatorname{grad}(p) - \rho^{\mathrm{LR}}\,\boldsymbol{b}\right], \tag{2.126}$$

where the definition of the partial density in Eq. (2.6) is utilized. The Darcy parameter k_{L} as a material parameter describing the permeability of the porous solid with respect to the liquid is introduced and postulated as

$$k_{\mathrm{L}} := \frac{\left(n^{\mathrm{L}}\right)^2}{\beta^{\mathrm{L}}} = \text{constant} \tag{2.127}$$

to simplify the relation. The combination of seepage velocity and volume fraction of the liquid, also called filter velocity, is referred to as specific liquid flux $\boldsymbol{q} = n^{\mathrm{L}}\,\boldsymbol{w}_{\mathrm{LS}}$.

Summarizing, the remaining equations to solve are the balance equations of momentum and mass of the mixture as

$$\begin{aligned} \operatorname{div}(\boldsymbol{\sigma}) + \rho\,\boldsymbol{b} &= \boldsymbol{0}\,, \\ \operatorname{div}\left[\boldsymbol{x}'_{\mathrm{S}} - k_{\mathrm{L}}\operatorname{grad}(p) + k_{\mathrm{L}}\,\rho^{\mathrm{LR}}\,\boldsymbol{b}\right] &= 0 \end{aligned} \tag{2.128}$$

with the motion of the solid $\boldsymbol{\chi}_{\mathrm{S}}$, respectively the displacement of the solid $\boldsymbol{u}_{\mathrm{S}}$, and the pore pressure p as unknown fields.

This set of equations is solved with the FEM which is presented in Chapter 3. Within this framework, it is often beneficial to formulate the equations with respect to the reference formulation. For this purpose, the corresponding global form of the balance of momentum of the mixture in Eq. $(2.128)_1$ is transformed by using the divergence theorem and the transport theorems in Eq. (2.16) such that

$$\begin{aligned} \int_{\mathcal{B}} \left[\operatorname{div}(\boldsymbol{\sigma}) + \rho\,\boldsymbol{b}\right] \mathrm{d}v &= \int_{\partial\mathcal{B}} \boldsymbol{\sigma}\cdot\boldsymbol{n}\,\mathrm{d}a + \int_{\mathcal{B}} \rho\,\boldsymbol{b}\,\mathrm{d}v \\ &= \int_{\partial\mathcal{B}_{0\mathrm{S}}} \boldsymbol{\sigma}\cdot\left(J_{\mathrm{S}}\,\boldsymbol{F}_{\mathrm{S}}^{-T}\cdot\boldsymbol{N}_{\mathrm{S}}\right)\mathrm{d}A_{\mathrm{S}} + \int_{\mathcal{B}_{0\mathrm{S}}} J_{\mathrm{S}}\,\rho\,\boldsymbol{b}\,\mathrm{d}V_{\mathrm{S}} \\ &= \int_{\partial\mathcal{B}_{0\mathrm{S}}} \boldsymbol{P}\cdot\boldsymbol{N}_{\mathrm{S}}\,\mathrm{d}A_{\mathrm{S}} + \int_{\mathcal{B}_{0\mathrm{S}}} \rho_{0\mathrm{S}}\,\boldsymbol{b}\,\mathrm{d}V_{\mathrm{S}} \\ &= \int_{\mathcal{B}_{0\mathrm{S}}} \left[\operatorname{Div}_{\mathrm{S}}(\boldsymbol{P}) + \rho_{0\mathrm{S}}\,\boldsymbol{b}\right]\mathrm{d}V_{\mathrm{S}} \end{aligned} \tag{2.129}$$

with the density of the mixture with respect to the reference configuration solid

$$\rho_{0\mathrm{S}} = J_{\mathrm{S}}\,\rho \tag{2.130}$$

and the definition of the first Piola-Kirchhoff stress tensor in Eq. (2.33) applied to the stress of the mixture as

$$\boldsymbol{P} = J_{\mathrm{S}}\,\boldsymbol{\sigma}\cdot\boldsymbol{F}_{\mathrm{S}}^{-T} = J_{\mathrm{S}}\left(\boldsymbol{\sigma}^{\mathrm{S}} + \boldsymbol{\sigma}^{\mathrm{L}}\right)\cdot\boldsymbol{F}_{\mathrm{S}}^{-T} = \boldsymbol{P}^{\mathrm{S}} + \boldsymbol{P}^{\mathrm{L}}\,. \tag{2.131}$$

The operator $\operatorname{Div}_{\mathrm{S}}$ indicates that the divergence is taken with respect to the position vector of the solid constituent in the reference configuration as

$$\operatorname{Div}_{\mathrm{S}}(\bullet) = \frac{\partial(\bullet)}{\partial\boldsymbol{X}_{\mathrm{S}}} : \boldsymbol{I}\,. \tag{2.132}$$

The reformulation of the balance of mass of the mixture starts with the global form of Eq. (2.123) without including the relation for the specific liquid flux $n^{\mathrm{L}}\,\boldsymbol{w}_{\mathrm{LS}}$ for the sake of clarity. Using once more the divergence theorem and the transport theorems in Eq. (2.16) leads to

$$\begin{aligned}\int_{\mathcal{B}} \left[\operatorname{div}(\boldsymbol{x}'_{\mathrm{S}} + n^{\mathrm{L}}\,\boldsymbol{w}_{\mathrm{LS}})\right]\,\mathrm{d}v &= \int_{\mathcal{B}} \operatorname{div}(\boldsymbol{x}'_{\mathrm{S}})\,\mathrm{d}v + \int_{\partial\mathcal{B}} n^{\mathrm{L}}\,\boldsymbol{w}_{\mathrm{LS}}\cdot\boldsymbol{n}\,\mathrm{d}a \\ &= \int_{\mathcal{B}_{0\mathrm{S}}} J_{\mathrm{S}}\,\operatorname{div}(\boldsymbol{x}'_{\mathrm{S}})\,\mathrm{d}V_{\mathrm{S}} + \int_{\partial\mathcal{B}_{0\mathrm{S}}} n^{\mathrm{L}}\,\boldsymbol{w}_{\mathrm{LS}}\cdot\left(J_{\mathrm{S}}\,\boldsymbol{F}_{\mathrm{S}}^{-T}\cdot\boldsymbol{N}_{\mathrm{S}}\right)\mathrm{d}A_{\mathrm{S}} \\ &= \int_{\mathcal{B}_{0\mathrm{S}}} J_{\mathrm{S}}\,(\boldsymbol{E}_{\mathrm{S}})'_{\mathrm{S}} : \boldsymbol{C}_{\mathrm{S}}^{-1}\,\mathrm{d}V_{\mathrm{S}} + \int_{\partial\mathcal{B}_{0\mathrm{S}}} n^{\mathrm{L}}\,\boldsymbol{w}_{\mathrm{LS0S}}\cdot\boldsymbol{N}_{\mathrm{S}}\,\mathrm{d}A_{\mathrm{S}} \\ &= \int_{\mathcal{B}_{0\mathrm{S}}} \left[\operatorname{Div}_{\mathrm{S}}(n^{\mathrm{L}}\,\boldsymbol{w}_{\mathrm{LS0S}}) + J_{\mathrm{S}}\,(\boldsymbol{E}_{\mathrm{S}})'_{\mathrm{S}} : \boldsymbol{C}_{\mathrm{S}}^{-1}\right]\,\mathrm{d}V_{\mathrm{S}}\end{aligned} \tag{2.133}$$

with the shifted seepage velocity

$$\boldsymbol{w}_{\mathrm{LS0S}} = J_{\mathrm{S}}\,\boldsymbol{F}_{\mathrm{S}}^{-1}\cdot\boldsymbol{w}_{\mathrm{LS}}\,. \tag{2.134}$$

Additionally, Eq. (2.26) and (2.105) are used to show the identity

$$(\boldsymbol{E}_{\mathrm{S}})'_{\mathrm{S}} : \boldsymbol{C}_{\mathrm{S}}^{-1} = (\boldsymbol{F}_{\alpha}^{T}\cdot\boldsymbol{D}_{\alpha}\cdot\boldsymbol{F}_{\alpha}) : (\boldsymbol{F}_{\alpha}^{-1}\cdot\boldsymbol{F}_{\alpha}^{-T}) = \boldsymbol{D}_{\alpha} : \boldsymbol{I} = \operatorname{div}(\boldsymbol{x}'_{\alpha})\,. \tag{2.135}$$

In summary, the set of equations to solve in (2.128) is reformulated to the local forms of the balance of momentum of the mixture and the balance of mass of the mixture with respect to the reference configuration as

$$\begin{aligned}\operatorname{Div}_{\mathrm{S}}(\boldsymbol{P}) + \rho_{0\mathrm{S}}\,\boldsymbol{b} &= \boldsymbol{0}\,, \\ \operatorname{Div}_{\mathrm{S}}(n^{\mathrm{L}}\,\boldsymbol{w}_{\mathrm{LS0S}}) + J_{\mathrm{S}}\,(\boldsymbol{E}_{\mathrm{S}})'_{\mathrm{S}} : \boldsymbol{C}_{\mathrm{S}}^{-1} &= 0\end{aligned} \tag{2.136}$$

which will serve as starting point for the FEM derivations.

2.7 Remarks on the Single Solid Phase Model and Linear Theory

In the course of this chapter, the TPM is presented at first for the general case of k constituents before it is reduced to a binary model which is investigated within this thesis. In contrast to this, the FEM is presented in Chapter 3 at first for a single component solid material to introduce the procedure and notation as convenient as possible. This reduces the problem to solving the balance of linear momentum of the solid phase

$$\operatorname{Div}_{\mathrm{S}}(\boldsymbol{P}^{\mathrm{S}}) + \rho^{\mathrm{S}}_{0\mathrm{S}}\,\boldsymbol{b} = \boldsymbol{0} \quad \text{respectively} \quad \operatorname{Div}(\boldsymbol{P}) + \rho_0\,\boldsymbol{b} = \boldsymbol{0} \tag{2.137}$$

for the unknown displacement of the solid $\boldsymbol{u}_{\mathrm{S}}$, respectively $\boldsymbol{u}$.

In addition to this, the first numerical example of the MIEL method in Chapter 6 investigates linear elasticity to get deeper insights into the method before switching to the more complex TPM. Towards a linear theory, a St. Venant-Kirchhoff material law is assumed

with $\boldsymbol{S} = \mathbb{C} : \boldsymbol{E}$ where the fourth order elasticity tensor $\mathbb{C}$ is constant. With this, the balance of linear momentum in Eq. (2.137) is reformulated to

$$\operatorname{Div}\left[\boldsymbol{F} \cdot (\mathbb{C} : \boldsymbol{E})\right] + \rho_0 \, \boldsymbol{b} = \boldsymbol{0} \,. \tag{2.138}$$

Furthermore, the Green-Lagrange strain tensor in Eq. (2.19) can be rewritten for a single solid constituent to

$$\boldsymbol{E} = \frac{1}{2}\left(\boldsymbol{F}^T \cdot \boldsymbol{F} - \boldsymbol{I}\right) = \frac{1}{2}\left(\operatorname{Grad} \boldsymbol{u} + \operatorname{Grad}^T \boldsymbol{u} + \operatorname{Grad}^T \boldsymbol{u} \cdot \operatorname{Grad} \boldsymbol{u}\right) . \tag{2.139}$$

Introducing the assumption of small deformations as $|\operatorname{Grad} \boldsymbol{u}| \ll 1$ makes the non-linear term in this expression negligible leading to the infinitesimal strain tensor $\boldsymbol{\varepsilon}$ as

$$\boldsymbol{\varepsilon} = \frac{1}{2}\left(\operatorname{Grad} \boldsymbol{u} + \operatorname{Grad}^T \boldsymbol{u}\right) . \tag{2.140}$$

The same assumption has the effect that $\boldsymbol{F} \approx \boldsymbol{1}$ and $J \approx 1$. As a consequence there are no longer distinguishable configurations which allows to write the balance of linear momentum as

$$\operatorname{div}(\boldsymbol{\sigma}^*) + \rho^* \, \boldsymbol{b} = \boldsymbol{0} \tag{2.141}$$

with the density ρ^* and the stress obeying Hooke's law which can be written as

$$\boldsymbol{\sigma}^* = \rho^* \, \frac{\partial \psi^{\mathrm{H}}}{\partial \boldsymbol{\varepsilon}} \tag{2.142}$$

in accordance to Eq. (2.111) with the strain energy function given by

$$\psi^{\mathrm{S}} = \psi^{\mathrm{H}}(\boldsymbol{\varepsilon}) = \frac{1}{\rho^*}\left\{\frac{\lambda^{\mathrm{S}}}{2}[\operatorname{tr}(\boldsymbol{\varepsilon})]^2 + \mu^{\mathrm{S}} \operatorname{tr}(\boldsymbol{\varepsilon} \cdot \boldsymbol{\varepsilon})\right\} . \tag{2.143}$$

3 Finite Element Method

The Finite Element Method is introduced in this chapter with focus on the applied models within this thesis and to introduce a generally applicable notation to allow for a simple derivation of the MIEL method in Chapter 5. For further details on the FEM, the reader is referred to well known textbooks on this method, e.g. Zienkiewicz et al. [2013], Bathe [1996], Wriggers [2008].

The chapter starts with the derivation of the FEM for finite elasticity to introduce the procedure and notation at a comparatively simple model. Subsequently, the same strategy is applied for the binary TPM approach. Afterwards, both models are unified in a general notation before the numerical treatment is presented. This chapter closes with an overview on all selected element formulations within this thesis.

3.1 FEM for Finite Elasticity

As an introduction into the FEM in terms of structure and notation, the problem of finite elasticity is discussed. For this purpose, a simple pure displacement formulation has been chosen.

3.1.1 Weak Form and its Linearization

Starting point is the balance of momentum in Eq. (2.137) as

$$- \{\mathrm{Div}[\boldsymbol{P}(\boldsymbol{u})] + \rho_0\, \boldsymbol{b}\} = \boldsymbol{0} \tag{3.1}$$

including the indication that the stress $\boldsymbol{P}$ only depends in the displacement $\boldsymbol{u}$. The sign of the equation is chosen as minus even though this is irrelevant from the mathematical point of view. Nevertheless, this choice is reasonable with respect to the solution procedure since it leads to a positive definite system matrix. Applying the standard Galerkin method by multiplying a test function $\delta\boldsymbol{u}$ which satisfies $\delta\boldsymbol{u} = \boldsymbol{0}$ on $\partial\mathcal{B}_{0u}$ and integrating over the domain leads to

$$- \int_{\mathcal{B}_0} [\mathrm{Div}(\boldsymbol{P}) + \rho_0\, \boldsymbol{b}] \cdot \delta\boldsymbol{u}\, \mathrm{d}V = 0\,. \tag{3.2}$$

Reformulating the first term

$$- \mathrm{Div}(\boldsymbol{P}) \cdot \delta\boldsymbol{u} = - \mathrm{Div}(\boldsymbol{P}^T \cdot \delta\boldsymbol{u}) + \boldsymbol{P} : \mathrm{Grad}(\delta\boldsymbol{u}) \tag{3.3}$$

and applying Gauss theorem as

$$- \int_{\mathcal{B}_0} \mathrm{Div}(\boldsymbol{P}^T \cdot \delta\boldsymbol{u})\, \mathrm{d}V = - \int_{\partial\mathcal{B}_{0t}} (\boldsymbol{P} \cdot \boldsymbol{N}) \cdot \delta\boldsymbol{u}\, \mathrm{d}A \tag{3.4}$$

leads to

$$\int_{\mathcal{B}_0} \boldsymbol{P} : \mathrm{Grad}(\delta\boldsymbol{u})\, \mathrm{d}V - \int_{\mathcal{B}_0} \rho_0\, \boldsymbol{b} \cdot \delta\boldsymbol{u}\, \mathrm{d}V - \int_{\partial\mathcal{B}_0} (\boldsymbol{P} \cdot \boldsymbol{N}) \cdot \delta\boldsymbol{u}\, \mathrm{d}A = 0\,. \tag{3.5}$$

Inserting the Cauchy theorem $\boldsymbol{t}_0 = \boldsymbol{P} \cdot \boldsymbol{N}$ and $\delta\boldsymbol{F} = \delta(\boldsymbol{I} + \mathrm{Grad}\,\boldsymbol{u}) = \mathrm{Grad}(\delta\boldsymbol{u})$ yields

$$\int_{\mathcal{B}_0} \boldsymbol{P} : \delta\boldsymbol{F}\, \mathrm{d}V - \int_{\mathcal{B}_0} \rho_0\, \boldsymbol{b} \cdot \delta\boldsymbol{u}\, \mathrm{d}V - \int_{\partial\mathcal{B}_{0t}} \bar{\boldsymbol{t}}_0 \cdot \delta\boldsymbol{u}\, \mathrm{d}A = 0\,. \tag{3.6}$$

Here the boundary has been decomposed as $\partial\mathcal{B}_0 = \partial\mathcal{B}_{0u} \cup \partial\mathcal{B}_{0t}$ with $\partial\mathcal{B}_{0u} \cap \partial\mathcal{B}_{0t} = \emptyset$ such that Dirichlet and Neumann boundary conditions are applied as $\boldsymbol{u} = \overline{\boldsymbol{u}}$ on $\partial\mathcal{B}_{0u}$ and $\boldsymbol{t}_0 = \overline{\boldsymbol{t}}_0$ on $\partial\mathcal{B}_{0t}$.

In case of a hyperelastic material behavior, it can be described by a strain energy density function $\psi(\boldsymbol{C})$. For this case, the second Piola-Kirchhoff stress tensor $\boldsymbol{S}$ and the elasticity tensor $\mathbb{C}$ are defined in agreement with Eq. (2.111) and (2.34) as

$$\boldsymbol{S} := 2\,\rho_0\,\frac{\partial\psi}{\partial\boldsymbol{C}} \quad \text{and} \quad \mathbb{C} := 2\,\frac{\partial\boldsymbol{S}}{\partial\boldsymbol{C}} = 4\,\rho_0\,\frac{\partial^2\psi}{\partial\boldsymbol{C}\otimes\partial\boldsymbol{C}}\,. \tag{3.7}$$

The choice of the symmetric $\boldsymbol{S}$ and $\boldsymbol{C}$ as appearing quantities is in general advantageous compared to the unsymmetric $\boldsymbol{P}$ and $\boldsymbol{F}$. Therefore, the first term in Eq. (3.6) is reformulated as

$$\boldsymbol{P} : \delta\boldsymbol{F} = (\boldsymbol{F}\cdot\boldsymbol{S}) : \delta\boldsymbol{F} = \boldsymbol{S} : (\boldsymbol{F}^T\cdot\delta\boldsymbol{F}) = \boldsymbol{S} : \mathrm{sym}(\boldsymbol{F}^T\cdot\delta\boldsymbol{F}) = \boldsymbol{S} : \frac{1}{2}\delta\boldsymbol{C}\,. \tag{3.8}$$

leading to the weak form

$$G(\boldsymbol{u},\delta\boldsymbol{u}) := \int_{\mathcal{B}_0} \boldsymbol{S} : \frac{1}{2}\delta\boldsymbol{C}\;\mathrm{d}V - \int_{\mathcal{B}_0}\rho_0\,\boldsymbol{b}\cdot\delta\boldsymbol{u}\;\mathrm{d}V - \int_{\partial\mathcal{B}_{0t}}\overline{\boldsymbol{t}}_0\cdot\delta\boldsymbol{u}\;\mathrm{d}A = 0\,. \tag{3.9}$$

An equivalent way to derive these equations for hyperelastic problems is starting from the potential

$$\Pi(\boldsymbol{u}) := \int_{\mathcal{B}_0}\rho_0\,\psi\;\mathrm{d}V - \int_{\mathcal{B}_0}\rho_0\,\boldsymbol{b}\cdot\boldsymbol{u}\;\mathrm{d}V - \int_{\partial\mathcal{B}_{0t}}\overline{\boldsymbol{t}}_0\cdot\boldsymbol{u}\;\mathrm{d}A\,. \tag{3.10}$$

The first variation of this potential with respect to the displacement leads exactly to the weak form in Eq. (3.9).

A simple and very robust possibility to solve such nonlinear equations is Newton's method. For this procedure, the linearization of the weak form is needed

$$\mathrm{Lin}\,G(\boldsymbol{u},\delta\boldsymbol{u},\Delta\boldsymbol{u}) = G(\boldsymbol{u},\delta\boldsymbol{u}) + \Delta G(\boldsymbol{u},\delta\boldsymbol{u},\Delta\boldsymbol{u})\,. \tag{3.11}$$

For the sake of simplicity, the volume load $\rho_0\,\boldsymbol{b}$ and surface traction $\overline{\boldsymbol{t}}_0$ are assumed to be conservative, respectively independent from the displacements. With this, the increment ΔG is given by

$$\Delta G(\boldsymbol{u},\delta\boldsymbol{u},\Delta\boldsymbol{u}) := \int_{\mathcal{B}_0}\Delta\boldsymbol{S} : \frac{1}{2}\delta\boldsymbol{C}\;\mathrm{d}V + \int_{\mathcal{B}_0}\boldsymbol{S} : \frac{1}{2}\Delta\delta\boldsymbol{C}\;\mathrm{d}V\,. \tag{3.12}$$

3.1.2 Discretization

The key idea of the FEM is the approximation of the physical domain $\mathcal{B}_0$ by $\mathcal{B}_0^h$. The approximated domain $\mathcal{B}_0^h$ consists of an assembly of (non-overlapping) element domains as

$$\mathcal{B}_0 \approx \mathcal{B}_0^h = \bigcup_{e=1}^{n_e}\mathcal{B}_0^e\,, \tag{3.13}$$

where n_e denotes the number of finite elements. Within these elements, the geometry and the unknown field, respectively its variation and increment, are approximated with

help of nodes and their corresponding shape functions. The number and positions of these nodes depend on the type of the element. The different types of finite elements which are used throughout this thesis are described in Section 3.5. The most commonly used isoparametric concept applies the same shape functions for the approximation of the geometry as well as the displacement, such that in general

$$\begin{aligned}
\boldsymbol{X} \approx \boldsymbol{X}^h &= \sum_{I=1}^{n_{_u}} N_u^I(\boldsymbol{\xi})\, \boldsymbol{X}^I &&= \hat{\boldsymbol{N}}_u \cdot \hat{\boldsymbol{X}}\,, \\
\boldsymbol{u} \approx \boldsymbol{u}^h &= \sum_{I=1}^{n_{_u}} N_u^I(\boldsymbol{\xi})\, \boldsymbol{d}_u^I &&= \hat{\boldsymbol{N}}_u \cdot \boldsymbol{d}_u\,, \\
\delta\boldsymbol{u} \approx \delta\boldsymbol{u}^h &= \sum_{I=1}^{n_{_u}} N_u^I(\boldsymbol{\xi})\, \delta\boldsymbol{d}_u^I &&= \hat{\boldsymbol{N}}_u \cdot \delta\boldsymbol{d}_u\,, \\
\Delta\boldsymbol{u} \approx \Delta\boldsymbol{u}^h &= \sum_{I=1}^{n_{_u}} N_u^I(\boldsymbol{\xi})\, \Delta\boldsymbol{d}_u^I &&= \hat{\boldsymbol{N}}_u \cdot \Delta\boldsymbol{d}_u
\end{aligned} \tag{3.14}$$

holds for a typical element. The number of nodes per element for the interpolation of the displacement is stated as $n_{\_u}$. The shape function for the displacement at node I is denoted with $N_u^I(\boldsymbol{\xi})$, defined in the parameter space $\boldsymbol{\xi}$. The displacements at node I, their variation and increment are given by $\boldsymbol{d}_u^I$, $\delta\boldsymbol{d}_u^I$ and $\Delta\boldsymbol{d}_u^I$. This notation allows the handling of multiple unknown fields at the same node. As an alternative arrangement, the quantities at the nodes are listed one after another for the entire element as

$$\begin{aligned}
\hat{\boldsymbol{X}} &:= \{\hat{X}_1^1, \hat{X}_2^1, \hat{X}_3^1, ..., \hat{X}_1^{n_{_u}}, \hat{X}_2^{n_{_u}}, \hat{X}_3^{n_{_u}}\}\,, \\
\boldsymbol{d}_u &:= \{d_{u1}^1, d_{u2}^1, d_{u3}^1, ..., d_{u1}^{n_{_u}}, d_{u2}^{n_{_u}}, d_{u3}^{n_{_u}}\}\,, \\
\delta\boldsymbol{d}_u &:= \{\delta d_{u1}^1, \delta d_{u2}^1, \delta d_{u3}^1, ..., \delta d_{u1}^{n_{_u}}, \delta d_{u2}^{n_{_u}}, \delta d_{u3}^{n_{_u}}\}\,, \\
\Delta\boldsymbol{d}_u &:= \{\Delta d_{u1}^1, \Delta d_{u2}^1, \Delta d_{u3}^1, ..., \Delta d_{u1}^{n_{_u}}, \Delta d_{u2}^{n_{_u}}, \Delta d_{u3}^{n_{_u}}\}\,.
\end{aligned} \tag{3.15}$$

The matrix $\hat{\boldsymbol{N}}_u$ contains the shape functions of all nodes in a compatible manner. Please observe that along with this quantity the notation switched from tensor notation in a physical sense to a more general array notation. This array notation uses the same operators as before but allows arbitrarily shaped arrays as $\hat{\boldsymbol{N}}_u = (\hat{N}_u)_{ij}$ with $i \in \{1, ..., n_{\text{dimensions}}\}$ and $j \in \{1, ..., n_{d_u}\}$ where n_{d_u} is the number of displacement degrees of freedom per element. Even though the classical matrix notation would be sufficient for this specific array, it lacks the ability of handling arrays of higher dimensions which will arise in the following.

The classical way of deriving the system of equation to solve, namely the right-hand-side vector and system matrix, includes the incorporation of Voigt's notation and strain matrices. These matrices, such as the *B-matrix*, are frequently used for a neat notation and implementation, exemplary $\delta\boldsymbol{C}^h = \boldsymbol{B} \cdot \delta\boldsymbol{d}_u$. For more details, see e.g. Zienkiewicz et al. [2013]. The implementations related to this thesis are realized with the software *AceGen* which is capable of automatic differentiation and code optimization. Because of that, the complexity reduction, classically achieved by Voigt's notation, can be omitted and the notation will focus on the discrete degrees of freedom.

After inserting the discretization, the weak form in Eq. (3.9) can be written for a typical

element e in array notation as

$$\begin{aligned} G_u^e(\boldsymbol{d}_u, \delta\boldsymbol{d}_u) &= \int_{\mathcal{B}_0^e} \boldsymbol{S}^h : \frac{1}{2}\delta\boldsymbol{C}^h \,\mathrm{d}V - \int_{\mathcal{B}_0^e} \rho_0\, \boldsymbol{b} \cdot \delta\boldsymbol{u}^h \,\mathrm{d}V - \int_{\partial\mathcal{B}_{0t}^e} \bar{\boldsymbol{t}}_0 \cdot \delta\boldsymbol{u}^h \,\mathrm{d}A \\ &= \delta\boldsymbol{d}_u \cdot \Bigg\{ \int_{\mathcal{B}_0^e} \frac{1}{2}\left[\left(\frac{\partial\boldsymbol{C}^h}{\partial\boldsymbol{d}_u}\right)^{\overset{13}{T}}\right]^{\overset{23}{T}} : \boldsymbol{S}^h \,\mathrm{d}V \\ &\qquad \underbrace{- \int_{\mathcal{B}_0^e} \hat{\boldsymbol{N}}_u^T \cdot \rho_0\, \boldsymbol{b} \,\mathrm{d}V - \int_{\partial\mathcal{B}_{0t}^e} \hat{\boldsymbol{N}}_u^T \cdot \bar{\boldsymbol{t}}_0 \,\mathrm{d}A}_{\boldsymbol{r}_u} \Bigg\}. \end{aligned} \tag{3.16}$$

The transformation of the term in the first integral is more evident in index notation as

$$(S^h)_{ij}\,\frac{1}{2}\,(\delta C^h)_{ij} = (S^h)_{ij}\,\frac{1}{2}\,\frac{\partial (C^h)_{ij}}{\partial (d_u)_k}\,(\delta d_u)_k\,. \tag{3.17}$$

The expression $\partial\boldsymbol{C}^h/\partial\boldsymbol{d}_u$ contains the same information as the classical *B-matrix*, here in its unmodified version, stored in a three dimensional array. The specific structure is omitted at this point. The element right-hand side vector corresponding to the unknown field $\boldsymbol{u}$ is identified as $\boldsymbol{r}_u$. Applying the discretization to Eq. (3.12) leads for a typical element e to

$$\Delta G_u^e(\boldsymbol{d}_u, \delta\boldsymbol{d}_u, \Delta\boldsymbol{d}_u) = \int_{\mathcal{B}_0^e} \Delta\boldsymbol{S}^h : \frac{1}{2}\delta\boldsymbol{C}^h \,\mathrm{d}V + \int_{B_0^e} \boldsymbol{S}^h : \frac{1}{2}\,\Delta\delta\boldsymbol{C}^h \,\mathrm{d}V \tag{3.18}$$

The expression in the first integral is reformulated as

$$\begin{aligned} \Delta\boldsymbol{S}^h : \frac{1}{2}\delta\boldsymbol{C}^h &= \left(\frac{\partial\boldsymbol{S}^h}{\partial\boldsymbol{C}^h} : \frac{\partial\boldsymbol{C}^h}{\partial\boldsymbol{d}_u} \cdot \Delta\boldsymbol{d}_u\right) : \left(\frac{1}{2}\,\frac{\partial\boldsymbol{C}^h}{\partial\boldsymbol{d}_u} \cdot \delta\boldsymbol{d}_u\right) \\ &= \delta\boldsymbol{d}_u \cdot \left\{ \frac{1}{2}\left[\left(\frac{\partial\boldsymbol{C}^h}{\partial\boldsymbol{d}_u}\right)^{\overset{13}{T}}\right]^{\overset{23}{T}} : \mathbb{C}^h : \frac{\partial\boldsymbol{C}^h}{\partial\boldsymbol{d}_u} \right\} \cdot \Delta\boldsymbol{d}_u \end{aligned} \tag{3.19}$$

while the expression in the second integral leads to

$$\boldsymbol{S}^h : \frac{1}{2}\,\Delta\delta\boldsymbol{C}^h = \boldsymbol{S}^h : \frac{1}{2}\,\Delta\left(\frac{\partial\boldsymbol{C}^h}{\partial\boldsymbol{d}_u} \cdot \delta\boldsymbol{d}_u\right) = \delta\boldsymbol{d}_u \cdot \left(\frac{1}{2}\,\boldsymbol{S}^h : \frac{\partial^2\boldsymbol{C}^h}{\partial\boldsymbol{d}_u \otimes \partial\boldsymbol{d}_u}\right) \cdot \Delta\boldsymbol{d}_u\,. \tag{3.20}$$

Inserting both expressions into Eq. (3.18) yields

$$\Delta G_u^e = \delta\boldsymbol{d}_u \cdot \Bigg\{ \underbrace{\int_{\mathcal{B}_0^e} \frac{1}{2}\left(\left(\frac{\partial\boldsymbol{C}^h}{\partial\boldsymbol{d}_u}\right)^{\overset{13}{T}}\right)^{\overset{23}{T}} : \mathbb{C}^h : \frac{\partial\boldsymbol{C}^h}{\partial\boldsymbol{d}_u} \,\mathrm{d}V + \int_{\mathcal{B}_0^e} \frac{1}{2}\,\boldsymbol{S}^h : \frac{\partial^2\boldsymbol{C}^h}{\partial\boldsymbol{d}_u \otimes \partial\boldsymbol{d}_u} \,\mathrm{d}V}_{\boldsymbol{k}_{uu}} \Bigg\} \cdot \Delta\boldsymbol{d}_u\,, \tag{3.21}$$

where $\boldsymbol{k}_{uu}$ is the element matrix corresponding to the unknown field $\boldsymbol{u}$. This rather complex formulation of the element right-hand side vector and element matrix by including the indirect way via the chain rule is only outlined to show the resemblance to the classic notation. Observe that for this single field formulation $\delta\boldsymbol{d} = \delta\boldsymbol{d}_u$, $\Delta\boldsymbol{d} = \Delta\boldsymbol{d}_u$, $\boldsymbol{r} = \boldsymbol{r}_u$

and $\boldsymbol{k} = \boldsymbol{k}_{uu}$ holds. With this, the linearization of the discretized weak form of a typical element e can be written as

$$\operatorname{Lin} G^e = \delta \boldsymbol{d} \cdot (\boldsymbol{r} + \boldsymbol{k} \cdot \Delta \boldsymbol{d}) \,. \tag{3.22}$$

It is noteworthy that the element matrix and consequently the system matrix is symmetric in pure elasticity. The assembly of the element contributions and the solution procedure of the global system of equation is discussed within a generalized notation in Section 3.3.

3.2 FEM for the Theory of Porous Media

The FEM within the TPM is in general a bit more demanding compared to pure elasticity, which is presented in Section 3.1. This is due to the fact that the TPM always includes multiple equations and consequently multiple degrees of freedom to solve. Additionally, a time discretization scheme has to be included.

3.2.1 Weak Form and its Linearization

The equations to solve for the derived binary model are given in Eq. (2.136) where the local statement of the balance of momentum of the mixture can be written as

$$-\left\{\operatorname{Div}_{\mathrm{S}}[\boldsymbol{P}(\boldsymbol{u}_{\mathrm{S}}, p)] + \rho_{0\mathrm{S}}\, \boldsymbol{b}\right\} = \boldsymbol{0} \tag{3.23}$$

and the local statement of the balance of mass of the mixture as

$$\operatorname{Div}_{\mathrm{S}}[n^{\mathrm{L}}(\boldsymbol{u}_{\mathrm{S}})\, \boldsymbol{w}_{\mathrm{LS0S}}(\boldsymbol{u}_{\mathrm{S}}, p)] + J_{\mathrm{S}}(\boldsymbol{u}_{\mathrm{S}})\, [\boldsymbol{E}_{\mathrm{S}}]'_{\mathrm{S}}(\boldsymbol{u}_{\mathrm{S}}) : \boldsymbol{C}_{\mathrm{S}}^{-1}(\boldsymbol{u}_{\mathrm{S}}) = 0 \tag{3.24}$$

where for each quantity the dependencies on the unknown fields, namely the solid displacement $\boldsymbol{u}_{\mathrm{S}}$ and the pore pressure p, are attached. It is apparent that both equation depend on both unknown fields. In agreement with Section 3.1.1, the signs of both equations are chosen to enable a straight forward derivation leading to a positive definite system matrix in the following. Applying the standard Galerkin method to both equations by multiplying the test function $\delta \boldsymbol{u}_{\mathrm{S}}$ with $\boldsymbol{u}_{\mathrm{S}} = \boldsymbol{0}$ on $\partial \mathcal{B}_{0\mathrm{S}u}$ to the balance of linear momentum of the mixture, respectively δp with $\delta p = 0$ on $\partial \mathcal{B}_{0\mathrm{S}p}$ to the balance of mass of the mixture, and integrating over the control space of the solid in reference configuration leads to

$$-\int_{\mathcal{B}_{0\mathrm{S}}} [\operatorname{Div}_{\mathrm{S}}(\boldsymbol{P}) + \rho_{0\mathrm{S}}\, \boldsymbol{b}] \cdot \delta \boldsymbol{u}_{\mathrm{S}} \, \mathrm{d}V_{\mathrm{S}} = 0 \tag{3.25}$$

and

$$\int_{\mathcal{B}_{0\mathrm{S}}} \left[\operatorname{Div}_{\mathrm{S}}(n^{\mathrm{L}}\, \boldsymbol{w}_{\mathrm{LS0S}}) + J_{\mathrm{S}}\, (\boldsymbol{E}_{\mathrm{S}})'_{\mathrm{S}} : \boldsymbol{C}_{\mathrm{S}}^{-1}\right] \delta p \, \mathrm{d}V_{\mathrm{S}} = 0 \,. \tag{3.26}$$

Equation (3.25) is transformed analogous to Eq. (3.3)-(3.4) leading to the weak form

$$G_u(\boldsymbol{u}_{\mathrm{S}}, p, \delta \boldsymbol{u}_{\mathrm{S}}) := \int_{\mathcal{B}_{0\mathrm{S}}} \boldsymbol{P} : \delta \boldsymbol{F}_{\mathrm{S}} \, \mathrm{d}V_{\mathrm{S}} - \int_{\mathcal{B}_{0\mathrm{S}}} \rho_{0\mathrm{S}}\, \boldsymbol{b} \cdot \delta \boldsymbol{u}_{\mathrm{S}} \, \mathrm{d}V_{\mathrm{S}} - \int_{\partial \mathcal{B}_{0\mathrm{S}t}} \overline{\boldsymbol{t}}_{0\mathrm{S}} \cdot \delta \boldsymbol{u}_{\mathrm{S}} \, \mathrm{d}A_{\mathrm{S}} = 0 \tag{3.27}$$

with $\delta \boldsymbol{F}_{\mathrm{S}} = \operatorname{Grad}_{\mathrm{S}}(\delta \boldsymbol{u}_{\mathrm{S}})$ and $\boldsymbol{t}_{0\mathrm{S}} = \boldsymbol{P} \cdot \boldsymbol{N}_{\mathrm{S}}$ as the traction vector acting on both constituents. Additionally, the boundary is decomposed as $\partial \mathcal{B}_{0\mathrm{S}} = \partial \mathcal{B}_{0\mathrm{S}u} \cup \partial \mathcal{B}_{0\mathrm{S}t}$ with $\partial \mathcal{B}_{0\mathrm{S}u} \cap \partial \mathcal{B}_{0\mathrm{S}t} = \emptyset$ such that Dirichlet boundary conditions on the solid displacement are

applied as $\boldsymbol{u}_{\mathrm{S}} = \overline{\boldsymbol{u}}_{\mathrm{S}}$ on $\partial\mathcal{B}_{0\mathrm{S}u}$ and the corresponding Neumann boundary conditions as $\boldsymbol{t}_{0\mathrm{S}} = \overline{\boldsymbol{t}}_{0\mathrm{S}}$ on $\partial\mathcal{B}_{0\mathrm{S}t}$. Eq. (3.26) is reformulated in a similar fashion with

$$\mathrm{Div}_{\mathrm{S}}(n^{\mathrm{L}}\,\boldsymbol{w}_{\mathrm{LS0S}})\,\delta p = \mathrm{Div}_{\mathrm{S}}(n^{\mathrm{L}}\,\boldsymbol{w}_{\mathrm{LS0S}}\,\delta p) - n^{\mathrm{L}}\,\boldsymbol{w}_{\mathrm{LS0S}}\cdot\mathrm{Grad}_{\mathrm{S}}(\delta p) \tag{3.28}$$

and

$$\int_{\mathcal{B}_{0\mathrm{S}}} \mathrm{Div}_{\mathrm{S}}(n^{\mathrm{L}}\,\boldsymbol{w}_{\mathrm{LS0S}}\,\delta p)\,\mathrm{d}V_{\mathrm{S}} = \int_{\partial\mathcal{B}_{0\mathrm{S}}} n^{\mathrm{L}}\,\boldsymbol{w}_{\mathrm{LS0S}}\,\delta p\cdot\boldsymbol{N}_{\mathrm{S}}\,\mathrm{d}A_{\mathrm{S}} \tag{3.29}$$

towards the weak form

$$\begin{aligned} G_p(\boldsymbol{u}_{\mathrm{S}}, p, \delta p) := &-\int_{\mathcal{B}_{0\mathrm{S}}} n^{\mathrm{L}}\,\boldsymbol{w}_{\mathrm{LS0S}}\cdot\mathrm{Grad}_{\mathrm{S}}(\delta p)\,\mathrm{d}V_{\mathrm{S}} + \int_{\partial\mathcal{B}_{0\mathrm{S}q}} \overline{q}_{0\mathrm{S}}\,\delta p\,\mathrm{d}A_{\mathrm{S}} \\ &+ \int_{\mathcal{B}_{0\mathrm{S}}} J_{\mathrm{S}}\,(\boldsymbol{E}_{\mathrm{S}})'_{\mathrm{S}} : \boldsymbol{C}_{\mathrm{S}}^{-1}\,\delta p\,\mathrm{d}V_{\mathrm{S}} = 0 \end{aligned} \tag{3.30}$$

with $q_{0\mathrm{S}} = (n^{\mathrm{L}}\,\boldsymbol{w}_{\mathrm{LS0S}})\cdot\boldsymbol{N}_{\mathrm{S}}$ as the specific liquid flux over the surface of $\mathcal{B}_{0\mathrm{S}}$. Here, the boundary has been decomposed as $\partial\mathcal{B}_{0\mathrm{S}} = \partial\mathcal{B}_{0\mathrm{S}p}\cup\partial\mathcal{B}_{0\mathrm{S}q}$ with $\partial\mathcal{B}_{0\mathrm{S}p}\cap\partial\mathcal{B}_{0\mathrm{S}q} = \emptyset$ such that Dirichlet and Neumann boundary conditions on the pressure field are applied as $p = \overline{p}$ on $\partial\mathcal{B}_{0\mathrm{S}p}$ and $q_{0\mathrm{S}} = \overline{q}_{0\mathrm{S}}$ on $\partial\mathcal{B}_{0\mathrm{S}q}$. The total weak form is given by

$$G(\boldsymbol{u}_{\mathrm{S}}, p, \delta\boldsymbol{u}_{\mathrm{S}}, \delta p) := G_u(\boldsymbol{u}_{\mathrm{S}}, p, \delta\boldsymbol{u}_{\mathrm{S}}) + G_p(\boldsymbol{u}_{\mathrm{S}}, p, \delta p) = 0\,. \tag{3.31}$$

To solve this nonlinear equation, Newton's method can be applied which requires the linearization of the weak form, see Eq. (3.11), as

$$\mathrm{Lin}\,G(\boldsymbol{u}_{\mathrm{S}}, p, \delta\boldsymbol{u}_{\mathrm{S}}, \delta p, \Delta\boldsymbol{u}_{\mathrm{S}}, \Delta p) = G(\boldsymbol{u}_{\mathrm{S}}, p, \delta\boldsymbol{u}_{\mathrm{S}}, \delta p) + \Delta G(\boldsymbol{u}_{\mathrm{S}}, p, \delta\boldsymbol{u}_{\mathrm{S}}, \delta p, \Delta\boldsymbol{u}_{\mathrm{S}}, \Delta p) \tag{3.32}$$

with $\Delta G := \Delta G_u + \Delta G_p$. Assuming a conservative volume load $\rho_{0\mathrm{S}}\,\boldsymbol{b}$, surface traction $\bar{t}_{0\mathrm{S}}$ and fluid flux $\overline{q}_{0\mathrm{S}}$ leads to

$$\Delta G_u := \int_{\mathcal{B}_{0\mathrm{S}}} \Delta\boldsymbol{P} : \delta\boldsymbol{F}_{\mathrm{S}}\,\mathrm{d}V_{\mathrm{S}} \tag{3.33}$$

and

$$\Delta G_p := -\int_{\mathcal{B}_{0\mathrm{S}}} \Delta\left[n^{\mathrm{L}}\,\boldsymbol{w}_{\mathrm{LS0S}}\right]\cdot\mathrm{Grad}_{\mathrm{S}}(\delta p)\,\mathrm{d}V_{\mathrm{S}} + \int_{\mathcal{B}_{0\mathrm{S}}} \Delta\left[J_{\mathrm{S}}\,(\boldsymbol{E}_{\mathrm{S}})'_{\mathrm{S}} : \boldsymbol{C}_{\mathrm{S}}^{-1}\right]\,\delta p\,\mathrm{d}V_{\mathrm{S}} \tag{3.34}$$

for the increments of the weak form. Please note that the increments are written quite general at this point. They will be further investigated after introducing the discretization.

3.2.2 Discretization

The basic structure of the discretization scheme for a multi-physical problem as within the TPM is nearly identical to pure elasticity in Section 3.1.2 such as the presented array notation. Because of this, the general explanations here focus on the differences to the single field formulation. The approximation of the control space of the solid in reference configuration is written in agreement with Eq. (3.13) as

$$\mathcal{B}_{0\mathrm{S}} \approx \mathcal{B}_{0\mathrm{S}}^{h} = \bigcup_{e=1}^{n_e} \mathcal{B}_{0\mathrm{S}}^{e}\,. \tag{3.35}$$

In contrast to this, an extension of the approximations of the geometry, the unknown fields, their variations and increments is needed compared to finite elasticity in Eq. (3.14) due to the pressure p as second unknown field such that

$$
\begin{aligned}
\boldsymbol{X}_\mathrm{S} &\approx \boldsymbol{X}_\mathrm{S}^h &&= \sum_{I=1}^{n_{n\_u}} N_u^I(\boldsymbol{\xi})\, \boldsymbol{X}_\mathrm{S}^I &&= \hat{\boldsymbol{N}}_u \cdot \hat{\boldsymbol{X}}_\mathrm{S}\,, \\
\boldsymbol{u}_\mathrm{S} &\approx \boldsymbol{u}_\mathrm{S}^h &&= \sum_{I=1}^{n_{n\_u}} N_u^I(\boldsymbol{\xi})\, \boldsymbol{d}_u^I &&= \hat{\boldsymbol{N}}_u \cdot \boldsymbol{d}_u\,, \\
\delta\boldsymbol{u}_\mathrm{S} &\approx \delta\boldsymbol{u}_\mathrm{S}^h &&= \sum_{I=1}^{n_{n\_u}} N_u^I(\boldsymbol{\xi})\, \delta\boldsymbol{d}_u^I &&= \hat{\boldsymbol{N}}_u \cdot \delta\boldsymbol{d}_u\,, \\
\Delta\boldsymbol{u}_\mathrm{S} &\approx \Delta\boldsymbol{u}_\mathrm{S}^h &&= \sum_{I=1}^{n_{n\_u}} N_u^I(\boldsymbol{\xi})\, \Delta\boldsymbol{d}_u^I &&= \hat{\boldsymbol{N}}_u \cdot \Delta\boldsymbol{d}_u\,, \\
p &\approx p^h &&= \sum_{I=1}^{n_{n\_p}} N_p^I(\boldsymbol{\xi})\, \boldsymbol{d}_p^I &&= \hat{\boldsymbol{N}}_p \cdot \boldsymbol{d}_p\,, \\
\delta p &\approx \delta p^h &&= \sum_{I=1}^{n_{n\_p}} N_p^I(\boldsymbol{\xi})\, \delta\boldsymbol{d}_p^I &&= \hat{\boldsymbol{N}}_p \cdot \delta\boldsymbol{d}_p\,, \\
\Delta p &\approx \Delta p^h &&= \sum_{I=1}^{n_{n\_p}} N_p^I(\boldsymbol{\xi})\, \Delta\boldsymbol{d}_p^I &&= \hat{\boldsymbol{N}}_p \cdot \Delta\boldsymbol{d}_p\,,
\end{aligned}
\tag{3.36}
$$

with the element vectors in the style of Eq. (3.15) as

$$
\begin{aligned}
\hat{\boldsymbol{X}}_\mathrm{S} &:= \{\hat{X}_1^1, \hat{X}_2^1, \hat{X}_3^1, ..., \hat{X}_1^{n_{n\_u}}, \hat{X}_2^{n_{n\_u}}, \hat{X}_3^{n_{n\_u}}\}\,, \\
\boldsymbol{d}_u &:= \{d_{u1}^1, d_{u2}^1, d_{u3}^1, ..., d_{u1}^{n_{n\_u}}, d_{u2}^{n_{n\_u}}, d_{u3}^{n_{n\_u}}\}\,, \\
\delta\boldsymbol{d}_u &:= \{\delta d_{u1}^1, \delta d_{u2}^1, \delta d_{u3}^1, ..., \delta d_{u1}^{n_{n\_u}}, \delta d_{u2}^{n_{n\_u}}, \delta d_{u3}^{n_{n\_u}}\}\,, \\
\Delta\boldsymbol{d}_u &:= \{\Delta d_{u1}^1, \Delta d_{u2}^1, \Delta d_{u3}^1, ..., \Delta d_{u1}^{n_{n\_u}}, \Delta d_{u2}^{n_{n\_u}}, \Delta d_{u3}^{n_{n\_u}}\}\,, \\
\boldsymbol{d}_p &:= \{d_p^1, ..., d_p^{n_{n\_p}}\}\,, \\
\delta\boldsymbol{d}_p &:= \{\delta d_p^1, ..., \delta d_p^{n_{n\_p}}\}\,, \\
\Delta\boldsymbol{d}_p &:= \{\Delta d_p^1, ..., \Delta d_p^{n_{n\_p}}\}\,.
\end{aligned}
\tag{3.37}
$$

It is important that the number of nodes per element with respect to the unknown fields, denoted as n_{n_u} and n_{n_p}, do not have to be equal. This means that different interpolations can be used for the different unknown fields, leading to varying numbers of degrees of freedom for the different fields within the same element. As a consequence, it is necessary to define the nodal shape functions for the displacements N_u^I and those for the pressure N_p^I separately. More details on a reasonable choice of shape functions and those used within this thesis are given in Section 3.5 after deriving the structure of the system of equations to solve in the following.

As a final piece it is necessary to define the relation between the solid velocity $\boldsymbol{x}'_\mathrm{S}$ which is part of the appearing material time derivative of the Green-Lagrange strain $(\boldsymbol{E}_\mathrm{S})'_\mathrm{S}$ and the

unknown field $\boldsymbol{u}_\mathrm{S}$. For this purpose the implicit Euler method is chosen as time integration scheme such that

$$\boldsymbol{x}'_\mathrm{S} = (\boldsymbol{u}_\mathrm{S})'_\mathrm{S} := \frac{\boldsymbol{u}_\mathrm{S} - \boldsymbol{u}_\mathrm{S}^{(n)}}{\Delta t} \tag{3.38}$$

holds with $\boldsymbol{u}_\mathrm{S}^{(n)}$ as the solid displacement at the previous time step and the current time increment Δt.

Inserting the discretization into the weak form of the balance of momentum of the mixture in Eq. (3.27) leads for a typical element e to

$$\begin{aligned} G_u^e(\boldsymbol{d}_u, \boldsymbol{d}_p, \delta\boldsymbol{d}_u) &= \int_{\mathcal{B}_{0\mathrm{S}}^e} \boldsymbol{P}^h : \delta\boldsymbol{F}_\mathrm{S}^h \,\mathrm{d}V_\mathrm{S} - \int_{\mathcal{B}_{0\mathrm{S}}^e} \rho_{0\mathrm{S}}\, \boldsymbol{b} \cdot \delta\boldsymbol{u}_\mathrm{S}^h \,\mathrm{d}V_\mathrm{S} - \int_{\partial\mathcal{B}_{0\mathrm{S}t}^e} \bar{\boldsymbol{t}}_{0\mathrm{S}} \cdot \delta\boldsymbol{u}_\mathrm{S}^h \,\mathrm{d}A_\mathrm{S} \\ &= \delta\boldsymbol{d}_u \cdot \Bigg\{ \int_{\mathcal{B}_{0\mathrm{S}}^e} \left[\left(\frac{\partial\, \boldsymbol{F}_\mathrm{S}^h}{\partial\, \boldsymbol{d}_u} \right)^{\frac{13}{T}} \right]^{\frac{23}{T}} : \boldsymbol{P}^h \,\mathrm{d}V_\mathrm{S} \\ &\qquad \underbrace{- \int_{\mathcal{B}_{0\mathrm{S}}^e} \hat{\boldsymbol{N}}_u^T \cdot \rho_{0\mathrm{S}}\, \boldsymbol{b} \,\mathrm{d}V_\mathrm{S} - \int_{\partial\mathcal{B}_{0\mathrm{S}t}^e} \hat{\boldsymbol{N}}_u^T \cdot \bar{\boldsymbol{t}}_{0\mathrm{S}} \,\mathrm{d}A_\mathrm{S}}_{\boldsymbol{r}_u} \Bigg\} \end{aligned} \tag{3.39}$$

with the element right-hand side vector related to the displacement degrees of freedom $\boldsymbol{r}_u$. The corresponding element right-hand side vector with respect to the pressure degrees of freedom $\boldsymbol{r}_p$ is derived by inserting the discretization into the weak form of the balance of mass of the mixture in Eq. (3.30) such that

$$\begin{aligned} G_p^e(\boldsymbol{d}_u, \boldsymbol{d}_p, \delta\boldsymbol{d}_p) &= - \int_{\mathcal{B}_{0\mathrm{S}}^e} [n^\mathrm{L}\, \boldsymbol{w}_{\mathrm{LS0S}}]^h \cdot [\mathrm{Grad}_\mathrm{S}(\delta p)]^h \,\mathrm{d}V_\mathrm{S} + \int_{\partial\mathcal{B}_{0\mathrm{S}q}^e} \overline{q}_{0\mathrm{S}}\, \delta p^h \,\mathrm{d}A_\mathrm{S} \\ &\quad + \int_{\mathcal{B}_{0\mathrm{S}}^e} [J_\mathrm{S}\, (\boldsymbol{E}_\mathrm{S})'_\mathrm{S} : \boldsymbol{C}_\mathrm{S}^{-1}]^h\, \delta p^h \,\mathrm{d}V_\mathrm{S} \\ &= \delta\boldsymbol{d}_p \cdot \Bigg\{ - \int_{\mathcal{B}_{0\mathrm{S}}^e} \left(\frac{\partial [\mathrm{Grad}_\mathrm{S}(p)]^h}{\partial \boldsymbol{d}_p} \right)^T \cdot [n^\mathrm{L}\, \boldsymbol{w}_{\mathrm{LS0S}}]^h \,\mathrm{d}V_\mathrm{S} \\ &\qquad \underbrace{+ \int_{\partial\mathcal{B}_{0\mathrm{S}q}^e} \hat{\boldsymbol{N}}_p\, \overline{q}_{0\mathrm{S}} \,\mathrm{d}A_\mathrm{S} + \int_{\mathcal{B}_{0\mathrm{S}}^e} \hat{\boldsymbol{N}}_p\, [J_\mathrm{S}\, (\boldsymbol{E}_\mathrm{S})'_\mathrm{S} : \boldsymbol{C}_\mathrm{S}^{-1}]^h \,\mathrm{d}V_\mathrm{S}}_{\boldsymbol{r}_p} \Bigg\}. \end{aligned} \tag{3.40}$$

The increments of the weak form ΔG_u and ΔG_p in Eq. (3.33) and (3.34) are split at element level as

$$\Delta G_u^e = \Delta_u G_u^e + \Delta_p G_u^e \quad \text{and} \quad \Delta G_p^e = \Delta_u G_p^e + \Delta_p G_p^e \tag{3.41}$$

to simplify the derivation of the element matrix. The operator Δ_u implies that the increment is evaluated with respect to the solid displacement field respectively the pressure field in case of Δ_p. For the analysis of the different terms and their dependencies it would be beneficial to write everything straight forward in terms of the unknown fields. But

this would lead to rather lengthy expressions within the framework of the TPM. As a consequence the introduced fields as the seepage velocity are used further on but their dependencies on the unknown fields are given in Eq. (3.23) and (3.24). The increments of the weak forms with respect to the different unknown fields read as

$$\Delta_u G_u^e = \int_{\mathcal{B}_{0\mathrm{S}}^e} \Delta_u \boldsymbol{P}^h : \delta \boldsymbol{F}_{\mathrm{S}}^h \, \mathrm{d}V_{\mathrm{S}} = \delta \boldsymbol{d}_u \cdot \underbrace{\left\{ \int_{\mathcal{B}_{0\mathrm{S}}^e} \left[\left(\frac{\partial \, \delta \boldsymbol{F}_{\mathrm{S}}^h}{\partial \boldsymbol{d}_u} \right)^{\frac{13}{T}} \right]^{\frac{23}{T}} : \frac{\partial \boldsymbol{P}^h}{\partial \boldsymbol{d}_u} \, \mathrm{d}V_{\mathrm{S}} \right\}}_{\boldsymbol{k}_{uu}} \cdot \Delta \boldsymbol{d}_u \,, \tag{3.42}$$

$$\Delta_p G_u^e = \int_{\mathcal{B}_{0\mathrm{S}}^e} \Delta_p \boldsymbol{P}^h : \delta \boldsymbol{F}_{\mathrm{S}}^h \, \mathrm{d}V_{\mathrm{S}} = \delta \boldsymbol{d}_u \cdot \underbrace{\left\{ \int_{\mathcal{B}_{0\mathrm{S}}^e} \left[\left(\frac{\partial \, \delta \boldsymbol{F}_{\mathrm{S}}^h}{\partial \boldsymbol{d}_u} \right)^{\frac{13}{T}} \right]^{\frac{23}{T}} : \frac{\partial \boldsymbol{P}^h}{\partial \boldsymbol{d}_p} \, \mathrm{d}V_{\mathrm{S}} \right\}}_{\boldsymbol{k}_{up}} \cdot \Delta \boldsymbol{d}_p \,, \tag{3.43}$$

$$\begin{aligned} \Delta_u G_p^e &= - \int_{\mathcal{B}_{0\mathrm{S}}^e} \Delta_u [n^{\mathrm{L}} \boldsymbol{w}_{\mathrm{LS0S}}]^h \cdot [\mathrm{Grad}_{\mathrm{S}}(\delta p)]^h \, \mathrm{d}V_{\mathrm{S}} + \int_{\mathcal{B}_{0\mathrm{S}}^e} \Delta_u [J_{\mathrm{S}} \, (\boldsymbol{E}_{\mathrm{S}})'_{\mathrm{S}} : \boldsymbol{C}_{\mathrm{S}}^{-1}]^h \, \delta p^h \, \mathrm{d}V_{\mathrm{S}} \\ &= \delta \boldsymbol{d}_p \cdot \Bigg\{ - \int_{\mathcal{B}_{0\mathrm{S}}^e} \left(\frac{\partial [\mathrm{Grad}_{\mathrm{S}}(\delta p)]^h}{\partial \boldsymbol{d}_p} \right)^T \cdot \frac{\partial [n^{\mathrm{L}} \boldsymbol{w}_{\mathrm{LS0S}}]^h}{\partial \boldsymbol{d}_u} \, \mathrm{d}V_{\mathrm{S}} \\ &\qquad \underbrace{+ \int_{\mathcal{B}_{0\mathrm{S}}^e} \hat{\boldsymbol{N}}_p \frac{\partial [J_{\mathrm{S}} \, (\boldsymbol{E}_{\mathrm{S}})'_{\mathrm{S}} : \boldsymbol{C}_{\mathrm{S}}^{-1}]^h}{\partial \boldsymbol{d}_u} \, \mathrm{d}V_{\mathrm{S}} \Bigg\}}_{\boldsymbol{k}_{pu}} \cdot \Delta \boldsymbol{d}_u \end{aligned} \tag{3.44}$$

and

$$\begin{aligned} \Delta_p G_p^e &= - \int_{\mathcal{B}_{0\mathrm{S}}^e} \Delta_p [n^{\mathrm{L}} \boldsymbol{w}_{\mathrm{LS0S}}]^h \cdot [\mathrm{Grad}_{\mathrm{S}}(\delta p)]^h \, \mathrm{d}V_{\mathrm{S}} \\ &= \delta \boldsymbol{d}_p \cdot \underbrace{\left\{ - \int_{\mathcal{B}_{0\mathrm{S}}^e} \left(\frac{\partial [\mathrm{Grad}_{\mathrm{S}}(\delta p)]^h}{\partial \boldsymbol{d}_p} \right)^T \cdot \frac{\partial [n^{\mathrm{L}} \boldsymbol{w}_{\mathrm{LS0S}}]^h}{\partial \boldsymbol{d}_p} \, \mathrm{d}V_{\mathrm{S}} \right\}}_{\boldsymbol{k}_{pp}} \cdot \Delta \boldsymbol{d}_p \end{aligned} \tag{3.45}$$

with the submatrices of the element matrix $\boldsymbol{k}_{uu}$, $\boldsymbol{k}_{up}$, $\boldsymbol{k}_{pu}$ and $\boldsymbol{k}_{pp}$. With this, the linearization of the discrete weak for for a typical element can be written as

$$\begin{aligned} \mathrm{Lin}\, G^e &= \begin{bmatrix} \delta \boldsymbol{d}_u \\ \delta \boldsymbol{d}_p \end{bmatrix} \cdot \left[\begin{bmatrix} \boldsymbol{r}_u \\ \boldsymbol{r}_p \end{bmatrix} + \begin{bmatrix} \boldsymbol{k}_{uu} & \boldsymbol{k}_{up} \\ \boldsymbol{k}_{pu} & \boldsymbol{k}_{pp} \end{bmatrix} \cdot \begin{bmatrix} \Delta \boldsymbol{d}_u \\ \Delta \boldsymbol{d}_p \end{bmatrix} \right] \\ &= \delta \boldsymbol{d} \cdot (\boldsymbol{r} + \boldsymbol{k} \cdot \Delta \boldsymbol{d}) \,. \end{aligned} \tag{3.46}$$

Please note that the structure of the linearized weak form is similar to the one in finite elasticity in Eq. (3.22). A generalization in notation in combination with the assembly and solving the global system of equations is presented in Section 3.3. Taking a closer look at the element matrix, it is important to state that in contrast to the pure elasticity formulation in Section 3.1 the element matrix and consequently the system matrix is non-symmetric since $\boldsymbol{k}_{up} \neq \boldsymbol{k}_{pu}^T$. In addition to that, even if the submatrices are non-zero from

the equation point of view, the matrix $\boldsymbol{k}_{pp}$ tend to zero for several applications. The reason is the dependence on the seepage velocity $\boldsymbol{w}_{\mathrm{LS}}$ and therefore on the Darcy parameter k_{L} which is often close to zero, e.g. $k_{\mathrm{L}} = 10^{-7}\,\frac{\mathrm{m}^4}{\mathrm{Ns}}$ or lower. This fact has influence on choosing the interpolation order of the unknown fields which is addressed in Section 3.5.

3.3 Generalization

This section deals with a generalized notation of the weak form leading to the derivation and the solution algorithm of the global system of equations. The notation is applicable to a wide range of problems which can be approximated with the FEM and therefore covers the pure elasticity formulation in Section 3.1 as well as the formulation in the framework of the TPM in Section 3.2.

At first, element vectors are introduced following the concept of Eq. (3.15) and (3.37) as

$$\begin{aligned} \boldsymbol{d} &= \bigcup \{\boldsymbol{d}_\alpha, \boldsymbol{d}_\beta, \boldsymbol{d}_\gamma, ...\} \\ \delta\boldsymbol{d} &= \bigcup \{\delta\boldsymbol{d}_\alpha, \delta\boldsymbol{d}_\beta, \delta\boldsymbol{d}_\gamma, ...\} \\ \Delta\boldsymbol{d} &= \bigcup \{\Delta\boldsymbol{d}_\alpha, \Delta\boldsymbol{d}_\beta, \Delta\boldsymbol{d}_\gamma, ...\} \end{aligned} \tag{3.47}$$

where α, β and γ indicate possible distinct unknown fields. With these vectors, containing all degrees of freedoms, their variations and increments of a typical element, the corresponding weak form can be written in general as

$$G^e := \delta\boldsymbol{d} \cdot \boldsymbol{r}(\boldsymbol{d})\,. \tag{3.48}$$

The element right-hand side vector $\boldsymbol{r}$ can be identified with help of the standard Galerkin method as shown at the formulations above or alternatively, if a potential $\boldsymbol{\Pi}$ exists, directly by $\boldsymbol{r}(\boldsymbol{d}) = \partial\boldsymbol{\Pi}/\partial\boldsymbol{d}$. The increment follows to

$$\Delta G^e := \frac{\partial G^e}{\partial \boldsymbol{d}} \cdot \Delta\boldsymbol{d} = \delta\boldsymbol{d} \cdot \frac{\partial \boldsymbol{r}}{\partial \boldsymbol{d}} \cdot \Delta\boldsymbol{d} = \delta\boldsymbol{d} \cdot \boldsymbol{k}(\boldsymbol{d}) \cdot \Delta\boldsymbol{d} \tag{3.49}$$

with the element matrix $\boldsymbol{k}$. Towards the system of equations to solve, the element contributions are assembled to the system right-hand side vector and system matrix as

$$\boldsymbol{R} = \mathop{\mathsf{A}}_{e=1}^{n_e} \boldsymbol{r} \qquad \text{and} \qquad \boldsymbol{K} = \mathop{\mathsf{A}}_{e=1}^{n_e} \boldsymbol{k}\,. \tag{3.50}$$

During the assembly procedure, the element contributions are inserted into their global counterparts at the correct location, depending on the position of the element degrees of freedom in $\boldsymbol{d}$ within the global degrees of freedom in $\boldsymbol{D}$. After this, we may write the global discretized linearized weak form as

$$\mathrm{Lin}\, G^h = G^h + \Delta G^h = \delta\boldsymbol{D} \cdot \Big(\boldsymbol{R}(\boldsymbol{D}) + \boldsymbol{K}(\boldsymbol{D}) \cdot \Delta\boldsymbol{D}\Big) = 0\,. \tag{3.51}$$

Formally, the system matrix can be derived directly from the system right-side vector as $\boldsymbol{K} = \partial\boldsymbol{R}/\partial\boldsymbol{D}$. To be able to solve the boundary value problem, the Dirichlet boundary conditions have to be imposed. For this purpose, a split of the set of degrees of freedom is introduced as $\boldsymbol{D} = \boldsymbol{D}_f \cup \boldsymbol{D}_b$ with $\boldsymbol{D}_f \cap \boldsymbol{D}_b = \emptyset$. Therein, $\boldsymbol{D}_f$ are free degrees of freedom

and $\boldsymbol{D}_b$ those with imposed Dirichlet boundary conditions. With this, the linearization of the weak form can be rewritten to

$$\begin{aligned}&\delta\boldsymbol{D}_f \cdot \left(\boldsymbol{R}_f + \frac{\partial \boldsymbol{R}_f}{\partial \boldsymbol{D}_f} \cdot \Delta\boldsymbol{D}_f + \frac{\partial \boldsymbol{R}_f}{\partial \boldsymbol{D}_b} \cdot \Delta\boldsymbol{D}_b \right) \\ &+ \delta\boldsymbol{D}_b \cdot \left(\boldsymbol{R}_b + \frac{\partial \boldsymbol{R}_b}{\partial \boldsymbol{D}_f} \cdot \Delta\boldsymbol{D}_f + \frac{\partial \boldsymbol{R}_b}{\partial \boldsymbol{D}_b} \cdot \Delta\boldsymbol{D}_b \right) = 0\end{aligned} \tag{3.52}$$

or

$$\begin{bmatrix} \delta\boldsymbol{D}_f \\ \delta\boldsymbol{D}_b \end{bmatrix} \cdot \left[\begin{bmatrix} \boldsymbol{R}_f \\ \boldsymbol{R}_b \end{bmatrix} + \begin{bmatrix} \boldsymbol{K}_{ff} & \boldsymbol{K}_{fb} \\ \boldsymbol{K}_{bf} & \boldsymbol{K}_{bb} \end{bmatrix} \cdot \begin{bmatrix} \Delta\boldsymbol{D}_f \\ \Delta\boldsymbol{D}_b \end{bmatrix} \right] = 0\,. \tag{3.53}$$

The definition of the variations include that they vanish on the parts of the boundary occupied by Dirichlet boundary conditions, respectively $\delta\boldsymbol{D}_b = \boldsymbol{0}$. Thus, the second term in Eq. (3.52) is irrelevant for the solution of the boundary value problem problem. Using the arbitrariness of $\delta\boldsymbol{D}_f$, the increments of the real degrees of freedom are computed as

$$\Delta\boldsymbol{D}_f = (\boldsymbol{K}_{ff})^{-1} \cdot (-\boldsymbol{R}_f - \boldsymbol{K}_{fb} \cdot \Delta\boldsymbol{D}_b)\,. \tag{3.54}$$

3.4 Algorithmic Treatment

The algorithmic treatment for a single scale FEM simulation in summarized in Table 3.1. It is applicable for time-dependent problems as well as for quasi-static ones. The general notation allows for a constant or flexible time incrementation Δt while t_n is the time at the last converged time step. The load application factor λ_{load} is introduced as a function of time t to enable a stepwise application of nonzero Dirichlet and Neumann boundary conditions. The end time of the simulation is denoted by t_{end}. For quasi-static investigations, the time t represents a pseudo-time which is used to define the load stepping. The residual for each time step has been defined according to Eq. (3.54) as

$$\boldsymbol{R}_s(\boldsymbol{D}, \lambda_{\text{load}}) := -\boldsymbol{R}_f(\boldsymbol{D}, \lambda_{\text{load}}) - \boldsymbol{K}_{fb}(\boldsymbol{D}) \cdot \Delta\boldsymbol{D}_b(\boldsymbol{D}_b, \lambda_{\text{load}})\,, \tag{3.55}$$

where $\boldsymbol{R}_f$ contains the applied Neumann boundary conditions while $\Delta\boldsymbol{D}_b$ represents the current increment on the Dirichlet boundary conditions, both dependent on the load factor λ_{load}.

The iteration loop continues until the ratio of current energy E and reference energy E_{ref} is smaller than the predefined tolerance $\text{tol} = 10^{-16}$. The current energy is defined as $E = \boldsymbol{R}_s \cdot \Delta\boldsymbol{D}_f$. In general, the reference energy E_{ref} is the initial energy at the first iteration of the current step. But since many boundary value problems within the TPM converge against a steady state, the definition of the reference energy requires a special treatment. Close to steady state, the initial residuum and consequently the initial degrees of freedom increment vector within a step is that small that the standard energy ratio criterion can not be met due to limited computer precision. Because of that, for such simulations the reference energy E_{ref} is kept constant for all following steps during the simulation starting from the first iteration within the step after the whole external load has been applied. This handling of the termination criterion of the Newton iteration loop follows Taylor and Govindjee [2020].

Table 3.1: Algorithmic treatment for single scale FEM.

LOAD-/ TIME-STEPPING

While $t < t_{\text{end}}$

Set current time: $t = t_n + \Delta t$

Set current load: $\lambda_{\text{load}} = \lambda_{\text{load}}(t)$

ITERATION LOOP

While $E/E_{\text{ref}} > \text{tol}$

ELEMENT LOOP

Do $e = 1, ..., n_e$

Compute $\boldsymbol{r}$ and $\boldsymbol{k}$

End do

Assembly: $\boldsymbol{R} = \mathop{\mathsf{A}}_{e=1}^{n_e} \boldsymbol{r}, \quad \boldsymbol{K} = \mathop{\mathsf{A}}_{e=1}^{n_e} \boldsymbol{k}$

Solve $\boldsymbol{K}_{ff} \cdot \Delta \boldsymbol{D}_f = \boldsymbol{R}_s$ for $\Delta \boldsymbol{D}_f$

Update $\boldsymbol{D} = \boldsymbol{D} + \Delta \boldsymbol{D}$

End

End

3.5 Selection of Finite Element Formulations

This section introduces the different element formulations which are chosen for the numerical examples within this thesis. But the focus is on getting an overview on the different topologies rather than details on specific shape functions. The latter are listed in Appendix A. Since the chosen approaches are quite standard, please consult typical FEM literature as mentioned in the beginning of this chapter for more information than provided.

The first numerical examples in Chapter 6 investigate the MIEL method for small strain elasticity, introduced in Section 2.7. The purpose of this choice is to gain insights on effects which are induced by this multiscale approach at a rather simple problem compared to the TPM. A wide range of elements is applied on both scales of the MIEL method to gather as many information as possible. These elements are presented in Figure 3.1 along with their respective number of degrees of freedom n_d.

A black bullet indicates a node related to the displacement where each node corresponds to two degrees of freedom in the two dimensional case. The first letter within the element label denotes the shape of the respective element, Q for quadrilateral and T for triangular. The following number represents the interpolation order within the shape functions. The optional letter S after the interpolation order stands for a Serendipity element formulation while the remaining ones are of Lagrange type. All elements but the T2 element are applied

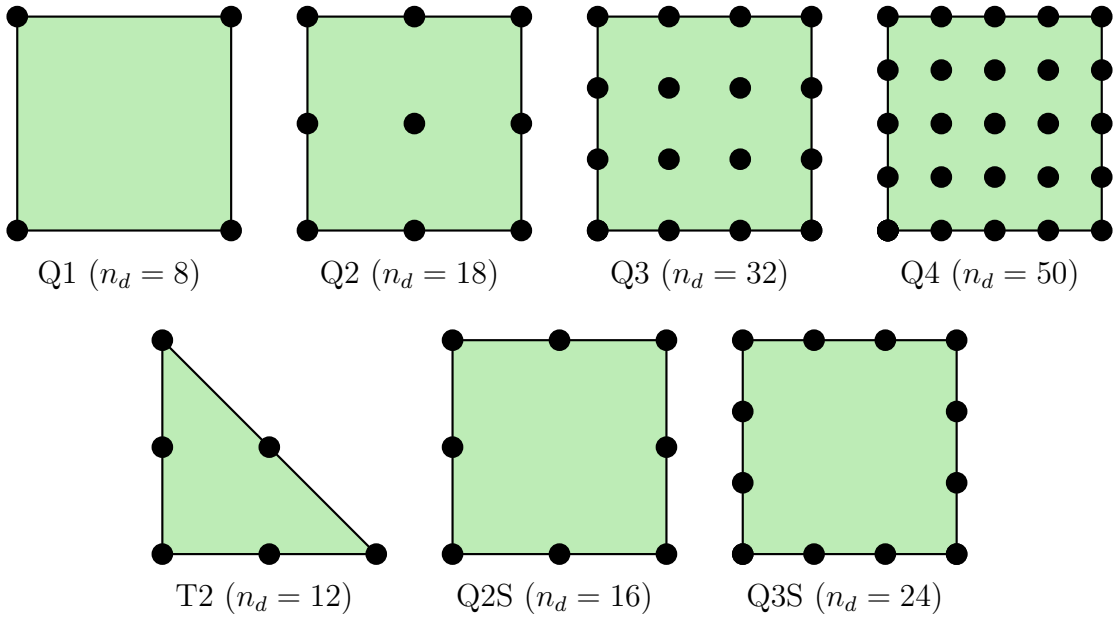

Figure 3.1: Finite element formulations for computations with single solid phase model.

on both scales within the examples. The T2 element is chosen as microscopic element for an analysis of elliptical heterogeneities.

The element choice within the TPM itself and especially within the MIEL method demands a little more effort compared to a single solid phase model. All microscopic elements are chosen to be Taylor-Hood elements where the solid displacement is interpolated quadratically while the pressure is approximated with a linear interpolation, going back on Taylor and Hood [1973]. This element formulation is proven to be stable from a mathematical point of view for the challenging case of a saddle point problem in linear elasticity within mixed FEM, see Boffi et al. [2013]. Even though the problem arising from the binary model leads to a fully populated and unsymmetric system matrix by theory, it tends towards a saddle point problem for very small Darcy parameters. Nevertheless, there is no theoretical proof for stability in finite strain theory but the element formulation is favorable within the TPM with small Darcy parameters compared to standard elements which assume equal interpolation order for all unknown fields to avoid pressure oscillations, cf. Markert et al. [2010] and Bertrand et al. [2022]. The macroscopic elements are of generalized Taylor-Hood type which indicates that the displacement interpolation is always one order higher than the pressure interpolation. Since it is beneficial for the MIEL method to only allow macroscopic element degrees of freedom on the boundary of the elements, serendipity interpolation functions are applied for higher orders. All elements which are used in the numerical examples in Chapter 7 are shown in Figure 3.2 along with their label and number of degrees of freedom.

Once more, each black bullet represents a node corresponding to the solid displacement with two degrees of freedom while the square with grey background indicates a pressure node with a single degree of freedom. The labels are built in a similar fashion as before but with the additional information corresponding to the interpolation of the pressure as second unknown field. The Q2Q1 and T2T1 element are used as microscopic and single scale elements while the Q2SQ1 and Q3SQ2S serve as macroscopic elements. The reduced amount of different microscopic scale element options compared to above is in agreement

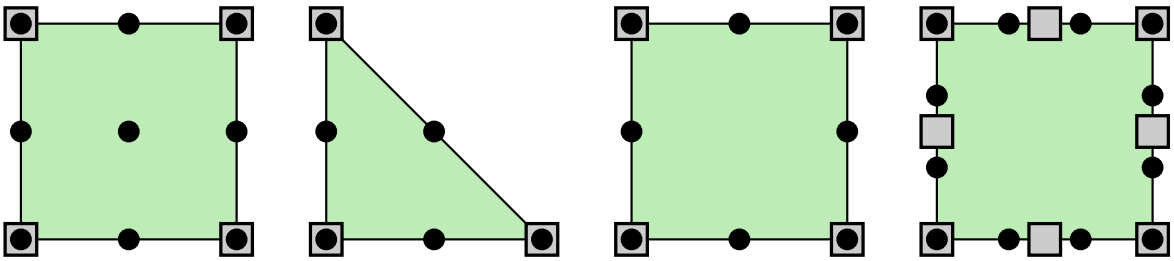

Figure 3.2: Finite element formulations for computations with binary TPM model.

with the findings in the first numerical examples of small strain elasticity. Higher order macroscopic elements with Serendipity approach are not reasonable within the MIEL method because of appearing inner nodes which is outlined in more detail in Chapter 5.

Please note that the line elements which are used to apply nonzero Neumann boundary conditions are not depicted separately. They are always chosen conforming to the interpolation on the corresponding edge of the respective single or microscopic scale element. More details on the application of Neumann boundary conditions within the MIEL method are given in Chapter 5.

4 Discussion on FE² for TPM and Body Loads in Elasticity

As mentioned in Chapter 1, the treatment of the Theory of Porous Media or similar approaches considering fluid-solid interactions are comparatively rare within the FE² scheme. Early stages of research leading to this thesis investigated the behavior of unit cells within the TPM, see Maike et al. [2016]. It revealed that the typical assumption for periodic responses on microscopic level in case of periodic boundary conditions does not hold in case of an applied macroscopic flux. The vector valued flux applied to the microscopic problem induces an unidirectional deformation of the solid phase. This is in contrast to the effect of exemplary a solid strain as a second order tensor. With this, the microscopic response is no longer periodic and directly dependent on the size of the microscopic domain. This leads to the impression to require a special treatment or additional constraint in case of such a loading.

To gain further insights on these effects, body loads in elasticity within the FE² scheme are considered rather than the TPM because of a lower complexity of the equations. That is a suitable step since a body load in elasticity acts comparable to a pressure gradient on the solid displacement within the TPM. This becomes evident by inserting the mixture stress in Eq. (2.113) into the balance of momentum in Eq. (2.128) such that

$$\operatorname{div}(\boldsymbol{\sigma}_{\mathrm{E}}^{\mathrm{S}} - p\,\boldsymbol{I}) + \rho\,\boldsymbol{b} = \operatorname{div}(\boldsymbol{\sigma}_{\mathrm{E}}^{\mathrm{S}}) - \operatorname{grad}(p) + \rho\,\boldsymbol{b} = \boldsymbol{0}\,. \tag{4.1}$$

Based on this, the next section presents a framework for the treatment of body forces in elasticity within the classical first order FE² scheme including a consistent derivation of the lower level boundary conditions. In the last section of this chapter, this framework is discussed at a simple model problem to investigate its applicability and limitations.

4.1 Theoretical Framework

The following derivation is meant to highlight the differences to the common first order FE² scheme such that some details are omitted for the sake of clarity. If the reader is not familiar with this multiscale approach, an overview article such as Schröder [2014] is recommended. Additionally, the structure of the following derivation is outlined in a similar fashion. The strategy to include body forces into the scheme follows the idea by de Souza Neto et al. [2015].

Starting point is the balance of momentum in Eq. (2.137) with $\boldsymbol{f}_0 = \rho_0\,\boldsymbol{b}$ such that the equation on macroscopic scale respectively its microscopic scale counterpart are given by

$$\operatorname{Div}_{\boldsymbol{X}^{\mathrm{M}}}(\boldsymbol{P}^{\mathrm{M}}) + \boldsymbol{f}_0^{\mathrm{M}} = \boldsymbol{0} \qquad \text{and} \qquad \operatorname{Div}_{\boldsymbol{X}^{\mathrm{m}}}(\boldsymbol{P}^{\mathrm{m}}) + \boldsymbol{f}_0^{\mathrm{m}} = \boldsymbol{0} \tag{4.2}$$

where the index M indicates a macroscopic quantity and the index m a microscopic one. An extended macro-homogeneity condition to define the scale transition including body loads is introduced as

$$\boldsymbol{P}^{\mathrm{M}} : \delta\boldsymbol{F}^{\mathrm{M}} - \boldsymbol{f}_0^{\mathrm{M}} \cdot \delta\boldsymbol{u}^{\mathrm{M}} = \frac{1}{V^{\mathrm{m}}} \int_{\mathcal{B}_0^{\mathrm{m}}} \boldsymbol{P}^{\mathrm{m}} : \delta\boldsymbol{F}^{\mathrm{m}} - \boldsymbol{f}_0^{\mathrm{m}} \cdot \delta\boldsymbol{u}^{\mathrm{m}}\,\mathrm{d}V^{\mathrm{m}} \tag{4.3}$$

with V^{m} as the volume of the corresponding RVE. Therein, the consideration of the body forces in addition to the stresses as in the classical approach is straight forward. They are added on both scales multiplied with the respective virtual displacement as their

conjugated quantity of virtual work. The ansatz for the microscopic displacement is given as a first order approach by

$$\boldsymbol{u}^{\mathrm{m}} := \boldsymbol{u}^{\mathrm{M}} + \left(\boldsymbol{F}^{\mathrm{M}} - \boldsymbol{I}\right) \cdot \boldsymbol{X}^{\mathrm{m}} + \widetilde{\boldsymbol{u}}^{\mathrm{m}} \tag{4.4}$$

with the displacement fluctuations on the microscopic scale $\widetilde{\boldsymbol{u}}^{\mathrm{m}}$ and the macroscopic deformation gradient

$$\boldsymbol{F}^{\mathrm{M}} = \boldsymbol{I} + \frac{\partial \boldsymbol{u}^{\mathrm{M}}}{\partial \boldsymbol{X}^{\mathrm{M}}} \,. \tag{4.5}$$

In general, all macroscopic quantities, here $\boldsymbol{u}^{\mathrm{M}}$ and $\boldsymbol{F}^{\mathrm{M}}$, are independent of the microscopic position $\boldsymbol{X}^{\mathrm{m}}$. The microscopic deformation gradient follows to

$$\boldsymbol{F}^{\mathrm{m}} = \boldsymbol{I} + \frac{\partial \boldsymbol{u}^{\mathrm{m}}}{\partial \boldsymbol{X}^{\mathrm{m}}} = \boldsymbol{F}^{\mathrm{M}} + \frac{\partial \widetilde{\boldsymbol{u}}^{\mathrm{m}}}{\partial \boldsymbol{X}^{\mathrm{m}}} = \boldsymbol{F}^{\mathrm{M}} + \widetilde{\boldsymbol{F}}^{\mathrm{m}} \tag{4.6}$$

such that it consists of a constant macroscopic part and the microscopic fluctuation gradient as

$$\widetilde{\boldsymbol{F}}^{\mathrm{m}} := \frac{\partial \widetilde{\boldsymbol{u}}^{\mathrm{m}}}{\partial \boldsymbol{X}^{\mathrm{m}}} \,. \tag{4.7}$$

In comparison to the common first order FE² scheme, the ansatz for the microscopic displacement in Eq. (4.4) differs by the inclusion of the macroscopic displacement. The consideration of this rigid body motion of the corresponding RVE is unnecessary in the absence of body forces since the weak forms of the balance equations, respectively the macro-homogeneity condition, only include the gradient of the microscopic displacement. Consequently, the ansatz has to be adjusted if the microscopic displacement appears in the governing equations as in the present case. To close the framework, relations between the macroscopic and microscopic counterparts have to be introduced. The macroscopic displacement is defined as

$$\begin{aligned} \boldsymbol{u}^{\mathrm{M}} := \frac{1}{V^{\mathrm{m}}} \int_{\mathcal{B}_0^{\mathrm{m}}} \boldsymbol{u}^{\mathrm{m}} \,\mathrm{d}V^{\mathrm{m}} &= \frac{1}{V^{\mathrm{m}}} \int_{\mathcal{B}_0^{\mathrm{m}}} \boldsymbol{u}^{\mathrm{M}} + \left(\boldsymbol{F}^{\mathrm{M}} - \boldsymbol{I}\right) \cdot \boldsymbol{X}^{\mathrm{m}} + \widetilde{\boldsymbol{u}}^{\mathrm{m}} \,\mathrm{d}V^{\mathrm{m}} \\ &= \boldsymbol{u}^{\mathrm{M}} + \left(\boldsymbol{F}^{\mathrm{M}} - \boldsymbol{I}\right) \cdot \frac{1}{V^{\mathrm{m}}} \int_{\mathcal{B}_0^{\mathrm{m}}} \boldsymbol{X}^{\mathrm{m}} \,\mathrm{d}V^{\mathrm{m}} + \frac{1}{V^{\mathrm{m}}} \int_{\mathcal{B}_0^{\mathrm{m}}} \widetilde{\boldsymbol{u}}^{\mathrm{m}} \,\mathrm{d}V^{\mathrm{m}} \,. \end{aligned} \tag{4.8}$$

Postulating the origin of the RVE at its geometric center such that

$$\int_{\mathcal{B}_0^{\mathrm{m}}} \boldsymbol{X}^{\mathrm{m}} \,\mathrm{d}V^{\mathrm{m}} = \boldsymbol{0} \tag{4.9}$$

leads to the constraint on the microscopic displacement fluctuations

$$\int_{\mathcal{B}_0^{\mathrm{m}}} \widetilde{\boldsymbol{u}}^{\mathrm{m}} \,\mathrm{d}V^{\mathrm{m}} = \boldsymbol{0} \,. \tag{4.10}$$

While this constraint is fulfilled a priori in the absence of body forces in elasticity within the FE² scheme for suitable boundary conditions on the RVE, it has to be enforced separately for nonzero body forces. The consequences on the solution space of the microscopic problem have a major impact on the discussion in Section 4.2. The macroscopic deformation gradient is defined as

$$\boldsymbol{F}^{\mathrm{M}} := \frac{1}{V^{\mathrm{m}}} \int_{\mathcal{B}_0^{\mathrm{m}}} \boldsymbol{F}^{\mathrm{m}} \,\mathrm{d}V^{\mathrm{m}} = \frac{1}{V^{\mathrm{m}}} \int_{\mathcal{B}_0^{\mathrm{m}}} \boldsymbol{F}^{\mathrm{M}} + \widetilde{\boldsymbol{F}}^{\mathrm{m}} \,\mathrm{d}V^{\mathrm{m}} = \boldsymbol{F}^{\mathrm{M}} + \frac{1}{V^{\mathrm{m}}} \int_{\mathcal{B}_0^{\mathrm{m}}} \widetilde{\boldsymbol{F}}^{\mathrm{m}} \,\mathrm{d}V^{\mathrm{m}} \tag{4.11}$$

which leads to

$$\int_{\mathcal{B}_0^{\mathrm{m}}} \widetilde{\boldsymbol{F}}^{\mathrm{m}} \,\mathrm{d}V^{\mathrm{m}} = \int_{\partial\mathcal{B}_0^{\mathrm{m}}} \widetilde{\boldsymbol{u}}^{\mathrm{m}} \otimes \boldsymbol{N}^{\mathrm{m}} \,\mathrm{d}A^{\mathrm{m}} = \boldsymbol{0} \tag{4.12}$$

as further constraint. In contrast to Eq. (4.10), this constraint is fulfilled automatically by choosing one of the lower level boundary conditions derived in the following. With all these relations, the macro-homogeneity condition in Eq. (4.3) can be reformulated as

$$\begin{aligned}
\boldsymbol{P}^{\mathrm{M}} : \delta\boldsymbol{F}^{\mathrm{M}} - \boldsymbol{f}_0^{\mathrm{M}} \cdot \delta\boldsymbol{u}^{\mathrm{M}} = \frac{1}{V^{\mathrm{m}}} \int_{\mathcal{B}_0^{\mathrm{m}}} & \boldsymbol{P}^{\mathrm{m}} : \left(\delta\boldsymbol{F}^{\mathrm{M}} + \delta\widetilde{\boldsymbol{F}}^{\mathrm{m}}\right) \\
& - \boldsymbol{f}_0^{\mathrm{m}} \cdot \left(\delta\boldsymbol{u}^{\mathrm{M}} + \delta\boldsymbol{F}^{\mathrm{M}} \cdot \boldsymbol{X}^{\mathrm{m}} + \delta\widetilde{\boldsymbol{u}}^{\mathrm{m}}\right) \mathrm{d}V^{\mathrm{m}} \\
= \frac{1}{V^{\mathrm{m}}} \int_{\mathcal{B}_0^{\mathrm{m}}} & \boldsymbol{P}^{\mathrm{m}} - \boldsymbol{f}_0^{\mathrm{m}} \otimes \boldsymbol{X}^{\mathrm{m}} \,\mathrm{d}V^{\mathrm{m}} : \delta\boldsymbol{F}^{\mathrm{M}} - \frac{1}{V^{\mathrm{m}}} \int_{\mathcal{B}_0} \boldsymbol{f}_0^{\mathrm{m}} \,\mathrm{d}V^{\mathrm{m}} \cdot \delta\boldsymbol{u}^{\mathrm{M}} \\
& + \frac{1}{V^{\mathrm{m}}} \int_{\mathcal{B}_0^{\mathrm{m}}} \boldsymbol{P}^{\mathrm{m}} : \delta\widetilde{\boldsymbol{F}}^{\mathrm{m}} - \boldsymbol{f}_0^{\mathrm{m}} \cdot \delta\widetilde{\boldsymbol{u}}^{\mathrm{m}} \,\mathrm{d}V^{\mathrm{m}} .
\end{aligned} \tag{4.13}$$

The condition is fulfilled if the microscopic problem is solved with respect to the fluctuations as

$$\int_{\mathcal{B}_0^{\mathrm{m}}} \boldsymbol{P}^{\mathrm{m}} : \delta\widetilde{\boldsymbol{F}}^{\mathrm{m}} - \boldsymbol{f}_0^{\mathrm{m}} \cdot \delta\widetilde{\boldsymbol{u}}^{\mathrm{m}} \,\mathrm{d}V^{\mathrm{m}} = 0 \tag{4.14}$$

and if the macroscopic stress and body load are computed by

$$\boldsymbol{P}^{\mathrm{M}} := \frac{1}{V^{\mathrm{m}}} \int_{\mathcal{B}_0^{\mathrm{m}}} \boldsymbol{P}^{\mathrm{m}} - \boldsymbol{f}_0^{\mathrm{m}} \otimes \boldsymbol{X}^{\mathrm{m}} \,\mathrm{d}V^{\mathrm{m}} \tag{4.15}$$

and

$$\boldsymbol{f}_0^{\mathrm{M}} := \frac{1}{V^{\mathrm{m}}} \int_{\mathcal{B}_0^{\mathrm{m}}} \boldsymbol{f}_0^{\mathrm{m}} \,\mathrm{d}V^{\mathrm{m}} . \tag{4.16}$$

Different sets of consistent boundary and constraint conditions for the microscopic problem can be derived by rearranging Eq. (4.14). The first reformulation utilize the additive split of the stress $\boldsymbol{P}^{\mathrm{m}} = \boldsymbol{P}^{\mathrm{M}} + \widetilde{\boldsymbol{P}}^{\mathrm{m}}$ and the body load $\boldsymbol{f}_0^{\mathrm{m}} = \boldsymbol{f}_0^{\mathrm{M}} + \widetilde{\boldsymbol{f}}_0^{\mathrm{m}}$ as well as Eq. (4.4) and Eq. (4.6) for the microscopic displacement and deformation. Additionally, the constraints in Eq. (4.10) and Eq. (4.12) on the microscopic displacement fluctuation and microscopic deformation fluctuation are exploited. With this, the first transformation of Eq. (4.14) reads as

$$\begin{aligned}
& \int_{\mathcal{B}_0^{\mathrm{m}}} \left(\boldsymbol{P}^{\mathrm{M}} + \widetilde{\boldsymbol{P}}^{\mathrm{m}}\right) : \delta\widetilde{\boldsymbol{F}}^{\mathrm{m}} - \left(\boldsymbol{f}_0^{\mathrm{M}} + \widetilde{\boldsymbol{f}}_0^{\mathrm{m}}\right) \cdot \delta\widetilde{\boldsymbol{u}}^{\mathrm{m}} \,\mathrm{d}V^{\mathrm{m}} = 0 \\
\Leftrightarrow \quad & \int_{\mathcal{B}_0^{\mathrm{m}}} \widetilde{\boldsymbol{P}}^{\mathrm{m}} : \delta\widetilde{\boldsymbol{F}}^{\mathrm{m}} - \widetilde{\boldsymbol{f}}_0^{\mathrm{m}} \cdot \delta\widetilde{\boldsymbol{u}}^{\mathrm{m}} \,\mathrm{d}V^{\mathrm{m}} = 0 \\
\Leftrightarrow \quad & \int_{\mathcal{B}_0^{\mathrm{m}}} \left(\boldsymbol{P}^{\mathrm{m}} - \boldsymbol{P}^{\mathrm{M}}\right) : \left(\delta\boldsymbol{F}^{\mathrm{m}} - \delta\boldsymbol{F}^{\mathrm{M}}\right) \\
& \qquad - \left(\boldsymbol{f}_0^{\mathrm{m}} - \boldsymbol{f}_0^{\mathrm{M}}\right) \cdot \left(\delta\boldsymbol{u}^{\mathrm{m}} - \delta\boldsymbol{u}^{\mathrm{M}} - \delta\boldsymbol{F}^{\mathrm{M}} \cdot \boldsymbol{X}^{\mathrm{m}}\right) \mathrm{d}V^{\mathrm{m}} = 0 .
\end{aligned} \tag{4.17}$$

This equation leads to the possible constraint combinations

$$\boldsymbol{P}^{\mathrm{m}} = \boldsymbol{P}^{\mathrm{M}} \quad \text{and} \quad \boldsymbol{f}_0^{\mathrm{m}} = \boldsymbol{f}_0^{\mathrm{M}} \quad \forall \boldsymbol{X}^{\mathrm{m}} \in \mathcal{B}_0^{\mathrm{m}} \tag{4.18}$$

and

$$\boldsymbol{F}^{\mathrm{m}} = \boldsymbol{F}^{\mathrm{M}} \quad \text{and} \quad \boldsymbol{u}^{\mathrm{m}} = \boldsymbol{u}^{\mathrm{M}} + \boldsymbol{F}^{\mathrm{M}} \cdot \boldsymbol{X}^{\mathrm{m}} \quad \forall \boldsymbol{X}^{\mathrm{m}} \in \mathcal{B}_0^{\mathrm{m}} \,. \tag{4.19}$$

The assumption of constant stress combined with constant body load on the microscopic problem is associated to the estimate of Reuss while a constant deformation gradient respectively a linear displacement defined by macroscopic quantities corresponds to the estimate of Voigt. The second line in Eq. (4.17) can be transformed as well to

$$\begin{aligned}
&\int_{\mathcal{B}_0^{\mathrm{m}}} \widetilde{\boldsymbol{P}}^{\mathrm{m}} : \mathrm{Grad}_{\boldsymbol{X}^{\mathrm{m}}} \left(\delta \widetilde{\boldsymbol{u}}^{\mathrm{m}}\right) - \widetilde{\boldsymbol{f}}_0^{\mathrm{m}} \cdot \delta \widetilde{\boldsymbol{u}}^{\mathrm{m}} \, \mathrm{d}V^{\mathrm{m}} = 0 \\
\Leftrightarrow \quad & - \int_{\mathcal{B}_0^{\mathrm{m}}} \mathrm{Div}_{\boldsymbol{X}^{\mathrm{m}}} \left(\widetilde{\boldsymbol{P}}^{\mathrm{m}}\right) \cdot \delta \widetilde{\boldsymbol{u}}^{\mathrm{m}} - \widetilde{\boldsymbol{f}}_0^{\mathrm{m}} \cdot \delta \widetilde{\boldsymbol{u}}^{\mathrm{m}} \, \mathrm{d}V^{\mathrm{m}} + \int_{\partial \mathcal{B}_0^{\mathrm{m}}} \left(\widetilde{\boldsymbol{P}}^{\mathrm{m}} \cdot \boldsymbol{N}^{\mathrm{m}}\right) \cdot \delta \widetilde{\boldsymbol{u}}^{\mathrm{m}} \, \mathrm{d}A^{\mathrm{m}} = 0 \\
\Leftrightarrow \quad & \int_{\partial \mathcal{B}_0^{\mathrm{m}}} \left(\boldsymbol{t}_0^{\mathrm{m}} - \boldsymbol{P}^{\mathrm{M}} \cdot \boldsymbol{N}^{\mathrm{m}}\right) \cdot \left(\delta \boldsymbol{u}^{\mathrm{m}} - \delta \boldsymbol{u}^{\mathrm{M}} - \delta \boldsymbol{F}^{\mathrm{M}} \cdot \boldsymbol{X}^{\mathrm{m}}\right) \, \mathrm{d}A^{\mathrm{m}} = 0 \,,
\end{aligned} \tag{4.20}$$

where the divergence theorem, the differential equation on microscopic scale in Eq. (4.2) and the constraint in Eq. (4.10) have been utilized. The reformulation reveals that the macro-homogeneity condition can be fulfilled by either Neumann boundary conditions

$$\boldsymbol{t}_0^{\mathrm{m}} = \boldsymbol{P}^{\mathrm{M}} \cdot \boldsymbol{N}^{\mathrm{m}} \quad \forall \boldsymbol{X}^{\mathrm{m}} \in \partial \mathcal{B}_0^{\mathrm{m}} \tag{4.21}$$

or Dirichlet boundary conditions

$$\boldsymbol{u}^{\mathrm{m}} = \boldsymbol{u}^{\mathrm{M}} + \boldsymbol{F}^{\mathrm{M}} \cdot \boldsymbol{X}^{\mathrm{m}} \quad \forall \boldsymbol{X}^{\mathrm{m}} \in \partial \mathcal{B}_0^{\mathrm{m}} \,. \tag{4.22}$$

For the derivation of periodic boundary conditions, the boundary of the microscopic problem is decomposed into two parts as $\partial \mathcal{B}_0^{\mathrm{m}} = \partial \mathcal{B}_0^{\mathrm{m}+} \cup \partial \mathcal{B}_0^{\mathrm{m}-}$ where every point $\boldsymbol{X}^{\mathrm{m}+} \in \partial \mathcal{B}_0^{\mathrm{m}+}$ has a corresponding point $\boldsymbol{X}^{\mathrm{m}-} \in \partial \mathcal{B}_0^{\mathrm{m}-}$ with outward unit normals $\boldsymbol{N}^{m+}$ and $\boldsymbol{N}^{m-}$. With this, the last line in Eq. (4.20) can be rewritten as

$$\begin{aligned}
&\int_{\partial \mathcal{B}_0^{\mathrm{m}}} \left(\boldsymbol{t}_0^{\mathrm{m}} - \boldsymbol{P}^{\mathrm{M}} \cdot \boldsymbol{N}^{\mathrm{m}}\right) \cdot \delta \widetilde{\boldsymbol{u}}^{\mathrm{m}} \, \mathrm{d}A^{\mathrm{m}} = 0 \\
\Leftrightarrow \quad & \int_{\partial \mathcal{B}_0^{\mathrm{m}+}} \left(\boldsymbol{t}_0^{\mathrm{m}+} - \boldsymbol{P}^{\mathrm{M}} \cdot \boldsymbol{N}^{\mathrm{m}+}\right) \cdot \delta \widetilde{\boldsymbol{u}}^{+\mathrm{m}} \, \mathrm{d}A^{\mathrm{m}} + \int_{\partial \mathcal{B}_0^{\mathrm{m}-}} \left(\boldsymbol{t}_0^{\mathrm{m}-} - \boldsymbol{P}^{\mathrm{M}} \cdot \boldsymbol{N}^{\mathrm{m}-}\right) \cdot \delta \widetilde{\boldsymbol{u}}^{-\mathrm{m}} \, \mathrm{d}A^{\mathrm{m}} = 0 \\
\Leftrightarrow \quad & \int_{\partial \mathcal{B}_0^{\mathrm{m}+}} \left(\boldsymbol{t}_0^{\mathrm{m}+} - \boldsymbol{P}^{\mathrm{M}} \cdot \boldsymbol{N}^{\mathrm{m}+}\right) \cdot \delta \widetilde{\boldsymbol{u}}^{+\mathrm{m}} \, \mathrm{d}A^{\mathrm{m}} + \int_{\partial \mathcal{B}_0^{\mathrm{m}+}} \left(\boldsymbol{t}_0^{\mathrm{m}-} + \boldsymbol{P}^{\mathrm{M}} \cdot \boldsymbol{N}^{\mathrm{m}+}\right) \cdot \delta \widetilde{\boldsymbol{u}}^{+\mathrm{m}} \, \mathrm{d}A^{\mathrm{m}} = 0 \\
\Leftrightarrow \quad & \int_{\partial \mathcal{B}_0^{\mathrm{m}+}} \left(\boldsymbol{t}_0^{\mathrm{m}+} + \boldsymbol{t}_0^{\mathrm{m}-}\right) \cdot \delta \widetilde{\boldsymbol{u}}^{\mathrm{m}+} \, \mathrm{d}A^{\mathrm{m}} = 0
\end{aligned} \tag{4.23}$$

including the assumption of periodic displacement fluctuations as $\widetilde{\boldsymbol{u}}^{\mathrm{m}+} = \widetilde{\boldsymbol{u}}^{\mathrm{m}-}$. The expression is fulfilled in case of antiperiodic tractions $\boldsymbol{t}_0^{\mathrm{m}+} = -\boldsymbol{t}_0^{\mathrm{m}-}$.

The derived constraint and boundary conditions are very similar to those in the classical first order FE^2 scheme without body loads, cf. Schröder [2014]. An important difference is the additional kinematic constraint on the fluctuations in Eq. (4.10) which has to be enforced on the microscopic problem.

4.2 Limitations on Accuracy on Microscopic Scale

All sets of derived boundary and constraint conditions in the previous section satisfy the macro-homogeneity condition and are therefore energetically admissible within this multiscale approach. Nevertheless, they lead to limitations for the achievable accuracy on the microscopic level in case of applied body forces. This effect is investigated in a simple model problem of a block of homogeneous material without lateral contraction which is loaded by a constant unidirectional body load, illustrated in Figure 4.1.

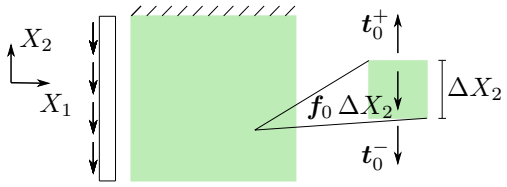

Figure 4.1: Hanging block with constant body load.

The analytical solution of this quasi one-dimensional problem results in a linear strain distribution and accordingly a quadratic displacement response in 2-direction. Therein, each material point experiences a displacement in negative 2-direction. By definition, none of the derived boundary and constraint conditions is able to cover that analytical solution of a linear strain respectively stress on the microscopic scale. Even the usually superior periodic boundary conditions lack of this capability which becomes evident by comparing the requirement of antiperiodic tractions with the balance equation at a small volume element of the body, depicted in Figure 4.1, revealing $\boldsymbol{t}_0^+ = \boldsymbol{t}_0^- + \boldsymbol{f}_0\,\Delta X_2$. To solve this conflict, the assumption of scale separation can be included where the RVE size is very small compared to the overall body such that ΔX_2 tends towards zero. With this, the influence of the body load can be identified as small or even negligible on the microscopic scale. Nevertheless, it reveals that the size of the RVE is not arbitrary for such a formulation, even for homogeneous materials.

A closer look is taken at the expected microscopic responses for the derived sets of boundary and constraint conditions. In case of any remaining degrees of freedom on the RVE after applying the boundary conditions, as exemplary valid for the Dirichlet or periodic version, each material point would tend to displace in direction of the uniform body force, here the negative 2-direction. But for such cases, the kinematic constraint in Eq. (4.10) prevents any fluctuation. As a consequence, the microscopic problem can only capture the deformation state which is prescribed macroscopically, here a constant strain at the most. The effect of a constant body load, analytically leading to a linear strain, can not be represented on the microscopic scale within a first order FE^2 scheme. Submitting the macroscopic strain gradient to the microscopic problem within a higher order FE^2 ap-

proach is promising for a constant body load but would lead to analogous limitations in case of a more complex body load.

Transferring these findings to the TPM by considering the structure of Eq. (4.1), the effect of microscopic fluid flux, respectively the microscopic pressure gradient, on the solid displacement cannot be captured if not prescribed by macroscopic counterparts. Nevertheless, the presented framework for the treatment of body load in elasticity is energetically consistent but the observed limitation is inherent to this multiscale approach. Consequently, if capturing these effects on the microscale is important for a specific application, considering a framework without scale separation is reasonable.

5 Mesh-in-Element Method

The Mesh-in-Element method is a multiscale approach which is based on the discretization of the domain into finite elements. It can be applied to any type of problem which fits in the generalized FEM framework introduced in Section 3.3. But in contrast to single scale FEM, an additional discretization layer is added such that each element on the macroscopic scale contains an underlying microscopic problem. In the following derivations, an M is added to the labels of macroscopic quantities and an m to those corresponding to microscopic ones.

The physical domain, here $\mathcal{B}_{0\mathrm{S}}$ as the most general case within this thesis, is approximated by the domain $\mathcal{B}_{0\mathrm{S}}^{\mathrm{M},h}$. This domain is discretized by n_e^{M} macroscopic elements as

$$\mathcal{B}_{0\mathrm{S}} \approx \mathcal{B}_{0\mathrm{S}}^{\mathrm{M},h} = \bigcup_{e=1}^{n_e^{\mathrm{M}}} \mathcal{B}_{0\mathrm{S}}^{\mathrm{M},e} \,. \tag{5.1}$$

In addition to that, every macroscopic element is approximated by the microscopic domain $\mathcal{B}_{0\mathrm{S}}^{\mathrm{m},h}$ which consists of n_e^{m} microscopic elements as

$$\mathcal{B}_{0\mathrm{S}}^{\mathrm{M},e} \approx \mathcal{B}_{0\mathrm{S}}^{\mathrm{m},h} = \bigcup_{e=1}^{n_e^{\mathrm{m}}} \mathcal{B}_{0\mathrm{S}}^{\mathrm{m},e} \,. \tag{5.2}$$

With this distinction between macroscopic and microscopic domains, their discretizations and approximations in can be introduced independent from each other. Compared to Chapter 3, every quantity which has been defined there exists twice within the MIEL method, once belonging to the macroscopic scale and once to the microscopic problem. This leads to the different vectors of degrees of freedom as $\boldsymbol{D}^{\mathrm{M}}$ for the macroscopic problem, $\boldsymbol{d}^{\mathrm{M}}$ for one macroscopic element, $\boldsymbol{D}^{\mathrm{m}}$ for one microscopic problem and $\boldsymbol{d}^{\mathrm{m}}$ for one microscopic element. The same holds analogously for the variations and increments of the degrees of freedom.

The strong coupling between the scales within the MIEL method is depicted in Figure 5.1. Different element colors in the illustration of the microscopic scale problem indicate different material definitions.

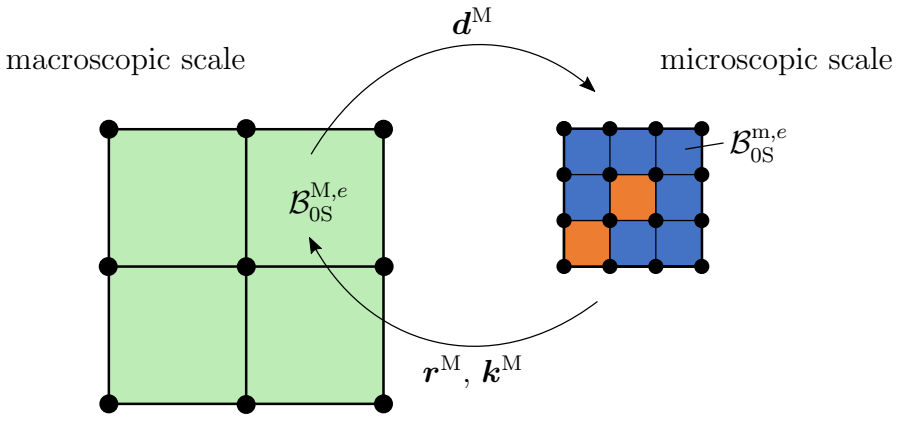

Figure 5.1: Concept and scale transition of the MIEL method.

The size, shape and deformation of the microscopic problem is determined by the respective macroscopic element. In detail, the degrees of freedom on the boundary of the microscopic problem and potential inner degrees of freedom corresponding to inner macroscopic

element nodes are prescribed such that they match the interpolation of the macroscopic element. This leads to the coupling condition for a single macroscopic element and its underlying microscopic problem as

$$\boldsymbol{D}_b^{\mathrm{m}} = \boldsymbol{T} \cdot \boldsymbol{d}^{\mathrm{M}} \qquad \forall \quad \boldsymbol{X}_{\mathrm{S}}^{\mathrm{m},J} \in (\boldsymbol{X}_{\mathrm{S}}^{\mathrm{M},I} \cup \partial\mathcal{B}_{0\mathrm{S}}^{\mathrm{m},h}) \tag{5.3}$$

with $\boldsymbol{D}_b^{\mathrm{m}}$ as degrees of freedom on the microscopic problem with Dirichlet boundary conditions, $\boldsymbol{T}$ as scale transition matrix, $\boldsymbol{d}^{\mathrm{M}}$ as degrees of freedom of the corresponding macroscopic element, $\boldsymbol{X}_{\mathrm{S}}^{\mathrm{m},J}$ as initial position vector of the node J of the microscopic problem, $\boldsymbol{X}_{\mathrm{S}}^{\mathrm{M},I}$ as initial position vector of the macroscopic element node I and $\partial\mathcal{B}_{0\mathrm{S}}^{\mathrm{m},h}$ as the discretized boundary of the microscopic problem in reference configuration. The scale transition matrix $\boldsymbol{T} = \boldsymbol{T}(N_\alpha^{\mathrm{M},I}(\boldsymbol{X}_{\mathrm{S}}^{\mathrm{m},J}))$ contains the nodal shape functions $N_\alpha^{\mathrm{M},I}$ for the interpolated field α of the macroscopic element evaluated at the position of the microscopic node which corresponds to the respective microscopic degrees of freedom. More details on this matrix follow in Section 5.3.

The scale coupling strategy within the MIEL method is a very intuitive, robust and numerically efficient possibility. On the other hand, it is rather restrictive tending to resulting in too stiff responses in elasticity as pointed out in Markovič and Ibrahimbegović [2004]. However, they investigated macroscopic elements of linear interpolation order such that the impact of the scale coupling condition can be reduced by a higher order macroscopic element interpolation as analyzed in the numerical examples in Chapter 6. In general, the scale coupling condition in Eq. (5.3) enables a free choice of macroscopic element interpolation order. Nevertheless, it is reasonable for many applications to focus on interpolations with exclusively nodes on the boundary of the element. With this, no constraint is applied to any inner degree of freedom of the microscopic problem which is favorable in case of heterogeneities. In addition to that, an eventual inner macroscopic element node requires a coinciding node on the microscopic problem for a straight forward application of the coupling condition. If this is not the case, an advanced method to spread the constraint to nodes in the vicinity of the macroscopic node position is required which is not in the scope of this thesis. Furthermore, this thesis only uses quadrilateral macroscopic elements and consequently quadrilateral microscopic problems since this shape is dominant within the literature review on multiscale methods within this thesis.

This chapter continues with the derivation of the microscopic and macroscopic problem based on the notation of the generalized FEM framework in Section 3.3. First, the structure of the microscopic problem is outlined before the extraction of the macroscopic system of equation is described. The chapter is completed by an explanation of the construction of the scale transition matrix and the algorithmic treatment of the method.

5.1 Microscopic Problem

The derivation of the microscopic problem to solve is quite straight forward. The discretized weak form of a microscopic problem corresponding to a single macroscopic element can be written in terms of the microscopic degrees of freedom $\boldsymbol{D}^{\mathrm{m}}$ and the their variations $\delta\boldsymbol{D}^{\mathrm{m}}$ as

$$G^{\mathrm{m},h} := \delta\boldsymbol{D}^{\mathrm{m}} \cdot \boldsymbol{R}^{\mathrm{m}}(\boldsymbol{D}^{\mathrm{m}})\,, \tag{5.4}$$

where $\boldsymbol{R}^{\mathrm{m}}$ is the right-hand-side vector of the microscopic problem which can be built up in standard fashion by an assembly over all microscopic element contributions $\boldsymbol{r}^{\mathrm{m}}$. The increment of the discretized linearized weak form follows formally to

$$\Delta G^{\mathrm{m},h} := \frac{\partial G^{\mathrm{m}}}{\partial \boldsymbol{D}^{\mathrm{m}}} \cdot \Delta \boldsymbol{D}^{\mathrm{m}} = \delta \boldsymbol{D}^{\mathrm{m}} \cdot \frac{\partial \boldsymbol{R}^{\mathrm{m}}}{\partial \boldsymbol{D}^{\mathrm{m}}} \cdot \Delta \boldsymbol{D}^{\mathrm{m}} = \delta \boldsymbol{D}^{\mathrm{m}} \cdot \boldsymbol{K}^{\mathrm{m}} \cdot \Delta \boldsymbol{D}^{\mathrm{m}} \,, \tag{5.5}$$

where $\boldsymbol{K}^{\mathrm{m}}$ is the microscopic problem system matrix which is assembled by the microscopic element matrices $\boldsymbol{k}^{\mathrm{m}}$. A split of the set of microscopic degrees of freedom is introduced as $\boldsymbol{D}^{\mathrm{m}} = \boldsymbol{D}_f^{\mathrm{m}} \cup \boldsymbol{D}_b^{\mathrm{m}}$ with $\boldsymbol{D}_f^{\mathrm{m}} \cap \boldsymbol{D}_b^{\mathrm{m}} = \emptyset$. Therein, $\boldsymbol{D}_f^{\mathrm{m}}$ are free microscopic degrees of freedom and $\boldsymbol{D}_b^{\mathrm{m}}$ those with imposed Dirichlet boundary conditions. This split is illustrated for a small microscopic problem example in Figure 5.2 for a case where both unknown fields are interpolated by linear quadrilateral elements and the corresponding macroscopic element does not include inner nodes.

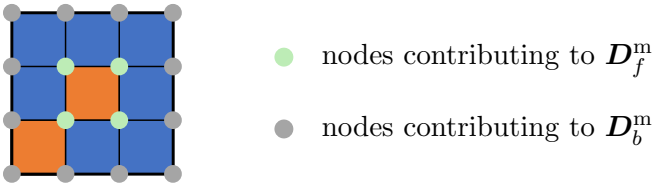

Figure 5.2: Split of microscopic problem degrees of freedom into two sets.

With this and the analogous split for the variations and increments, the linearization of the weak form can be rewritten to

$$\begin{aligned} &\delta \boldsymbol{D}_f^{\mathrm{m}} \cdot \left(\boldsymbol{R}_f^{\mathrm{m}} + \frac{\partial \boldsymbol{R}_f^{\mathrm{m}}}{\partial \boldsymbol{D}_f^{\mathrm{m}}} \cdot \Delta \boldsymbol{D}_f^{\mathrm{m}} + \frac{\partial \boldsymbol{R}_f^{\mathrm{m}}}{\partial \boldsymbol{D}_b^{\mathrm{m}}} \cdot \Delta \boldsymbol{D}_b^{\mathrm{m}} \right) \\ &+ \delta \boldsymbol{D}_b^{\mathrm{m}} \cdot \left(\boldsymbol{R}_b^{\mathrm{m}} + \frac{\partial \boldsymbol{R}_b^{\mathrm{m}}}{\partial \boldsymbol{D}_f^{\mathrm{m}}} \cdot \Delta \boldsymbol{D}_f^{\mathrm{m}} + \frac{\partial \boldsymbol{R}_b^{\mathrm{m}}}{\partial \boldsymbol{D}_b^{\mathrm{m}}} \cdot \Delta \boldsymbol{D}_b^{\mathrm{m}} \right) = 0 \end{aligned} \tag{5.6}$$

or

$$\begin{bmatrix} \delta \boldsymbol{D}_f^{\mathrm{m}} \\ \delta \boldsymbol{D}_b^{\mathrm{m}} \end{bmatrix} \cdot \left[\begin{bmatrix} \boldsymbol{R}_f^{\mathrm{m}} \\ \boldsymbol{R}_b^{\mathrm{m}} \end{bmatrix} + \begin{bmatrix} \boldsymbol{K}_{ff}^{\mathrm{m}} & \boldsymbol{K}_{fb}^{\mathrm{m}} \\ \boldsymbol{K}_{bf}^{\mathrm{m}} & \boldsymbol{K}_{bb}^{\mathrm{m}} \end{bmatrix} \cdot \begin{bmatrix} \Delta \boldsymbol{D}_f^{\mathrm{m}} \\ \Delta \boldsymbol{D}_b^{\mathrm{m}} \end{bmatrix} \right] = 0 \,. \tag{5.7}$$

With the classical requirement on the variation at positions with Dirichlet boundary conditions $\delta \boldsymbol{D}_b^{\mathrm{m}} = \boldsymbol{0}$ and the arbitrariness of $\delta \boldsymbol{D}_f^{\mathrm{m}}$, the increments of the real microscopic degrees of freedom are computed as

$$\Delta \boldsymbol{D}_f^{\mathrm{m}} = (\boldsymbol{K}_{ff}^{\mathrm{m}})^{-1} \cdot \left(-\boldsymbol{R}_f^{\mathrm{m}} - \boldsymbol{K}_{fb}^{\mathrm{m}} \cdot \Delta \boldsymbol{D}_b^{\mathrm{m}} \right) \tag{5.8}$$

which is the same system of equations to solve as for a single scale computation. This reveals that from an implementational point of view, the microscopic problem can be solved with a standard finite element and does not require any modifications at this point.

5.2 Macroscopic Problem

In contrast to the microscopic problem, the derivation of the macroscopic problem in terms of the macroscopic right-hand-side vector $\boldsymbol{R}^{\mathrm{M}}$ and system matrix $\boldsymbol{K}^{\mathrm{M}}$ requires more attention. The goal is to rewrite the discretized linearized weak form of the microscopic problem in terms of the degrees of freedom of the corresponding macroscopic element. The coupling between the scales is defined by Eq. (5.3) including the microscopic degrees of freedom with Dirichlet boundary conditions $\boldsymbol{D}_b^{\mathrm{m}}$. Because of that, static condensation following Guyan [1965] is applied by inserting Eq. (5.8) into the system of equations resulting from Eq. (5.7)

$$\boldsymbol{R}_b^{\mathrm{m}} + \boldsymbol{K}_{bf}^{\mathrm{m}} \cdot \Delta \boldsymbol{D}_f^{\mathrm{m}} + \boldsymbol{K}_{bb}^{\mathrm{m}} \cdot \Delta \boldsymbol{D}_b^{\mathrm{m}} = 0 \tag{5.9}$$

leading to

$$\boldsymbol{R}_b^{\mathrm{m}} + \boldsymbol{K}_{bf}^{\mathrm{m}} \cdot \boldsymbol{K}_{ff}^{\mathrm{m}\,-1} \cdot \left(-\boldsymbol{R}_f^{\mathrm{m}} - \boldsymbol{K}_{fb}^{\mathrm{m}} \cdot \Delta \boldsymbol{D}_b^{\mathrm{m}}\right) + \boldsymbol{K}_{bb}^{\mathrm{m}} \cdot \Delta \boldsymbol{D}_b^{\mathrm{m}} = 0\,. \tag{5.10}$$

A condensed discretized weak form of the microscopic problem can be written in terms of the increments of the degrees of freedom with Dirichlet boundary conditions as

$$G_c^{\mathrm{m},h} := \delta \boldsymbol{D}_b^{\mathrm{m}} \cdot (\boldsymbol{R}_c^{\mathrm{m}} + \boldsymbol{K}_c^{\mathrm{m}} \cdot \Delta \boldsymbol{D}_b^{\mathrm{m}}) = 0 \tag{5.11}$$

with

$$\boldsymbol{R}_c^{\mathrm{m}} = \boldsymbol{R}_b^{\mathrm{m}} - \boldsymbol{K}_{bf}^{\mathrm{m}} \cdot \boldsymbol{K}_{ff}^{\mathrm{m}\,-1} \cdot \boldsymbol{R}_f^{\mathrm{m}} \tag{5.12}$$

and

$$\boldsymbol{K}_c^{\mathrm{m}} = \boldsymbol{K}_{bb}^{\mathrm{m}} - \boldsymbol{K}_{bf}^{\mathrm{m}} \cdot \boldsymbol{K}_{ff}^{\mathrm{m}\,-1} \cdot \boldsymbol{K}_{fb}^{\mathrm{m}}\,, \tag{5.13}$$

where $\boldsymbol{R}_c^{\mathrm{m}}$ and $\boldsymbol{K}_c^{\mathrm{m}}$ denote the condensed microscopic system right-hand side vector and system matrix. Please note, that even if $\delta \boldsymbol{D}_b^{\mathrm{m}} = \boldsymbol{0}$, this condition is not employed at this point because the equation is not to be solved but used for the coupling between the scales. A subsequent application of the coupling condition in terms of

$$\delta \boldsymbol{D}_b^{\mathrm{m}} = \boldsymbol{T} \cdot \delta \boldsymbol{d}^{\mathrm{M}} \quad \text{and} \quad \Delta \boldsymbol{D}_b^{\mathrm{m}} = \boldsymbol{T} \cdot \Delta \boldsymbol{d}^{\mathrm{M}} \tag{5.14}$$

leads to

$$(\delta \boldsymbol{d}^{\mathrm{M}} \cdot \boldsymbol{T}^{T}) \cdot \left(\boldsymbol{R}_c^{\mathrm{m}} + \boldsymbol{K}_c^{\mathrm{m}} \cdot \boldsymbol{T} \cdot \Delta \boldsymbol{d}^{\mathrm{M}}\right) = 0\,. \tag{5.15}$$

This equation can be interpreted as the linearized discretized weak form of the corresponding macroscopic element as

$$\mathrm{Lin}\, G^{\mathrm{M},e} = G^{\mathrm{M},e} + \Delta G^{\mathrm{M},e} = 0 \tag{5.16}$$

with

$$G^{\mathrm{M},e} := \delta \boldsymbol{d}^{\mathrm{M}} \cdot \boldsymbol{r}^{\mathrm{M}} \tag{5.17}$$

and

$$\Delta G^{\mathrm{M},e} := \delta \boldsymbol{d}^{\mathrm{M}} \cdot \boldsymbol{k}^{\mathrm{M}} \cdot \Delta \boldsymbol{d}^{\mathrm{M}}\,. \tag{5.18}$$

With this in hand, the element right-hand-side vector and element matrix of the macroscopic element corresponding to the respective microscopic problem can be written as

$$\boldsymbol{r}^{\mathrm{M}} = \boldsymbol{T}^{\mathrm{T}} \cdot \boldsymbol{R}_c^{\mathrm{m}} \tag{5.19}$$

and

$$\boldsymbol{k}^{\mathrm{M}} = \boldsymbol{T}^{\mathrm{T}} \cdot \boldsymbol{K}_{c}^{\mathrm{m}} \cdot \boldsymbol{T} \,. \tag{5.20}$$

From this point, the macroscopic system of equations with the right-hand-side vector $\boldsymbol{R}^{\mathrm{M}}$ and system matrix $\boldsymbol{K}^{\mathrm{M}}$ can be assembled and solved in usual manner.

Please observe that the macroscopic element right-hand-side vector and element matrix are extracted from the corresponding quantities of the microscopic problem. This implies that the macroscopic element is only used for the correct transfer of the macroscopic element degrees of freedom to the microscopic scale and the assembly of the macroscopic system of equations. All remaining field quantities are only computed on microscopic level where the material formulation and constitutive relations are evaluated As a consequence, integration over the domain has only to be done on the microscopic scale but not on the macroscopic scale.

Noteworthy is the proper application of external surface loads. If the macroscopic and microscopic element interpolation do not coincide, more specific if the macroscopic interpolation order is higher than its microscopic counterpart, an application of external forces on the macroscopic problem can lead to a non-conforming macroscopic right-hand-side vector $\boldsymbol{R}^{\mathrm{M}}$ resulting in non-physical solutions. They have to be applied to the microscopic problem instead even though they do not alter the microscopic problem solution itself since all degrees of freedoms on the boundary of the microscopic problem are occupied by Dirichlet boundary conditions in case of microscopic problems without holes. But the surface loads are considered during the extraction of the macroscopic element right-hand-side vector within $\boldsymbol{R}_{b}^{\mathrm{m}}$.

As a concluding remark on the extraction of the element right-hand-side vector and the element matrix of the macroscopic element, it should be stated that there exists at least one further possibility which deviates from the presented procedure in this section. Zupan and Korelc [2018] do the extraction with aid of a sensitivity analysis and show that their approach is numerically more efficient for larger microscopic problems. This is due to the fact that their strategy does not rely on building a Schur complement as within static condensation which becomes more and more demanding with an increasing microscopic problem size.

5.3 Scale Transition Matrix

The scale transition matrix $\boldsymbol{T}$ ensures that the degrees of freedom with Dirichlet boundary conditions on the microscopic problem are set to the magnitude of the respective interpolated macroscopic field in agreement with Eq. (5.3). To investigate the specific structure of the matrix, the interpolation of a single degree of freedom of type $\mathcal{U}$ is written as

$$D_{b,\mathcal{U}}^{\mathrm{m},J} = \sum_{I=1}^{n_{n,\mathcal{U}}^{\mathrm{M}}} N_{\mathcal{U}}^{\mathrm{M},I}(\boldsymbol{\xi}^{\mathrm{M}}(\boldsymbol{X}_{\mathrm{S}}^{\mathrm{m},J}))\, d_{\mathcal{U}}^{\mathrm{M},I} = \bar{\boldsymbol{N}}_{\mathcal{U}}^{\mathrm{M}} \cdot \boldsymbol{d}_{\mathcal{U}}^{\mathrm{M}} \,. \tag{5.21}$$

This relation appears to be the standard interpolation within the isoparametric concept but with one important difference. Compared to the mapping within the typical FEM procedure, the parametric coordinates $\boldsymbol{\xi}^{\mathrm{M}}$ are not known a priori as exemplary in case of numerical integration. They have to be determined first dependent on the position of the microscopic node in focus $\boldsymbol{X}_{\mathrm{S}}^{\mathrm{m},J}$ before the shape functions can be evaluated. Before

this procedure is discussed in detail, the structure of the transition matrix is investigated. The vector $\bar{\boldsymbol{N}}_{\mathcal{U}}^{\mathrm{M}}$ consists of the macroscopic shape functions which are evaluated at $\boldsymbol{\xi}^{\mathrm{M}}$ corresponding to $\boldsymbol{X}_{\mathrm{S}}^{\mathrm{m},J}$. Consequently, these values are used to build one row in the transition matrix $\boldsymbol{T}$. Since the vector $\boldsymbol{d}^{\mathrm{M}}$ usually contains multiple degrees of freedom varying in direction or field, the vector $\bar{\boldsymbol{N}}_{\mathcal{U}}^{\mathrm{M}}$ can not just be copied into the matrix but its entries have to be put in the matching positions. Depending on the macroscopic element type, this can lead to many zeros in the transition matrix. Therefore, the size of the matrix $\boldsymbol{T}$ depends on the interpolation order of the macroscopic element and the mesh density of the microscopic problem, i.e. the number of degrees of freedom with Dirichlet boundary conditions on the microscopic problem equals the number of rows, while the degrees of freedom of the corresponding macroscopic element defines the number of columns. Since the transition matrix is evaluated with respect to the coordinates $\boldsymbol{X}_{\mathrm{S}}^{\mathrm{m},J}$ in reference configuration, it is sufficient to calculate it once at the beginning of the simulation.

An example for the construction of the scale transition matrix is given with respect to the discretization depicted in Figure 5.3. The scalar unknown fields α and β are interpolated by linear quadrilateral elements on both scales. The chosen discretization is the simplest possibility to show all aspects of the matrix at the smallest possible size.

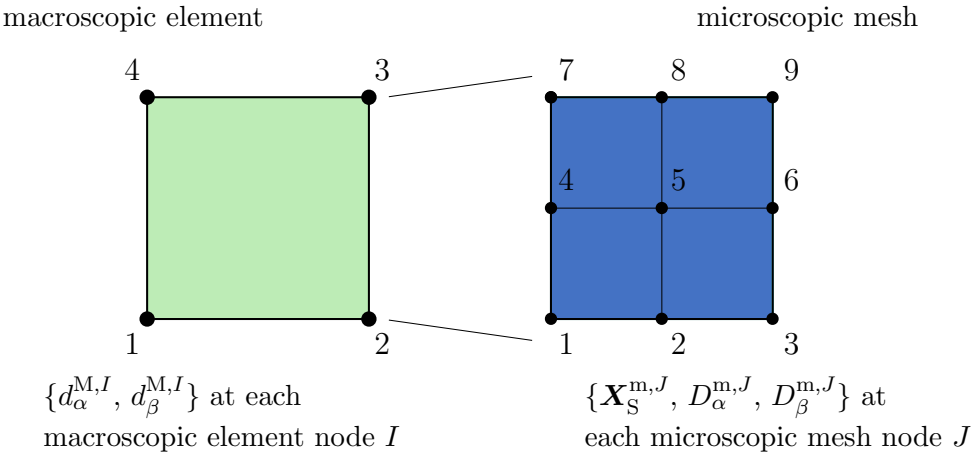

Figure 5.3: Exemplary discretization within the MIEL method.

The vectors of all degrees of freedom of the macroscopic element $\boldsymbol{d}^{\mathrm{M}}$ and of those along the boundary of the respective micro problem $\boldsymbol{D}_b^{\mathrm{m}}$ are within this example given as

$$\begin{aligned}
\boldsymbol{d}^{\mathrm{M,ex}} &= \{d_\alpha^{\mathrm{M},1}, d_\alpha^{\mathrm{M},2}, d_\alpha^{\mathrm{M},3}, d_\alpha^{\mathrm{M},4}, d_\beta^{\mathrm{M},1}, d_\beta^{\mathrm{M},2}, d_\beta^{\mathrm{M},3}, d_\beta^{\mathrm{M},4}\}\,, \\
\boldsymbol{D}_b^{\mathrm{m,ex}} &= \{D_\alpha^{\mathrm{m},1}, D_\alpha^{\mathrm{m},2}, D_\alpha^{\mathrm{m},3}, D_\alpha^{\mathrm{m},4}, D_\alpha^{\mathrm{m},6}, D_\alpha^{\mathrm{m},7}, D_\alpha^{\mathrm{m},8}, D_\alpha^{\mathrm{m},9}, \\
&\qquad D_\beta^{\mathrm{m},1}, D_\beta^{\mathrm{m},2}, D_\beta^{\mathrm{m},3}, D_\beta^{\mathrm{m},4}, D_\beta^{\mathrm{m},6}, D_\beta^{\mathrm{m},7}, D_\beta^{\mathrm{m},8}, D_\beta^{\mathrm{m},9}\}\,.
\end{aligned} \tag{5.22}$$

This leads to the scale transition matrix in (5.23), where the abbreviated notation $N_{\mathcal{U}}^I(\boldsymbol{X}^J) = N_{\mathcal{U}}^{\mathrm{M},I}(\boldsymbol{\xi}^{\mathrm{M}}(\boldsymbol{X}_{\mathrm{S}}^{\mathrm{m},J}))$ is applied for the sake of clarity, cf. Eq. (5.21).

The structure of the matrix implies that it is beneficial to store the submatrices with respect to the different unknown fields separately in case of large micro problems to reduce the memory requirement. In addition to that, after evaluation, each row has at the most two non-zero entries in case of a linear macroscopic element. That is because only two

$$\boldsymbol{T}^{\mathrm{ex}} = \begin{bmatrix}
N_\alpha^1(\boldsymbol{X}^1) & N_\alpha^2(\boldsymbol{X}^1) & N_\alpha^3(\boldsymbol{X}^1) & N_\alpha^4(\boldsymbol{X}^1) & 0 & 0 & 0 & 0 \\
N_\alpha^1(\boldsymbol{X}^2) & N_\alpha^2(\boldsymbol{X}^2) & N_\alpha^3(\boldsymbol{X}^2) & N_\alpha^4(\boldsymbol{X}^2) & 0 & 0 & 0 & 0 \\
N_\alpha^1(\boldsymbol{X}^3) & N_\alpha^2(\boldsymbol{X}^3) & N_\alpha^3(\boldsymbol{X}^3) & N_\alpha^4(\boldsymbol{X}^3) & 0 & 0 & 0 & 0 \\
N_\alpha^1(\boldsymbol{X}^4) & N_\alpha^2(\boldsymbol{X}^4) & N_\alpha^3(\boldsymbol{X}^4) & N_\alpha^4(\boldsymbol{X}^4) & 0 & 0 & 0 & 0 \\
N_\alpha^1(\boldsymbol{X}^6) & N_\alpha^2(\boldsymbol{X}^6) & N_\alpha^3(\boldsymbol{X}^6) & N_\alpha^4(\boldsymbol{X}^6) & 0 & 0 & 0 & 0 \\
N_\alpha^1(\boldsymbol{X}^7) & N_\alpha^2(\boldsymbol{X}^7) & N_\alpha^3(\boldsymbol{X}^7) & N_\alpha^4(\boldsymbol{X}^7) & 0 & 0 & 0 & 0 \\
N_\alpha^1(\boldsymbol{X}^8) & N_\alpha^2(\boldsymbol{X}^8) & N_\alpha^3(\boldsymbol{X}^8) & N_\alpha^4(\boldsymbol{X}^8) & 0 & 0 & 0 & 0 \\
N_\alpha^1(\boldsymbol{X}^9) & N_\alpha^2(\boldsymbol{X}^9) & N_\alpha^3(\boldsymbol{X}^9) & N_\alpha^4(\boldsymbol{X}^9) & 0 & 0 & 0 & 0 \\
0 & 0 & 0 & 0 & N_\beta^1(\boldsymbol{X}^1) & N_\beta^2(\boldsymbol{X}^1) & N_\beta^3(\boldsymbol{X}^1) & N_\beta^4(\boldsymbol{X}^1) \\
0 & 0 & 0 & 0 & N_\beta^1(\boldsymbol{X}^2) & N_\beta^2(\boldsymbol{X}^2) & N_\beta^3(\boldsymbol{X}^2) & N_\beta^4(\boldsymbol{X}^2) \\
0 & 0 & 0 & 0 & N_\beta^1(\boldsymbol{X}^3) & N_\beta^2(\boldsymbol{X}^3) & N_\beta^3(\boldsymbol{X}^3) & N_\beta^4(\boldsymbol{X}^3) \\
0 & 0 & 0 & 0 & N_\beta^1(\boldsymbol{X}^4) & N_\beta^2(\boldsymbol{X}^4) & N_\beta^3(\boldsymbol{X}^4) & N_\beta^4(\boldsymbol{X}^4) \\
0 & 0 & 0 & 0 & N_\beta^1(\boldsymbol{X}^6) & N_\beta^2(\boldsymbol{X}^6) & N_\beta^3(\boldsymbol{X}^6) & N_\beta^4(\boldsymbol{X}^6) \\
0 & 0 & 0 & 0 & N_\beta^1(\boldsymbol{X}^7) & N_\beta^2(\boldsymbol{X}^7) & N_\beta^3(\boldsymbol{X}^7) & N_\beta^4(\boldsymbol{X}^7) \\
0 & 0 & 0 & 0 & N_\beta^1(\boldsymbol{X}^8) & N_\beta^2(\boldsymbol{X}^8) & N_\beta^3(\boldsymbol{X}^8) & N_\beta^4(\boldsymbol{X}^8) \\
0 & 0 & 0 & 0 & N_\beta^1(\boldsymbol{X}^9) & N_\beta^2(\boldsymbol{X}^9) & N_\beta^3(\boldsymbol{X}^9) & N_\beta^4(\boldsymbol{X}^9)
\end{bmatrix}, \tag{5.23}$$

nodes of the macroscopic element contribute to the interpolation of any degree of freedom on the boundary of the microscopic problem. With this, the scale transition matrix ends up sparse which enables for an efficient use of memory. The simplest case can be shown within this example by assuming that the meshes on both scales only consist of square shaped elements in the reference configuration as implied in Figure 5.3. The corresponding scale transition matrix is given in (5.23). The determination of these entries is easy for this example but more compex in general.

The challenge is the determination of the macroscopic parametric coordinates in dependence on the position of the respective microscopic node as $\boldsymbol{\xi}^{\mathrm{M}}(\boldsymbol{X}_{\mathrm{S}}^{\mathrm{m},J})$. Following the macroscopic approximation of the geometry corresponding to Eq. $(3.36)_1$ based on the shape functions of the macroscopic displacement $\hat{\boldsymbol{N}}_u^{\mathrm{M}}$, the occurring system of equations with the unknown $\boldsymbol{\xi}^{\mathrm{M}}$ for a microscopic node at $\boldsymbol{X}_{\mathrm{S}}^{\mathrm{m},J}$ can be written as

$$\boldsymbol{X}_{\mathrm{S}}^{\mathrm{m},J} = \hat{\boldsymbol{N}}_u^{\mathrm{M}}(\boldsymbol{\xi}^{\mathrm{M}}) \cdot \hat{\boldsymbol{X}}_{\mathrm{S}}^{\mathrm{M}} \quad \text{with} \quad \boldsymbol{\xi}^{\mathrm{M}} \in \mathbb{R}^d \tag{5.25}$$

with d as the number of spatial dimensions of the problem. This, in general non-linear, system of equation can be solved with an iterative procedure as Newton's method.

Even though this method is quite fast and robust for such an application, building the matrix $\boldsymbol{T}$ can be accelerated significantly for macroscopic elements which only have nodes along its boundary. The procedure is explained for quadrilateral two-dimensional macroscopic elements, but is adaptable for other element formulations or three dimensions as

$$\boldsymbol{T}^{\mathrm{ex}} = \left[\begin{array}{cccccccc} 1 & 0 & 0 & 0 & 0 & 0 & 0 & 0 \\ 0.5 & 0.5 & 0 & 0 & 0 & 0 & 0 & 0 \\ 0 & 1 & 0 & 0 & 0 & 0 & 0 & 0 \\ 0.5 & 0 & 0 & 0.5 & 0 & 0 & 0 & 0 \\ 0 & 0.5 & 0.5 & 0 & 0 & 0 & 0 & 0 \\ 0 & 0 & 0 & 1 & 0 & 0 & 0 & 0 \\ 0 & 0 & 0.5 & 0.5 & 0 & 0 & 0 & 0 \\ 0 & 0 & 1 & 0 & 0 & 0 & 0 & 0 \\ 0 & 0 & 0 & 0 & 1 & 0 & 0 & 0 \\ 0 & 0 & 0 & 0 & 0.5 & 0.5 & 0 & 0 \\ 0 & 0 & 0 & 0 & 0 & 1 & 0 & 0 \\ 0 & 0 & 0 & 0 & 0.5 & 0 & 0 & 0.5 \\ 0 & 0 & 0 & 0 & 0 & 0.5 & 0.5 & 0 \\ 0 & 0 & 0 & 0 & 0 & 0 & 0 & 1 \\ 0 & 0 & 0 & 0 & 0 & 0 & 0.5 & 0.5 \\ 0 & 0 & 0 & 0 & 0 & 0 & 1 & 0 \end{array}\right] \tag{5.24}$$

well. Along an edge of a Lagrange or Serendipity quadrilateral element, only the nodes along this specific edge contribute to the interpolation. Therefore, it is valid to just use a line element of the same interpolation order as the macroscopic element along each edge. With this, the complexity compared to Eq. (5.25) reduces since the dimension of the unknown $\boldsymbol{\xi}^{\mathrm{M}}$ is decreased by one. This leads to two equations and one unknown for the case of the introduced line element as

$$\boldsymbol{X}_{\mathrm{S}}^{\mathrm{m},J} = \hat{\boldsymbol{N}}_{u}^{\mathrm{M,red}}(\boldsymbol{\xi}^{\mathrm{M}}) \cdot \hat{\boldsymbol{X}}_{\mathrm{S}}^{\mathrm{M,red}} \quad \text{with} \quad \boldsymbol{\xi}^{\mathrm{M}} \in \mathbb{R}^{d-1}\,, \tag{5.26}$$

where $\hat{\boldsymbol{N}}_{u}^{\mathrm{M,red}}$ and $\hat{\boldsymbol{X}}_{\mathrm{S}}^{\mathrm{M,red}}$ are the reduced sets of macroscopic element shape functions and coordinates. Within this thesis, these equations have been solved analytically in advance for shape functions of polynomial degree up to four, leading to a set of formulas. For an efficient implementation, these resulting equations have been optimized within the capabilities of *Mathematica* and implemented inside of multiple if-statements to choose the correct formula for the respective situation. This approach leads to a speed up about factor ten compared to Newton's method. This effect vanishes for computations including a large number of load or time steps since the scale transition matrix is built only once at the beginning of the simulation.

5.4 Algorithmic Treatment

The algorithmic treatment of the MIEL method is summarized in Table 5.1 and Table 5.2. The strategy is outlined for problems which might contain microscopic sub-steps. The global time t is taken to define the load application factor λ_{load}. This factor controls the application of the nonzero Dirichlet boundary conditions on the macroscopic scale and the nonzero Neumann boundary conditions. The macroscopic problem residual is given by

$$\boldsymbol{R}_s^{\text{M}}(\boldsymbol{D}^{\text{m}}, \lambda_{\text{load}}) := -\boldsymbol{R}_f^{\text{M}}(\boldsymbol{D}^{\text{M}}, \lambda_{\text{load}}) - \boldsymbol{K}_{fb}^{\text{M}}(\boldsymbol{D}^{\text{M}}) \cdot \Delta \boldsymbol{D}_b^{\text{M}}(\boldsymbol{D}_b^{\text{M}}, \lambda_{\text{load}})\,, \tag{5.27}$$

where $\boldsymbol{R}_f^{\text{M}}$ contain the applied Neumann boundary conditions and $\Delta \boldsymbol{D}_b^{\text{M}}$ denotes the increment on the Dirichlet boundary conditions. The microscopic problem residual is defined as

$$\boldsymbol{R}_s^{\text{m}}(\boldsymbol{D}^{\text{m}}, \lambda_{\text{load}}^{\text{m}}, \lambda_{\text{dbc}}^{\text{m}}) := -\boldsymbol{R}_f^{\text{m}}(\boldsymbol{D}^{\text{m}}, \lambda_{\text{load}}^{\text{m}}) - \boldsymbol{K}_{fb}^{\text{m}}(\boldsymbol{D}^{\text{m}}) \cdot \Delta \boldsymbol{D}_b^{\text{m}}(\boldsymbol{D}_b^{\text{m}}, \lambda_{\text{dbc}}^{\text{m}})\,. \tag{5.28}$$

Comparing these residuals with the single scale version in Eq. (3.55), the existence of the additional load factor $\lambda_{\text{dbc}}^{\text{m}}$ is noteworthy. The load factor $\lambda_{\text{load}}^{\text{m}}$ depends directly on the global load factor $\lambda_{\text{load}}(t)$ which controls the application of the Neumann boundary conditions and the nonzero macroscopic Dirichlet boundary conditions. In contrast to this, the factor $\lambda_{\text{dbc}}^{\text{m}}$ becomes relevant in case of microscopic sub-stepping for the stepwise application of the change in Dirichlet boundary conditions on the microscopic problem which is redefined each macroscopic iteration by the scale transition. The time on microscopic level t^{m} is important for the microscopic sub-stepping as well since it enables the time incrementation on microscopic level via Δt^{m}. The subscript n at $(\boldsymbol{D}_b^{\text{m}})_n$ and $\boldsymbol{d}_n^{\text{M}}$ refers to the state of the field after the last converged macroscopic step. The focus within the algorithmic treatment is on the nested type of the two iterative solution schemes, the application of the microscopic boundary conditions in terms of the macroscopic degrees of freedom and the extraction of the macroscopic tangent and residual. Please note that solving the microscopic problem is not necessary in case of no microscopic sub-stepping to extract the macroscopic element right-hand side vector and element matrix.

The convergence criteria on both scales correspond to the introduced single scale energy criterion in Section 3.4. The macroscopic iteration loop continues until the ratio of current macroscopic energy E^{M} and reference macroscopic energy $E_{\text{ref}}^{\text{M}}$ is smaller than the predefined tolerance $\text{tol}^{\text{M}} = 10^{-16}$. The current macroscopic energy is defined as $E^{\text{M}} = \boldsymbol{R}_s^{\text{M}} \cdot \Delta \boldsymbol{D}_f^{\text{M}}$. Following the single scale argumentation in Section 3.4, the reference macroscopic energy $E_{\text{ref}}^{\text{M}}$ is in general the initial energy at the first macroscopic iteration of the current macroscopic step. In contrast to this, the macroscopic reference energy $E_{\text{ref}}^{\text{M}}$ is kept constant for all following steps during the simulation starting from the first macroscopic iteration within the step after the whole external load has been applied for problems which converge against steady state. The criterion is nearly analogous for the microscopic iteration loop which continues until the ratio of current microscopic energy $E^{\text{m}} = \boldsymbol{R}_s^{\text{m}} \cdot \Delta \boldsymbol{D}_f^{\text{m}}$ and reference microscopic energy $E_{\text{ref}}^{\text{m}}$ is smaller than the predefined tolerance $\text{tol}^{\text{m}} = 10^{-16}$. But in contrast to its macroscopic counterpart, the microscopic reference energy $E_{\text{ref}}^{\text{m}}$ is kept constant for all following steps during a simulation towards steady state starting from the second macroscopic iteration within the step after the whole external load has been applied. This modification is necessary since there is no change in microscopic boundary conditions in the first macroscopic iteration. Additionally, the

Table 5.1: Algorithmic treatment for MIEL: Macroscopic scale.

MACROSCOPIC LOAD-/ TIME-STEPPING

While $t < t_{\text{end}}$

Set current time: $t = t + \Delta t$

Set current load: $\lambda_{\text{load}} = \lambda_{\text{load}}(t)$

MACROSCOPIC ITERATION LOOP

While $E^{\text{M}}/E^{\text{M}}_{\text{ref}} > \text{tol}^{\text{M}}$

MACROSCOPIC ELEMENT LOOP

Do $e^{\text{M}} = 1, ..., n^{\text{M}}_e$

Load microscopic problem at state of last converged macroscopic step

Pass $\boldsymbol{d}^{\text{M}}$, Δt and $\Delta\lambda_{\text{load}}$ to microscopic problem

SOLVING MICROSCOPIC PROBLEMS

See Table 5.2

Extraction of $\boldsymbol{r}^{\text{M}}$ and $\boldsymbol{k}^{\text{M}}$

$$\boldsymbol{r}^{\text{M}} = \boldsymbol{T}^{\text{T}} \cdot \boldsymbol{R}^{\text{m}}_c \quad \text{with} \quad \boldsymbol{R}^{\text{m}}_c = \boldsymbol{R}^{\text{m}}_b - \boldsymbol{K}^{\text{m}}_{bf} \cdot \boldsymbol{K}^{\text{m}\,-1}_{ff} \cdot \boldsymbol{R}^{\text{m}}_f$$

$$\boldsymbol{k}^{\text{M}} = \boldsymbol{T}^{\text{T}} \cdot \boldsymbol{K}^{\text{m}}_c \cdot \boldsymbol{T} \quad \text{with} \quad \boldsymbol{K}^{\text{m}}_c = \boldsymbol{K}^{\text{m}}_{bb} - \boldsymbol{K}^{\text{m}}_{bf} \cdot \boldsymbol{K}^{\text{m}\,-1}_{ff} \cdot \boldsymbol{K}^{\text{m}}_{fb}$$

End do

Macroscopic assembly: $\boldsymbol{R}^{\text{M}} = \mathop{\mathsf{A}}_{e^{\text{M}}=1}^{n^{\text{M}}_e} \boldsymbol{r}^{\text{M}}, \quad \boldsymbol{K}^{\text{M}} = \mathop{\mathsf{A}}_{e^{\text{M}}=1}^{n^{\text{M}}_e} \boldsymbol{k}^{\text{M}}$

Solve $\boldsymbol{K}^{\text{M}}_{ff} \cdot \Delta\boldsymbol{D}^{\text{M}}_f = \boldsymbol{R}^{\text{M}}_s$ for $\Delta\boldsymbol{D}^{\text{M}}_f$

Update: $\boldsymbol{D}^{\text{M}} = \boldsymbol{D}^{\text{M}} + \Delta\boldsymbol{D}^{\text{M}}$

End

Save states of all microscopic problems

End

reference energy $E^{\text{m}}_{\text{ref}}$ is chosen to be the maximum of the energies obtained from all microscopic problems at this state. This is enforced because some microscopic problems might be close to a steady state at the first time steps after load application in case of large dimensions or low Darcy parameters within the TPM which became evident during the simulation of the numerical examples in Section 7.

Table 5.2: Algorithmic treatment for MIEL: Microscopic scale.

MICROSCOPIC LOAD-/ TIME-STEPPING

While $t^{\mathrm{m}} < t$

Set current time: $t^{\mathrm{m}} = t^{\mathrm{m}} + \Delta t^{\mathrm{m}}$

Set current load: $\lambda^{\mathrm{m}}_{\mathrm{load}} = \lambda_{\mathrm{load}}(t^{\mathrm{m}})$

Set $\boldsymbol{D}^{\mathrm{m}}_b = (\boldsymbol{D}^{\mathrm{m}}_b)_n + \lambda^{\mathrm{m}}_{\mathrm{dbc}}\, \boldsymbol{T} \cdot (\boldsymbol{d}^{\mathrm{M}} - \boldsymbol{d}^{\mathrm{M}}_n)$

MICROSCOPIC ITERATION LOOP

While $E^{\mathrm{m}}/E^{\mathrm{m}}_{\mathrm{ref}} > \mathrm{tol}^{\mathrm{m}}$

MICROSCOPIC ELEMENT LOOP

Do $e^{\mathrm{m}} = 1, ..., n^{\mathrm{m}}_e$

Compute $\boldsymbol{r}^{\mathrm{m}}$ and $\boldsymbol{k}^{\mathrm{m}}$

End do

Microscopic assembly: $\boldsymbol{R}^{\mathrm{m}} = \mathop{\mathsf{A}}_{e^{\mathrm{m}}=1}^{n^{\mathrm{m}}_e} \boldsymbol{r}^{\mathrm{m}}, \quad \boldsymbol{K}^{\mathrm{m}} = \mathop{\mathsf{A}}_{e^{\mathrm{m}}=1}^{n^{\mathrm{m}}_e} \boldsymbol{k}^{\mathrm{m}}$

Solve $\boldsymbol{K}^{\mathrm{m}}_{ff} \cdot \Delta \boldsymbol{D}^{\mathrm{m}}_f = \boldsymbol{R}^{\mathrm{m}}_s$ for $\Delta \boldsymbol{D}^{\mathrm{m}}_f$

Update $\boldsymbol{D}^{\mathrm{m}} = \boldsymbol{D}^{\mathrm{m}} + \Delta \boldsymbol{D}^{\mathrm{m}}$

End

End

6 Numerical Examples - MIEL Method for Elasticity

Before the MIEL method is applied to the Theory of Porous Media, the approach is investigated in detail for small strain elasticity, see Section 2.7. The simpler structure of the system of equation to solve helps to get a first impression of the capabilities and limitations of the MIEL method. As a first example, a hanging block of homogeneous material under different loading scenarios is investigated. The application of a multiscale scheme is not advantageous compared to single scale computation for homogeneous materials. Nevertheless, the boundary value problem is chosen due to the available analytical solution which allows to obtain reliable insights with respect to the different element formulations and mesh densities on both scales. Cook's Membrane serves as the second example, again with a homogeneous material definition. The focus is on a comparison of the MIEL method to a single scale computation in terms of the convergence of the tip displacement and the occurring stress distributions for different element formulations and mesh densities. The third example is a tensile test where a heterogeneous material behavior is applied. The single scale computation of the more complex structure is taken as a reference solution to investigate the deviations introduced by the MIEL method in terms of the appearing field quantities. The findings obtained by this set of numerical examples should help to develop general guidelines for the application of the MIEL method before switching to the more demanding Theory of Porous Media.

6.1 Hanging Block

This first numerical example has the purpose to analyze the basic characteristics of the MIEL method. To achieve this, an academic boundary value problem is chosen where an analytical solution is at hand. Therein, no unit system is introduced to focus solely on the numerical effects of the presented multiscale approach compared to the analytical solution.

6.1.1 Boundary Value Problem

The investigated problem is a hanging block with an edge length of 10, clamped at the top which is shown in Figure 6.1.

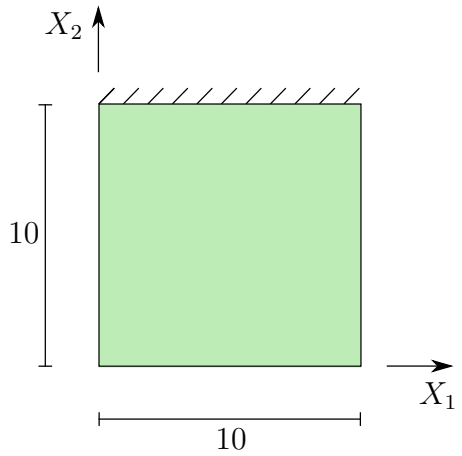

Figure 6.1: Hanging Block: Body and Dirichlet boundary conditions.

The material is homogeneous and obeys Hooke's law with a Young's modulus of $E = 2000$, a Poisson's ratio of $\nu = 0$ and a density of $\rho = 20$. Please note, that there is no need for a multiscale method for such a simple problem since a single scale approach would always be superior without material heterogeneities. Nevertheless, the MIEL method is applied to gain a first understanding of this approach. For this purpose, four different load cases are applied, as depicted in Figure 6.2 and summarized in Table 6.1.

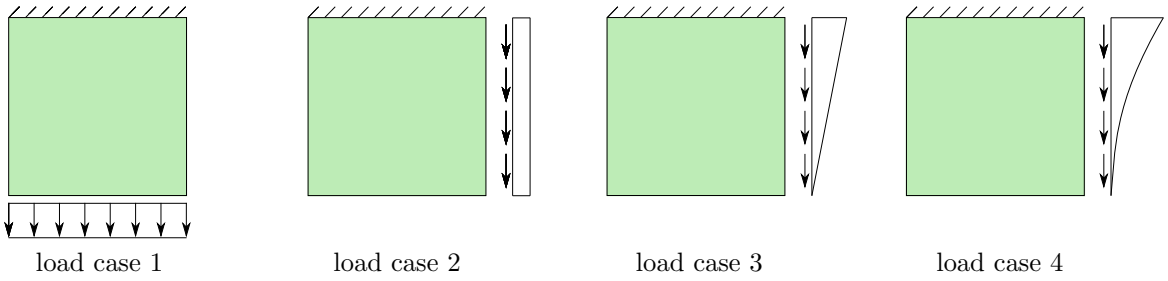

Figure 6.2: Hanging Block: Load case 1, load case 2, load case 3 and load case 4.

load case	description	loading function
1	constant traction at the bottom	$t_2 = -200$
2	constant volume load	$f_2 = -1\,\rho$
3	linear volume load	$f_2 = -0.2\,\rho\,X_2$
4	quadratic volume load	$f_2 = -0.03\,\rho\,X_2^2$

Table 6.1: Hanging Block: Definition of load cases.

The loading amplitudes are chosen in a way, that the total applied force in 2-direction is $\sum F_2 = -2000$ while $F_1 = 0$ holds at any point within the domain for each load case.

6.1.2 Analytical Solution

As the Poisson's ratio is set to zero, there is no deformation in 1-direction from the physical point of view. Because of this, the analytical solutions can be computed with the theory of a one-dimensional truss under different loading scenarios. Due to the simplicity of the problem, only these characteristics of the solutions which are important for the interpretation of the computational results are condensed in Table 6.2. The maximum strain $\max(\varepsilon_{22})$ always occurs at the clamping at the top while the maximum displacement $\max(u_2)$ arises at the bottom end of the block.

load case	$\max(\varepsilon_{22})$	order(ε_{22})	$\max(u_2)$	order(u_2)
1	0.1	constant	1	linear
2	0.1	linear	0.5	quadratic
3	0.1	quadratic	0.33	cubic
4	0.1	cubic	0.25	quartic

Table 6.2: Hanging Block: Analytical solutions.

6.1.3 Discretization

Numerous MIEL simulations with varying discretizations on both scales are carried out to get a broad overview on the effects of the element choice and number on the obtained results. Quadrilateral elements from first to fourth order, including some serendipity formulations, are chosen in every possible combination with respect to both scales. All meshes used for this analysis are structured. Most of the meshes on the macroscopic scale consist only of a single macroscopic element. The microscopic mesh density is chosen in dependence on the specific microscopic element with the goal that the number of microscopic degrees of freedom are in the same range. In detail, an 8×8 mesh is used for the Q1 microscopic mesh, a 4×4 for Q2, Q2S, Q3 and Q3S and a 2×2 mesh for the Q4 microscopic mesh. An exemplary discretization by one macroscopic Q2 element and 64 microscopic Q1 elements, labeled as $\mathrm{Q2^M Q1^m}$ 1/64, is presented in Figure 6.3.

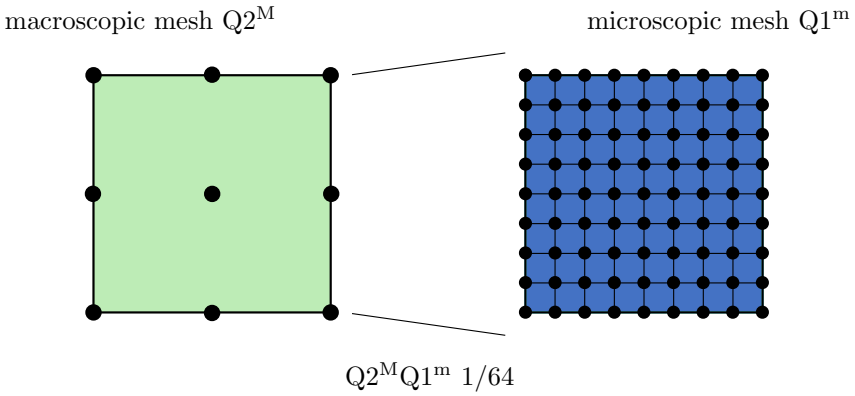

Figure 6.3: Hanging Block: Exemplary macroscopic and underlying microscopic mesh.

The microscopic mesh has to contain more degrees of freedom on its boundary and in total, compared to the associated macroscopic element. This is a minor restriction on the method since such a multiscale approach should usually resolve microscopic heterogeneities which need way more degrees on freedom in comparison to a single macroscopic element.

6.1.4 Results

For a first overview and analysis of the numerical results investigating simulations containing a single macroscopic element, the following color code is introduced:

- The numerical results match the analytical solution.
- The numerical results match the analytical solution on the macroscopic scale but lack of accuracy on the microscopic scale due to a too low microscopic interpolation order.
- The numerical results on the macroscopic scale lack of accuracy due to a too low macroscopic interpolation order. As a consequence, the results on the microscopic scale reveal a non-physical response.
- Open problem: Non-physical response on both scales which can not be explained with the other findings of this numerical example.

The results in terms of the color code are shown in Table 6.3. Therein, each sub-table covers one load case where the row indicates the macroscopic scale element type (M) while the column denotes the microscopic element type (m). Before analyzing an example for each color in detail, the overall results are outlined.

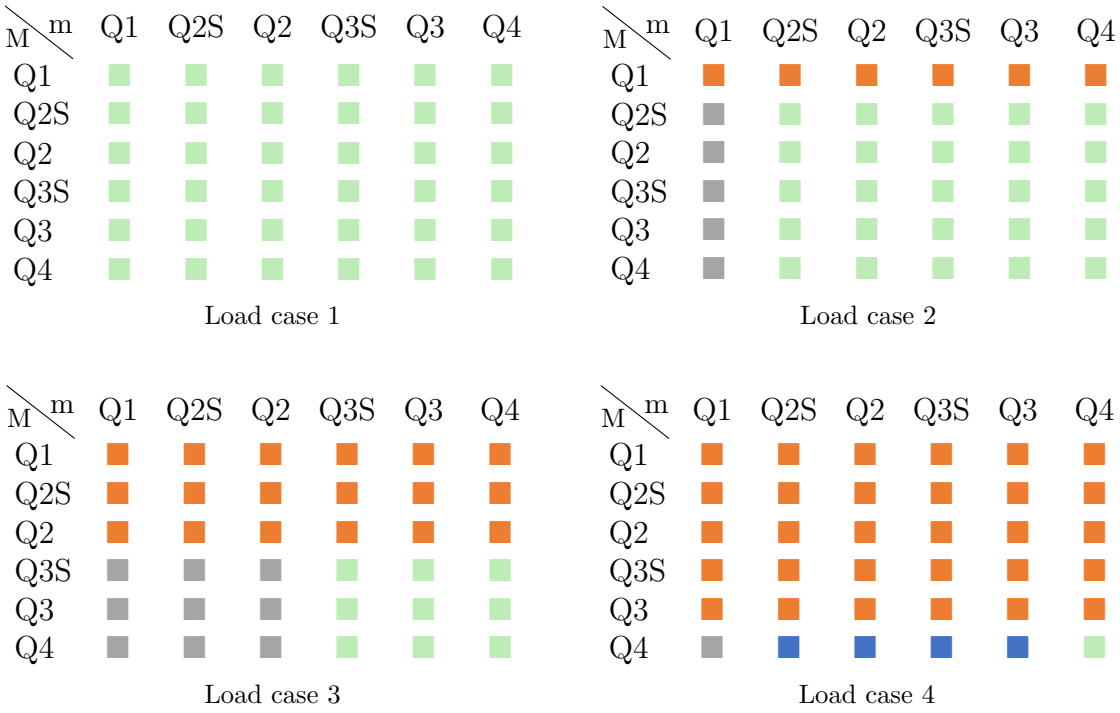

Table 6.3: Hanging Block: Color code results; macroscopic vs. microscopic elements.

At first, a closer look is taken at the green entries where the analytical solution is perfectly matched on both scales. This is the case when the interpolation order of both, microscopic and macroscopic element, is at least of the order of the analytical solution in terms of the displacement. This is consistent with the theory of the Finite Element Method but not very helpful in applications if the analytical solution, respectively its order, is unknown. The second dominating color in the tables is red, where the order of the macroscopic element is lower than the order of the analytical solution. Here, the incapability of the single macroscopic element to describe the analytical solution leads to a non-physical response on the microscopic scale. This effect is the crucial finding of this numerical example and will be investigated in detail in the progression of this section. Please observe that the effect can not be circumvented by choice of a higher order microscopic element. Those cases where the macroscopic element interpolation order is equal or higher than the analytical solution, but the microscopic element interpolation order is lower, are marked in grey. Here, no non-physical responses arise but the accuracy on the microscopic scale is not perfect due to the low interpolation order on the microscopic scale. This effect does not need a special treatment within the MIEL method since it is due to the nature of an approximating numerical method as the FEM. At last there are four entries in the table of load case 4 which are marked blue even though they would be expected to be grey with the findings beforehand. Here, unexpected non-physical responses arise on both scales which is an effect which can currently not be explained.

In the following, one example for each color will be analyzed in detail with focus on the red case. All examples besides the blue one will be taken from load case two, representing a constant volume load. Every example is investigated in terms of contour plots of the microscopic quantities u_1, u_2 and ε_{22}. The structure is plotted in its undeformed shape for an easier comparison of the different examples. Additionally, diagrams of u_2 and ε_{22} against the coordinate X_2 evaluated at fixed $X_1 = 0$ and $X_1 = 5$, representing the left boundary and the vertical midline, are shown. There is no explicit investigation of the macroscopic degrees of freedom enclosed since they are included in the microscopic displacements via the scale coupling conditions and consequently do not offer any further insights.

Example ■: Load case 2 - $\mathbf{Q2^MQ2^m}$

This example examines the case when both, the macroscopic and the microscopic element interpolation order, are at least of the order of the analytical solution of the displacement. Figure 6.4 shows the desired contour plots, namely no displacement in 1-direction and no X_1 dependency in the displacement and strain in 2-direction. With this, the diagrams in Figure 6.5 are only presented for the sake of completeness as they reveal that the analytical solution solution is matched along the left boundary as well as on the vertical midline.

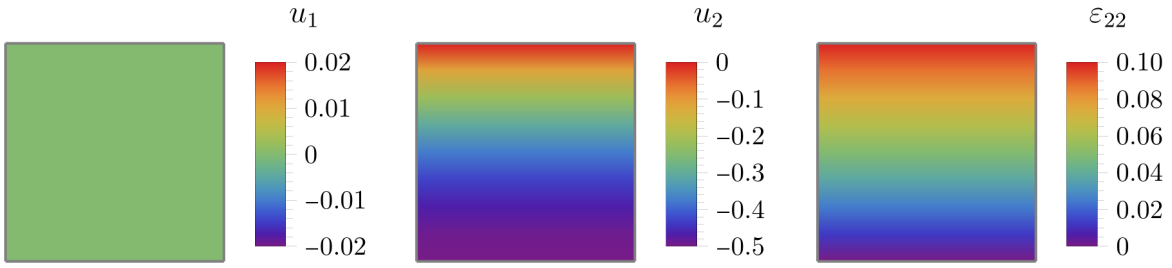

Figure 6.4: Hanging Block, load case 2: $Q2^MQ2^m$ 1/16 contour plots.

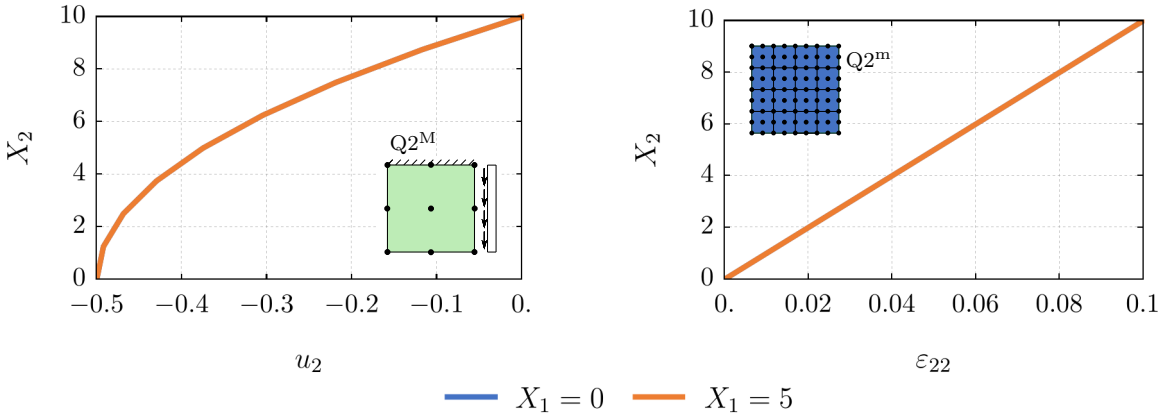

Figure 6.5: Hanging Block, load case 2: $Q2^MQ2^m$ 1/16 line plots.

Example ■: Load case 2 - $\mathbf{Q2^MQ1^m}$

Here, the possibility of a sufficient interpolation order on the macroscopic scale but a too low interpolation order on the microscale to represent the analytical solution is analyzed. The contour plots in Figure 6.6 show the expected zero displacement in 1-direction. The

vertical displacement does not perfectly match the analytical solution but the eight linear elements over the height in this example cover the quadratic function quite well, as visible in the line plot in Figure 6.7. The low interpolation order becomes more evident from the piecewise constant ε_{22} strains which obviously do not cover the linear analytical solution. But, as usual for the Finite Element Method, this effect tends to vanish with an increasing number of microscopic elements and is no special characteristic of the MIEL method. Please observe that all distributions are still independent from the X_1 position as for the green marked example beforehand.

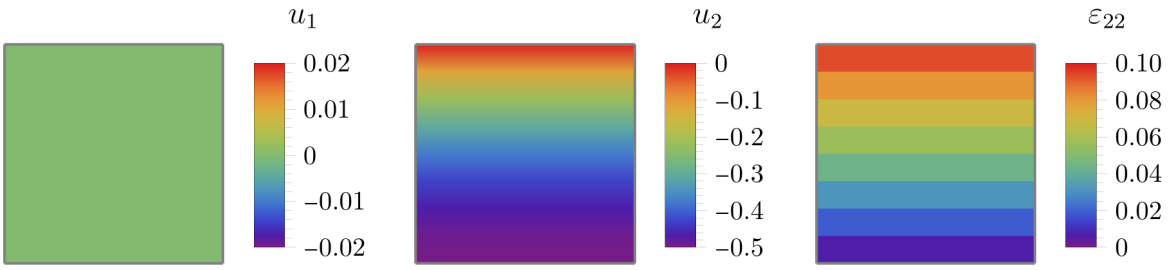

Figure 6.6: Hanging Block, load case 2: $Q2^{M}Q1^{m}$ 1/64 contour plots.

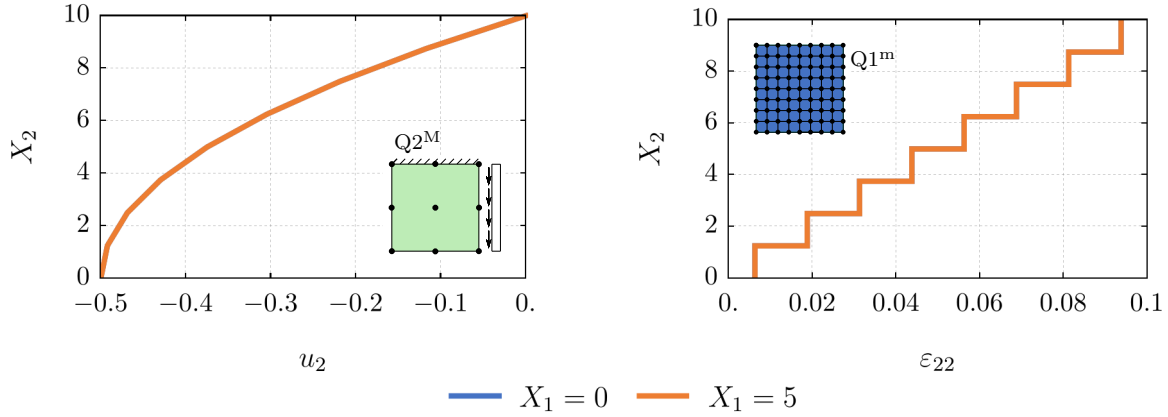

Figure 6.7: Hanging Block, load case 2: $Q2^{M}Q1^{m}$ 1/64 line plots.

Example ■: Load case 2 - $Q1^{M}Q1^{m}$

The most important finding at this numerical example is for the situation when the interpolation order of macroscopic element is lower than the order of the corresponding analytical solution. In the present example, the macroscopic linear Q1 element can not capture the quadratic reference solution. For a single scale computation, this would just lead to a poor approximation, but not to non-physical effects. In contrast to this, Figure 6.8 reveals displacements in 1-direction obtained by applying the MIEL method. To understand this effect, the vertical displacements are analyzed, especially in the line plot in Figure 6.9. The X_1 position is no longer irrelevant for this distribution. Since the scale coupling condition transfers the macroscopic degrees of freedom to the boundary of the microscopic problem, the distribution is forced to be linear on the left edge at $X_1 = 0$ in the presented example. On the contrary, the inner degrees of freedom are without this constraint and tend to follow the quadratic behavior, imposed by the constant body force. This mismatch between boundary and inner degrees of freedom leads to the non-physical

displacements in horizontal direction as result of the scale coupling strategy used within the MIEL method.

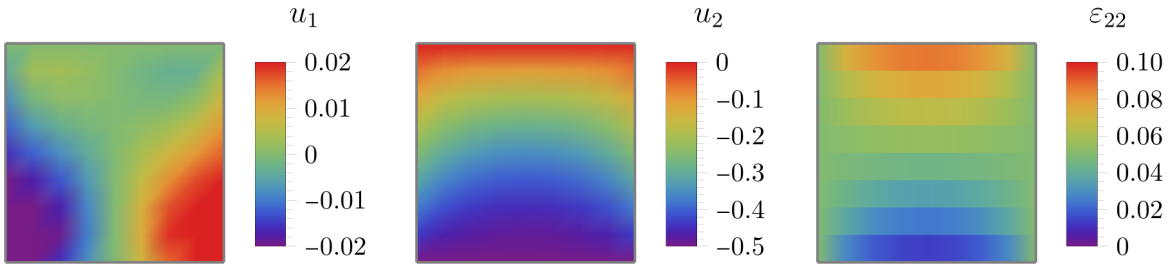

Figure 6.8: Hanging Block, load case 2: $Q1^{M}Q1^{m}$ 1/64 contour plots.

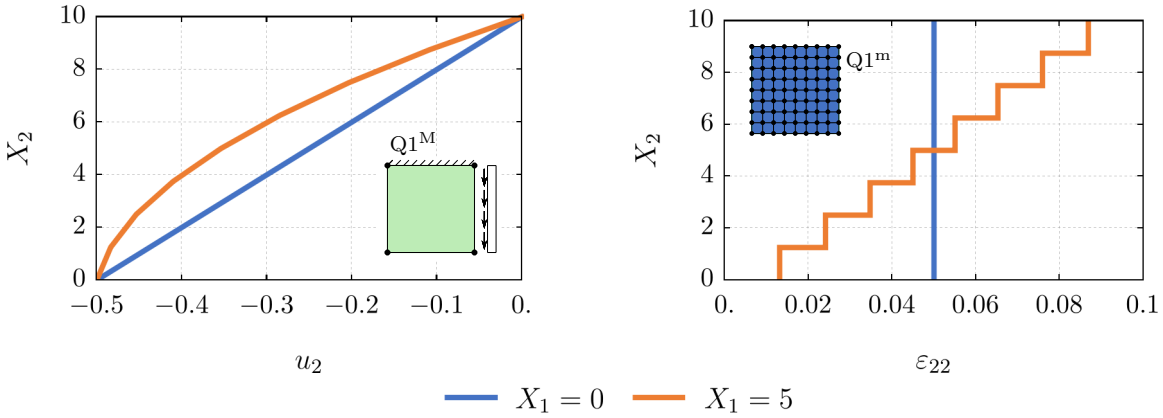

Figure 6.9: Hanging Block, load case 2: $Q1^{M}Q1^{m}$ 1/64 line plots.

This effect is examined in more detail for the constant volume load at load case 2 in the following. However, the obtained results can be applied to any loading scenario. At first, still a single macroscopic Q1 element is chosen while the microscopic discretization varies in interpolation order and mesh density. The maximum magnitude of the displacement in 1-direction $\max|u_1|$ is taken as an error indicator which should tend to zero for the present boundary value problem. Figure 6.10 shows a convergence study where $\max|u_1|$ is plotted against the number of equations of the microscopic problem for different types of microscopic elements.

The graphs reveal that the maximum displacement converges against the same value, independent from the microscopic element formulation. This is plausible in terms of the theory of the Finite Element Method but still noteworthy with respect to the MIEL method. It shows that possibly occurring non-physical effects can not be prevented or reduced by the discretization of the microscopic problem. With this in hand, the focus is now on the macroscopic discretization. It has already been shown that the choice of the macroscopic element formulation can avoid non-physical effects but is not convenient if the order of the analytical solution is not known beforehand. Consequently, the influence of the macroscopic mesh density is investigated. Again, the second load case is used, now with a fixed microscopic mesh of 64 Q2 elements which has proven to solve the microscopic problem sufficiently accurate with 578 microscopic problem equations, see Figure 6.10. A convergence study of the maximum magnitude of the displacement in 1-direction $\max|u_1|$ against the number of equations of the macroscopic problem for the choice of Q1 macroscopic elements is shown in Figure 6.11.

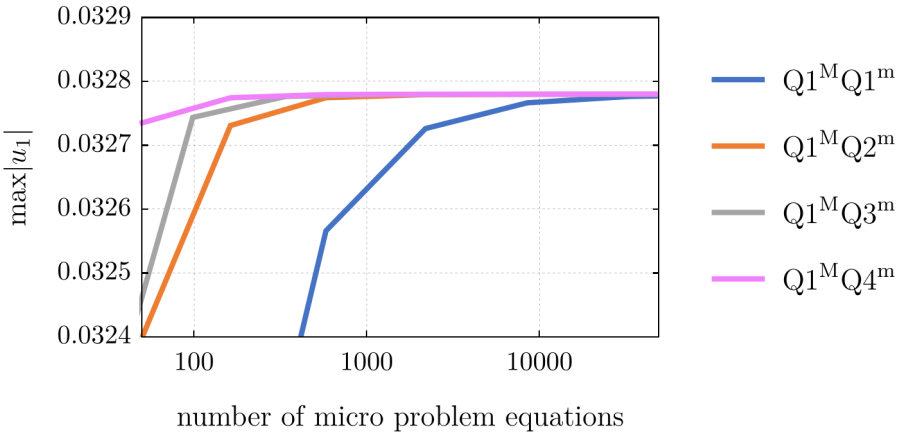

Figure 6.10: Hanging Block, load case 2: Q1^{M}Qx^{m} $1/n_e^{m}$, microscopic convergence study.

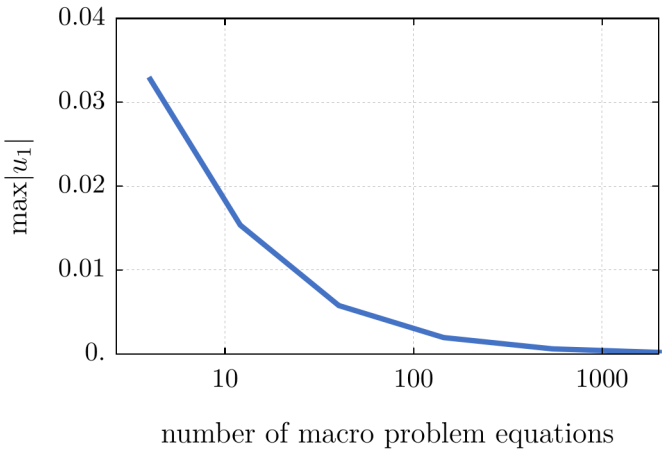

Figure 6.11: Hanging Block, load case 2: Q1^{M}Q2^{m} $n_e^{M}/64$ macroscopic convergence study.

The graph reveals that the non-physical effect vanishes with an increasing number of macroscopic elements. This is consistent since an increasing number of linear segments leads to a better approximation of the quadratic analytical solution which holds for this boundary value problem. Therefore, the effect of the restriction on the shape of the boundary of the microscopic problem by the interpolation order of the macroscopic element reduces with the number of macroscopic elements.

Example ■: Load case 4 - Q4^{M}Q2^{m}

This numerical example is completed by an anomaly of load case 4. Comparing to the other load cases, a sufficient interpolation order at the macroscopic element but a too weak interpolation order on the microscopic problem with respect to the analytical solution should not lead to non-physical effects, see the grey marked examples in Table 6.3. But this observation does not hold for load case 4 with a single Q4 macroscopic element and exemplary Q2 microscopic elements, as shown in Figure 6.12.

Even if the contour plots of the u_2 displacement and the ε_{22} strain seem to match the reference solution, the distribution of the horizontal displacement u_1 differs from zero. The magnitude of the horizontal displacement is not severe, but still to high to neglect. It

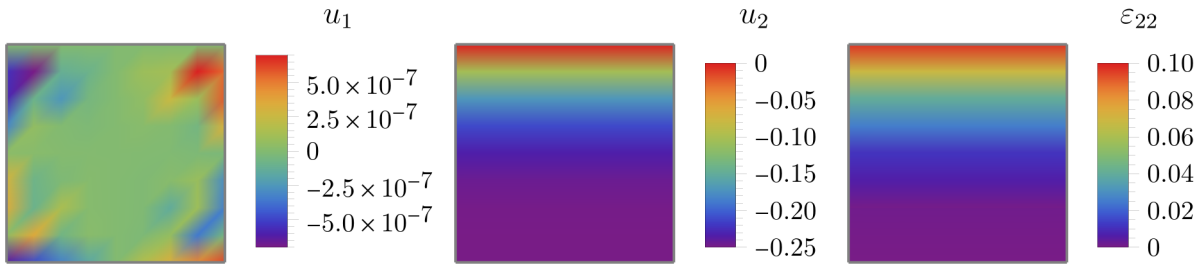

Figure 6.12: Hanging Block, load case 4: $Q4^{M}Q2^{m}$ 1/16 contour plots.

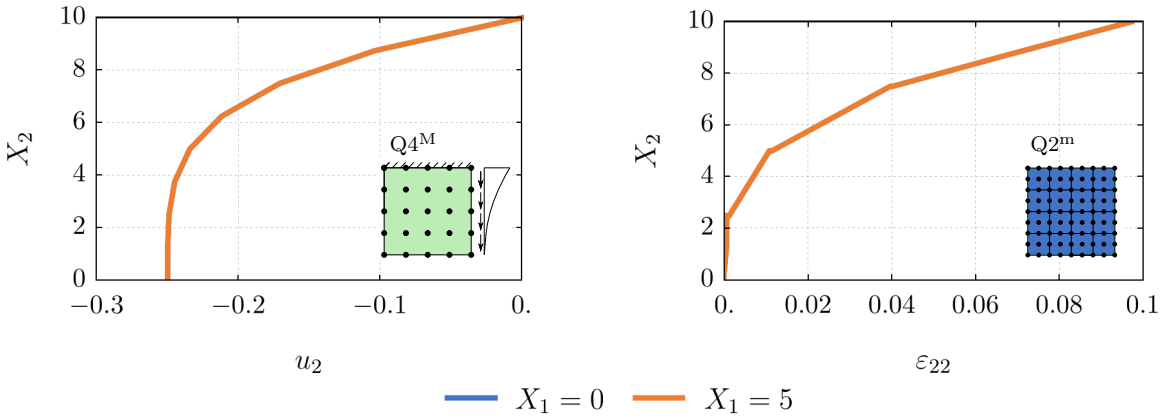

Figure 6.13: Hanging Block, load case 4: $Q4^{M}Q2^{m}$ 1/16 line plots.

converges towards zero for an increasing total number of microscopic equations, no matter whether the increase is triggered by macroscopic or microscopic mesh refinement. To this point, the reason for this effect is still an open problem. Most likely, it will vanish for more advanced applications since the meshes will be fine enough.

6.2 Cook's Membrane

The second numerical example for elasticity is Cook's membrane with a homogeneous material behavior. Even though this problem does not require a multiscale approach to be solved sufficiently accurate, it is taken to investigate the convergence of the MIEL method in terms of displacements and stresses in comparison to a single scale simulation.

6.2.1 Boundary Value Problem

The boundary value problem of the tapered cantilever beam called Cook's membrane is depicted in Figure 6.14. The geometry is defined by its four corner points as $P_1 = (0/0)\,\text{mm}$, $P_2 = (48/44)\,\text{mm}$, $P_3 = (48/60)\,\text{mm}$ and $P_4 = (0/44)\,\text{mm}$. The membrane is clamped on the left edge and a traction of $\bar{t}_2 = 1\,\text{kN/mm}^2$ is applied on the right edge. The material is homogeneous with a Young's modulus of $E = 200\,\text{kN/mm}^2$ and a Poisson's ration of $\nu = 0.35$.

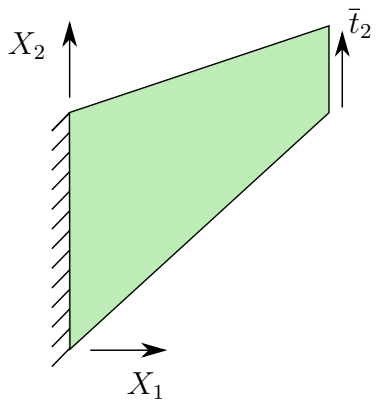

Figure 6.14: Cook's Membrane: Body and boundary conditions.

6.2.2 Discretization

This boundary value problem is investigated with respect to quadrilateral elements of first and second order of interpolation. The simulations with linear interpolations use Q1 elements for the single scale computations as well as for the MIEL method on both scales. An exemplary mesh for the MIEL method is shown in Figure 6.15. In contrast to this, Q2S elements are chosen for the macroscopic problem while Q2 elements discretize the microscopic one within the MIEL method for the analysis of quadratic elements. As a consequence, both quadratic formulations are taken for the single scale computation, depending on the respective focus.

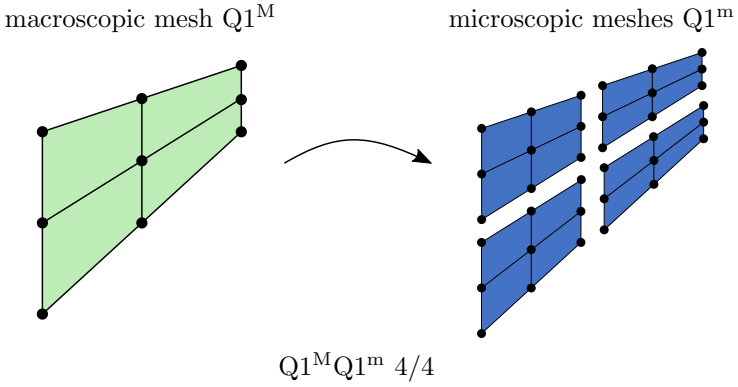

Figure 6.15: Cook's Membrane: Exemplary macroscopic and microscopic meshes.

6.2.3 Results

The convergence behavior of the displacement of the top right corner of the membrane, in the following referred as tip displacement, is evaluated. Since the MIEL method includes two discretization levels, the comparison with the single scale computation is done twice. At first with respect to the discretization of the macroscopic problem and afterwards with focus on the discretization of the microscopic problem. Both strategies are not meant to determine the performance of the MIEL method compared to a single scale computation. For this purpose, one would need to compare the computation time rather than the mesh density to include the parallelizability of the MIEL method. Nevertheless, such an analysis is not meaningful for such a simple boundary value problem with homogeneous

material. Therefore, the following diagrams should give insights into the influence of the discretizations on both scales on the overall results, here in terms of the tip displacement. Figure 6.16 shows the tip displacement against the number of single scale elements, respectively macroscopic elements within the MIEL method for linear elements (left) and quadratic elements (right). The two orange symbols at each MIEL method discretization level indicate the variance of the results depending on the mesh density of the microscopic problem.

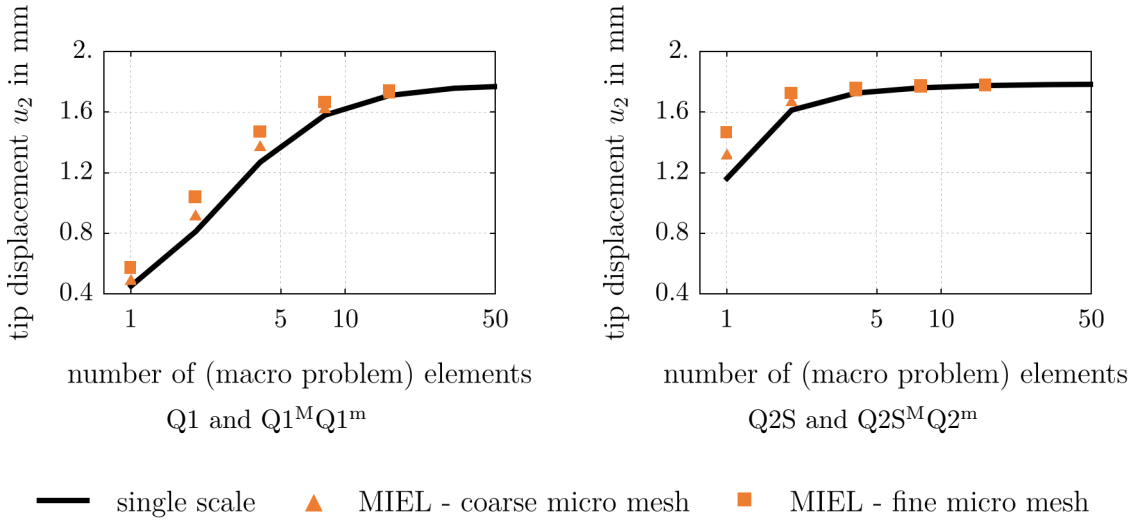

Figure 6.16: Cook's membrane: Tip displacement convergence.

The tip displacement obtained by the MIEL method is always higher compared to the single scale solution. This is a consequence of a softening effect induced by the higher number of degrees of freedom on the microscopic problem compared to the single scale element. Within the MIEL method the tip displacement increases for a constant macroscopic mesh with finer microscopic meshes and converge against a specific value. For coarse macroscopic meshes, this value is still far of the converged overall tip displacement. Additionally, the effect of improving the single scale solution vanishes for finer macroscopic meshes. A different perspective on the same issues gives Figure 6.17 where the tip displacement is plotted against the number of single scale elements, respectively this time total microscopic elements for a fixed number of macroscopic elements within the MIEL method for linear elements (left) and quadratic elements (right).

Both diagrams show the convergence of the MIEL method for a fixed number of macroscopic elements against a specific value of tip displacement with increasing number of microscopic elements. This value is always lower in comparison to the single scale solution and therefore further away from converged overall solution. This indicates that the MIEL method is not a good choice for such a problem. But that is no surprise since the investigated homogeneous boundary value problem is not in the scope of application of the method. Nevertheless, the diagrams could be redesigned in favor of the MIEL method by not plotting against the total number of microscopic elements as presented. This is because the total number of microscopic elements implies that the microscopic problems have to be solved one after another which can be avoided by solving the different microscopic problems fully parallelized. A closer look on the computational time will be taken

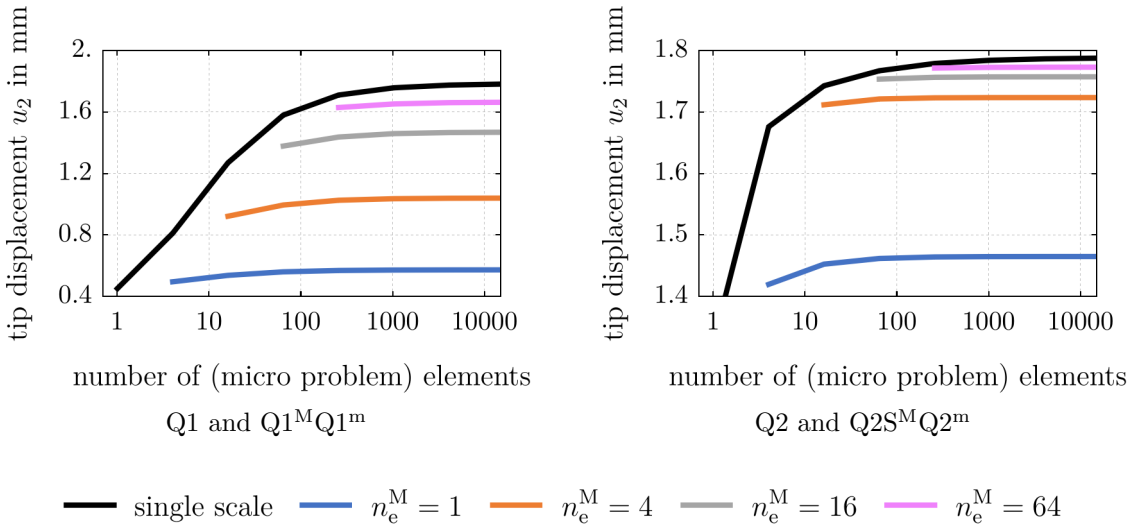

Figure 6.17: Cook's membrane: Tip displacement convergence.

at the numerical example within the TPM in Section 7.2.

To complete the investigation of the Cook's membrane problem, the contour plots of the displacement u_1 and the stress σ_{11} on the undeformed structure are presented in Figures 6.18 and 6.19. For this analysis, quadratic elements are used with a discretization leading to 256 elements either on single scale or as sum of all microscopic problems within the MIEL method. In each figure, the plots for single scale and MIEL simulations with 1, 4 and 16 macroscopic elements are arranged from left to right.

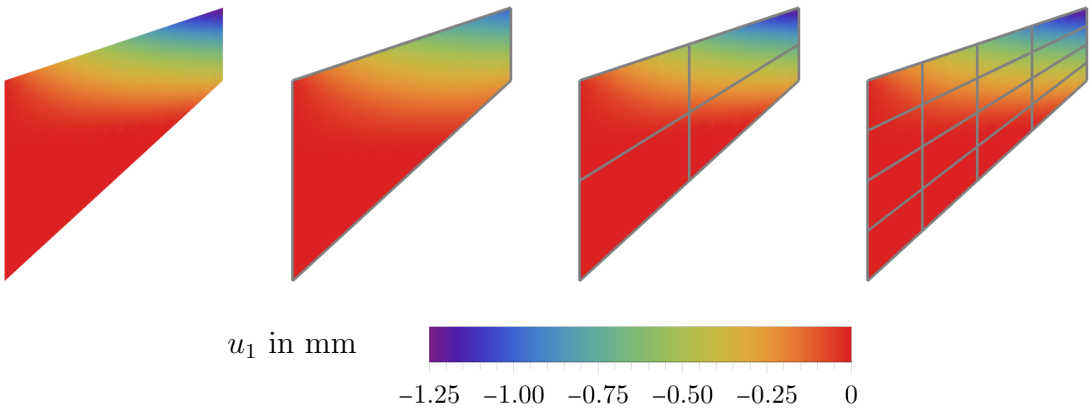

Figure 6.18: Cook's membrane: u_1 for single scale with $n_e = 256$ and for MIEL with $n_{\mathrm{e}}^{\mathrm{M}} = \{1, 4, 16\}$ and $\sum n_e^{\mathrm{m}} = 256$.

The accordance between the results obtained by the MIEL method and the single scale simulation which is taken as the reference increases with a higher number of macroscopic elements. While the results for a single macroscopic element differ a bit in magnitude, there is no difference apparent for the finest macroscopic discretization. These findings support those from the diagrams discussed before. A more detailed analysis of the convergence of the appearing quantities is given in the next, more complex example.

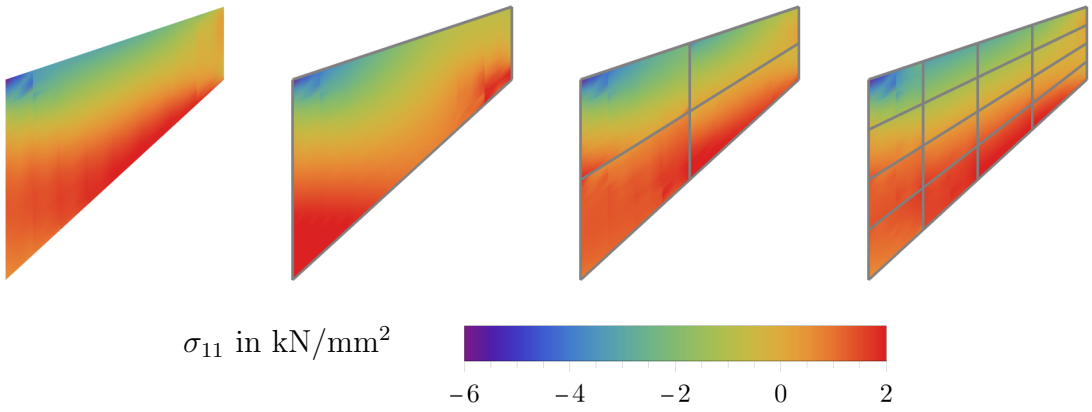

Figure 6.19: Cook's membrane: σ_{11} for single scale with $n_e = 256$ and for MIEL with $n_e^{\mathrm{M}} = \{1, 4, 16\}$ and $\sum n_e^{\mathrm{m}} = 256$.

6.3 Tensile Test

The last numerical example for elasticity deals with a heterogeneous structure including two different materials. The behavior of the MIEL method is compared in terms of the appearing field quantities to a reference single scale computation.

6.3.1 Boundary Value Problem

The specimen has a rectangular shape with a width of $w = 4\,\mathrm{cm}$ and a height of $h = 12\,\mathrm{cm}$ and consists of a matrix material with uniformly distributed elliptic inclusions, as depicted in Figure 6.20.

The body can be divided into identical substructures as squares of edge length 1 cm with a centric elliptic inclusion which is defined by

$$\left(\frac{X_1^*}{a}\right)^2 + \left(\frac{X_2^*}{b}\right)^2 = 1 \tag{6.1}$$

with the half-axes $a = 0.4\,\mathrm{cm}$ and $b = 0.2\,\mathrm{cm}$. The origin of the local X_1^*-X_2^*-coordinate system is located in the center of the square. The elliptic inclusion is rotated by an angle of $\alpha = 45°$ around this origin. The parameters for the material definitions of the matrix and the inclusions are given in Table 6.4.

	E in kN/cm^2	ν
Matrix	1000	0.3
Inclusion	10000	0.3

Table 6.4: Tensile test: Material properties.

The specimen is loaded as a displacement driven tensile test. Dirichlet boundary conditions are applied at the top edge as $\overline{\boldsymbol{u}} = (0, 0.2)^T\mathrm{cm}$ and at the bottom edge as $\overline{\boldsymbol{u}} = (0, -0.2)^T\mathrm{cm}$.

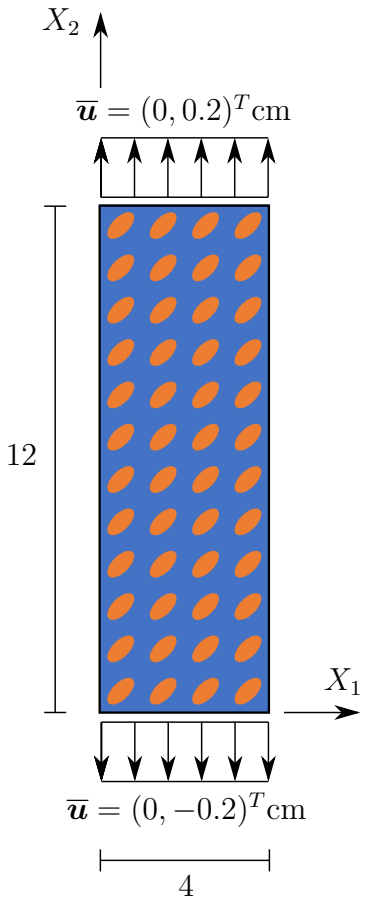

Figure 6.20: Tensile Test: Body and boundary conditions.

6.3.2 Discretization

The boundary value problem is solved with a single scale approach and the MIEL method. To be able to compare the numerical results in a reasonable way, the single scale mesh coincides the assembly of all microscopic meshes within the MIEL method for all computation. To achieve this, the master mesh in Figure 6.21 is introduced which occupies the region of one substructure which has been identified before.

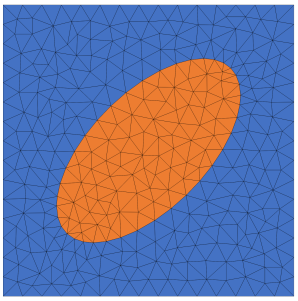

Figure 6.21: Tensile test: Master mesh.

The master mesh consists of 620 quadratic triangular elements (T2). This leads to a total number of 29760 elements if the master mesh is arranged in a 4 times 12 pattern to match the shape of the boundary value problem as required for the single scale analysis. As macroscopic elements for the MIEL method, quadrilateral serendipity elements of

first, second and third order with no internal nodes, namely Q1, Q2S and Q3S elements are investigated. For each element, three different macroscopic meshes are considered, as depicted in Figure 6.22.

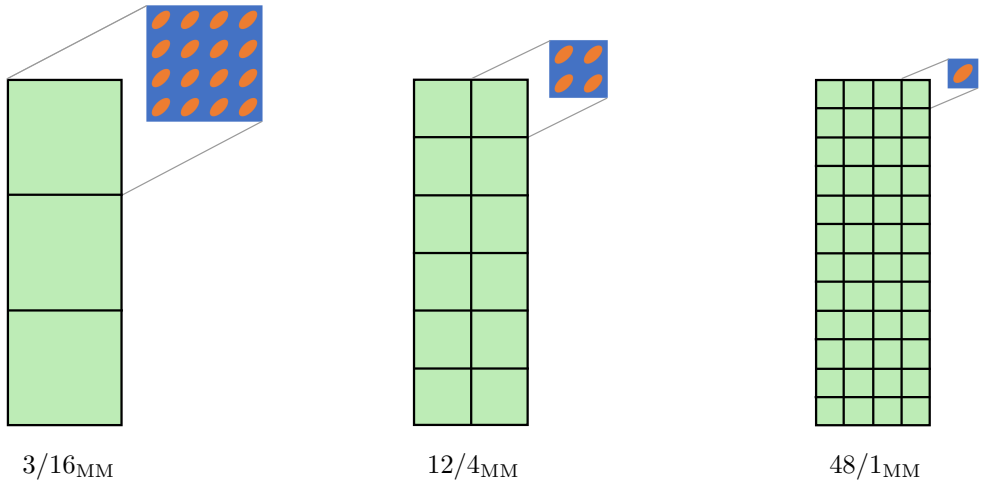

Figure 6.22: Tensile Test: Macroscopic and corresponding microscopic meshes.

The number of master meshes used to define the microscopic problem depends on the size of the corresponding macroscopic element. Therefore, the coarsest mesh $3/16_{\mathrm{MM}}$ with 3 macroscopic elements contains 16 master meshes per microscopic problem. In contrast, the second mesh $12/4_{\mathrm{MM}}$ with 12 macroscopic elements occupy 4 master meshes for each microscopic problem. Consequently, for the finest macroscopic mesh $48/1_{\mathrm{MM}}$ with 48 macroscopic elements, the microscopic problems only contain a single master mesh.

6.3.3 Results

The stress σ_{11} is taken as an exemplary quantity to investigate the convergence behavior with respect to varying macroscopic element formulation and macroscopic mesh densities. For each macroscopic element choice, the contour plot of the single scale computation is presented as reference solution next to those corresponding to the the discretizations $3/16_{\mathrm{MM}}$, $12/4_{\mathrm{MM}}$ and $48/1_{\mathrm{MM}}$. In all contour plots, the deformed structure is shown with a scaling factor of 10 to highlight the differences. The results for linear Q1 macroscopic elements are presented in Figure 6.23.

The deformation of the specimen of the single scale solution differs significantly from those obtained with the MIEL method. While the left and right boundary of the single scale result is corrugated due to the softer matrix around the stiffer inclusions, the MIEL method with linear macroscopic elements is not able to capture this effect. Beyond that, a too coarse macroscopic mesh with linear elements is too restrictive to localize the necking of the specimen in a accurate way. Only the discretization $48/1_{\mathrm{MM}}$ is able to reproduce approximately the outer shape of the single scale solution but without the corrugation. The distributions of the σ_{11}-stress suffer from the restrictions on the deformation. The plots of $3/16_{\mathrm{MM}}$ and $12/4_{\mathrm{MM}}$ are very different to the reference solution. Nevertheless, the characteristics for $48/1_{\mathrm{MM}}$ are in good agreement with the single scale solution besides that the regions of minimal and maximal amplitudes are slightly too large. Figure 6.24 shows the contour plots for the choice of quadratic Q2S macroscopic elements.

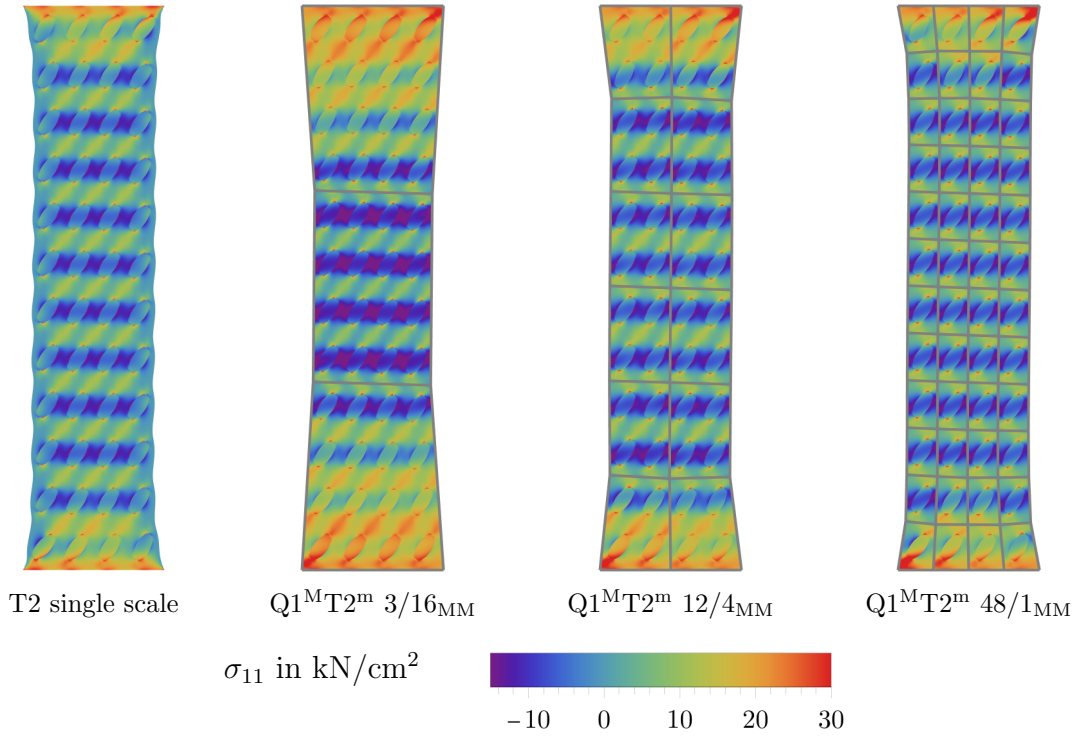

Figure 6.23: Tensile Test: σ_{11} contour plots for T2 single scale and MIEL with $Q1^{M}T2^{m}$.

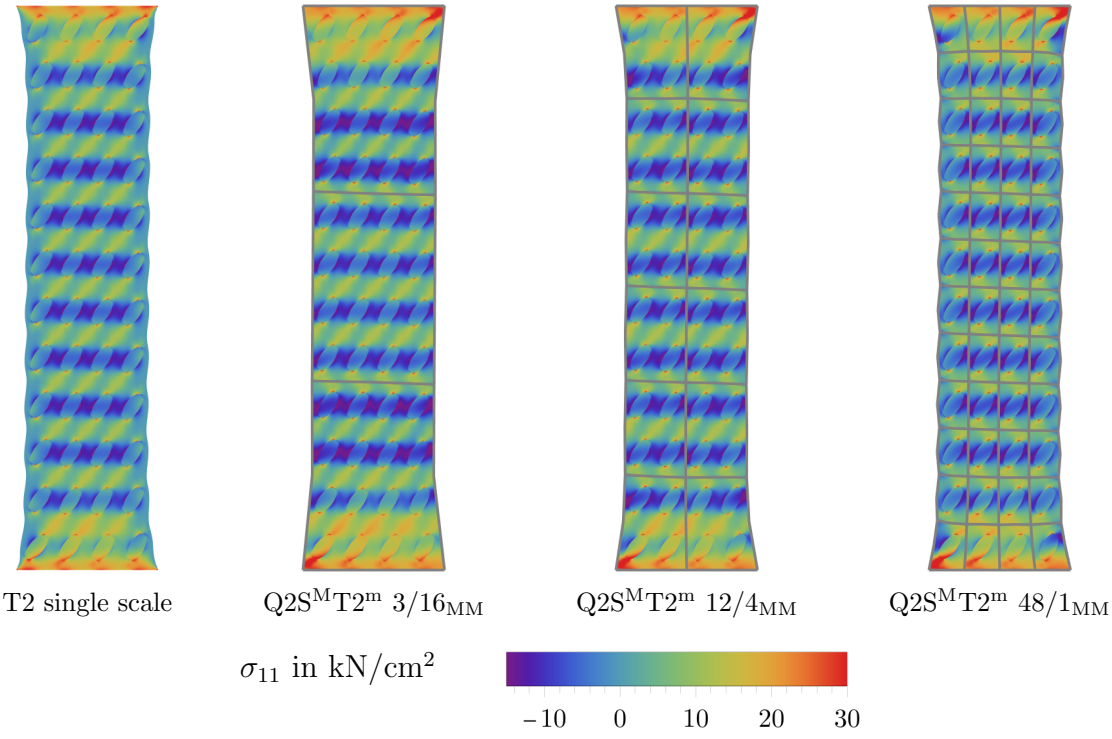

Figure 6.24: Tensile Test: σ_{11} contour plots for T2 single scale and MIEL with $Q2S^{M}T2^{m}$.

In contrast to linear macroscopic elements, the Q2S elements are way more suitable for such boundary value problems. Even the $3/16_{MM}$ discretization can capture the necking effect quite well due to the capability of a quadratic curve for the macroscopic element edge. Additionally, the quadratic interpolation enables the fine macroscopic mesh $48/1_{MM}$

to reproduce a slight corrugation at the left and right edge. As a consequence of the better approximation of the displacement, the stress distributions for $3/16_{\mathrm{MM}}$ with the Q2S element is superior to the Q1 macroscopic element at the corresponding macroscopic mesh density. However, the difference vanishes for the finer macroscopic discretizations in terms of the main characteristics. Only the regions of extrema are slightly smaller for the quadratic interpolation compared to the linear one and therefore closer to the reference solution. Conclusively, the contour plots for the cubic Q3S macroscopic elements are presented in Figure 6.25.

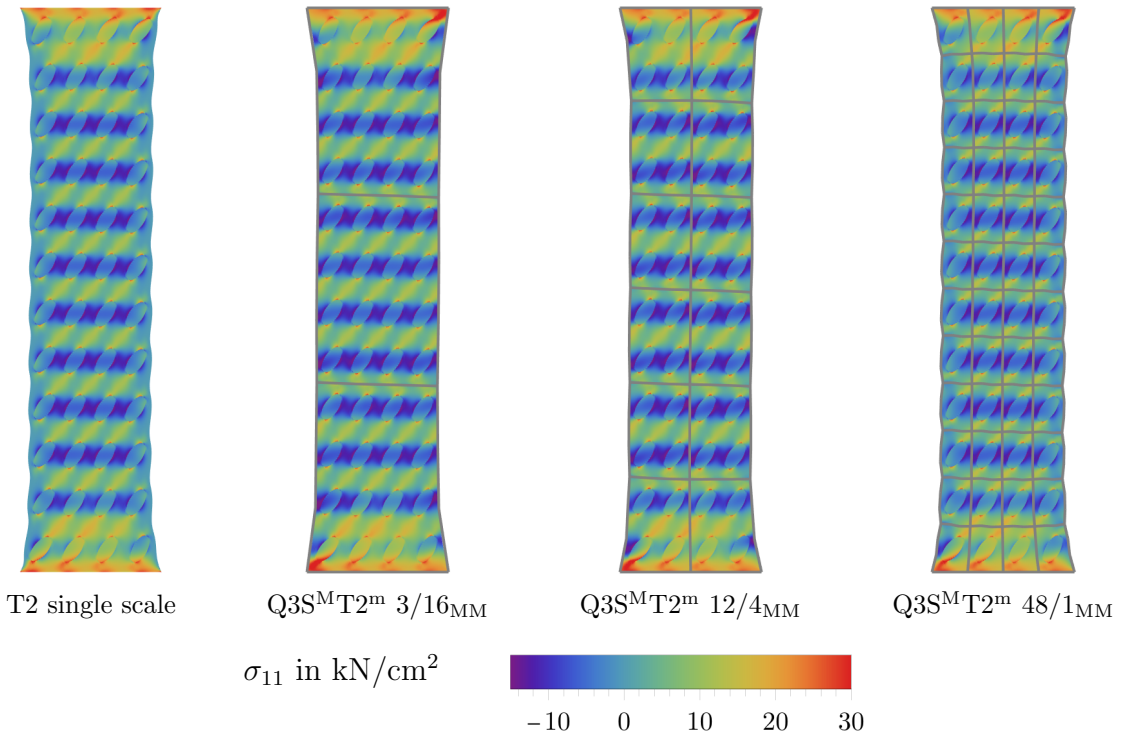

Figure 6.25: Tensile Test: σ_{11} contour plots for T2 single scale and MIEL with Q3S$^{\mathrm{M}}$T2$^{\mathrm{m}}$.

In accordance with the findings above, the cubic interpolation within the macroscopic elements enhance the performance compared to the Q1 and Q2S element. The necking effect is well captured even by the coarsest macroscopic mesh. Therefore, the stress distribution is in good agreement with the reference solution for all MIEL macroscopic mesh densities. Again, the finest mesh stands out due to the capability to capture the corrugation even though the interpolation order of the macroscopic element is still too low to completely match the single scale solution.

In conclusion of the analysis of the contour plots, the linear Q1 macroscopic elements are too restrictive for this boundary value problem. For the quadratic and cubic macroscopic elements, the highest macroscopic mesh density $48/1_{\mathrm{MM}}$ is advantageous to the others in terms of the resulting displacement fields and therefore as well with respect to the stress distribution, even though this effect is hardly visible.

To analyze the effect of the different discretizations on the accuracy of the MIEL method with respect to the reference single scale computation, a regularized norm for exemplary

field quantity $\bullet$ is defined as

$$\frac{||(\bullet)_{\text{single scale}} - (\bullet)_{\text{MIEL}}||}{||(\bullet)_{\text{single scale}}||} = \frac{\sqrt{\int_{\mathcal{B}} \left((\bullet)_{\text{single scale}} - (\bullet)_{\text{MIEL}} \right)^2 \mathrm{d}V}}{\sqrt{\int_{\mathcal{B}} \left((\bullet)_{\text{single scale}} \right)^2 \mathrm{d}V}} \,. \tag{6.2}$$

This value for the quantification of the overall deviation from the reference solution enables an easier analysis than the slight differences appearing in the contour plots. This norm is evaluated for all macroscopic element choices, macroscopic mesh densities and appearing field quantities. The obtained results using Q1 macroscopic elements are shown in Table 6.5.

	$3/16_{\text{MM}}$	$12/4_{\text{MM}}$	$48/1_{\text{MM}}$
u_1 in cm	$3.06 \cdot 10^{-1}$	$1.23 \cdot 10^{-1}$	$6.38 \cdot 10^{-2}$
u_2 in cm	$2.69 \cdot 10^{-2}$	$1.00 \cdot 10^{-2}$	$8.98 \cdot 10^{-3}$
ε_{11}	$3.44 \cdot 10^{-1}$	$2.26 \cdot 10^{-1}$	$2.19 \cdot 10^{-1}$
ε_{22}	$7.52 \cdot 10^{-2}$	$7.46 \cdot 10^{-2}$	$8.93 \cdot 10^{-2}$
ε_{12}	$5.64 \cdot 10^{-1}$	$5.94 \cdot 10^{-1}$	$6.77 \cdot 10^{-1}$
σ_{11} in kN/cm^2	$9.93 \cdot 10^{-1}$	$6.17 \cdot 10^{-1}$	$5.58 \cdot 10^{-1}$
σ_{22} in kN/cm^2	$6.60 \cdot 10^{-2}$	$7.22 \cdot 10^{-2}$	$8.53 \cdot 10^{-2}$
σ_{12} in kN/cm^2	$5.86 \cdot 10^{-1}$	$5.98 \cdot 10^{-1}$	$6.54 \cdot 10^{-1}$

Table 6.5: Tensile test: Regularized norms for Q1 macroscopic elements.

The norms of the displacements reduce with increasing mesh density as expected. The initial value of the u_1 displacement is higher and consequently improves more significantly compared to the 2-direction. This can be explained by the boundary value problem itself because the u_2 displacements deflection is mainly predefined by the boundary conditions. The derived quantities as strains and stresses reveal a slightly different behavior. While the norms for ε_{11} and σ_{11} reduce with finer macroscopic meshes, those for the remaining directions sometimes increase. This effect stays the same for the results in Table 6.6 for the quadratic macroscopic element.

	$3/16_{\text{MM}}$	$12/4_{\text{MM}}$	$48/1_{\text{MM}}$
u_1 in cm	$1.02 \cdot 10^{-1}$	$5.22 \cdot 10^{-2}$	$4.26 \cdot 10^{-2}$
u_2 in cm	$7.14 \cdot 10^{-3}$	$5.14 \cdot 10^{-3}$	$7.27 \cdot 10^{-3}$
ε_{11}	$1.93 \cdot 10^{-1}$	$1.83 \cdot 10^{-1}$	$1.74 \cdot 10^{-1}$
ε_{22}	$5.43 \cdot 10^{-2}$	$6.43 \cdot 10^{-2}$	$8.38 \cdot 10^{-2}$
ε_{12}	$4.59 \cdot 10^{-1}$	$4.84 \cdot 10^{-1}$	$5.56 \cdot 10^{-1}$
σ_{11} in kN/cm^2	$5.40 \cdot 10^{-1}$	$4.85 \cdot 10^{-1}$	$3.97 \cdot 10^{-1}$
σ_{22} in kN/cm^2	$5.20 \cdot 10^{-2}$	$6.14 \cdot 10^{-2}$	$7.37 \cdot 10^{-2}$
σ_{12} in kN/cm^2	$4.62 \cdot 10^{-1}$	$4.67 \cdot 10^{-1}$	$5.25 \cdot 10^{-1}$

Table 6.6: Tensile test: Regularized norms for Q2S macroscopic elements.

Overall, the norms are a little bit lower compared to the linear elements above. As expectable, this tendency proceeds for the results of the cubic macroscopic element in Table 6.7.

	$3/16_{\mathrm{MM}}$	$12/4_{\mathrm{MM}}$	$48/1_{\mathrm{MM}}$
u_1 in cm	$4.61 \cdot 10^{-2}$	$4.20 \cdot 10^{-2}$	$1.33 \cdot 10^{-2}$
u_2 in cm	$3.69 \cdot 10^{-3}$	$5.04 \cdot 10^{-3}$	$1.41 \cdot 10^{-3}$
ε_{11}	$1.62 \cdot 10^{-1}$	$1.73 \cdot 10^{-1}$	$8.79 \cdot 10^{-2}$
ε_{22}	$4.73 \cdot 10^{-2}$	$6.27 \cdot 10^{-2}$	$3.58 \cdot 10^{-2}$
ε_{12}	$3.78 \cdot 10^{-1}$	$4.45 \cdot 10^{-1}$	$2.54 \cdot 10^{-1}$
σ_{11} in kN/cm^2	$4.38 \cdot 10^{-1}$	$4.49 \cdot 10^{-1}$	$1.88 \cdot 10^{-1}$
σ_{22} in kN/cm^2	$4.62 \cdot 10^{-2}$	$5.94 \cdot 10^{-2}$	$2.64 \cdot 10^{-2}$
σ_{12} in kN/cm^2	$3.81 \cdot 10^{-1}$	$4.34 \cdot 10^{-1}$	$2.20 \cdot 10^{-1}$

Table 6.7: Tensile test: Regularized norms for Q3S macroscopic elements.

The improvement from cubic to quadratic macroscopic elements in more significant than from quadratic to linear macroscopic elements. Here, the coarsest macroscopic mesh $3/16_{\mathrm{MM}}$ with Q3S macroscopic elements has an overall lower deviation from the reference solution than the $48/1_{\mathrm{MM}}$ discretization with Q2S macroscopic elements. Analyzing the results for the cubic macroscopic elements in detail, some norms increase from the $3/16_{\mathrm{MM}}$ to the $12/4_{\mathrm{MM}}$ macroscopic mesh density, but get all to their lowest overall value for the finest discretization $48/1_{\mathrm{MM}}$. Summarizing the investigation of the norms, more macroscopic degrees of freedom help to reduce the deviation from the reference solution with some exceptions. The influence of the restrictions on the microscopic problems by the macroscopic element choice and therefore the overall results is dominant for such coarse macroscopic meshes. To obtain a distinctive convergence for all quantities, a different boundary value problem would help which enables a way finer macroscopic mesh and consequently higher numbers of macroscopic degrees of freedom. Nevertheless, the presented investigation is sufficient to suggest the usage of higher order macroscopic elements within the MIEL method to reduce the impact of the comparatively strict scale coupling condition.

7 Numerical Examples - MIEL Method for TPM

After first insights into the MIEL method were gained in Chapter 6, the multiscale approach is applied to the TPM in the following. Three numerical examples are chosen to investigate the behavior and performance. All of them include consolidation which represent an important class of problems within the TPM. The first example starts with a problem of homogeneous material to verify the findings from the previous numerical examples. The second problem extends the first example towards heterogeneous material to gain further insights on the performance for more complex material distributions and is taken to examine a runtime analysis to evaluate numerical efficiency. The concluding third numerical example aims for a more realistic and reasonable application of the method compared to the previous academic problems including a significantly larger number of total equations. Please note that for all numerical examples the notation of the coordinate is simplified to $\boldsymbol{X}$. On the one hand, the TPM model only includes the reference configuration of the control space of the solid phase and on the other hand, there is no need to distinguish between macroscopic and microscopic coordinates within the analysis. In addition, external acceleration is neglected as $\boldsymbol{b} = \boldsymbol{0}$ to allow for an easier interpretation of the method based effects on the solution.

7.1 Homogeneous Consolidation Problem

A typical consolidation problem is chosen as a benchmark for the MIEL method within the framework of the TPM. Focus is on the reproducibility of the insights within the corresponding first examples of pure elasticity in Chapter 6.

7.1.1 Boundary Value Problem

The boundary value problem including the material parameters, which are given in Figure 7.1, is taken from de Boer et al. [1993] and Diebels and Ehlers [1996]. Homogeneous Neumann boundary conditions are applied to any degree of freedom along the boundary unless explicitly specified in the picture.

As already mentioned solving this boundary value problem with a homogeneous material definition does not require a multiscale approach. A comparatively coarse mesh within a single scale finite element computation is the best choice for an sufficiently accurate and efficient solution procedure. Nevertheless it is taken as sanity check for the applicability of the MIEL method within the TPM. All computations are set to finish at $t = 1500\,\mathrm{s}$ where a steady state is reached while the full load is applied within the first time step.

7.1.2 Discretization

A single scale computation with constant time stepping of $\Delta t = 1\,\mathrm{s}$ and a structured mesh consisting of 320 square shaped Q2Q1 elements serves as reference solution. The element abbreviation indicates a quadrilateral element with quadratic shape functions for the solid displacement and linear shape functions for the pressure. For a good comparability of the results, all MIEL computations use the same constant time stepping with $\Delta t = 1\,\mathrm{s}$ and no microscopic sub-stepping. The domain is discretized in a way that the Q2Q1 element formulation is used as microscopic element such that the total number of

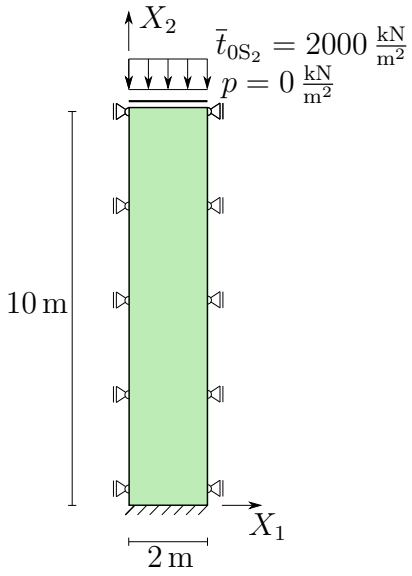

μ^{S}	$5583\ \frac{\text{kN}}{\text{m}^2}$
λ^{S}	$8375\ \frac{\text{kN}}{\text{m}^2}$
$n^{\text{S}}_{0\text{S}}$	0.67
k_{L}	$10^{-5}\ \frac{\text{m}^4}{\text{kN s}}$
ρ^{SR}	$2000\ \frac{\text{kg}}{\text{m}^3}$
ρ^{LR}	$1000\ \frac{\text{kg}}{\text{m}^3}$

Figure 7.1: Homogeneous consolidation: Boundary value problem and material parameters.

microscopic elements matches the 320 elements from the single scale computation. This leads in combination with the requirement of only square shaped macroscopic and microscopic elements to the investigated MIEL mesh densities depicted in Fig. 7.2. The coarsest macroscopic mesh, identified by 5/64, is discretized by $n_e^{\text{M}} = 5$ macroscopic elements where each microscopic problem consists of $n_e^{\text{m}} = 64$ microscopic elements. The same interpretation hold for the remaining two computations 20/16 and 80/4.

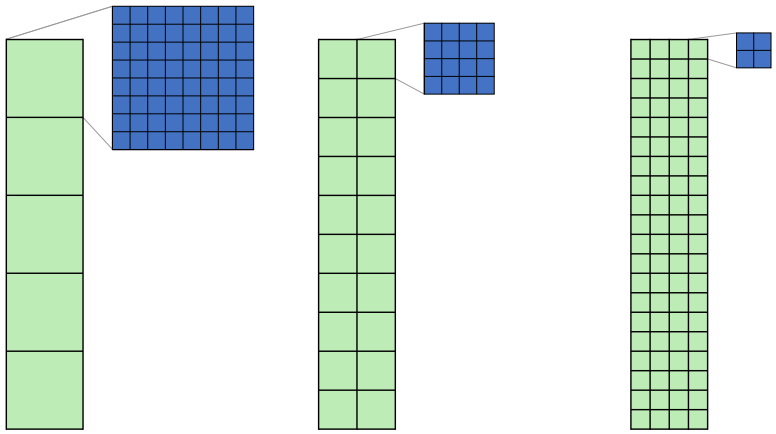

Figure 7.2: Homogeneous consolidation: Investigated mesh densities within MIEL method.

Since it is beneficial within the MIEL method to use macroscopic element formulations which only have nodes on their boundaries, the generalized Taylor-Hood elements Q2SQ1 and Q3SQ2S are considered as macroscopic elements. Therein, the S indicates the usage of serendipity shape functions.

7.1.3 Results

At first, the computation with the coarsest macroscopic mesh combined with the lower order macroscopic element Q2SQ1$^{\mathrm{M}}$ 5/64 is compared to the single scale solution. The evolution of the vertical displacement at the top mid point at $\boldsymbol{X} = (1, 10)\,\mathrm{m}$ and of the pressure at the bottom mid point at $\boldsymbol{X} = (1, 0)\,\mathrm{m}$ over time are depicted in Figure 7.3.

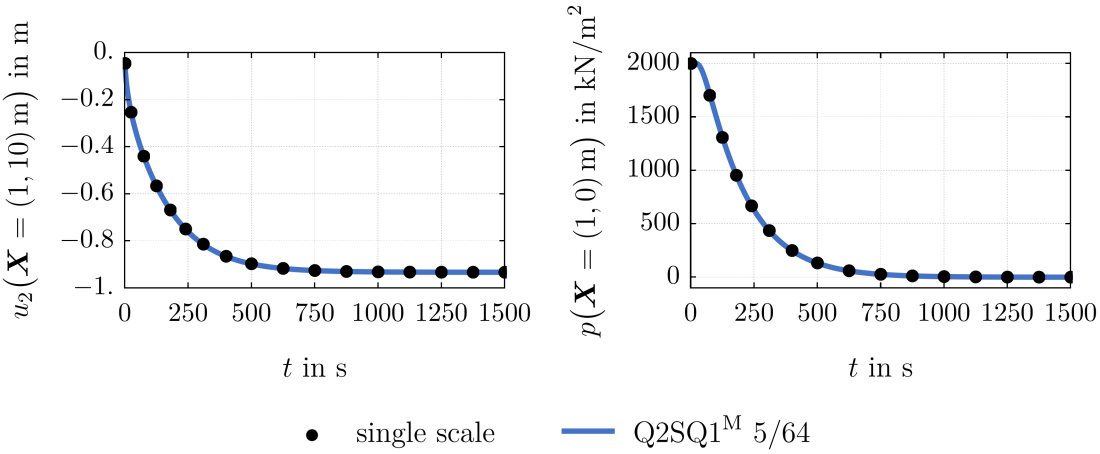

Figure 7.3: Homogeneous consolidation: Top displacement and bottom pressure over time.

The graphs reveal a good agreement of the MIEL method with the single scale computation. This leads to the conclusion that the MIEL method in general is applicable within the framework of the TPM. The graphs corresponding to finer macroscopic discretizations or higher macroscopic element interpolation orders are omitted in this figure since both variations only further improve the agreement.

Nevertheless, a corresponding effect to the the non-physical displacement in 1-direction in Chapter 6 can be observed. It is most apparent after the first time step for this boundary value problem since at this step the pressure gradients are the highest throughout the simulation. This correspondence is discussed in the following. The pressure against the X_2 position is plotted in Figure 7.4 for all MIEL simulations in comparison to the single scale reference solution.

While the pressure is independent from X_1 for the single scale computation, it varies for the MIEL computations, most apparent for coarse macroscopic discretizations. The pressure comparison is carried out along the left boundary at $X_1 = 0\,\mathrm{m}$ and the vertical mid-line at $X_1 = 1\,\mathrm{m}$ where the deviations are most apparent. This effect is due to the constraints on the boundaries of the microscopic problems by the choice of the macroscopic element, in this case a linear or quadratic interpolation of the pressure. While the pressure on the boundary is forced to have a linear, respectively quadratic behavior, it has more freedom to tend towards the reference solution of the single scale computation inside of the microscopic problem. This difference is visible in particular for Q2SQ1$^{\mathrm{M}}$ 5/64 as the coarsest macroscopic mesh in combination with the lower macroscopic interpolation order. Despite that effect, the nonphysical peaks in pressure over $p = 2000\,\mathrm{kN/m^2}$ for the 5/64 meshes are common within the TPM in case of too coarse (macroscopic) discretizations.

Even though the restrictive boundary constraint is an inherent drawback of the MIEL

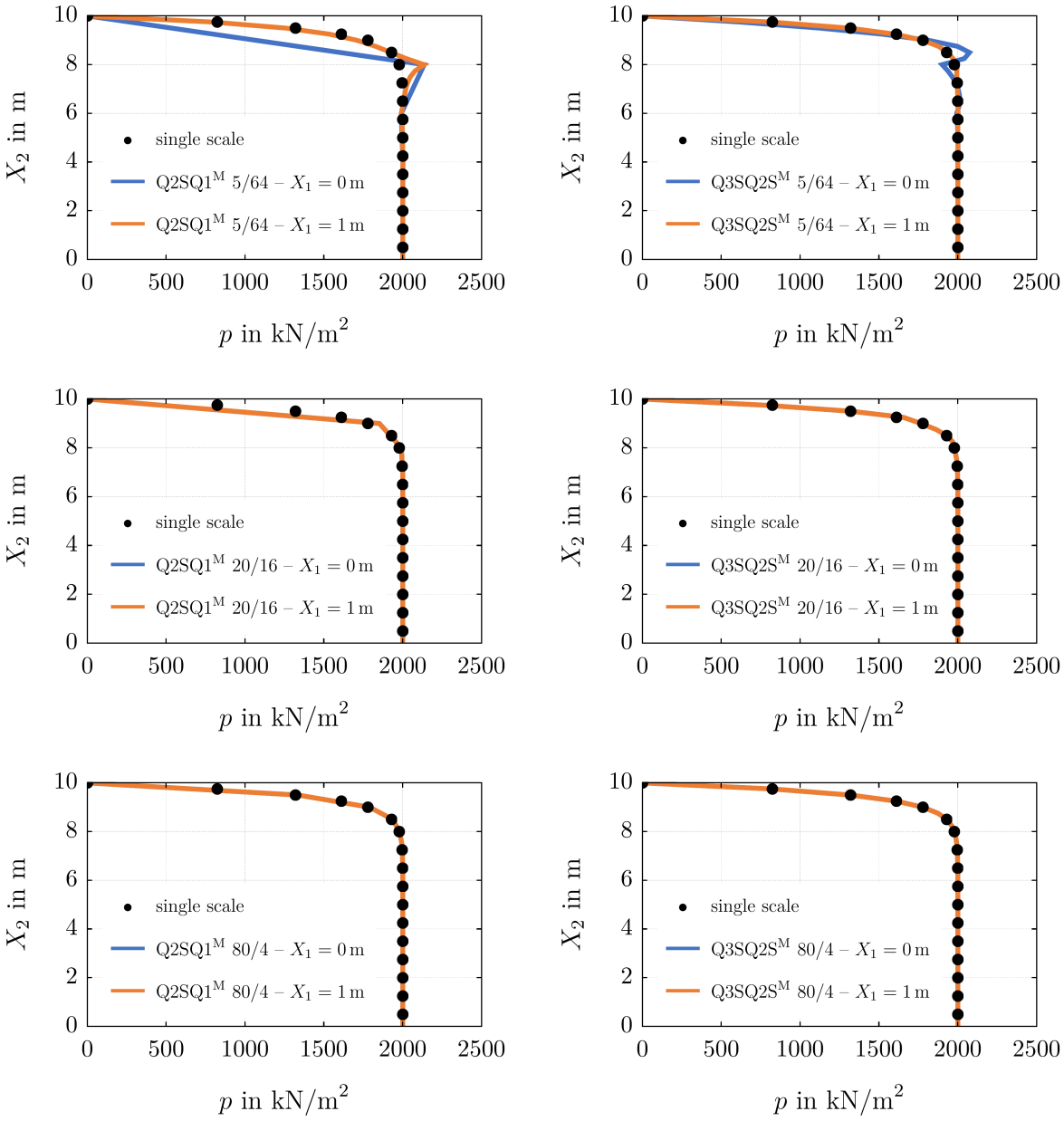

Figure 7.4: Homogeneous consolidation: Pressure against X_2 at $t = 1\,s$.

method within the TPM, it can be well controlled by the two common methods to improve accuracy in finite element methods. Figure 7.4 reveals that increasing the macroscopic mesh density or the macroscopic element interpolation order reduces the impact by great extent. In case of the discretizations 20/16 and 80/4, the pressure distributions appear independent from X_1 within the resolution of the presented graphs. In additions to that, the results of the Q3SQ2S^{M} computations are closer to the single scale reference solution since the boundary constraint is less restrictive.

As a consequence of the deviations of pressure between the boundary and inner points of the microscopic problem, nonphysical u_1 displacements emerge as shown in Figure 7.5, again for $t = 1\,s$.

In accordance with the findings above with respect to the pressure, these displacements

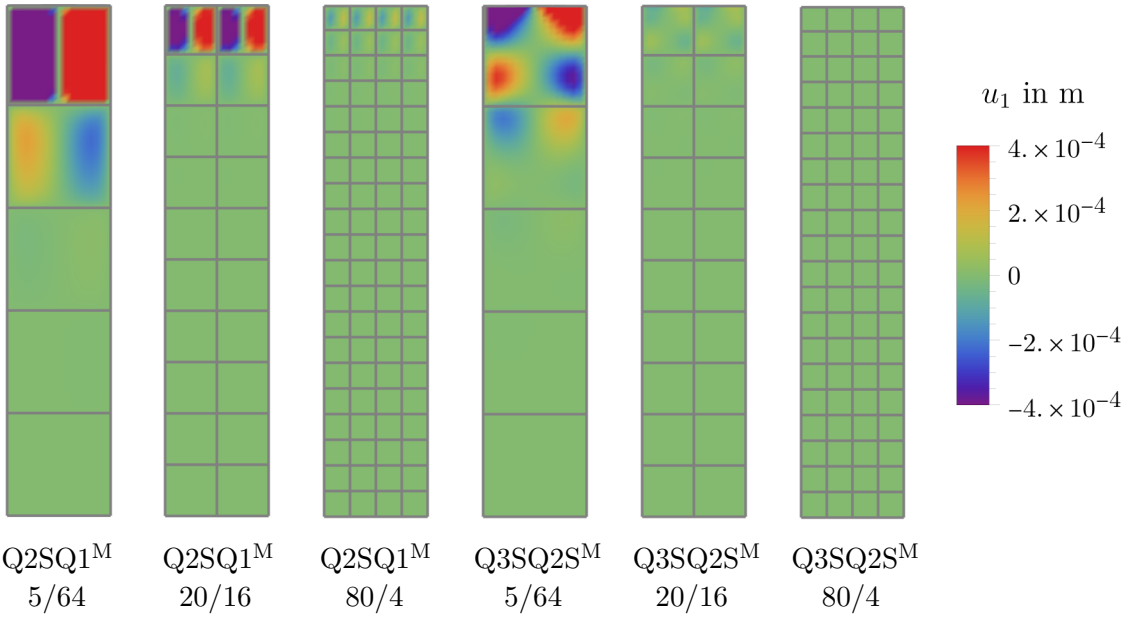

Figure 7.5: Homogeneous consolidation: u_1 at $t = 1\,\mathrm{s}$.

are solely related to the MIEL method since they do not appear for the single scale computation which is reasonable for the chosen nearly one-dimensional boundary value problem. Even though the contour plots only reveal displacements in the upper macroscopic elements, they are existent in the lower elements as well but of much lower magnitude. This is in agreement with Figure 7.4 where the major deviations in pressure for the MIEL computation occur between $X_2 = 6\,\mathrm{m}$ and $X_2 = 10\,\mathrm{m}$. Supplementary to Figure 7.4, Figure 7.5 highlights the major influence of the macroscopic mesh density on the model induced error. The non-physical displacements reduce substantially with an increasing number of macroscopic elements. In addition to that, a higher macroscopic interpolation order at a constant level of macroscopic mesh density improves the result as expected. Please observe that the pattern of the u_1 displacements within one microscopic problem changes from Q2SQ1$^{\mathrm{M}}$ to Q3SQ2S$^{\mathrm{M}}$ due to the increased interpolation order and its consequences on the boundary constraint.

To supports the previous findings, the maximum u_1 displacements and the error e_{u_2} of the vertical displacement of the top mid point for varying MIEL computations with respect to the reference computation are listed in Table 7.1 and Table 7.2. Therein, the error

$$e_{u_2} = \frac{u_2^{\mathrm{MIEL}} - u_2^{\text{single scale}}}{u_2^{\text{single scale}}}$$

is based on the displacement $u_2^{\text{single scale}} = -4.58 \cdot 10^{-2}\,\mathrm{m}$. Both of the error measures are suitable for the chosen discretizations. The u_1 displacements would be zero in the ideal case and the u_2 displacement can not be any more accurate than the single scale result for the chosen set up of a constant number of single scale respectively total number of microscopic problem elements, as shown in Section 6.2 for elasticity.

The analysis of the computation with Q2SQ1 as macroscopic element in Table 7.1 reveals that the increase of macroscopic elements leads to a significant enhancement. But taking into account the results for the Q3SQ2S macroscopic element in Table 7.2, it is apparent that the choice of the macroscopic element interpolation order has an even greater

Table 7.1: Homogeneous consolidation: $\max(u_1)$ and e_{u_2} for Q2SQ1$^{\mathrm{M}}$ at $t = 1\,\mathrm{s}$.

$n_e^{\mathrm{M}}/n_e^{\mathrm{m}}$	5/64	20/16	80/4
$\max(u_1)$ in m	$3.10 \cdot 10^{-3}$	$7.08 \cdot 10^{-4}$	$1.33 \cdot 10^{-4}$
e_{u_2}	$-1.87 \cdot 10^{-1}$	$-8.45 \cdot 10^{-2}$	$-1.93 \cdot 10^{-2}$

Table 7.2: Homogeneous consolidation: $\max(u_1)$ and e_{u_2} for Q3SQ2S$^{\mathrm{M}}$ at $t = 1\,\mathrm{s}$.

$n_e^{\mathrm{M}}/n_e^{\mathrm{m}}$	5/64	20/16	80/4
$\max(u_1)$ in m	$1.01 \cdot 10^{-3}$	$9.39 \cdot 10^{-5}$	$6.98 \cdot 10^{-7}$
e_{u_2}	$-8.18 \cdot 10^{-4}$	$-4.51 \cdot 10^{-3}$	$3.81 \cdot 10^{-6}$

influence on the chosen error measures. The undesired u_1 displacements become nearly negligible compared to the magnitude of the u_2 displacements which again is in good agreement with the reference solution itself. In general, the MIEL computations tend to overestimate the vertical displacement at the top mid point compared to the reference solution. This is in agreement with single scale simulations for coarse meshes and therefore poor pressure interpolations within the presented TPM formulation. Please note that this is contrary to the behavior of the pure elasticity model in Chapter 6.

Based on the results of the present numerical example, the MIEL method is well applicable within the TPM. All findings match those from pure elasticity in the previous chapter. The higher interpolation order of the macroscopic element is the better choice even though its influence on the numerical costs have to be taken into account which is done in the next example. The improvement of a higher mesh density on the microscopic problem is limited by the macroscopic mesh density. On the other hand, the overall accuracy can be enhanced by a finer macroscopic mesh which is in agreement with standard FEM theory.

7.2 Heterogeneous Consolidation Problem

The second numerical example is a modification of the previous consolidation problem to a heterogeneous material distribution. It is taken to investigate the influence of micro-heterogeneities on the performance of the MIEL method and to compare the computational costs with respect to the single scale computation.

7.2.1 Boundary Value Problem

The boundary value problem is defined in Figure 7.1. The previous example is extended by a second material definition which reduces the Darcy parameter by a factor of 100. The initial material definition is taken as matrix material while the modified one models a horizontal elliptical inclusion within a master mesh shown in Figure 7.6.

7.2.2 Discretization

The master mesh consists of 676 triangular Taylor-Hood elements with quadratic displacement and linear pressure interpolation (T2T1). It is arranged in an 8 by 40 grid to model the single scale boundary value problem of the heterogeneous consolidation problem which is taken as reference solution. In total, 320 master meshes lead to 216 320 T2T1

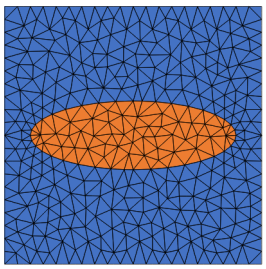

matrix	k_{L}	$10^{-5}\ \frac{\mathrm{m}^4}{\mathrm{kN\,s}}$
inclusion	k_{L}	$10^{-7}\ \frac{\mathrm{m}^4}{\mathrm{kN\,s}}$

Figure 7.6: Heterogeneous consolidation: Master mesh and Darcy parameter.

elements resulting in 974 240 degrees of freedom for the single scale computation. This reference solution is compared to three different MIEL discretizations which are depicted in Figure 7.7. These meshes are designed in a way that the total number of microscopic elements matches the number of single scale elements. This exemplary leads to the MIEL discretization $20/16_{\mathrm{MM}}$ which consists of 20 macroscopic elements while each macroscopic element contains a microscopic problem built by 16 master meshes. Please note that the number of degrees of freedom varies between the MIEL discretizations and the single scale mesh in contrast to the number of elements because of the changing total number of degrees of freedom with Dirichlet boundary conditions depending on the MIEL microscopic problem number and size. All MIEL computations only use Q3SQ2S macroscopic elements as a result of the previous analysis of the homogeneous consolidation problem.

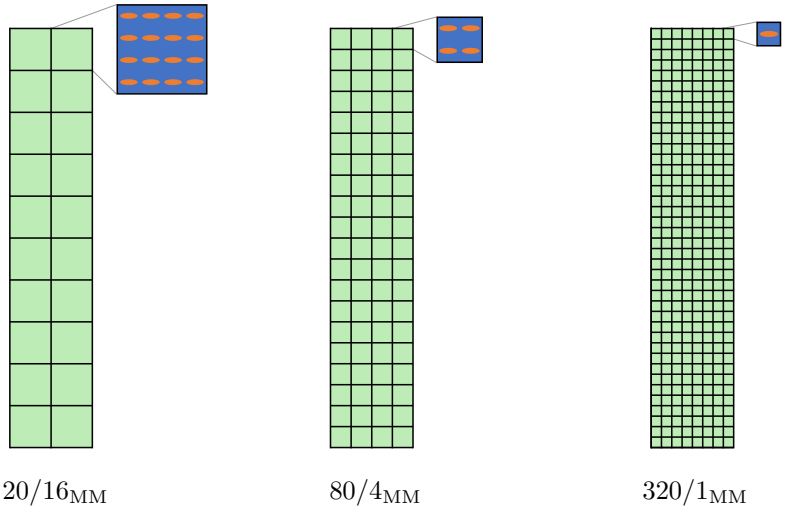

Figure 7.7: Heterogeneous consolidation: Investigated mesh densities within MIEL method.

7.2.3 Results

Due to the resemblance with the previous consolidation problem, a few findings can be exploited during the analysis. At first, the evolution of the vertical displacement u_2 at the top mid point $\boldsymbol{X} = (1, 10)\,\mathrm{m}$ and the pressure p at the bottom mid point $\boldsymbol{X} = (1, 0)\,\mathrm{m}$ during the computation up to $t = 1500\,\mathrm{s}$ are shown in Figure 7.8 for the single scale computation and exemplary the MIEL $\mathrm{Q3SQ2S}^{\mathrm{M}}$ $80/4_{\mathrm{MM}}$ simulation.

Both graphs show a good agreement of the MIEL simulation with its single scale counterpart. The overall diffusion process is slower compared to the homogeneous consolidation

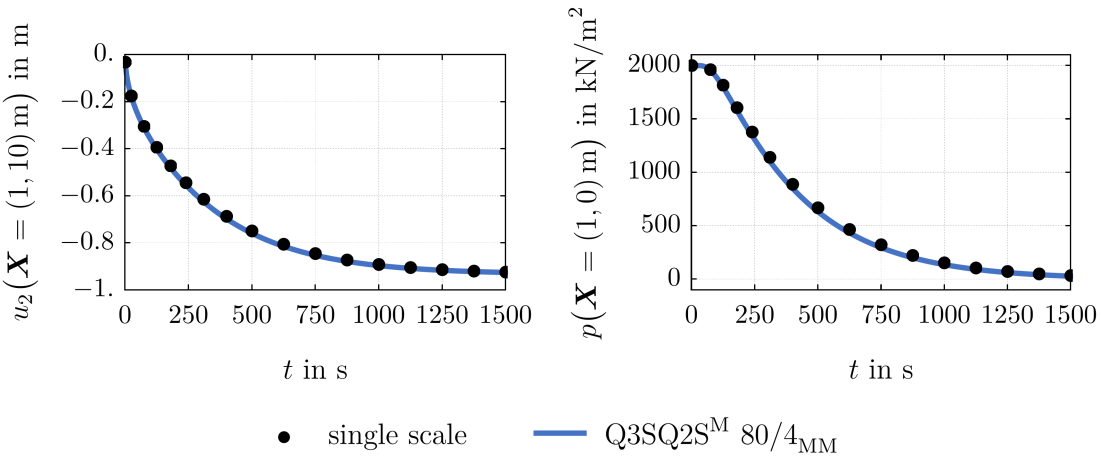

Figure 7.8: Heterogeneous consolidation: Top displacement and bottom pressure over time.

problem in Figure 7.3 which is reasonable due to the less permeable inclusions. Furthermore, the MIEL computation slightly overestimates the bottom pressure relaxation and consequently the vertical top displacement during consolidation in comparison to the single scale solution. This fact corresponds to the findings in the homogeneous consolidation in Tables 7.1 and 7.2 concerning a poor pressure interpolation due to coarse macroscopic meshes. This effect is more pronounced for the heterogeneous structure since the constraint on the degrees of freedom along the microscopic problem boundary is more severe compared to the homogeneous case.

The effect of the boundary constraint on the overall response is further investigated in terms of the vertical specific flux $q_2 = n^{\mathrm{L}} w_{\mathrm{LS}_2}$, exemplary at time $t = 10\,\mathrm{s}$ within the MIEL simulation Q3SQ2S$^{\mathrm{M}}$. For this purpose, three vertical cutting lines throughout the whole specimen with constant X_2 values are defined in Figure 7.9. All cuts run through the second column of macroscopic elements in case of the MIEL simulation.

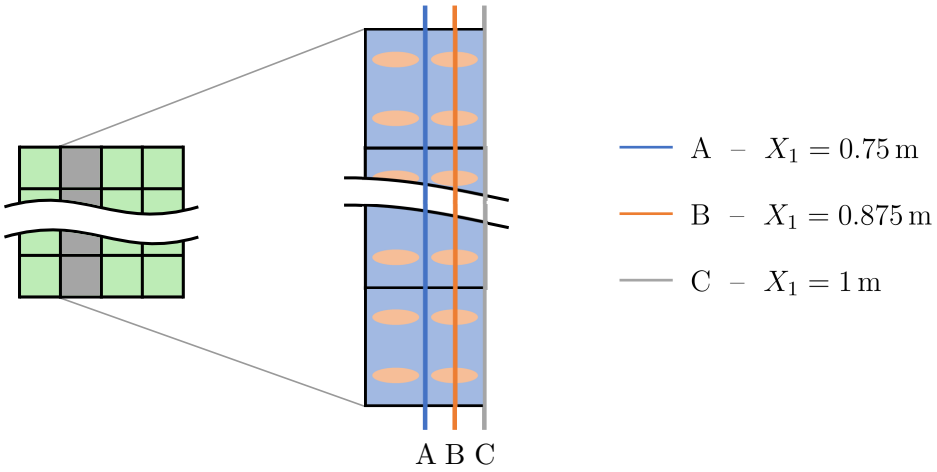

Figure 7.9: Heterogeneous consolidation: Cutting lines for flux investigation.

Cut A runs only through matrix material in the middle of the microscopic problems, cut B passes alternating matrix material and the 40 inclusions over the height and cut C runs again only through matrix material but on the boundaries of the microscopic

problems. The obtained flux distributions for the three cuts are compared for the single scale computation and the MIEL simulation in Figure 7.10.

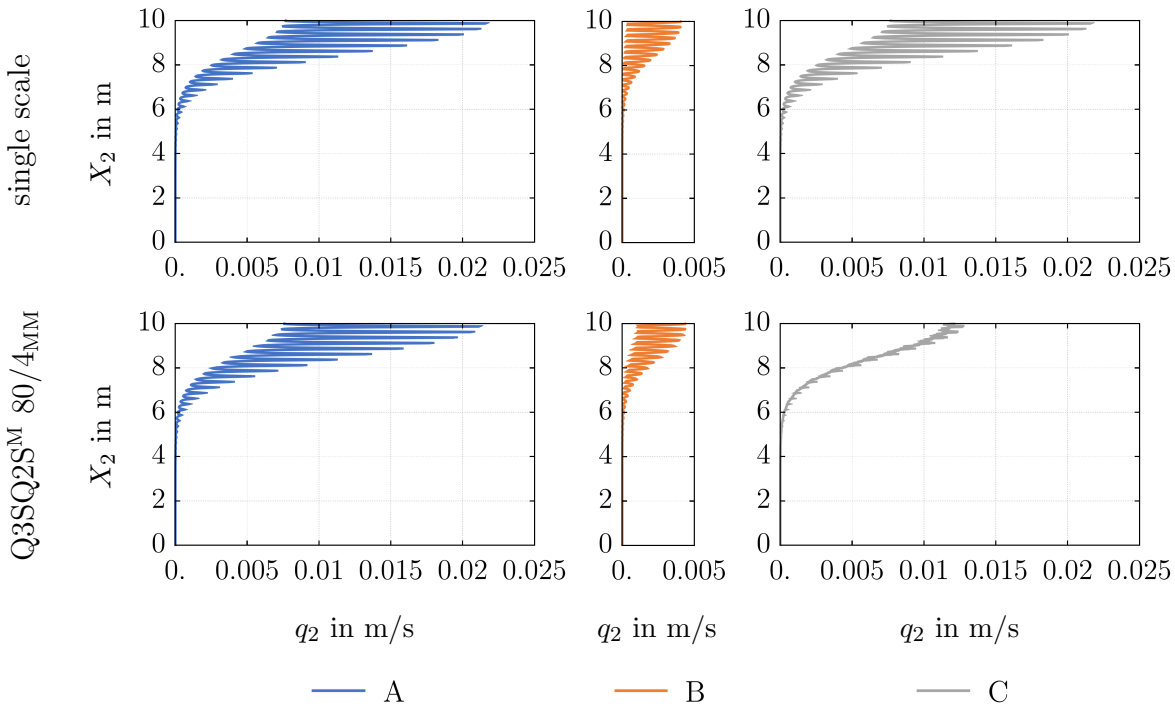

Figure 7.10: Heterogeneous consolidation: Specific flux q_2 against X_2 at $t = 10\,\mathrm{s}$.

The single scale solution reveals the expected result where the flux is oscillating over the height because of the heterogeneities while the flux in general gets greater towards the top since the fluid can exit the control space of the solid there. Additionally, the lower Darcy parameter in the inclusions leads to a smaller flux along the inclusions at cut B resulting in a higher flux along the lines with only matrix material, cut A and C. The MIEL computation is able to capture the described flux distribution of the single scale reference solution well for cut A and cut B where the influence of the boundary constraint on the microscopic problem vanishes. In contrast to this, the flux distribution along cut C is not able to capture the oscillations. All degrees of freedom along cut C belong to boundaries of microscopic problem which are restricted by the respective macroscopic element interpolation. The flux oscillation depend mainly on the underlying pressure gradient which is linear interpolated for the Q3SQ2S macroscopic element. Consequently, the loss of such oscillations due to the microscopic heterogeneities along the boundary of the microscopic problems is a discretization error which is inherent to the MIEL method. This effect introduces another layer of complexity to the choice of macroscopic mesh density. A finer macroscopic mesh enables for a better overall solution but adds more boundary constraints to the numerical model.

One possibility to compensate this drawback is the reduction of computational time utilizing parallelization of the microscopic problems. The presented model boundary value problem with nearly one million degrees of freedom is still solvable with a single scale computation on a single kernel. Nevertheless, the following runtime analysis is a good indicator for larger problems where the single scale approach reaches its limits. For reliable results, all computations have been solved three times and the obtained wall timings are

averaged. To get these results in a reasonable amount of time, only the first ten seconds of each computation are investigated. For the sake of clarity, the duration of pre-processing is excluded for the analysis since it requires about 20% of the full simulation time for the ten second simulation but is negligible with respect to 1500 seconds. Please note that the possibility of multi-threading is omitted in all simulations. The diagram in Figure 7.11 shows the duration of the single scale computation on a single kernel as a reference line. In contrast to this, the computational time required for solving the microscopic problems for the different MIEL discretizations is depicted in dependence of the number of kernels. Computing the solution of the microscopic problems includes distributing the current state of macroscopic element degrees of freedom to their respective microscopic problem, loading the last saved state of the microscopic problems from a file, solving them and returning macroscopic element tangent and residual or saving the current state of the microscopic problem in a file in case of a converged macroscopic step.

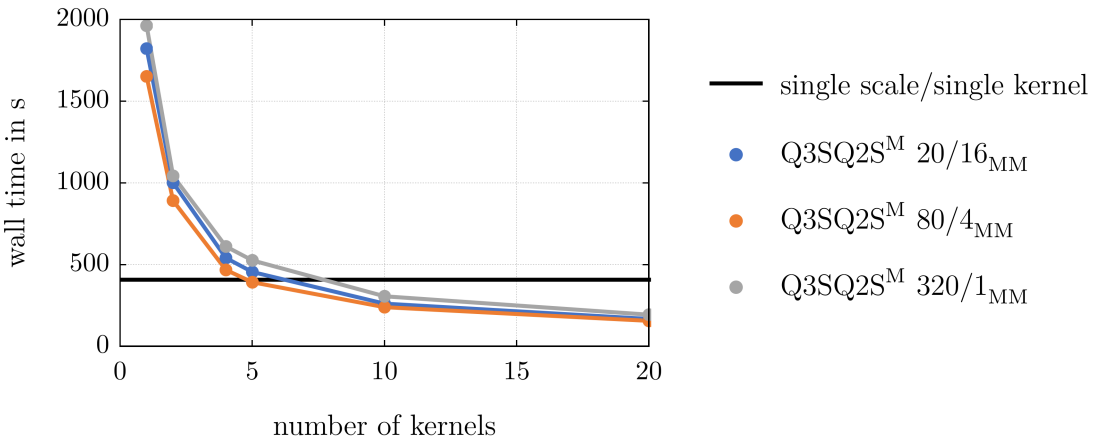

Figure 7.11: Heterogeneous consolidation: Runtimes of parallelized MIEL computations.

The diagram shows that the MIEL method is beneficial for this boundary value problem over the single scale approach if at least five kernels are available. Below this number, the computation time exceeds the reference time of the single scale simulation. In contrast to this, the MIEL method is significantly faster in case of ten kernels or more. Comparing the three MIEL discretizations reveals a slight advantage of the MIEL Q3SQ2S^{M} 80/4$_{MM}$ computation independent from the number of kernels. This discretization has the best ratio of number of microscopic problems and degrees of freedom per microscopic problem. The analysis shows that the available number of kernels is the crucial factor for the total MIEL computation time compared to the number of macroscopic elements. Please note that this interpretation is specific for the chosen discretization where the biggest microscopic problem within MIEL Q3SQ2S^{M} 20/16$_{MM}$ contains only around 50 000 degrees of freedom. Significantly larger microscopic problems respectively number of total microscopic elements would alter this interpretation towards the choice of more macroscopic elements to reduce the microscopic problem size. In general, the MIEL method would benefit within this runtime analysis if the computationally more efficient sensitivity analysis would be employed, as proposed by Zupan and Korelc [2020], in contrast to the current implementation of static condensation with subsequent transformation. Additionally a modified microscopic problem saving and loading strategy based on random access memory rather than the hard disk drive may improve the overall efficiency.

To conclude the analysis of MIEL microscopic problem parallelization, a closer look is taken in Figure 7.12 at the strong scaling of exemplary the discretization MIEL Q3SQ2S$^{\mathrm{M}}$ $80/4_{\mathrm{MM}}$. In both diagrams, the scaling is compared to the ideal one which is constructed by dividing the initial single kernel computation time by the number of kernels. The left diagram shows the scaling of the procedure to solve the microscopic problems as described above. The right one only includes the parallelized part of loading, solving and saving the microscopic problems without the distribution of macroscopic degrees of freedom and returning the microscopic problem responses to the corresponding macroscopic elements.

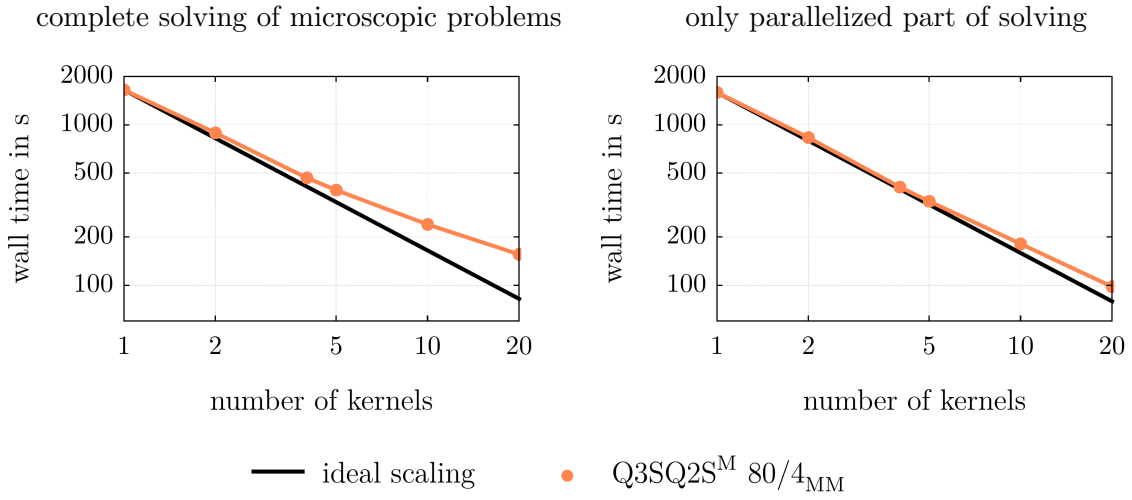

Figure 7.12: Heterogeneous consolidation: Strong scaling analysis for Q3SQ2S$^{\mathrm{M}}$ $80/4_{\mathrm{MM}}$.

The efficiency of the scaling is defined as real computation time divided by the ideal time. With this, the apparent performance loss of the full microscopic problem solution procedure for an increasing number of kernels in the left diagram can be quantified by an efficiency of 53% for 20 kernels. The loss is significantly smaller if only the parallelized part is taken into account in the right diagram of Figure 7.12 leading to an efficiency of 81%. This analysis reveals that around 20% of the theoretical parallelization potential is lost because of the used built in *Mathematica* routines for parallelization and roughly additional 30% due to the required data transfer within the current implementation of the MIEL microscopic problem solution procedure.

Summarizing this numerical example, the kernel parallelization is crucial for the MIEL method to be competitive in terms of overall performance against the single scale approach for problem sizes which are solvable within a single scale computation. For computations with heterogeneous microscopic structures and moderate problem sizes as the presented example, a single scale approach is favorable since there is no information loss due to boundary constraints on the microscopic problems. Additionally, the computation time of each single scale, macroscopic or microscopic problem can be reduced by multi-threading in *Mathematica* if the machine is capable of it. This possibility has been omitted for this analysis but the single scale computation would benefit the most from it. Consequently, the MIEL method aims for total problem sizes a few orders of magnitudes larger than the one in this example.

7.3 Pile Wall

The last numerical example is a MIEL computation where the total number of microscopic problem equations exceeds the reasonable problem size within a classical single scale computation. The problem is designed closer to a realistic application compared to the academic examples before which where used to describe the behavior of the TPM within the MIEL method.

7.3.1 Boundary Value Problem

The investigated situation of consolidation along a pile wall next to a excavation pit is shown on the left in Figure 7.13. The pile wall is supported by two beams to prevent its bending. The surrounding buildings and soils, depicted in light grey, are assumed to be rigid and impermeable to water. This leads to the boundary conditions of the numerical model on the right in Figure 7.13 where only the soil is considered and the deformation of the pile wall is assumed negligibly small. Again, all degrees of freedom along the boundary with no Dirichlet boundary conditions applied and not specifically depicted otherwise in the model, are occupied by homogeneous Neumann boundary conditions.

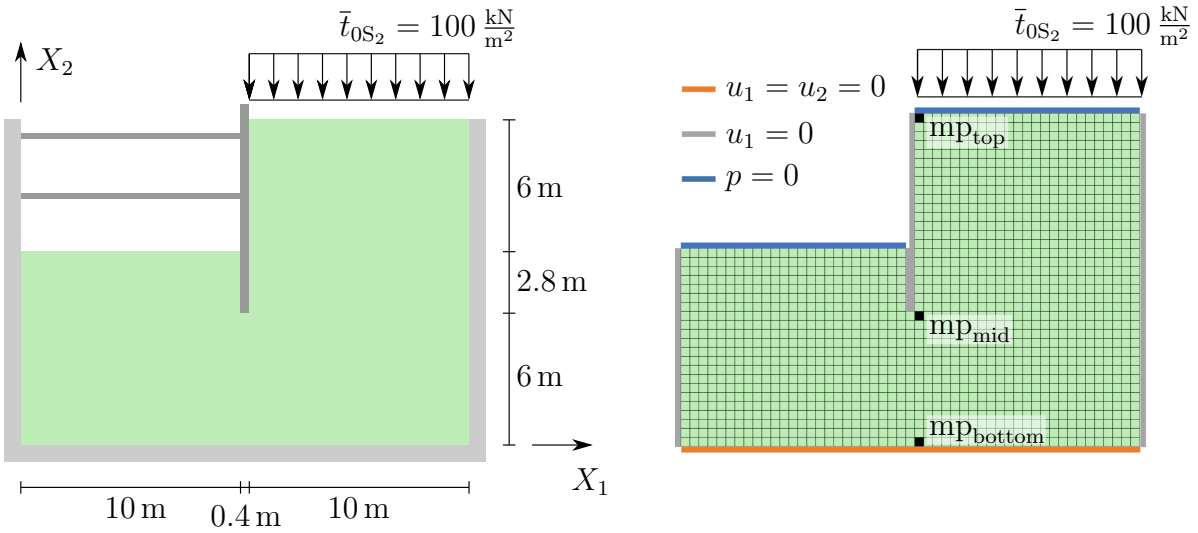

Figure 7.13: Pile wall: Problem (left) and model (right).

The load is applied linear within the first simulated second and the resulting fluid flow and vertical displacement are investigated. Three different types of soil are defined to model the microscopic problems, loamy sand, clay sand and rock. Their material parameters within the binary TPM model are given in Table 7.3.

The percentage of each soil is dependent on the X_2 coordinate within the model, according to Figure 7.14. In detail, the X_2 coordinate of the center of each microscopic problem is taken to identify its distribution. Subsequently, the elements in the structured mesh of each microscopic problem are randomly assigned in agreement with the determined ratios.

Table 7.3: Pile wall: Material definitions.

	loamy sand	clay sand	rock
E^{S} in kN/m^2	$2.5 \cdot 10^4$	$1.25 \cdot 10^4$	$6 \cdot 10^7$
ν^{S}	0.3	0.35	0.2
$n^{\mathrm{S}}_{0\mathrm{S}}$	0.7	0.7	0.99
k_{L} in m^4/kN s	$1 \cdot 10^{-5}$	$1 \cdot 10^{-7}$	$1 \cdot 10^{-12}$
ρ^{SR} in t/m^3	2.3	2.3	2.7
ρ^{LR} in t/m^3	1.0	1.0	1.0

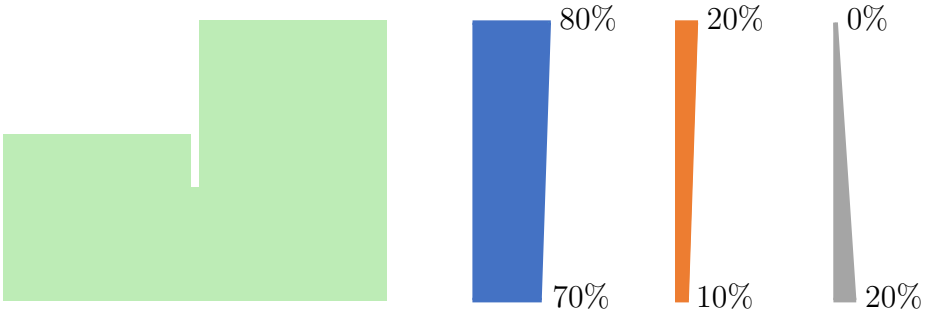

Figure 7.14: Pile wall: Material distribution depending on X_2: loamy sand, clay sand, rock.

7.3.2 Discretization

The domain is meshed by square shaped macroscopic elements of edge length 0.4 m leading to a number of 1490 macroscopic elements respectively microscopic problems. The macroscopic element interpolation is chosen in accordance to the first numerical example within the TPM as Q3SQ2S resulting in a macroscopic problem size of 19457 equations. Each microscopic problem is discretized by 40 by 40 square shaped Q2Q1 elements leading to an initial microscopic element edge length of 1 cm. With this, every microscopic problem consists of 14803 equations which results in a total number of microscopic scale equations of 22 056 470. For comparison, three microscopic problems along the right edge of the pile wall are selected, depicted on the right hand side in Figure 7.13. At first, the one at the top macroscopic element layer, in the following referred to as $\mathrm{mp}_{\mathrm{top}}$, with the center point of the microscopic problem $\boldsymbol{X}_{\mathrm{mpc}} = (10.6, 14.6)\,\mathrm{m}$. Second, the microscopic problem next to the bottom of the pile wall with its center at $\boldsymbol{X}_{\mathrm{mpc}} = (10.6, 5.8)\,\mathrm{m}$ which is labeled as $\mathrm{mp}_{\mathrm{mid}}$. Third, the one at the bottom of the entire domain with the center point $\boldsymbol{X}_{\mathrm{mpc}} = (10.6, 0.2)\,\mathrm{m}$, denoted by $\mathrm{mp}_{\mathrm{bottom}}$. The meshes respectively the material distributions for these microscopic problems are shown in Figure 7.15. Therein, especially the increasing percentage of rock corresponding to an increasing soil depth becomes visible.

To reduce the computational costs, the time incrementation is not constant as in the previous examples. Since the changes within the field quantities are high at the beginning of the consolidation but vanish over time, it is reasonable to increase the size of the time

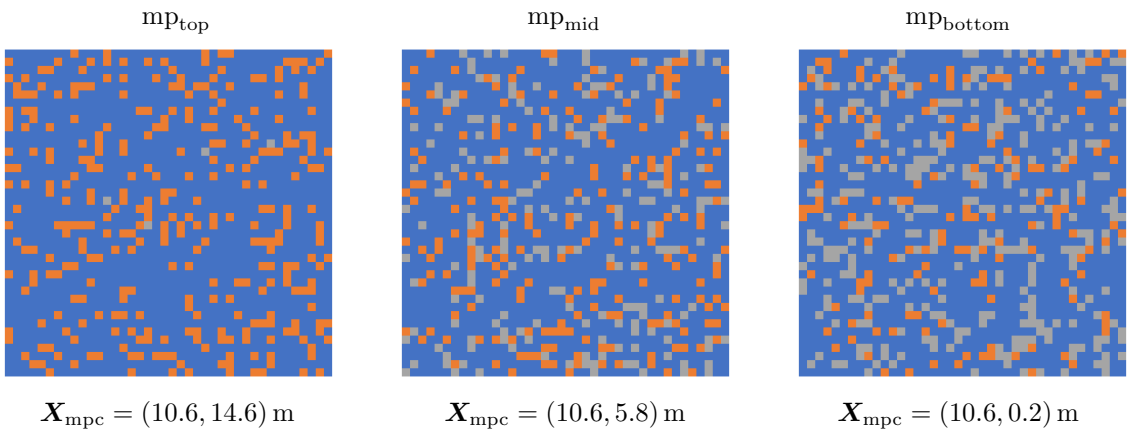

Figure 7.15: Pile wall: Material distributions of chosen microscopic problems.

increment gradually. Here, the first ten time steps with $\Delta t = 0.1\,\mathrm{s}$ are used for the load application. They are followed by 49 steps with $\Delta t = 1\,\mathrm{s}$, 35 steps with $\Delta t = 10\,\mathrm{s}$ and eight steps of $\Delta t = 50\,\mathrm{s}$ leading to a total simulation time of $t = 800\,\mathrm{s}$. No microscopic sub-stepping is applied such that all time steps are identical on macroscopic and microscopic scale.

7.3.3 Results

The simulation was run on 24 kernels leading to a computation time of 7 hours and 14 minutes. This includes saving microscopic problems states 153 470 times and loading them 603 450 times. These numbers indicate that the total number of time steps as well as the microscopic problem loading and saving procedure highly influence the numerical efficiency of the method. As a consequence, future work could aim for a speed-up via an adaptive time incrementation, the utilization of microscopic sub-stepping or a modified microscopic problem saving and loading strategy as mentioned in the previous example.

The vertical displacement over time is shown in Figure 7.16 for three points along the top surface of the soil.

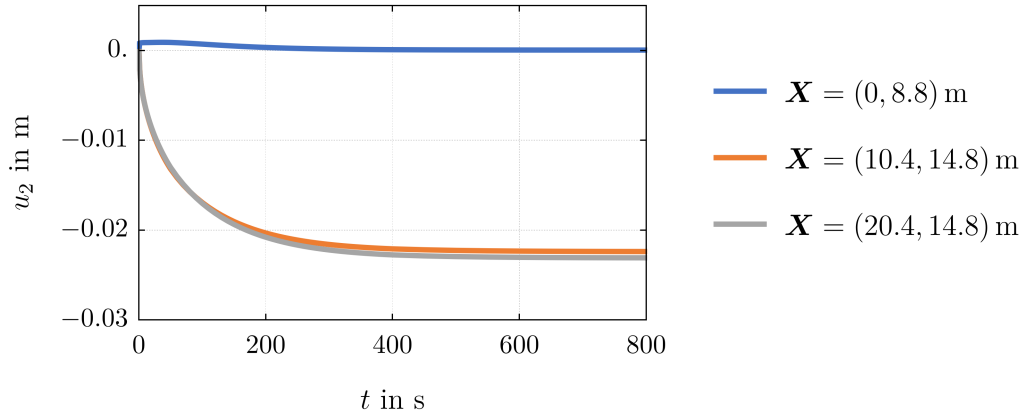

Figure 7.16: Pile wall: Vertical displacement over time at different points.

Two points are within the region of load application. The first one directly at the right

edge of the pile wall at $\boldsymbol{X} = (10.4, 14.8)\,\mathrm{m}$ and the second one at the top right corner of the investigated domain at $\boldsymbol{X} = (20.4, 14.8)\,\mathrm{m}$. Both points show the typical consolidation behavior similar to the findings for the corresponding points in the previous examples. Nevertheless, the final deformation of the point at the pile wall is a little less compared to the outer point. This observation might be unexpected due to the additional drainage possibility below the pile wall but can be explained by the applied TPM model. The approach assumes a continuous solid skeleton such that the neighboring area on the left hand side of the pile wall prevents a larger deformation of the observed point next to the top of the pile wall. The third investigated point is at the top left corner of the domain at $\boldsymbol{X} = (0, 8.8)\,\mathrm{m}$. The graph reveals that even this most distant surface point with respect to the pile wall is lifted in the beginning of the computation due to the liquid which is pressed into the left part of the domain. This effect vanishes over time with decreasing liquid pressure.

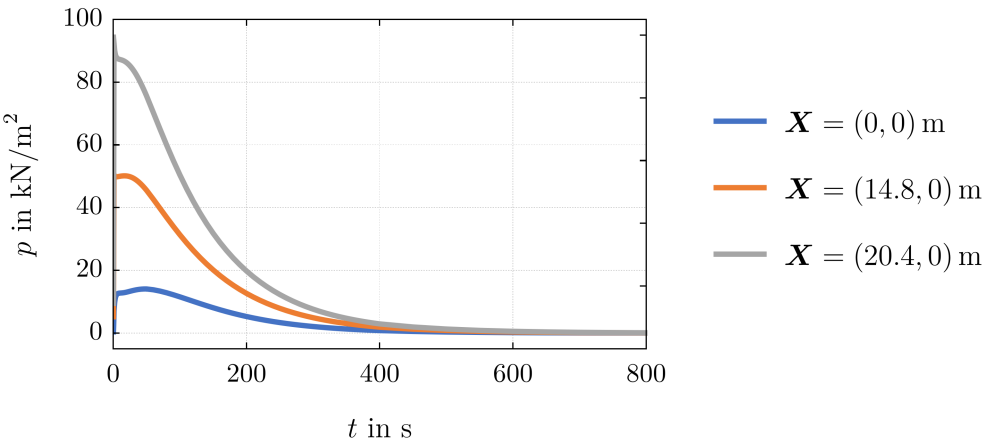

Figure 7.17: Pile wall: Pressure over time at different points.

The pressure is compared for three points as well but at the bottom of the domain over time in Figure 7.17. The graph corresponding to the bottom right point at $\boldsymbol{X} = (20.4, 0)\,\mathrm{m}$ shows a behavior similar to the bottom point within the initial homogeneous consolidation problem in Section 7.1. The magnitude of the pressure nearly matches the applied load at the first time steps before the pressure decreases over time. It converges towards zero respectively steady state. The pressure at $\boldsymbol{X} = (14.8, 0)\,\mathrm{m}$ below the right edge of the pile wall shows a similar behavior but at a much lower magnitude since the liquid can easily move to the left part of the domain in contrast to the situation at the bottom right point. In addition, the maximum pressure is not reached just after applying the full load but minimally after. This effect is visible more pronounced at point $\boldsymbol{X} = (0, 0)\,\mathrm{m}$ at the left bottom corner of the domain. It takes some time until the pressure adjusts in the regions of the domain which are more distant with respect to the load application surface or where the geometry is non-trivial. This observation is supported by the macroscopic specific flux vector plots for three different timings in Figure 7.18. The vectors show the flux direction while the underlying contour plot reveals its magnitude as $\|\boldsymbol{q}\|$ with $\boldsymbol{q} = n^{\mathrm{L}}\,\boldsymbol{w}_{\mathrm{LS}}$. Please note that the plots are based on post-processing data which are evaluated at positions of the macroscopic scale degrees of freedom such that not the full microscopic problem information is utilized.

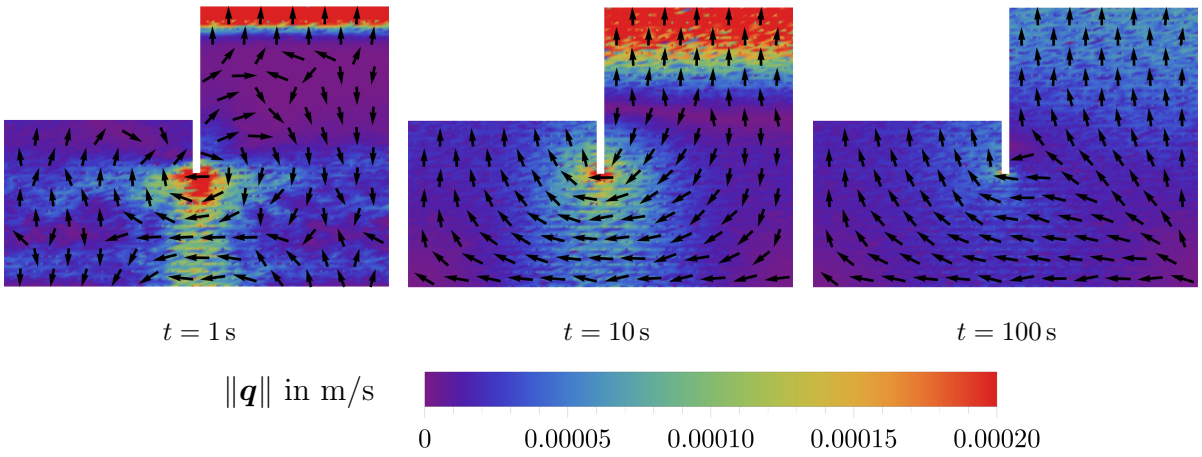

Figure 7.18: Pile wall: Macroscopic flux at different times.

While the vectors seem rather unstructured just after applying the load at $t = 1\,\mathrm{s}$, they appear well orientated at $t = 10\,\mathrm{s}$. Afterwards, the characteristic only changes slightly towards draining the bottom right corner as at $t = 100\,\mathrm{s}$ which stays similar until the end of the computation. The magnitude of the flux is highest at the area of external load application and at the bottom of the pile wall as expected. While the draining is quite local at the top soil layer at $t = 1\,\mathrm{s}$, it expands to lower layers with progressing simulation as visible at $t = 10\,\mathrm{s}$. At the same time, the magnitude decreases and tends in the end against zero respectively steady state. A closer look is taken at the fluxes at the exemplary microscopic problems in Figure 7.15 which are presented for the different timings in Figure 7.19.

The macroscopic effects of higher amplitudes at the top and at the bottom of the pile wall compared to the bottom of the domain as well as the overall decreasing amplitude over time are visible on the microscopic plots as well. Additionally, further insights on the draining process depending on the position of the microscopic problem can be gained. Since the nearly impermeable rock is almost absent at $\mathrm{mp}_{\mathrm{top}}$, the flux can adapt to its preferred direction quite easily. This leads in this case to nearly parallel vertical flux vectors. In contrast to this, the rock percentage is much higher at $\mathrm{mp}_{\mathrm{bottom}}$ including more obstacles for the liquid flow preventing a homogeneous flux through the microscopic problem. As a result, even though the overall flux is clearly orientated in horizontal direction, the flux vectors often vary slightly from the horizontal alignment. The third microscopic problem $\mathrm{mp}_{\mathrm{mid}}$ reveals the most informative plot since the flux just below the pile wall is orientated diagonally and the percentage of less permeable soil induces preferred drainage channels which become visible in the plots. Please observe that the flux orientations are nearly independent from time for the chosen microscopic problems. While slight differences between the timings can be detected for $\mathrm{mp}_{\mathrm{mid}}$, it is very difficult for for the other microscopic problems. But these observations are in agreement with the distributions in Figure 7.18 in terms of nearly steady macroscopic flux orientations near the specific microscopic problems. The analysis is completed by the comparison of the maximum flux amplitudes of macroscopic scale and microscopic problems, given in Table 7.4.

The list justifies the fine resolution of the microstructure since the amplitudes of the field

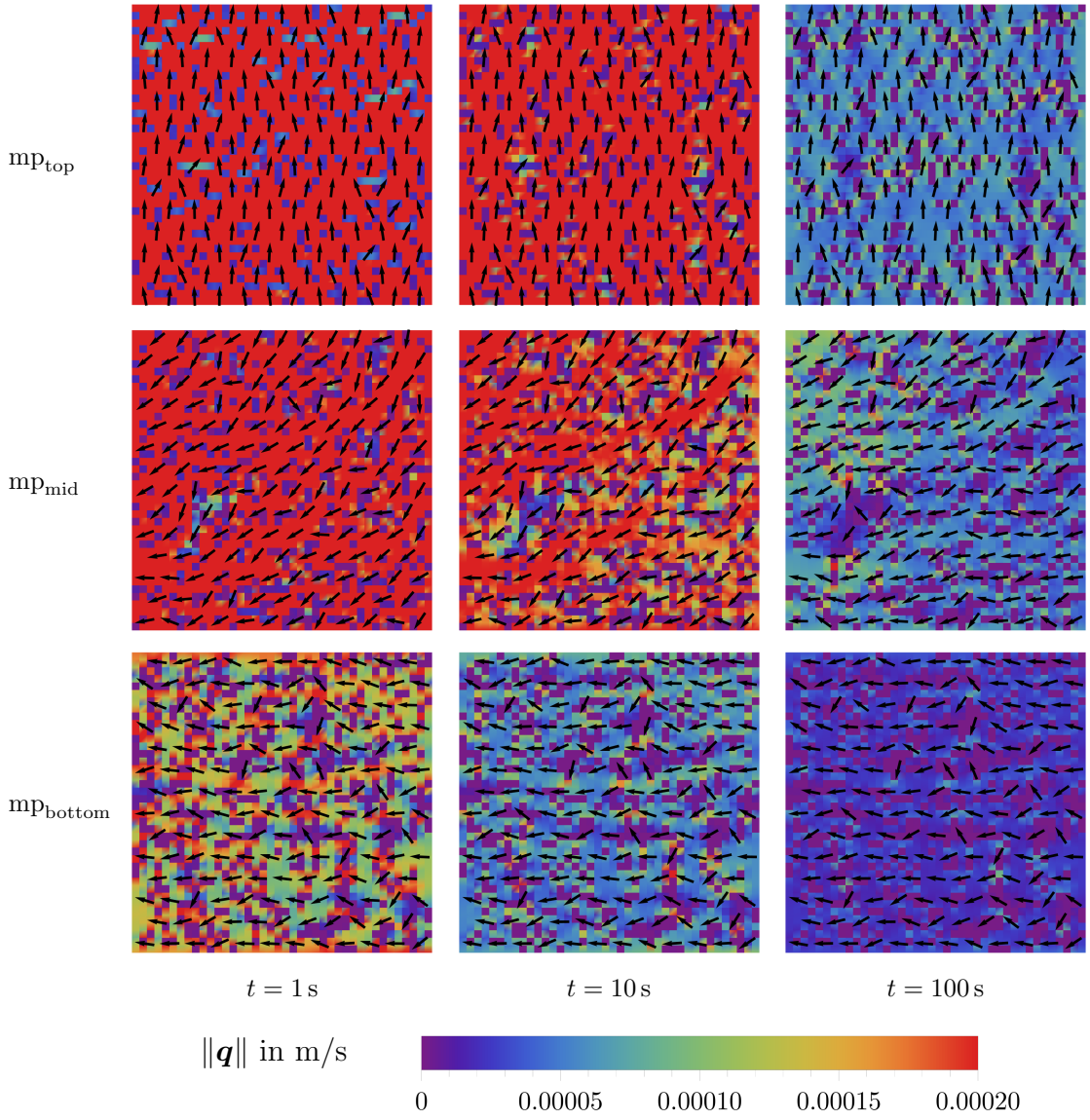

Figure 7.19: Pile wall: Microscopic flux at chosen microscopic problems at different times.

Table 7.4: Pile wall: $\max(\|\boldsymbol{q}\|)$ in m/s for macroscopic scale and chosen microscopic problems at different times.

	$t = 1\,\mathrm{s}$	$t = 10\,\mathrm{s}$	$t = 100\,\mathrm{s}$
macroscopic scale	$2.43 \cdot 10^{-3}$	$5.15 \cdot 10^{-4}$	$1.94 \cdot 10^{-4}$
$\mathrm{mp}_{\mathrm{top}}$	$5.13 \cdot 10^{-3}$	$1.05 \cdot 10^{-3}$	$1.81 \cdot 10^{-4}$
$\mathrm{mp}_{\mathrm{mid}}$	$2.37 \cdot 10^{-3}$	$9.13 \cdot 10^{-4}$	$2.35 \cdot 10^{-4}$
$\mathrm{mp}_{\mathrm{bottom}}$	$5.61 \cdot 10^{-4}$	$2.49 \cdot 10^{-4}$	$9.99 \cdot 10^{-5}$

quantities, here exemplary the magnitude of the flux vector, are in some situations higher on the microscopic problem compared to the macroscopic scale. With this, the MIEL method can exemplary help to resolve localization problems more accurate at reasonable computational costs compare to a classical single scale approach. Summarizing, this simulation gives an impression how the TPM can be combined with the MIEL method to

reduce the complexity of a fine resolved model by exploiting the parallelizability of the microscopic problems.

8 Summary and Outlook

This thesis dealt with the application and validation of the Theory of Porous Media within the framework of the Mesh-in-Element method as a combination of a classical homogenization scheme and a multiscale approach with strong scale coupling. The motivation of this strategy was outlined based on the challenge of exceeding numerical costs in case of the simulation of porous media with complex material heterogeneities. Besides the usefulness of the TPM for such problems, possible choices for additional multiscale schemes were discussed. In this context, approaches with a strong scale coupling appear advantageous since they avoid the discussion on the assumption of scale separation or possible size effects. The MIEL method was chosen over others due to its robust algorithm which only relies on the finite element discretization which makes it applicable to a wide range of problems. The subsequent chapter derived the TPM in a general manner as combination of the Theory of Mixtures and the Concept of Volume Fractions. The focus was set on a binary model consisting of one solid and one liquid phase to keep the complexity of the TPM model as low as possible to enable an undisguised investigation on its combination with the MIEL method. A reformulation was added towards a numerical efficient model before remarks on a single phase model and linear theory concluded this chapter in foresight of the first numerical examples. Subsequently, the Finite Element Method was first derived for finite elasticity before switching to the TPM. This order allowed an easy accessible introduction to the structure and notation within this thesis which differs slightly from the classical derivation such that it fits the MIEL theory. Following this goal, the FEM notation was generalized towards depending solely on degree of freedom vectors respectively its variations and linearization. The chapter was concluded by an overview on finite element formulations which were applied within this thesis. Afterwards, a short detour was taken to investigate the applicability of the FE^2 approach for TPM and body loads in elasticity following the mentioned issue for the assumption of scale separation of such problems within the introduction. The derivation of the lower level boundary conditions within the FE^2 scheme was shown for body loads in elasticity. All typical types of boundary conditions can be derived energetically consistent but exemplary a constant volume load can not trigger any microscopic fluctuation. This finding was interpreted with respect to the TPM within this multiscale approach such that the effect of the microscopic pressure gradient on the microscopic solid displacement could not be captured, supporting choosing of the MIEL method instead. The next chapter presented the theory of the MIEL method within a general notation making it applicable to a variety of problems. Focus was on the scale coupling condition, the resulting scale transition matrix, the extraction of macroscopic element right-hand-side vector and element matrix as well as on the algorithmic treatment. First insights on the characteristics of the MIEL method were gained by the analysis of numerical examples for elasticity. Besides an overall satisfying performance, the importance of the choice of macroscopic discretization became evident. Method induced non-physical effects could be significantly reduced by higher order interpolation functions or finer mesh densities on the macroscopic level. Additionally, higher order macroscopic interpolations softened the comparatively strict scale coupling condition such that the effects of heterogeneities on the microscopic problem were captured significantly better. The numerical examples of the MIEL method for TPM confirmed the findings from elasticity. Displacements and pressures over time within the MIEL method were in good agreement with the single scale reference solutions. Nevertheless, highly oscillating fields due to hetereogeneities were not captured well near microscopic problem

boundaries because of the scale coupling constraint. In contrast to this, incorporation of the parallelizability of the microscopic problem on multiple kernel enabled a considerable speed-up in computation time. Within the last numerical example, the MIEL method was able to solve a problem size above the capabilities of the single scale approach.

In summary, this thesis presented the combination of a homogenization approach with a multiscale scheme. This strategy is beneficial for applications where even after applying the TPM the problem remains too large for a single scale approach due to remaining heterogeneities. The numerical results are promising, even though the scale coupling condition limits the response in case of highly oscillating fields. Finer macroscopic discretizations or higher macroscopic interpolation functions reduce the impact of this microscopic problem boundary constraint condition.

Future research should apply macroscopic element formulations with even more degrees of freedom on their boundaries. This might imply the necessity of a special treatment for interior degrees of freedom of the macroscopic element within the scale transition. Another focus should be further reduction of computational costs. In this scope, time increment adaptivity and exploiting the possibility of microscopic sub-stepping seem promising. Additionally, using sensitivity analysis instead of static condensation and subsequent transformation as proposed in Zupan and Korelc [2020] leads to a speed-up especially for microscopic problems with many degrees of freedom. Further potential exists in a more efficient saving and loading management of the states of the microscopic problem. After these enhancements, the extension of the approach to the three dimensional case and the application of more complex TPM models would be natural further steps. In addition to that, comparing the performance and efficiency between the MIEL method presented in this thesis and the FE^2 method, cf. Ricken et al. [2022], for poroelastic materials would give further valuable insights into the multiscale approaches at hand.

A Details on Finite Element Selection

All element formulations which are used in this thesis are listed in this section. In detail, the topologies are depicted along with the nodal coordinates and the corresponding shape functions.

T1 - Linear Triangular Lagrange Element

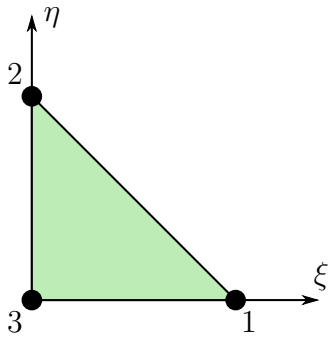

$$\boldsymbol{X}^1_{\mathrm{T1}} = (1,0) \qquad N^1_{\mathrm{T1}} = \xi$$
$$\boldsymbol{X}^2_{\mathrm{T1}} = (0,1) \qquad N^2_{\mathrm{T1}} = \eta$$
$$\boldsymbol{X}^3_{\mathrm{T1}} = (0,0) \qquad N^3_{\mathrm{T1}} = 1-\eta-\xi$$

Q1 - Linear Quadrilateral Lagrange Element

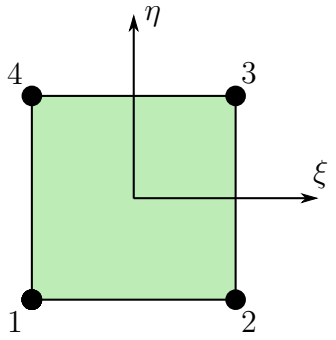

$$\boldsymbol{X}^1_{\mathrm{Q1}} = (-1,-1) \qquad N^1_{\mathrm{Q1}} = \frac{1}{4}(1-\eta)(1-\xi)$$
$$\boldsymbol{X}^2_{\mathrm{Q1}} = (1,-1) \qquad N^2_{\mathrm{Q1}} = \frac{1}{4}(1-\eta)(\xi+1)$$
$$\boldsymbol{X}^3_{\mathrm{Q1}} = (1,1) \qquad N^3_{\mathrm{Q1}} = \frac{1}{4}(\eta+1)(\xi+1)$$
$$\boldsymbol{X}^4_{\mathrm{Q1}} = (-1,1) \qquad N^4_{\mathrm{Q1}} = \frac{1}{4}(\eta+1)(1-\xi)$$

T2 - Quadratic Triangular Lagrange Element

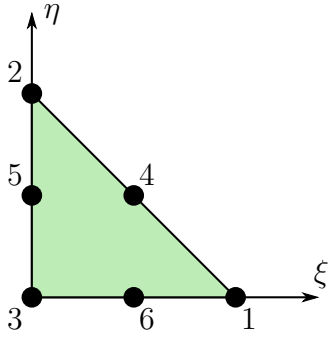

$$\boldsymbol{X}^1_{\mathrm{T2}} = (1,0) \qquad N^1_{\mathrm{T2}} = \xi(2\xi-1)$$
$$\boldsymbol{X}^2_{\mathrm{T2}} = (0,1) \qquad N^2_{\mathrm{T2}} = \eta(2\eta-1)$$
$$\boldsymbol{X}^3_{\mathrm{T2}} = (0,0) \qquad N^3_{\mathrm{T2}} = (\eta+\xi-1)(2\eta+2\xi-1)$$
$$\boldsymbol{X}^4_{\mathrm{T2}} = (\frac{1}{2},\frac{1}{2}) \qquad N^4_{\mathrm{T2}} = 4\eta\xi$$
$$\boldsymbol{X}^5_{\mathrm{T2}} = (0,\frac{1}{2}) \qquad N^5_{\mathrm{T2}} = -4\eta(\eta+\xi-1)$$
$$\boldsymbol{X}^6_{\mathrm{T2}} = (\frac{1}{2},0) \qquad N^6_{\mathrm{T2}} = -4\xi(\eta+\xi-1)$$

Q2 - Quadratic Quadrilateral Lagrange Element

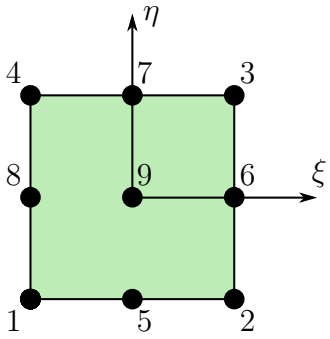

$$\boldsymbol{X}^1_{\mathrm{Q2}} = (-1,-1) \qquad N^1_{\mathrm{Q2}} = \frac{1}{4}(\eta-1)\eta(\xi-1)\xi$$

$$\boldsymbol{X}^2_{\mathrm{Q2}} = (1,-1) \qquad N^2_{\mathrm{Q2}} = \frac{1}{4}(\eta-1)\eta\xi(\xi+1)$$

$$\boldsymbol{X}^3_{\mathrm{Q2}} = (1,1) \qquad N^3_{\mathrm{Q2}} = \frac{1}{4}\eta(\eta+1)\xi(\xi+1)$$

$$\boldsymbol{X}^4_{\mathrm{Q2}} = (-1,1) \qquad N^4_{\mathrm{Q2}} = \frac{1}{4}\eta(\eta+1)(\xi-1)\xi$$

$$\boldsymbol{X}^5_{\mathrm{Q2}} = (0,-1) \qquad N^5_{\mathrm{Q2}} = -\frac{1}{2}(\eta-1)\eta\left(\xi^2-1\right)$$

$$\boldsymbol{X}^6_{\mathrm{Q2}} = (1,0) \qquad N^6_{\mathrm{Q2}} = -\frac{1}{2}\left(\eta^2-1\right)\xi(\xi+1)$$

$$\boldsymbol{X}^7_{\mathrm{Q2}} = (0,1) \qquad N^7_{\mathrm{Q2}} = -\frac{1}{2}\eta(\eta+1)\left(\xi^2-1\right)$$

$$\boldsymbol{X}^8_{\mathrm{Q2}} = (-1,0) \qquad N^8_{\mathrm{Q2}} = -\frac{1}{2}\left(\eta^2-1\right)(\xi-1)\xi$$

$$\boldsymbol{X}^9_{\mathrm{Q2}} = (0,0) \qquad N^9_{\mathrm{Q2}} = \left(\eta^2-1\right)\left(\xi^2-1\right)$$

Q2S - Quadratic Quadrilateral Serendipity Element

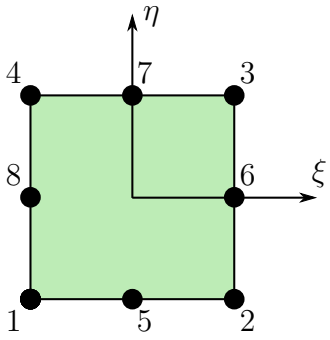

$$\boldsymbol{X}^1_{\mathrm{Q2S}} = (-1,-1) \quad N^1_{\mathrm{Q2S}} = -\frac{1}{4}(\eta-1)(\xi-1)(\eta+\xi+1)$$

$$\boldsymbol{X}^2_{\mathrm{Q2S}} = (1,-1) \quad N^2_{\mathrm{Q2S}} = \frac{1}{4}(\eta-1)(\xi+1)(\eta-\xi+1)$$

$$\boldsymbol{X}^3_{\mathrm{Q2S}} = (1,1) \quad N^3_{\mathrm{Q2S}} = \frac{1}{4}(\eta+1)(\xi+1)(\eta+\xi-1)$$

$$\boldsymbol{X}^4_{\mathrm{Q2S}} = (-1,1) \quad N^4_{\mathrm{Q2S}} = \frac{1}{4}(\xi-1)\left(-\eta^2+\eta\xi+\xi+1\right)$$

$$\boldsymbol{X}^5_{\mathrm{Q2S}} = (0,-1) \quad N^5_{\mathrm{Q2S}} = \frac{1}{2}(\eta-1)\left(\xi^2-1\right)$$

$$\boldsymbol{X}^6_{\mathrm{Q2S}} = (1,0) \quad N^6_{\mathrm{Q2S}} = -\frac{1}{2}\left(\eta^2-1\right)(\xi+1)$$

$$\boldsymbol{X}^7_{\mathrm{Q2S}} = (0,1) \quad N^7_{\mathrm{Q2S}} = -\frac{1}{2}(\eta+1)\left(\xi^2-1\right)$$

$$\boldsymbol{X}^8_{\mathrm{Q2S}} = (-1,0) \quad N^8_{\mathrm{Q2S}} = \frac{1}{2}\left(\eta^2-1\right)(\xi-1)$$

Q3 - Cubic Quadrilateral Lagrange Element

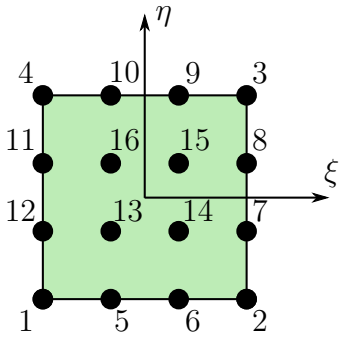

$$\boldsymbol{X}^{1}_{\mathrm{Q3}} = (-1,-1) \qquad N^{1}_{\mathrm{Q3}} = \frac{1}{256}\left(9\eta^3 - 9\eta^2 - \eta + 1\right)\left(9\xi^3 - 9\xi^2 - \xi + 1\right)$$

$$\boldsymbol{X}^{2}_{\mathrm{Q3}} = (1,-1) \qquad N^{2}_{\mathrm{Q3}} = -\frac{1}{256}\left(9\eta^3 - 9\eta^2 - \eta + 1\right)\left(9\xi^3 + 9\xi^2 - \xi - 1\right)$$

$$\boldsymbol{X}^{3}_{\mathrm{Q3}} = (1,1) \qquad N^{3}_{\mathrm{Q3}} = \frac{1}{256}\left(9\eta^3 + 9\eta^2 - \eta - 1\right)\left(9\xi^3 + 9\xi^2 - \xi - 1\right)$$

$$\boldsymbol{X}^{4}_{\mathrm{Q3}} = (-1,1) \qquad N^{4}_{\mathrm{Q3}} = -\frac{1}{256}\left(9\eta^3 + 9\eta^2 - \eta - 1\right)\left(9\xi^3 - 9\xi^2 - \xi + 1\right)$$

$$\boldsymbol{X}^{5}_{\mathrm{Q3}} = (-\frac{1}{3},-1) \qquad N^{5}_{\mathrm{Q3}} = -\frac{9}{256}\left(9\eta^3 - 9\eta^2 - \eta + 1\right)\left(3\xi^3 - \xi^2 - 3\xi + 1\right)$$

$$\boldsymbol{X}^{6}_{\mathrm{Q3}} = (\frac{1}{3},-1) \qquad N^{6}_{\mathrm{Q3}} = \frac{9}{256}\left(9\eta^3 - 9\eta^2 - \eta + 1\right)\left(3\xi^3 + \xi^2 - 3\xi - 1\right)$$

$$\boldsymbol{X}^{7}_{\mathrm{Q3}} = (1,-\frac{1}{3}) \qquad N^{7}_{\mathrm{Q3}} = \frac{9}{256}\left(3\eta^3 - \eta^2 - 3\eta + 1\right)\left(9\xi^3 + 9\xi^2 - \xi - 1\right)$$

$$\boldsymbol{X}^{8}_{\mathrm{Q3}} = (1,\frac{1}{3}) \qquad N^{8}_{\mathrm{Q3}} = -\frac{9}{256}\left(3\eta^3 + \eta^2 - 3\eta - 1\right)\left(9\xi^3 + 9\xi^2 - \xi - 1\right)$$

$$\boldsymbol{X}^{9}_{\mathrm{Q3}} = (\frac{1}{3},1) \qquad N^{9}_{\mathrm{Q3}} = -\frac{9}{256}\left(9\eta^3 + 9\eta^2 - \eta - 1\right)\left(3\xi^3 + \xi^2 - 3\xi - 1\right)$$

$$\boldsymbol{X}^{10}_{\mathrm{Q3}} = (-\frac{1}{3},1) \qquad N^{10}_{\mathrm{Q3}} = \frac{9}{256}\left(9\eta^3 + 9\eta^2 - \eta - 1\right)\left(3\xi^3 - \xi^2 - 3\xi + 1\right)$$

$$\boldsymbol{X}^{11}_{\mathrm{Q3}} = (-1,\frac{1}{3}) \qquad N^{11}_{\mathrm{Q3}} = \frac{9}{256}\left(3\eta^3 + \eta^2 - 3\eta - 1\right)\left(9\xi^3 - 9\xi^2 - \xi + 1\right)$$

$$\boldsymbol{X}^{12}_{\mathrm{Q3}} = (-1,-\frac{1}{3}) \qquad N^{12}_{\mathrm{Q3}} = -\frac{9}{256}\left(3\eta^3 - \eta^2 - 3\eta + 1\right)\left(9\xi^3 - 9\xi^2 - \xi + 1\right)$$

$$\boldsymbol{X}^{13}_{\mathrm{Q3}} = (-\frac{1}{3},-\frac{1}{3}) \qquad N^{13}_{\mathrm{Q3}} = \frac{81}{256}\left(3\eta^3 - \eta^2 - 3\eta + 1\right)\left(3\xi^3 - \xi^2 - 3\xi + 1\right)$$

$$\boldsymbol{X}^{14}_{\mathrm{Q3}} = (\frac{1}{3},-\frac{1}{3}) \qquad N^{14}_{\mathrm{Q3}} = -\frac{81}{256}\left(3\eta^3 - \eta^2 - 3\eta + 1\right)\left(3\xi^3 + \xi^2 - 3\xi - 1\right)$$

$$\boldsymbol{X}^{15}_{\mathrm{Q3}} = (\frac{1}{3},\frac{1}{3}) \qquad N^{15}_{\mathrm{Q3}} = \frac{81}{256}\left(3\eta^3 + \eta^2 - 3\eta - 1\right)\left(3\xi^3 + \xi^2 - 3\xi - 1\right)$$

$$\boldsymbol{X}^{16}_{\mathrm{Q3}} = (-\frac{1}{3},\frac{1}{3}) \qquad N^{16}_{\mathrm{Q3}} = -\frac{81}{256}\left(3\eta^3 + \eta^2 - 3\eta - 1\right)\left(3\xi^3 - \xi^2 - 3\xi + 1\right)$$

Q3S - Cubic Quadrilateral Serendipity Element

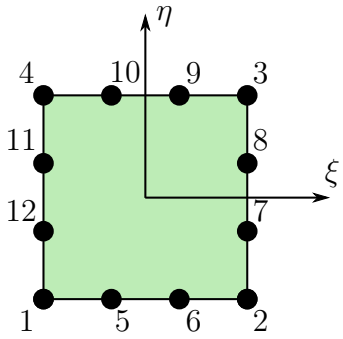

$$\boldsymbol{X}^{1}_{\mathrm{Q3S}} = (-1,-1) \qquad N^{1}_{\mathrm{Q3S}} = \frac{1}{32}(\eta-1)(\xi-1)\left(9\eta^2+9\xi^2-10\right)$$

$$\boldsymbol{X}^{2}_{\mathrm{Q3S}} = (1,-1) \qquad N^{2}_{\mathrm{Q3S}} = -\frac{1}{32}(\eta-1)(\xi+1)\left(9\eta^2+9\xi^2-10\right)$$

$$\boldsymbol{X}^{3}_{\mathrm{Q3S}} = (1,1) \qquad N^{3}_{\mathrm{Q3S}} = \frac{1}{32}(\eta+1)(\xi+1)\left(9\eta^2+9\xi^2-10\right)$$

$$\boldsymbol{X}^{4}_{\mathrm{Q3S}} = (-1,1) \qquad N^{4}_{\mathrm{Q3S}} = -\frac{1}{32}(\eta+1)(\xi-1)\left(9\eta^2+9\xi^2-10\right)$$

$$\boldsymbol{X}^{5}_{\mathrm{Q3S}} = (-\frac{1}{3},-1) \qquad N^{5}_{\mathrm{Q3S}} = -\frac{9}{32}(\eta-1)\left(3\xi^3-\xi^2-3\xi+1\right)$$

$$\boldsymbol{X}^{6}_{\mathrm{Q3S}} = (\frac{1}{3},-1) \qquad N^{6}_{\mathrm{Q3S}} = \frac{9}{32}(\eta-1)\left(3\xi^3+\xi^2-3\xi-1\right)$$

$$\boldsymbol{X}^{7}_{\mathrm{Q3S}} = (1,-\frac{1}{3}) \qquad N^{7}_{\mathrm{Q3S}} = \frac{9}{32}\left(3\eta^3-\eta^2-3\eta+1\right)(\xi+1)$$

$$\boldsymbol{X}^{8}_{\mathrm{Q3S}} = (1,\frac{1}{3}) \qquad N^{8}_{\mathrm{Q3S}} = -\frac{9}{32}\left(3\eta^3+\eta^2-3\eta-1\right)(\xi+1)$$

$$\boldsymbol{X}^{9}_{\mathrm{Q3S}} = (\frac{1}{3},1) \qquad N^{9}_{\mathrm{Q3S}} = -\frac{9}{32}(\eta+1)\left(3\xi^3+\xi^2-3\xi-1\right)$$

$$\boldsymbol{X}^{10}_{\mathrm{Q3S}} = (-\frac{1}{3},1) \qquad N^{10}_{\mathrm{Q3S}} = \frac{9}{32}(\eta+1)\left(3\xi^3-\xi^2-3\xi+1\right)$$

$$\boldsymbol{X}^{11}_{\mathrm{Q3S}} = (-1,\frac{1}{3}) \qquad N^{11}_{\mathrm{Q3S}} = \frac{9}{32}\left(3\eta^3+\eta^2-3\eta-1\right)(\xi-1)$$

$$\boldsymbol{X}^{12}_{\mathrm{Q3S}} = (-1,-\frac{1}{3}) \qquad N^{12}_{\mathrm{Q3S}} = -\frac{9}{32}\left(3\eta^3-\eta^2-3\eta+1\right)(\xi-1)$$

Q4 - Quartic Quadrilateral Element

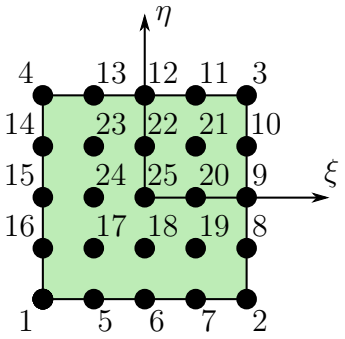

$$\boldsymbol{X}^{1}_{\mathrm{Q4}} = (-1,-1) \qquad N^{1}_{\mathrm{Q4}} = \frac{1}{36}\eta\left(4\eta^3-4\eta^2-\eta+1\right)\xi\left(4\xi^3-4\xi^2-\xi+1\right)$$

$$\boldsymbol{X}^{2}_{\mathrm{Q4}} = (1,-1) \qquad N^{2}_{\mathrm{Q4}} = \frac{1}{36}\eta\left(4\eta^3-4\eta^2-\eta+1\right)\xi\left(4\xi^3+4\xi^2-\xi-1\right)$$

$$\boldsymbol{X}^{3}_{\mathrm{Q4}} = (1,1) \qquad N^{3}_{\mathrm{Q4}} = \frac{1}{36}\eta\left(4\eta^3+4\eta^2-\eta-1\right)\xi\left(4\xi^3+4\xi^2-\xi-1\right)$$

$$\boldsymbol{X}^{4}_{\mathrm{Q4}} = (-1,1) \qquad N^{4}_{\mathrm{Q4}} = \frac{1}{36}\eta\left(4\eta^3+4\eta^2-\eta-1\right)\xi\left(4\xi^3-4\xi^2-\xi+1\right)$$

$$\boldsymbol{X}^{5}_{\mathrm{Q4}} = (-\frac{1}{2},-1) \qquad N^{5}_{\mathrm{Q4}} = -\frac{2}{9}\eta\left(4\eta^3-4\eta^2-\eta+1\right)\xi\left(2\xi^3-\xi^2-2\xi+1\right)$$

$$\boldsymbol{X}^{6}_{\mathrm{Q4}} = (0,-1) \qquad N^{6}_{\mathrm{Q4}} = \frac{1}{6}\eta\left(4\eta^3-4\eta^2-\eta+1\right)\left(4\xi^4-5\xi^2+1\right)$$

$$\boldsymbol{X}^{7}_{\mathrm{Q4}} = (\frac{1}{2},-1) \qquad N^{7}_{\mathrm{Q4}} = -\frac{2}{9}\eta\left(4\eta^3-4\eta^2-\eta+1\right)\xi\left(2\xi^3+\xi^2-2\xi-1\right)$$

$$\boldsymbol{X}^{8}_{\mathrm{Q4}} = (1,-\frac{1}{2}) \qquad N^{8}_{\mathrm{Q4}} = -\frac{2}{9}\eta\left(2\eta^3-\eta^2-2\eta+1\right)\xi\left(4\xi^3+4\xi^2-\xi-1\right)$$

$$\boldsymbol{X}^{9}_{\mathrm{Q4}} = (1,0) \qquad N^{9}_{\mathrm{Q4}} = \frac{1}{6}\left(4\eta^4-5\eta^2+1\right)\xi\left(4\xi^3+4\xi^2-\xi-1\right)$$

$$\boldsymbol{X}^{10}_{\mathrm{Q4}} = (1,\frac{1}{2}) \qquad N^{10}_{\mathrm{Q4}} = -\frac{2}{9}\eta\left(2\eta^3+\eta^2-2\eta-1\right)\xi\left(4\xi^3+4\xi^2-\xi-1\right)$$

$$\boldsymbol{X}^{11}_{\mathrm{Q4}} = (\frac{1}{2},1) \qquad N^{11}_{\mathrm{Q4}} = -\frac{2}{9}\eta\left(4\eta^3+4\eta^2-\eta-1\right)\xi\left(2\xi^3+\xi^2-2\xi-1\right)$$

$$\boldsymbol{X}^{12}_{\mathrm{Q4}} = (0,1) \qquad N^{12}_{\mathrm{Q4}} = \frac{1}{6}\eta\left(4\eta^3+4\eta^2-\eta-1\right)\left(4\xi^4-5\xi^2+1\right)$$

$$\boldsymbol{X}^{13}_{\mathrm{Q4}} = (-\frac{1}{2},1) \qquad N^{13}_{\mathrm{Q4}} = -\frac{2}{9}\eta\left(4\eta^3+4\eta^2-\eta-1\right)\xi\left(2\xi^3-\xi^2-2\xi+1\right)$$

$$\boldsymbol{X}^{14}_{\mathrm{Q4}} = (-1,\frac{1}{2}) \qquad N^{14}_{\mathrm{Q4}} = -\frac{2}{9}\eta\left(2\eta^3+\eta^2-2\eta-1\right)\xi\left(4\xi^3-4\xi^2-\xi+1\right)$$

$$\boldsymbol{X}^{15}_{\mathrm{Q4}} = (-1,0) \qquad N^{15}_{\mathrm{Q4}} = \frac{1}{6}\left(4\eta^4-5\eta^2+1\right)\xi\left(4\xi^3-4\xi^2-\xi+1\right)$$

$$\boldsymbol{X}^{16}_{\mathrm{Q4}} = (-1,-\frac{1}{2}) \qquad N^{16}_{\mathrm{Q4}} = -\frac{2}{9}\eta\left(2\eta^3-\eta^2-2\eta+1\right)\xi\left(4\xi^3-4\xi^2-\xi+1\right)$$

$$\boldsymbol{X}^{17}_{\mathrm{Q4}} = (-\frac{1}{2},-\frac{1}{2}) \qquad N^{17}_{\mathrm{Q4}} = \frac{16}{9}\eta\left(2\eta^3-\eta^2-2\eta+1\right)\xi\left(2\xi^3-\xi^2-2\xi+1\right)$$

$$\boldsymbol{X}^{18}_{\mathrm{Q4}} = (0,-\frac{1}{2}) \qquad N^{18}_{\mathrm{Q4}} = -\frac{4}{3}\eta\left(2\eta^3-\eta^2-2\eta+1\right)\left(4\xi^4-5\xi^2+1\right)$$

$$\boldsymbol{X}^{19}_{\mathrm{Q4}} = (\frac{1}{2},-\frac{1}{2}) \qquad N^{19}_{\mathrm{Q4}} = \frac{16}{9}\eta\left(2\eta^3-\eta^2-2\eta+1\right)\xi\left(2\xi^3+\xi^2-2\xi-1\right)$$

$$\boldsymbol{X}_{\mathrm{Q4}}^{20} = (\frac{1}{2}, 0) \qquad N_{\mathrm{Q4}}^{20} = -\frac{4}{3}\left(4\eta^4 - 5\eta^2 + 1\right)\xi\left(2\xi^3 + \xi^2 - 2\xi - 1\right)$$

$$\boldsymbol{X}_{\mathrm{Q4}}^{21} = (\frac{1}{2}, \frac{1}{2}) \qquad N_{\mathrm{Q4}}^{21} = \frac{16}{9}\eta\left(2\eta^3 + \eta^2 - 2\eta - 1\right)\xi\left(2\xi^3 + \xi^2 - 2\xi - 1\right)$$

$$\boldsymbol{X}_{\mathrm{Q4}}^{22} = (0, \frac{1}{2}) \qquad N_{\mathrm{Q4}}^{22} = -\frac{4}{3}\eta\left(2\eta^3 + \eta^2 - 2\eta - 1\right)\left(4\xi^4 - 5\xi^2 + 1\right)$$

$$\boldsymbol{X}_{\mathrm{Q4}}^{23} = (-\frac{1}{2}, \frac{1}{2}) \qquad N_{\mathrm{Q4}}^{23} = \frac{16}{9}\eta\left(2\eta^3 + \eta^2 - 2\eta - 1\right)\xi\left(2\xi^3 - \xi^2 - 2\xi + 1\right)$$

$$\boldsymbol{X}_{\mathrm{Q4}}^{24} = (-\frac{1}{2}, 0) \qquad N_{\mathrm{Q4}}^{24} = -\frac{4}{3}\left(4\eta^4 - 5\eta^2 + 1\right)\xi\left(2\xi^3 - \xi^2 - 2\xi + 1\right)$$

$$\boldsymbol{X}_{\mathrm{Q4}}^{25} = (0, 0) \qquad N_{\mathrm{Q4}}^{25} = \left(4\eta^4 - 5\eta^2 + 1\right)\left(4\xi^4 - 5\xi^2 + 1\right)$$

References

A. Abdulle. On a priori error analysis of fully discrete heterogeneous multiscale FEM. *Multiscale Modeling and Simulation*, 4:447–459, 2005. URL https://doi.org/10.1137/040607137.

K.-J. Bathe. *Finite element procedures*. Prentice Hall, New Jersey, 1996.

A. Bensoussan, J.-L. Lions, and G. Papanocolau. *Asymptotic analysis for periodic structures*. North-Holland, 1978.

F. Bertrand, M. Brodbeck, and T. Ricken. On robust discretization methods for poroelastic problems: Numerical examples and counter-examples. *Examples and Counterexamples*, 2:100087, 2022. URL https://doi.org/10.1016/j.exco.2022.100087.

M. A. Biot. General Theory of Three-Dimensional Consolidation. *Journal of Applied Physics*, 12(2):155–164, 1941. URL https://doi.org/10.1063/1.1712886.

M. A. Biot. Theory of Propagation of Elastic Waves in a Fluid-Saturated Porous Solid. I. Low-Frequency Range. *The Journal of the Acoustical Society of America*, 28(2): 168–178, 1956. URL https://doi.org/10.1121/1.1908239.

J. Bluhm. Modelling of saturated thermo-elastic porous solids with different phase temperatures. In W. Ehlers and J. Bluhm, editors, *Porous media*, pages 87–118. Springer, 2002. URL https://doi.org/10.1007/978-3-662-04999-0_2.

D. Boffi, F. Brezzi, and M. Fortin. *Mixed Finite Element Methods and Applications*. Springer, Heidelberg, 2013. URL https://doi.org/10.1007/978-3-642-36519-5.

R. M. Bowen. Part I - Theory of Mixtures. In A. C. Eringen, editor, *Continuum Physics*, page 1–127. Academic Press, 1976. URL https://doi.org/10.1016/B978-0-12-240803-8.50017-7.

R. M. Bowen. Incompressible porous media models by use of the theory of mixtures. *International Journal of Engineering Science*, 18:1129–1148, 1980. URL https://doi.org/10.1016/0020-7225(80)90114-7.

R. M. Bowen. Compressible porous media models by use of the theory of mixtures. *International Journal of Engineering Science*, 20:697–735, 1982. URL https://doi.org/10.1016/0020-7225(82)90082-9.

B. D. Coleman and W. Noll. The thermodynamics of elastic materials with heat conduction and viscosity. *Archive for Rational Mechanics and Analysis*, 13:167–178, 1963. URL https://doi.org/10.1007/BF01262690.

R. de Boer. *Theory of Porous Media – highlights in the historical development and current state*. Springer, 2000. URL https://doi.org/10.1007/978-3-642-59637-7.

R. de Boer. Trends in continuum mechanics of porous media. In J. Bear, editor, *Theory and applications of transport in porous media*. Springer, 2005.

R. de Boer and W. Ehlers. Theorie der Mehrkomponentenkontinua mit Anwendung auf bodenmechanische Probleme. Forschungsbericht aus dem fachbereich bauwesen 40, Universität - Gesamthochschule - Essen, 1986.

R. de Boer, W. Ehlers, and Z. Liu. One-dimensional transient wave propagation in fluid-saturated incompressible porous media. *Archive of Applied Mechanics*, 63(1):59–72, jan 1993. URL https://doi.org/10.1007/BF00787910.

E. de Souza Neto, P. Blanco, P. Sánchez, and R. Feijóo. An RVE-based multiscale theory of solids with micro-scale inertia and body force effects. *Mechanics of Materials*, 80: 136–144, 2015. URL https://doi.org/10.1016/j.mechmat.2014.10.007.

S. Diebels and W. Ehlers. Dynamic analysis of a fully saturated porous medium accounting for geometrical and material non-linearities. *International Journal for Numerical Methods in Engineering*, 39:81–97, 1996. URL https://doi.org/10.1002/(SICI)1097-0207(19960115)39:1⟨81::AID-NME840⟩3.0.CO;2-B.

W. E and B. Engquist. The heterogeneous multiscale methods. *Communications in Mathematical Sciences*, 1:87–132, 2003.

Y. Efendiev and T. Hou. *Multiscale Finite Element Methods - Theory and Applications*. Springer, 2009. URL https://doi.org/10.1007/978-0-387-09496-0.

W. Ehlers. *Poröse Medien - ein kontinuummechanisches Modell auf der Basis der Mischungstheorie*. Habilitationsschrift, Universität - Gesamthochschule - Essen, 1989.

W. Ehlers. Foundations of multiphasic and porous materials. In W. Ehlers and J. Bluhm, editors, *Porous media*, pages 3–86. Springer, 2002. URL https://doi.org/10.1007/978-3-662-04999-0_1.

B. Eidel and A. Fischer. The heterogeneous multiscale finite element method for the homogenization of linear elastic solids and a comparison with the FE^2 method. *Computer Methods in Applied Mechanics and Engineering*, 329:332–369, 2018. URL https://doi.org/10.1016/j.cma.2017.10.001.

F. Feyel and J.-L. Chaboche. FE^2 multiscale approach for modelling the elastoviscoplastic behavior of long fibre SiC/Ti composite materials. *Computer Methods in Applied Mechanics and Engineering*, 183:309–330, 2000. URL https://doi.org/10.1016/S0045-7825(99)00224-8.

J. Fish. *Practical multiscaling*. Wiley, 2014.

S. Forest. Homogenization methods and the mechanics of generalied continua, part 2. *Theoretical and Applied Mechanics*, 28–29:113–143, 2002. URL https://doi.org/10.2298/TAM0229113F.

M. Geers, V. Kouznetsova, and W. Brekelmans. Multi-scale computational homogenization: Trends and challenges. *Journal of Computational and Applied Mathematics*, 234 (7):2175–2182, 2010. URL https://doi.org/10.1016/j.cam.2009.08.077.

R. J. Guyan. Reduction of stiffness and mass matrices. *AIAA Journal*, 3(2):380–380, 1965. URL https://doi.org/10.2514/3.2874.

R. Hill. A self–consistent mechanics of composite materials. *Journal of the Mechanics and Physics of Solids*, 13:213–222, 1965. URL https://doi.org/10.1016/0022-5096(65)90010-4.

G. A. Holzapfel. *Nonlinear Solid Mechanics - A continuum Approach for Engineering*. John Wiley & Sons, LTD, 2000.

T. Y. Hou and X.-H. Wu. A Multiscale Finite Element Method for Elliptic Problems in Composite Materials and Porous Media. *Journal of Computational Physics*, 134(1): 169–189, 1997. ISSN 0021-9991. URL https://doi.org/10.1006/jcph.1997.5682.

T. Hughes. Multiscale phenomena: Green's functions, the Dirichlet-to-Neumann formulation, subgrid scale models, bubbles and the origins of stabilized methods. *Computer Methods in Applied Mechanics and Engineering*, 127:387–401, 1995. URL https://doi.org/10.1016/0045-7825(95)00844-9.

A. Hund and E. Ramm. Locality constraints within multiscale model for non-linear material behaviour. *International Journal for Numerical Methods in Engineering*, 70: 1613–1632, 2007. URL https://doi.org/10.1002/nme.1953.

A. Ibrahimbegović and D. Markovič. Strong coupling methods in multi-phase and multi-scale modeling of inelastic behavior of heterogeneous structures. *Computer Methods in Applied Mechanics and Engineering*, 192:3089–3107, 2003. URL https://doi.org/10.1016/S0045-7825(03)00342-6.

R. Jänicke and S. Diebels. Numerical homogenisation of micromorphic media. *Technische Mechanik*, 30:364–373, 2010.

R. Jänicke, B. Quintal, and H. Steeb. Numerical homogenization of mesoscopic loss in poroelastic media. *European Journal of Mechanics, A/Solids*, 49:382–395, 2015. URL https://doi.org/10.1016/j.euromechsol.2014.08.011.

J. Korelc. Automation of primal and sensitivity analysis of transient coupled problems. *Computational Mechanics*, 44(5):631–649, 2009. URL https://doi.org/10.1007/s00466-009-0395-2.

J. Korelc and P. Wriggers. *Automation of finite element methods*. Springer, 2016. URL https://doi.org/10.1007/978-3-319-39005-5.

V. Kouznetsova, W. Brekelmans, and F. Baaijens. An approach to micro-macro modeling of heterogeneous materials. *Computational Mechanics*, 27:37–48, 2001. URL https://doi.org/10.1007/s004660000212.

V. Kouznetsova, M. G. D. Geers, and W. A. M. Brekelmans. Multi-scale constitutive modelling of heterogeneous materials with a gradient-enhanced computational homogenization scheme. *International Journal for Numerical Methods in Engineering*, 54(8): 1235–1260, 2002. URL https://doi.org/10.1002/nme.541.

F. Larsson and K. Runesson. On two-scale adaptive FE analysis of micro-heterogeneous media with seamless scale-bridging. *Computer Methods in Applied Mechanics and Engineering*, 200(37):2662–2674, 2011. URL https://doi.org/10.1016/j.cma.2010.10.012.

S. Maike, J. Bluhm, J. Schröder, D. Brands, and T. Ricken. Macroscopic characterization of porous unit cells within the framework of the theory of porous media. In A. Zingoni, editor, *Insights and Innovations in Structural Engineering, Mechanics and Computation*. CRC Press, 2016. URL https://doi.org/10.1201/9781315641645.

S. Maike, J. Schröder, J. Bluhm, and T. Ricken. Application of the Theory of Porous Media to the Mesh-in-Element Method. *Computer Methods in Applied Mechanics and Engineering*, 2023. to be submitted.

K. Mandadapu, A. Sengupta, and P. Papadopoulos. A homogenization method for thermomechanical continua using extensive physical quantities. *Proceedings of the Royal Society London A*, 468:1696–1715, 2012. URL https://doi.org/10.1098/rspa.2011.0578.

J. Mandel. Plasticité classique et viscoplasticité. In *CISM course Nr. 97*. Springer, 1972.

B. Markert, Y. Heider, and W. Ehlers. Comparison of monolithic and splitting solution schemes for dynamic porous media problems. *International Journal for Numerical Methods in Engineering*, 82(11):1341–1383, 2010. URL https://doi.org/10.1002/nme.2789.

D. Markovič and A. Ibrahimbegović. On micro-macro interface conditions for micro scale based FEM for inelastic behavior of heterogeneous materials. *Computer Methods in Applied Mechanics and Engineering*, 193:5503–5523, 2004. URL https://doi.org/10.1016/j.cma.2003.12.072.

D. Markovič, R. Niekamp, A. Ibrahimbegović, H. Matthies, and R. Taylor. Multi-scale modeling of heterogeneous structures with inelastic constitutive behaviour: Part I - physical and mathematical aspects. *Engineering Computations*, 22(5-6):664–683, 2005. URL https://doi.org/10.1108/02644400910924780.

C. Miehe, J. Schotte, and J. Schröder. Computational micro-macro transitions and overall moduli in the analysis of polycrystals at large strains. *Computational Materials Science*, 16(1-4):372–382, 1999a. URL https://doi.org/10.1016/S0927-0256(99)00080-4.

C. Miehe, J. Schröder, and J. Schotte. Computational homogenization analysis in finite plasticity. Simulation of texture development in polycrystalline materials. *Computer Methods in Applied Mechanics and Engineering*, 171(3-4):387–418, 1999b. URL https://doi.org/10.1016/S0045-7825(98)00218-7.

S. Nemat-Nasser and M. Hori. *Micromechanics: Overall Properties of Heterogeneous Materials*. North Holland, 2 edition, 1999.

R. Niekamp, D. Markovič, A. Ibrahimbegović, H. Matthies, and R. Taylor. Multi-scale modelling of heterogeneous structures with inelastic constitutive behavior: Part II - software coupling implementation aspects. *Engineering Computations*, 26(1/2):6–28, 2009. URL https://doi.org/10.1108/02644400910924780.

K. Park and C. Felippa. A variational principle for the formulation of partitioned structural systems. *International Journal for Numerical Methods in Engineering*, 47:395–418, 2000. URL https://doi.org/10.1002/(SICI)1097-0207(20000110/30)47:1/3⟨395::AID-NME777⟩3.0.CO;2-9.

T. Ricken, J. Schröder, J. Bluhm, S. Maike, and F. Bartel. Theoretical formulation and computational aspects of a two-scale homogenization scheme combining the TPM and FE^2 method for poro-elastic fluid-saturated porous media. *International Journal of Solids and Structures*, 241:111412, 2022. URL https://doi.org/10.1016/j.ijsolstr.2021.111412.

S. Ricker, J. Mergheim, and P. Steinmann. On the multiscale computation of defect driving forces. *International Journal for Multiscale Computational Engineering*, 7:457–474, 2009. URL https://doi.org/10.1615/IntJMultCompEng.v7.i5.70.

E. Sanchez-Palencia. *Non-Homogeneous Media and Vibration Theory*, volume 127 of *Lecture Notes in Physics*. Springer, Berlin, 1980.

J. Schröder. A numerical two-scale homogenization scheme: the FE^2-method. In J. Schröder and K. Hackl, editors, *Plasticity and Beyond: Microstructures, Crystal-Plasticity and Phase Transitions*. Springer, 2014. URL https://doi.org/10.1007/978-0-387-09496-0.

J. Schröder, R. de Boer, and J. Bluhm. *Tensor Calculus for Engineers with Applications to Continuum and Computational Mechanics*. Springer, 2024. to appear.

R. Smit, W. Brekelmans, and H. Meijer. Prediction of the mechanical behavior of nonlinear heterogeneous systems by multi-level finite element modeling. *Computer Methods in Applied Mechanics and Engineering*, 155:181–192, 1998. URL https://doi.org/10.1016/S0045-7825(97)00139-4.

E. Stein and F.-J. Barthold. Elastizitätstheorie. In G. Mehlhorn, editor, *Der Ingenieurbau: Grundwissen*. Ernst and Sohn, 1996.

E. Tamsen and D. Balzani. A general, implicit, finite-strain FE^2 framework for the simulation of dynamic problems on two scales. *Computational Mechanics*, 67(5):1375–1394, 2021. URL https://doi.org/10.1007/s00466-021-01993-8.

C. Taylor and P. Hood. A numerical solution of the Navier-Stokes equations using the finite element technique. *Computers and Fluids*, 1:73–100, 1973. URL https://doi.org/10.1016/0045-7930(73)90027-3.

R. L. Taylor and S. Govindjee. *FEAP - A Finite Element Analysis Program, Version 8.6 User Manual*. Department of Civil and Environmental Engineering, University of California at Berkeley, 2020.

K. Terada, M. Hori, T. Kyoya, and N. Kikuchi. Simulation of the multi-scale convergence in computational homogenization approach. *International Journal of Solids and Structures*, 37:2285–2311, 2000. URL https://doi.org/10.1016/S0020-7683(98)00341-2.

C. Truesdell. *Rational thermodynamics*. Springer, 2nd edition, 1984.

C. Truesdell and W. Noll. *The Non-Linear Field Theories of Mechanics*. Springer, third edition, 2004.

C. Truesdell and R. Toupin. The Classical Field Theories. In S. Flügge, editor, *Principles of Classical Mechanics and Field Theory*, Encyclopedia of Physics. Springer, 1960. URL https://doi.org/10.1007/978-3-642-45943-6_2.

Wolfram Research, Inc. *Mathematica, Version 12.3*. 2021.

P. Wriggers. *Nonlinear finite element methods*. Springer, 2008. URL https://doi.org/10.1007/978-3-540-71001-1.

O. G. Zienkiewicz, R. L. Taylor, and J. Z. Zhu. *The Finite Element Method: Its Basis and Fundamentals*. Butterworth-Heinemann, 7 edition, 2013. URL https://doi.org/10.1016/C2009-0-24909-9.

N. Zupan and J. Korelc. Unified approach to sensitivity analysis based automation of multi-scale modelling. In J. Sorić, P. Wriggers, and O. Allix, editors, *Multiscale modeling of heterogeneous structures*. Springer, 2018. URL https://doi.org/10.1007/978-3-319-65463-8.

N. Zupan and J. Korelc. Sensitivity analysis based multi-scale methods of coupled path-dependent problems. *Computational Mechanics*, 65:229–248, 2020. URL https://doi.org/10.1007/s00466-019-01762-8.

Der Lebenslauf ist in der Online-Version aus Gründen des Datenschutzes nicht enthalten.

In dieser Schriftenreihe bisher erschienene Berichte:

Nr. 1 (2004) *Ein Modell zur Beschreibung finiter anisotroper elastoplastischer Deformationen unter Berücksichtigung diskreter Rissausbreitung*, J. Löblein, Dissertation, 2004.

Nr. 2 (2006) *Polyconvex Anisotropic Energies and Modeling of Damage applied to Arterial Walls*, D. Balzani, Dissertation, 2006.

Nr. 3 (2006) *Kontinuumsmechanische Modellierung ferroelektrischer Materialien im Rahmen der Invariatentheorie*, H. Romanowski, Dissertation, 2006.

Nr. 4 (2007) *Mehrskalen-Modellierung polykristalliner Ferroelektrika basierend auf diskreten Orientierungsverteilungsfunktionen*, I. Kurzhöfer, Dissertation, 2007.

Nr. 5 (2007) *Proceedings of the First Seminar on the Mechanics of Multifunctional Materials*, J. Schröder, D.C. Lupascu, D. Balzani (Ed.), Tagungsband, 2007.

Nr. 6 (2008) *Zur Modellierung und Simulation diskreter Rissausbreitungsvorgänge*, O. Hilgert, Dissertation, 2008.

Nr. 7 (2009) *Least-Squares Mixed Finite Elements for Solid Mechanics*, A. Schwarz, Dissertation, 2009.

Nr. 8 (2010) *Design of Polyconvex Energy Functions for All Anisotropy Classes*, V. Ebbing, Dissertation, 2010.

Nr. 9 (2012) *Modeling of Electro-Mechanically Coupled Materials on Multiple Scales*, M.-A. Keip, Dissertation, 2012.

Nr. 10 (2012) *Geometrical Modeling and Numerical Simulation of Heterogeneous Materials*, D. Brands, Dissertation, 2012.

Nr. 11 (2012) *Modeling and simulation of arterial walls with focus on damage and residual stresses*, S. Brinkhues, Dissertation, 2012.

Nr. 12 (2014) *Proceedings of the Second Seminar on the Mechanics of Multifunctional Materials*, J. Schröder, D.C. Lupascu, M.-A. Keip, D. Brands (Ed.), Tagungsband, 2014.

Nr. 13 (2016) *Mixed least squares finite element methods based on inverse stress-strain relations in hyperelasticity*, B. Müller, Dissertation, 2016.

Nr. 14 (2016) *Electromechanical Modeling and Simulation of Thin Cardiac Tissue Constructs*, R. Frotscher, Dissertation, 2016.

Nr. 15 (2017) *Least-squares mixed finite elements for geometrically nonlinear solid mechanics*, K. Steeger, Dissertation, 2017.

Nr. 16 (2017) *Scale-Bridging of Elasto-Plastic Microstructures using Statistically Similar Representative Volume Elements*, L. Scheunemann, Dissertation, 2017.

Nr. 17 (2018) *Modeling of Self-healing Polymers and Polymeric Composite Systems*, S. Specht, Dissertation, 2017.

Nr. 18 (2018) *Proceedings of the Third Seminar on the Mechanics of Multifunctional Materials*, J. Schröder, D.C. Lupascu, H. Wende, D. Brands (Ed.), Tagungsband, 2018.

Nr. 19 (2018) *Least-squares finite element methods with applications in fluid and solid mechanics*, C. Nisters, Dissertation, 2018.

Nr. 20 (2018) *A two-scale homogenization scheme for the prediction of magneto-electric product properties*, M. Labusch, Dissertation, 2018.

Nr. 21 (2019) *Modeling the passive mechanical response of soft tissues: constitutive modeling approaches, efficient parameter selection and subsequent adjustments due to residual stresses*, M. von Hoegen, Dissertation, 2019.

Nr. 22 (2019) *Constitutive modeling of female pelvic floor dysfunctions and reconstructive surgeries using prosthetic mesh implants*, A. Bhattarai, Dissertation, 2019.

Nr. 23 (2019) *A contribution to stress-displacement based mixed galerkin finite elements for hyperelasticity*, N. Viebahn, Dissertation, 2019.

Nr. 24 (2020) *Gefrier- und Auftauprozesse in gesättigten porösen Materialien - ein Modellierungskonzept im Rahmen der Theorie poröser Medien*, W.M. Bloßfeld, Dissertation, 2020.

Nr. 25 (2021) *Electromechanical modelling and simulation of hiPSC-derived cardiac cell cultures*, A. Jung, Dissertation, 2021.

Nr. 26 (2021) *Mixed and Hybrid Least-Squares FEM in Nonlinear Solid Mechanics*, M. Igelbüscher, Dissertation, 2021.

Nr. 27 (2023) *The Material Point Method for dynamic Metal Processing*, S. Maassen, Dissertation, 2023.

Nr. 28 (2023) *Modeling of Fluid-Structure Interactions with the Least-Squares FEM*, S. Averweg, Dissertation, 2023.

Nr. 29 (2023) *Numerical simulation of microstructural residual stresses of hot bulk forming parts with targeted cooling*, S. Hellebrand, Dissertation, 2023.

DOI: 10.17185/duepublico/82058
URN: urn:nbn:de:hbz:465-20240703-070049-7